EXPERIMENTAL INVESTIGATION OF A COMPACT HEAT EXCHANGER FOR THERMAL ENERGY STORAGE IN SUSTAINABILITY APPLICATIONS (FOR MITIGATING ENERGY-WATER NEXUS ISSUES)

A Thesis

by

RYAN MICHAEL VON NESS

Submitted to the Office of Graduate and Professional Studies of
Texas A&M University
in partial fulfillment of the requirements for the degree of

MASTER OF SCIENCE

Chair of Committee,	Debjyoti Banerjee
Committee Members,	Karen Kirkland
	David Claridge
	Morad Atif
Head of Department,	Andreas A. Polycarpou

December 2018

Major Subject: Mechanical Engineering

ABSTRACT

The application of a compact heat exchanger (CHX) as a latent heat thermal storage system (LHTESS) was explored in this study by employing phase change materials (PCM), for supplementing cooling loads of a dry-cooling platform. The melting and solidification times for a fixed mass of a chosen PCM was estimated from temperature measurements (recorded experimentally using a digital data acquisition system) performed in this study. A salt hydrate (lithium nitrate trihydrate) was chosen as the PCM for this study. The experiments were performed by varying the inlet temperature and flow rate, as well as the flow direction of the heat transfer fluid (HTF). Furthermore, the chosen CHX was fortified by filling it with aluminum porous foam that is impregnated with the chosen PCM.

The "*Cold-finger*" technique was implemented during the experiments to enhance the reliability of the TES system. This unique technique is implemented by leaving a fraction of the PCM mass solidified (which ensures partial melting of the PCM instead of complete melting) while thermal cycling experiments were performed involving repeated partial melting and complete solidification of the fixed mass of PCM in the CHX. These thermal cycling experiments were performed to monitor the range of subcooling required to initiate solidification. The "*Cold Finger"* technique enhances the reliability of these systems by enabling low values of subcooling. Complete melting can often cause the degree of subcooling required to initiate solidification to increase with each thermal cycle – thus compromising the reliability of the LHTESS. Hence, the *Cold Finger* technique is an effective strategy for

mitigating the reliability issues endemic with various PCMs, particularly salt-hydrates. The results obtained in this study demonstrate that subcooling of less than 1 °C was achieved by combining the Cold Finger strategy with counter-flow configuration of the CHX, thus realizing a LHTESS with enhanced reliability. The experimental results also show that flow rate and inlet temperature of the HTF do not significantly affect the level of subcooling.

The repeated thermal cycling experiments performed in this study show that the melting and freezing time are sensitive to both flow rate and inlet temperature of the HTF. The values for melting time and freezing time are more sensitive to the variations in the inlet temperature (than that of the flow rate of the HTF). Increasing the flow rate to achieve the same levels of instantaneous power ratings are associated with higher values of pump penalty to achieve the same goals. Hence, varying the inlet temperature of the HTF is a more effective strategy for enhancing the power rating of the LHTESS explored in this study. The experimental results also show that the uncertainty in estimating the energy storage capacity rating of the LHTESS in this study increases due to parasitic heat transfer (heat loss or gain from the surroundings). For the design conditions explored in this study, the achieved level of cooling exceeds 7 °C (which is more than the specified value of 5 °C targeted in this study). The effectiveness during melting was ~0.8 and during solidification was ~1 for the design conditions explored in this study (which is deemed to be adequate for the program requirements of this sponsored research project).

ACKNOWLEDGEMENTS

I would like to thank my committee chair, Dr. Banerjee, and my committee members, Dr. Vierow Kirkland, Dr. Atif, Dr. Claridge, and Dr. Dooley, for their guidance and support throughout the course of this research. This work was supported by ARPA-E (ARID) program, which consisted of an investigation team comprised of personnel from University of Cincinnati (Lead Institution), University of California at Berkeley, University of California at Los Angeles (UCLA), Boeing, EvapCo, and Maulbetsch Consulting. In addition, I would like to acknowledge support I received from various sources for performing research tasks at the Multi-Phase Flows and Heat Transfer Laboratory (MPFHTL), which also includes: Marine Robotic Vehicle (MRV) Systems, and the National Science Foundation Innovation Corps Program (NSF-ICorps).

Acknowledgements are also extended to Mr. Navin Kumar who synthesized and measured the thermal properties of the lithium nitrate trihydrate (section 2.2.1). Furthermore, I would like to acknowledge his contributions to setting up the experimental apparatus and his advice and guidance throughout the course of this research.

Thanks also to my friends, colleagues and the department faculty and staff for making my time at Texas A&M University a great experience. Finally, thanks to my mother, father, and sister for their encouragement.

CONTRIBUTORS AND FUNDING SOURCES

Contributors

This work was supervised by a dissertation committee consisting of Professor Debjyoti Banerjee (Advisor), Professor David Claridge of the Department of Mechanical Engineering, Morad Atif of the Department of Architectural Engineering, and Professor Karen Kirkland of the Department of Nuclear Engineering. The experimental work for section 2.1.1 was conducted by Navin Kumar of Texas A&M Department of Mechanical Engineering. Navin Kumar also assisted in the experimental setup (section 2.1).

All other work conducted for the thesis (or) dissertation was completed by the student independently.

Funding Sources

My graduate studies were supported by funding from the Department of Energy ARPA-E ARID Program under the Grant Number [DE-FOA-00001002]. This work was also made possible in part by funding from the Department of Engineering Academic and Student Affairs (e.g., for my Teaching Assistantships) at Texas A&M University. Its contents are solely the responsibility of the authors and do not necessarily represent the official views of the Department of Energy.

NOMENCLATURE

CHX	Compact Heat Exchanger
c_p	Specific heat (J/kg-K)
E	Energy
HTF	Heat Transfer Fluid
h_{fs}	Latent heat of fusion
LHTESS	Latent Heat Thermal Energy Storage System
LHTS	Latent Heat Thermal Storage
m	Mass
$\dot{m}$	Mass flowrate
P	Power
PCM	Phase Change Material
PHE	Plate Heat Exchanger
Pr	Prandtl Number
Re	Reynold's Number
TES	Thermal Energy Storage
T	Temperature
ΔT	Temperature difference
u	Statistical uncertainty
$\dot{V}$	Volumetric flow rate

Greek symbols

ε	Effectiveness
ρ	Density

Subscripts

avg	Average

TABLE OF CONTENTS

Page

LIST OF FIGURES

Page

LIST OF TABLES

Page

1 INTRODUCTION

1.1 Background

Currently in the U.S., the amount of fresh water utilized by power plants annually is more than the total human consumption of fresh water. With rising population trends nationally, there is increasing pressure on fresh water resources in the U.S. The bulk of the fresh water usage in the power plants is primarily for wet cooling (e.g., in cooling towers used for condensing the steam output from turbines). For example, ~41% of the total freshwater withdrawals are being used in thermoelectric power plants. In addition, ~3% of that freshwater is consumed completely (i.e., not returned directly to outside source) [1]. Switching to dry-cooling techniques is an effective way to mitigate this issue (only ~10% water withdrawals will be necessary when compared to ~41% for wet-cooling) [2]. Furthermore, there is no loss of water to evaporation for this technique. Thus, both water withdrawal and consumption are minimal. However, dry-cooling techniques are typically more expensive, less efficient than wet-cooling techniques, and considered unreliable (these power plants must shut down during peak hours of the day in hot weather). Thermal energy storage (TES) systems can be used to address the current drawbacks associated with dry-cooling techniques by serving as a supplemental cooling system.

With rising energy demand, increasing population, and heightened pressures on the fresh water resources, there is a need to shift to more sustainable practices involving more efficient power production with less waste. One approach to address

this issue involves switching from wet-cooling to dry-cooling. Dry-cooling can confer several advantages when supplemented with thermal energy storage (TES) systems.

A novel approach involves TES systems that utilize phase change materials (PCMs) with high latent heat storage values. PCMs are utilized in a variety of applications to either store or release energy by leveraging the high enthalpy associated with phase transition (e.g., melting and solidification). A brief overview of heat exchangers leveraging PCMs is provided next as a prelude to the exploration of the primary components of TES systems.

1.1.1 Phase Change Materials

In recent years, phase change materials (PCMs) have been explored in the research literature for thermal energy storage applications. The high latent heat of fusion values that PCMs exhibit has enabled their successful implementation in various applications. The phase transition can happen in three different ways: solid-liquid, solid-solid, and gas-liquid. The solid-liquid phase transition is typically employed in a majority of engineering applications involving PCMs because it is associated with smaller changes in volume for a given operating pressure and temperature. While the solid-solid phase transition phenomena provide all the benefits of the solid-liquid phase transition process, it suffers the disadvantage of having the lowest energy density of all the three types discussed here. The gas-liquid phase transition typically has the highest energy density but comes at the cost of a large changes in volume and pressure.

Typically, phase change materials (PCM) can be classified into three different categories: organic, inorganic, and eutectic. Organic PCMs are typically procured from natural resources and are generally inexpensive. Organic PCMs confer better reliability due to their noncorrosive properties. Despite the low cost and reliability, organic materials suffer from disadvantages arising from low thermal conductivity, lower melting points that are not well-defined (the mixtures of organic molecules in organic PCMs have phase transitions occurring over a range of temperatures rather than at a fixed point), and small ranges of operating temperatures (organic materials often become chemically unstable at elevated temperatures). Sometimes organic PCMs can also pose potential fire hazards. Inorganic PCMs typically consist of metals (usually with low melting points) or salts (either, pure/ anhydrous or chemically hydrated). Inorganic PCMs tend to have higher thermal conductivity values than organic PCMs but suffer from drawbacks associated with lower reliability during operation. The lower reliability accrues from phase segregation and often require high subcooling to initiate solidification (which in turn affects the reliability, since the degree of subcooling can change drastically with each thermal cycle involving complete melting and solidification). The third category, PCM eutectics, are comprised of two or more pure components mixed in a specific mass ratio. PCM eutectics tend to be higher cost options for a chosen TES.

Review of PCMs were reported by Kulacki [3], Abhat [4], Rathod and Banerjee [5], Zalba, et al. [6], and Sharma, et al. [7]. In these reviews PCMs were classified based on the material types and their thermo-physical properties. The brief

review provided here, is therefore primarily focused on studies in the literature involving heat exchangers with various architectures that were integrated with different types of PCMs for thermal energy storage (TES) applications.

*1.1.2 Heat Exchangers**

Heat exchangers are probably one of the most widely used platforms in any industry that involves heating or cooling. Typically, heat exchangers consist of a heat transfer element (core or matrix) and fluid distribution elements (manifolds, inlets and outlet pipes, seals, etc.). Heat exchangers can be classified based on flow configurations (parallel flow, counter flow, cross flow, etc.), mass flow rates, surface area to volume ratios (degree of compactness), modes of heat flux (e.g., with or without phase change) or heat transfer mechanisms (with or without radiation), etc. The thermal design of a heat exchanger is often performed using commercial or proprietary codes involving computational fluid dynamics (CFD)/ computational heat transfer (CHT). These simulations are performed to optimize the design of a heat exchanger. These design tasks often involve determination of the power rating and size of heat exchangers for a given set of constraints (e.g., operating temperatures, heating/ cooling loads, duty cycles, materials, fixed and operating costs, fouling/ corrosion over the life-cycle, etc.).

*Section 1.1.2 through 1.1.2.7 is an overview of heat exchangers paraphrased from Chapter 1 of [8]. This information is generally considered common knowledge; however, this source is used to give more depth to the content.

The power rating issues are often limited by the heat transfer rate constraints and the need to minimize pump penalty (i.e., to reduce the pressure drop for fluid flow in the heat exchanger). Some of the parameters/ inputs used in the design process include: geometry, size, flow arrangements (and flow rates), materials, fouling factors, and terminal inlet temperatures. The input parameters are then used to calculate the fluid outlet temperatures, total heat transfer rates, and pressure drop across the heat exchanger.

The sizing issues also involve the determination and selection of geometry/ configuration, flow direction, and material properties of the heat exchanger to achieve the specified heat transfer rates and pressure drop values for a given range of flow rates of the HTF. For a tubular heat exchanger, the size considerations depend primarily on the shell configurations (number of passes, type, diameter, and length) and tube (number of passes, diameter, number, layout, surface texturing, and pass arrangement). For plate heat exchangers, the sizing problem depends on the plate configuration (type, size, number, pass arrangement, surface texturing, etc.) and the gasket type.

Heat exchangers can also be classified as direct-contact and indirect-contact heat exchangers. In direct-contact heat exchangers, the hot and cold fluid streams mix (unless they are immiscible). These heat exchangers confer advantages such as high heat transfer rates, inexpensive construction, and minimal fouling. However, these heat exchangers are limited to applications where the two fluids are mutually

compatible. In indirect contact heat exchangers, the hot and cold fluids are separated by a surface that prevents the physical mixing of the two fluid streams. Indirect-contact heat exchangers are used more commonly then direct-contact heat exchangers and can be further classified into: direct-transfer type, storage type, and fluidized-bed exchanger. A schematic depicting the classification of different types of heat exchangers is shown in Figure 1 below.

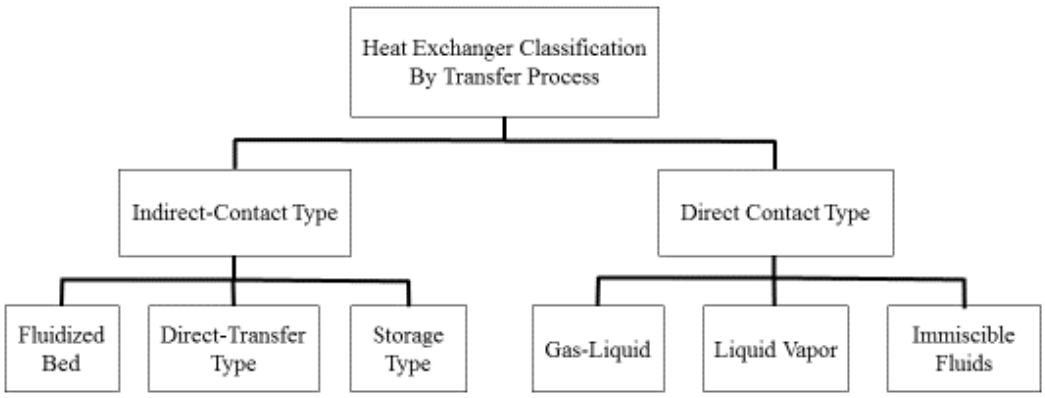

Figure 1: Heat Exchanger Classification, modified from [8].

The focus of this brief review will be limited to indirect-contact heat exchangers that are classified as tubular, plate, compact, and extended surface heat exchangers. Figure 2 shows a classification of the heat exchanger architectures.

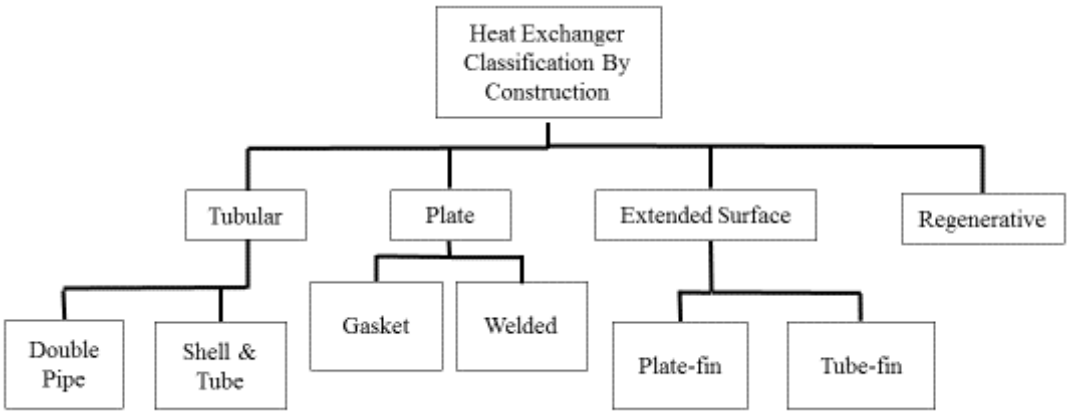

Figure 2: Classification of Heat Exchanger Architectures, modified from [8].

1.1.2.1 Tubular Heat Exchangers

Tubular heat exchangers typically operate at extreme pressures (very high pressures or in high vacuum) and for high values of pressure-differentials. The tubes are typically arranged in a circular assembly. Applications with rectangular or twisted tubes are also quite common. Design constraints typically mitigated by this type of heat exchangers involve limitations in size (e.g., tube length), diameter, and arrangements for the pipe arrays (e.g., staggered, rectangular, or circular layouts). Tubular heat exchangers are further classified into two categories: shell-and-tube and double-pipe arrangements.

1.1.2.2 Shell-and-Tube Heat Exchangers

Shell-and-tube heat exchangers are the most commonly used heat exchangers in commercial applications, particularly in process industries. Variation in the internal architectures of these heat exchangers is used to meet various targets involving desired

heat transfer and pressure drop requirements. Key advantages of using these heat exchangers is reduced thermal stresses, minimized leakage, ease of cleaning, ease of retrofitting (and plant maintenance), corrosion control (or monitoring), and accommodation of high asymmetric flows. In addition, they provide flexibility in modulating operating capacity in response to change in operating conditions. Hence, this enables operation over a large range of temperatures — from cryogenic conditions to high temperatures of ~1100 °C. Shell-and-tube heat exchangers are primarily limited by the materials used in their design. This is one of the main reasons they are used so extensively in process industries (such as petroleum or chemical processing industries).

The three most common types of shell-and-tube tube heat exchangers are: (1) fixed tube sheet design, (2) U-tube design, and (3) floating-head type. In most designs, the front head is fixed and the rear head is floating (allowing for anomalous thermal expansion). The major considerations for the front head heat exchangers are cost, maintenance, and operating pressures, while the major considerations for the rear head heat exchangers are allowance for thermal stress, removability (for cleaning), prevention of mixing, and minimized leakage. Furthermore, baffles can also be implemented into shell-and-tube heat exchangers (transverse and longitudinal types). The longitudinal baffles are primarily used to control overall flow direction while the transverse baffles are used to primarily support tubing during assembly and operation. The type of baffle used is largely determined by the desired heat transfer rates, flow rates, and allowable pressures. Other notable types of this heat exchanger include:

serpentine, helical, and bayonet tubes. In general, shell-and-tube heat exchangers could be used for just about any process application, considering their many advantages and multiple configurations available commercially off the shelf (COTS). Shell-and-tube heat exchangers are commonly used in steam generators, condensers, boiler feed water heaters, waste heat recovery applications, and oil coolers in power plants.

1.1.2.3 Double-Pipe Heat Exchangers

Double-pipe heat exchangers consist primarily of two concentric pipes with an inner pipe plain (sometimes finned). For these heat exchangers, one fluid flows through the inner tube and the other flows through the annular space. Typically counter flow heat exchangers are utilized in high performance applications. Parallel flow heat exchangers are used for constant wall temperature applications (e.g., for ensuring process safety). The double-pipe is one of the simplest configurations and confers several advantages, such as for minimizing anomalous flow distribution and for applications requiring less cleaning. Double-pipe heat exchangers are primarily used for small-capacity applications (for surface area typically less than $50m^2$) because they are relatively inexpensive (i.e., on the cost per unit area basis).

1.1.2.4 Plate Heat Exchangers

Plate heat exchangers (PHE) are usually realized by assembling multiple thin plates that can be either flat or corrugated. PHEs typically have a higher heat transfer

coefficient (about twice that of the shell-and-tube heat exchangers) and are not desirable for high pressure or high temperature applications. They are further broken down into the categories of gasket, welded, and brazed (each type greatly affects the amount of leakage). This review is limited to gasket and welded heat exchangers (esoteric PHEs are considered to be beyond the scope of this brief review).

1.1.2.5 Gasket Plate Heat Exchangers

Gasket plate heat exchangers have several thin plates (typically with a corrugated surface pattern) with gaskets sealing the edges, which is then held together with a frame. Because of the stacked thin plates, the flow passages are narrow, turbulent, and fouling resistant (which is attributed to the increases in shear stress). Furthermore, the plate is designed to be "hard" or "soft" based on the value of turbulence.

Gaskets are typically designed to compress to about 20–25% of their original thickness. This, in turn, provides leak tight joints without distorting the plates. Gaskets can be cemented or snapped on to the plate; some typical gasket materials are butyl, nitrile, silicone, and ethylene propylene rubber. However, in higher operating temperatures it is common to find gaskets made of compressed asbestos fiber and fluorinated rubber. The plate material is typically composed of materials—such as metals/alloys—that can be cold worked. High corrosion resistance is often desirable for the plate material. Applications involving highly corrosive fluids typically utilize graphite or polymer plates.

The key advantage of gasket plate heat exchangers is that they can be easily disassembled for cleaning and maintenance. Additional advantages include: flexibility for assembly/ disassembly (i.e., for swiftly increasing/ decreasing the capacity and power rating), the ability to handle high shear rates as well as high shear stresses, turbulence, and mixing (especially for plates with corrugation patterns). These features enable reduction in fouling (typically by 10 ~ 25%) and reduction in surface area (typically by 50%) compared to that of a shell-and-tube heat exchanger for the same application(s). With fouling being a huge issue in process industries (e.g., in petro-chemicals), this type of heat exchanger is often employed in these industries to mitigate operational issues.

Furthermore, the dead volume within plate heat exchangers is quite small and therefore less fluid is wasted during maintenance cycles (especially for expensive process chemicals). The high thermal effectiveness also facilitates economical low-grade heat recovery. Lastly, flow-induced vibrations, noise, thermal stresses, and entry impingement problems encountered in tubular heat exchangers are often obviated in plate heat exchangers.

Although gasket plate heat exchangers confer a multitude of advantages, they do have some disadvantages. Design conditions for plate heat exchangers typically do not allow for more than a maximum gauge pressure of 3 MPa. The gasket material restricts the use of plate heat exchangers in highly corrosive applications. Furthermore, the maximum temperature for gaskets is around 260 °C, where cheaper gaskets usually operate below 150 °C. Pinhole leaks are also hard to detect, and gasket life can be

limited (requiring frequent replacement). They are also not suited for toxic fluid applications that require prevention of any leakages. In general, gasket plate heat exchangers are commonly used in power plants, process industries (e.g., dairy, fruit juice/beverage, pharmaceutical, and biochemical industries). Applications requiring liquid-liquid heat transfer and easy cleaning as well as strict thermal control also utilize this type of heat exchangers (e.g., synthetic rubber, paper mills, and closed-circuit cooling systems).

1.1.2.6 Welded and Brazed Plate Heat Exchangers

Welded and brazed heat exchangers are often used for applications involving corrosive fluids, extreme operating temperatures, and pressure limitations (parameters which prevent the usage of gasket plate heat exchangers). The downside to this configuration is that welded and brazed heat exchangers are typically larger than the gasket PHE and often more expensive (due to the additional cost of welding or brazing). While this confers the advantage of a higher operating temperature (~350 °C) and pressure (~4 MPa), there is a loss of flexibility since these PHEs cannot be disassembled. These heat exchangers are typically made with materials such as stainless steel, copper, and titanium.

1.1.2.7 Compact Heat Exchangers

Compact heat exchangers are notable for their high surface area to volume ratio (β). This results in reduced form factors (space, size), weight, support structure, energy

requirements, cost, and low fluid inventory (where lower mass is often a higher priority than lower volume). In order to be classified as a compact heat exchanger, the surface area to volume ratio must be as follows [3]:

$$\text{Liquid or Two Phase Stream Side} \rightarrow \beta > 400 \text{ m}^2/\text{m}^3$$

$$\text{Gas Stream Side} \rightarrow \beta > 700 \text{ m}^2/\text{m}^3$$

where, β is the effective surface density for heat transfer and is often defined for a non-turbulent heat exchanger. Very few shell-and-tube heat exchangers fall under the classification of compact heat exchangers (since they typically have a surface area density of less than 100 m^2/m^3; however, this limit can be exceeded by employing high surface density finned tubing). It should also be noted that only about half of all plate heat exchangers can be classified as compact heat exchangers. In applications such as the electronic chip cooling, automotive and aerospace industry, maximizing the surface area density is important for minimizing the mass (and payload). There are no strict criteria for employing compact heat exchangers, as a variety of design configurations exist, and the choices of these design configurations are very application specific.

Compact heat exchanger designs are much more sensitive to deviations in joint configurations, geometric architectures, and materials selection. These issues, in turn, can cause complications during the manufacturing process. For example, imperfect brazing operations — where the mating between surfaces is not uniform — can cause

clearance and mechanical issues, leading to reduction in thermal performance and operational reliability (e.g., more prone to leakages and thermo-mechanical distortions). As capabilities for additive manufacturing progresses, it is likely these types of heat exchangers will be more useful in conventional applications rather than relegated to esoteric platforms (as additive manufacturing allows for the reliable creation of more complex geometric designs).

1.2 Literature Review

In contemporary literature, the integration of various heat exchanger configurations with phase change materials (PCMs) has been explored for applications in thermal energy storage (TES) systems. A brief literature review is provided in the following section in this regard. This review is limited to numerical and experimental studies in the literature. A majority of these literature reports were focused on tubular heat exchangers. A broad overview of these types of heat exchangers for TES applications were summarized by Agyenim, et al. [9] and Regin, et al. [10].

Agyenim, et al. [9] listed a range of design criteria involving integration of PCMs into heat exchangers and focused his review on a wide range of tubular heat exchangers, with many of these studies conducted in the temperature range of 0 °C ~ 60 °C (which is more amenable for consumer/ domestic applications). Hence, there is a need to extend these studies to higher temperatures for thermal energy storage applications, such as in solar and automotive industries.

The review by Regin, et al. [10] focused on the material aspects, such as the type of PCM and the encapsulation methods (macro-scale and micro-scale). Encapsulation methods are motivated by the desire to improve the performance of PCMs to enhance the strength, flexibility, corrosion resistance, and thermal stability. Macro-encapsulation can help avoid large-scale phase segregation and is extremely cost-effective for implementation, although it tends to have issues with corrosion. Micro-encapsulation has not been explored as extensively in the literature, though it shows great promise for realizing PCMs with high thermal conductivity and are typically used in thermal control applications.

1.2.1 Thermal Storage Heat Exchangers

Rathod and Banerjee [11] performed experiments using a double-pipe heat exchanger to explore its efficacy as a latent heat thermal energy storage system (LHTESS). For this experiment, the PCM (paraffin) was placed on the shell side of a vertical oriented double-pipe heat exchanger, where the mass flow rate and inlet temperature of the HTF were varied from 1 – 5 kg/minute and 75 – 85 °C, respectively. From this study, it was concluded that increasing the mass flow rate from 1 kg/ minute to 4 kg/ minute and the inlet temperature from 75 °C to 85 °C enabled reduction in melting time by 19% and 44%, respectively. This shows that the inlet temperature is a more sensitive parameter than the mass flow rate for reducing the melting time and therefore, the power rating of the LHTESS during melting. It was also observed that the melting of the PCM occurred faster at the top of the heat exchanger due to the thin

layer of liquid PCM that accumulates at the top. The authors reported that rapid melting on the surface of the inner tube causes the liquid phase to migrate to the top of the heat exchanger due to buoyancy forces and free convection. This observation therefore establishes convection heat transfer as a dominant transport mechanism during melting.

Hosseini, et al. [12] also explored the effects of the inlet temperature of the HTF on the efficacy of an LHTESS by performing both experimental and numerical studies involving a horizontal double-pipe heat exchanger. The mass of the PCM (RT50) stored in the annular space was 4 kg. The inlet temperature was varied from 70 °C to 80 °C at a constant mass flow rate of 1 Liter/minute (with an inlet temperature of 25 °C during solidification). By varying the inlet temperature from 70 °C to 80 °C the melt time was observed to decrease by 19% and 37%, respectively. A numerical study was conducted to predict the propagation of the melt front. The numerical results showed that faster melting occurred at the top of the heat exchanger, primarily due to free convection. From these results, the authors also concluded that the convection heat transfer dominates the transport mechanisms during melting.

Agarwal and Sarviya [13] performed experiments using a horizontal double-pipe heat exchanger with PCM (paraffin wax) filled in the annular space. As this study was geared more towards a solar dryer application, the inlet temperatures were marginally higher than that of the other contemporary studies in the literature. The maximum melting time was set to 8 hours (typical time of insolation during the day), where the main variable was set to be the inlet temperature (80 °C, 85 °C, and 90 °C)

with a constant mass flow rate of 3 g/s. The authors observed that for HTF inlet temperatures of 85°C and 90°C the melting time was reduced by 9% and 16%, respectively, when compared to that of 80 °C inlet temperature. For the solidification of the PCM, the mass flow rate was varied between 1.5 g/s, 2.2 g/s, and 3 g/s (for a constant inlet temperature of 30 °C). When the flow rate was decreased to 2.2 g/s and 1.5 g/s, the solidification time increased by 13% and 23%, respectively (compared to that of the 3 g/s). The authors concluded that this design for LHTESS is feasible for applications involving hot air drying of food products during night time while storing the heat from insolation during daytime.

Avci and Yazici [14] conducted experiments using a horizontal double-pipe heat exchanger with PCM (paraffin, PF56–58) on the annular side. All the experiments for melting and solidification were performed at a constant flow rate of 280 kg/ hour. The inlet temperature during melting was varied between values of 75 °C, 80 °C, and 90 °C and the inlet temperature during solidification was varied between 20 °C, 25 °C, and 30 °C. The authors reported that during the melting process the PCM near the tube initially started to melt (as this is a conduction dominated regime); however, in a short instant, the PCM started to accumulate at the top of the heat exchanger. As mentioned before, this occurs due to natural convection of the melted PCM around the tube causing accumulation of the liquid phase of the PCM at the top. This is because the density of melted PCM is lower than that of the solid PCM and thus the buoyancy force drives the liquid phase to the top of the heat exchanger. This shows that convection heat transfer dominates the transport processes during melting. It is also

shown that the increased inlet temperature decreases the total melting time as there is a larger temperature gradient in the system causing higher rates of heat transfer. During the solidification process, the authors observed that the solid phase of the PCM initially accumulated on the outer surface of the tube (flowing the HTF inside), and the melt front then expands out radially in the annular space. The authors concluded that after the initiation of solidification, the conduction mechanism becomes more dominant and the radial propagation of the solidification front becomes more uniform. As expected, progressively decreasing the inlet temperature speeds up the solidification process and conversely, progressively increasing it speeds up the melting process.

Kousha, et al. [15] investigated the effects of inclination angle on a double-pipe heat exchanger with PCM (RT35) experimentally and numerically. For this study a mass flow rate of 400 ml/min was used with the inlet temperatures of 70 °C, 75 °C, and 80 °C and inclination angles of 0°, 30°, 60°, and 90°. The melting process is more sensitive to the inclination angle than the solidification process. The horizontal orientation enables faster melting, but the vertical orientation enables faster solidification. In general, the melting process was observed to be more sensitive to changes in the operating temperatures than that of the solidification process. This study is in good agreement with prior reports in the literature.

Seddegh, et al. [16] performed experimental and numerical analyses on a large-scale double-pipe heat exchanger for visual observation of the effects of natural convection. During the experiments, melting occurred at an inlet temperature of 80 °C for a mass flow rate of 10 L/minute. During solidification the inlet temperature was

fixed at 10 °C for a mass flow rate of 10 L/minute. During the melting, the authors observed that the temperature at the top rises much faster than that at the bottom. The authors reported that the thickness of the thin layer of melted PCM around the inner tube changes very slowly as the melting process continues (since the melted liquid phase rises to the top). During the solidification process, there is a sudden drop in the temperature before a thin layer of solid PCM forms around the inner tube due to subcooling. This layer of solid PCM causes the thermal resistance to increase—which progressively increases as the thickness of the solidified layer of PCM increases with time. The authors reported that the PCM at the bottom of the tube solidified first due to the dominance of the buoyancy forces. This, in turn, shows that natural convection is present and is a dominant factor during both melting and solidification. The authors reported that the solidification front moved in the outward radial direction. While this investigation does a great job of visually showing the melt and solidification process, it is only applicable for large-scale systems. Smaller-scale systems are more likely to be conduction dominated during solidification, as the height of the thermal boundary layer can be less than the thickness of the melted PCM layer.

Double-pipe heat exchangers show great potential in thermal energy storage applications, since the low thermal conductivity of PCMs can limit their performance. To combat this issue, many systems implemented a variety of extended surfaces (fins, rings, etc.). A significant number of reports in the literature have explored the effect of both longitudinal and radial fins for increasing the rates of heat transfer and

therefore, in enhancing the power rating of these LHTESS during charging and discharging cycles.

Chiu and Martin [17] conducted an experimental and numerical investigation on the design and performance of a vertical heat exchanger with radial fins. The experimental set up was comprised of a finned-tube storage unit that was composed of aluminum (alloy 6082— which is lightweight and has less propensity for oxidation). The fins were 2 mm thick and had 30 mm spacing. The outer diameter of the tube was 10 mm with a wall thickness of 1.5 mm. The shell had a 0.65 liter storage capacity in a 85 mm diameter cylindrical tank (made of transparent poly-methyl-methacrylate glass—for enabling direct visualization). For the numerical simulations, fixed grid technique (enthalpy method) was used, as this enabled the same governing equation to be applied for both the solid and liquid phases. This method consists of integrating the latent heat with the specific heat of the material (which is appropriate as the phase change within the PCM occurs over a wide temperature range). The reliability of this model depends heavily on the accuracy of the thermo-physical properties of the PCM (e.g., specific heat capacity, latent heat capacity, thermal conductivity, range of phase change temperatures, viscosity, etc.). Therefore, a parametric study was conducted with the base model being a cylindrical finned tube storage tank with a 68 mm fin diameter and 30 mm spacing. When the latent heat was doubled, the needed phase change time increased by 38% and when it was halved it decreased by 22%; it was concluded that this nonlinearity is due to the radial geometry of the storage unit. When the thermal conductivity is doubled, the melt time is reduced by 25% and when halved,

the melt time is increased by 42%. The specific heat, temperature range, and heat loss contribute to less than 4% of the total melting and solidification time. Furthermore, the effects of doubling the specific heat and thermal conductivity led to a 50% increase and 30% decrease in melting, respectively. The fin spacing was observed to be the most influential parameter, as doubling this value lead to a 112% increase in solidification time and a 40% reduction in melting time. This shows that fins are more effective at enhancing the solidification process rather than the melting process.

Merlin, et al. [18] also performed experimental and numerical investigations using a vertical double-pipe heat exchanger with radial fins. Five different types of heat exchangers were explored in this study: (a) Copper tube, (b) Aluminum finned, (c) Copper finned, (d) Graphite powder, and (e) ENG matrix. All the heat exchangers were oriented vertically and were 1 m long. A numerical study was also conducted with the enthalpy method and the PCM was selected as Paraffin RT60 (melting between 55–60°C). The first test was performed using oil as the HTF (with Prandtl number, Pr =160 and for Reynolds number, Re = 1830). The authors observed that the melting profile was always initiated from the top which then progressed to bottom of the heat exchanger (i.e., regardless of the flow direction of the HTF). This was determined to be due to the lower density of the liquid paraffin that moves upwards as it melts. The authors reported that the melting rate for the aluminum finned heat exchanger (b) was about twice that of the base heat exchanger (a), but slower than that of the copper finned heat exchanger (c). The authors observed that since the mass of the PCM in cases (d) and (e) were smaller (than the other cases), therefore the results

for these cases are not amenable for comparison to the other cases involved in this study. However, case (e) is about twice as fast as (d) for the values of melt time. The performance with respect to the rate of melting (compared to that of the base heat exchanger) is two, three, and eight times higher for the aluminum finned, copper finned, and the two ENG/ PCM cases, respectively. The authors also noted that thin fins can provide a better performance (compared to that of the thicker fins) as higher rates of conduction heat transfer is achieved in this case. This difference is of the same order of magnitude for both the melting and solidification processes. The working fluid (oil) was replaced with that of water to achieve turbulent flow regimes in these studies (i.e., for Pr = 2.2 and Re = 70,500 at 80°C, where "Pr" denotes Prandtl number and "Re" denotes Reynolds number). The turbulent flow regime was established only for the ENG/ PCM design. The turbulent flow rates reduced the melting time by a factor of 10 compared to that of the laminar flow rates. A numerical model was also developed for the ENG/ PCM case using an axisymmetric enthalpy method where it was observed that the numerical predictions were consistent with that of the experimental measurements. The experimental results showed that the melting time increased sharply for thermal contact resistance values exceeding 10^{-4} [$(m^2K)/W$].

Hosseini, et al. [19] performed experiment investigation to explore the effect of fin height and Stephan number (St) on the time required for phase change (melting and solidification) using a double-pipe heat exchanger with a chosen PCM (RT50) placed in the annular space. The goal was to measure the temperature distribution as well as progression of the melting and solidification front (and the time required for

completing the phase change processes). The double-pipe heat exchanger was comprised of eight fins that were mounted and welded in a way that the tube axis coincided with the normal vector of the fin surface (that were equally spaced). The authors concluded that taller fins lead to a faster melting process due to the farther radial penetration of the heat (therefore the addition of fins could lead to an even faster melt rate). Based on the predictions from the numerical simulations the authors reported that increasing the fin size from 13 mm to 26 mm led to a 19% and 16% reduction in total melting and solidification time, respectively.

Al-Abidi, et al. [20] conducted an experimental investigation on a triplex tube heat exchanger (TTHX) with internal and external fins. The authors performed the experiments for both steady and unsteady conditions as well as for exploring the effect of mass flow rate on the melting time (the solidification process was subjected to different mass flow rates). The PCM was chosen to be TR82 (as the melting point of 82 °C satisfies the minimum temperature required for a liquid desiccant cooling system). Water was the chosen HTF in this study which flowed through both the inner and outer tubes. The authors observed that the PCM melted more on the bottom portion rather than the top portion of the heat exchanger - which they attributed to be due to the good thermal diffusion at the bottom while the top part is affected by entrance disturbance (this agrees with prior reports in the literature). The mass flow rate was varied parametrically at 4 kg/ minute, 8 kg/ minute, and 16 kg/minute while the HTF inlet temperature was maintained at a constant temperature of 90 °C. The authors reported that the melting time was reduced by 58% when the flow rate was increased

from 4 kg/ minute to 16 kg/ minute. However, it should also be noted that there was negligible enhancement of melting rate when the flow rate was increased from 4 kg/ minute to 8 kg/ minute. The authors attribute this to the fact that there is still laminar flow at 8 kg/ minute. Using the 8 kg/ minute flow rate as a base case, the inlet temperature was varied parametrically at 85 °C, 90 °C, 95 °C, and 100 °C. The authors did not observe any significant enhancement when the inlet temperature was increased from 90 °C to 95 °C, while the enhancement was 85% when the inlet temperature was increased from 85 °C to 100 °C. Based on the results garnered from the unsteady experiments, the authors concluded that unsteady inlet temperatures are ineffective for achieving any significant enhancement in the heat transfer rates, which means there needs to be a control scheme to maintain steady temperatures for these solar power applications. Furthermore, the results indicate that the increase in the values of inlet temperature is more effective than increasing the mass flow rates in enhancing heat transfer. Therefore, a control strategy is needed to maintain a constant inlet temperature for the HTF.

Shon, et al. [21] investigated heat transfer rate and efficiency of an automobile integrated with a thermal energy storage system. The TES heat exchanger was designed to hold 4.2 kg of PCM (xylitol) in place of the coolant. The only issue with using 4.2 kg of PCM is that it could prove ineffective if there is an excessive loss of thermal energy to the ambient or from the passenger compartment. The heat exchanger design was analyzed based on two main factors: (1) the fluid flow rate, and (2) PCM layer thickness (where an increase in fluid flow rate and a decrease in the PCM

thickness will help enhance the heat transfer process). The theoretical melting time was compared to that of the experimental results (about a 25% longer melting time was observed in the experiments - because the numerical model did not account for values of heat loss). Overall, the authors observed that the warmup time for the vehicle was shortened by about 33.7%, which lead to less consumption of fuel during the warm up phase. The authors speculated that if the PCM possessed a lower viscosity the values of the free convective heat transfer would be enhanced. However, it is likely that this could also lead to other issues associated with phase segregation.

García-Alonso, et al. [22] conducted an experimental investigation with a horizontal shell-and-tube heat exchanger containing PCM (salt hydrate) in the tube. The overall goal of this study was to compare the radial and axial heat transfer through the wall of the PCM tube. There were 24 tubes in the heat exchanger made with high density polyethylene. The shell was made of a stainless cylindrical tank that was externally insulated using a blanket. The cold reservoir was set to 20 °C and the hot reservoir was set to 50 °C in these experiments. The charging cycle was designed for an operation of 14 hours. Three air flow rates (160 m^3/ hour, 250 m^3/ hour, and 390 m^3/ hour) were chosen for the discharging cycle. The authors observed that the rate of heat transfer in the axial direction was negligible when compared to that of the radial direction.

Tao, et al. [23] used a 3-D model of a shell-and-tube heat exchanger to study the effects of loading the PCM on the tube side versus the shell side. The authors termed Model A as the configuration involving the loading of the PCM on the shell

side and Model B as that of the PCM in the tube side. The computational model was simplified by neglecting the effects of axial heat conduction and viscous dissipation. The flow of the HTF was also approximated by a 1-D fluid flow model. The inner tube radius was changed from 12.5 mm (Model A) to 21.65 mm (Model B): in order to ensure the same amount of PCM was used in each case. The authors reported that by placing the PCM on the tube side leads to an enhanced power rating. However, Model A and Model B provide about the same heat storage capacity. By accounting for convection, the power rating was enhanced by 13.9% and 28.5% for the shell-side and the tube-side heat exchangers, respectively. Based on the results of this simulation the authors recommended that the PCM be placed in the tube side for practical applications (which contradicts some of the recommendations reported in the contemporary literature).

Medrano, et al. [24] explored the application of small PCM (RT35) based thermal energy storage systems with a temperature range of 35 °C to 40 °C. For this study, five different heat exchanger configurations were investigated: (1) a simple double-pipe copper tube heat exchanger with PCM in the annular spacing; (2) the same heat exchanger in (1), but with a graphite matrix embedded in the PCM; (3) a double pipe heat exchanger with 13 radial copper fins; (4) a heat exchanger with aluminum fins and copper tubes; and 5) a small alfa laval gasket plate and frame heat exchanger (T2-BFG model). These five heat exchangers were selected because they are all about the same size (i.e., the same footprint or form factor). The authors performed experiments for 92 different configurations (all cases of full melt) realized by five

different heat exchangers, two temperature gradients, two flow rates, and at least two repeats for each test. It was concluded that heat exchanger (1) and (5) are not adequate for most practical applications because (1) has unacceptably low rates of heat transfer and (5) has the smallest average thermal power, highest weight, and only stores a small amount of PCM. Heat exchanger (4) was observed to achieve the highest thermal power rating (by a factor of 3 as compared to that of the second-best configuration in this study) and attained power ratings in excess of 1kW for both charging and discharging conditions (thus making it the best candidate for small scale PCM storage applications). Case (2) achieved the highest normalized thermal power of 700–800 W/m^2—an order of magnitude higher than the second-best case. Cases (2), (3), and (4) were the most promising configurations for real (practical engineering) applications. In contrast, Case (2) enabled the highest value of heat storage capacity.

Pirasaci and Goswami [25] conducted a numerical investigation on how LHTESS can be used in direct steam generation power plants. While steam generation power plants can typically use molten salts, there are many mass and cost advantages that can accrue from using PCMs. So, a simple shell-and-tube heat exchanger was designed and tested using the phase change of water to steam as the HTF (tube side) and a eutectic PCM on the shell side (eutectic of NaCl and $MgCl_2$). The purpose of the PCM was to heat the water to a superheated vapor. To investigate the effects of the heat exchanger the parameters that were of interest were the internal diameter of the tubes, distance between the tubes, flow path length, and the Reynolds number at the entry. The simulation was shut off once the exit temperature of the HTF fell below

580 °C (as it is then no longer useful for the turbine). It is shown that the effectiveness of the heat exchanger increases from 20% to 90% by increasing the length from 10 m to 150 m. The authors claim that the length is an important factor; however, with such an increase in length—from 10 m to 150 m—it makes sense to expect a dramatic increase in the heat exchanger effectiveness. The authors reported that the most optimum Reynolds number is 1271 (above this Reynolds number the effectiveness decreases). The effectiveness values are also strongly sensitive to the variation in the tube diameter since a smaller diameter leads to an increased effectiveness (at the cost of pump penalty). The effectiveness is weakly sensitive to the distance between the tubes, but plays a major role in enhancing the values of the energy storage capacity.

Ibrahim, et al. [26] performed a critical review of geometric parameters and thermal conductivity enhancement techniques being used in heat exchangers. Except for metallic PCMs, all PCMs exhibit low values of thermal conductivity and therefore require techniques to increase the rate of heat transfer (i.e., their power ratings). Some common techniques to mitigate these issues include adding fins, using multiple PCMs with different melting points, or even using a variety of different fin configurations as well as heat pipes integrated with PCMs. There are generally two types of heat pipes: wickless (or gravity assisted, also known as “thermosyphons”) and with wicks (e.g., screen mesh or sintered wicks). The most common configuration of heat pipes is the screen mesh type. A significant number of studies involving heat pipes are numerical, and therefore require more experimental attention. One method that is often implemented for integrating heat pipes is the multiple PCM configuration. The

purpose of the multiple PCM configuration is to maintain nearly constant temperature difference between the HTF and the PCM during charging and discharging cycles.

Aside from increasing the heat transfer (i.e., power rating), another option is to increase the thermal conductivity of the PCM. Generally, the thermal conductivity is improved by impregnation of porous materials of high thermal conductivity, addition of high conductivity material/nanoparticles or dispersion of low density materials at the base of the PCM. Typically, metal (e.g., aluminum) and graphite foams are the most common materials used for improving the thermal performance of energy storage systems involving PCMs. These techniques can help with reducing the mass (and/or volume fraction) of the TES platforms for enhancing their power ratings (which accrues at the expense of decrease in their net storage capacity). For future research, it seems that using a combination of: (a) the rate of heat transfer augmentation; and (b) thermal conductivity enhancements; are a good combination for optimizing the performance of the thermal energy storage systems.

Amagour, et al. [27] performed experimental investigation using a rectangular shell-and-tube heat exchanger. The heat exchanger was constructed using aluminum (for the inner tubes and fins) and glass (for the outer shell). The authors used the effectiveness-NTU method to assess the thermal performance and reported that increasing the flow rate caused the average effectiveness of the heat exchanger to decrease.

Khan and Khan [28] experimentally investigated a shell-and-tube heat exchanger with longitudinal fins. The authors concluded that this heat exchanger can

discharge 12 MJ of thermal energy to the HTF in 1.5 hours. The authors suggested that these types of systems can easily be implemented into domestic applications, where one can easily connect several of these systems to meet cooling or heating requirements.

Abdulateef, et al. [29] performed experiments by implementing longitudinal and triangular fins onto a triplex heat exchanger. Three different fin configurations were explored in this study: (1) internal, (2) internal-external, and (3) external. The authors reported that the external triangular fin configuration provided the highest level of heat transfer enhancements for solidification.

1.2.2 Other Heat Exchangers and Applications

Thermal energy storage applications span a vast range of industries (although a significant number of these contemporary applications are evolving quite rapidly), including: solar, automotive, and electronics industries. Kenisarin and Mahkamov [30]; Lazaro, et al. [31]; Lei, et al. [32]; and Zhang, et al. [33] all showed the practical and economic potential of adding PCM into buildings, primarily the building envelopes. Vakilaltojjar [34] explored how the installation of PCM in households might affect the peak load consumption of energy. Sharma, et al. [35] explored the potential application of PCM in solar power generation, i.e., Building-Integrated Concentrated Photovoltaics (BICPV) — where the PCM is integrated to help solve overheating issues. Shon, et al. [21] investigated an automobile coolant waste heat

recovery system, and the authors reported that the warm up time in a vehicle can be reduced by 33.7%.

1.3 Motivation and Goal

This study is motivated by the need to switch to more sustainable water usage in thermoelectric power generation (i.e., in conventional power plants) and to alleviate the pressure on natural resources involving freshwater supplies (withdrawal and consumption of fresh water by power plants) in the near future. This will require a switch from wet-cooling techniques to dry-cooling techniques. Dry-cooling techniques can reduce or eliminate water withdrawals, effluent discharge, and even minimize the impact of hot water discharge from cooling systems on aquatic life. Furthermore, dry-cooling techniques can be implemented in areas with arid climates and water supply constraints. Currently, wet-cooling is more efficient and cost-effective, but it comes at the expense of significant freshwater withdrawals. To ensure that fresh water supplies can meet the demands of the growing human population, water usage by power plants will need to be minimized.

Thus, the goal of this study is to enhance the effectiveness and reliability of the dry-cooling techniques (i.e., by mitigating their drawbacks—such as higher costs and lower efficiencies) by integration of these cooling platforms with supplemental cooling systems. PCM has been used in a few other thermal storage applications either to increase heat transfer or to cool air in condenser applications, which makes the use of thermal storage systems attractive as a supplemental unit for these applications (e.g.,

to mitigate peak loads). Hence, a thermal energy storage platform realized using a compact heat exchanger will be explored in this study, and experiments will be performed under different loading conditions. If the compact heat exchanger meets the constraints of the ARAP-E ARID program [36], then the heat exchanger will be considered a viable prototype. More details regarding the program constraints are discussed in section 1.4.

1.4 Objective

The objective of this study is to experimentally evaluate the viability of using a compact heat exchanger containing a chosen PCM (i.e., lithium nitrate trihydrate) for the realization of a supplemental cooling system (in alignment with the ARAP-E ARID program). The objectives include:

(1) Perform experiments to determine the efficacy of the "*Cold Finger*" technique in mitigating the reliability issues by reducing subcooling;

(2) Perform experiments to determine the thermal performance of the selected LHTESS. The thermal performance can be characterized in terms of total energy storage capacity, the average power rating, effectiveness, Stefan number, and evaluating the reliability of this cooling/ energy storage platform (i.e., by monitoring the variations in the amount of subcooling needed to initiate solidification of the PCM in the heat exchanger);

(3) Determine if the LHTESS meets the ARPA-E ARID program requirements, as summarized below:

a. Less than 1 °C of subcooling,
b. Maximum melting time of 30 minutes,
c. Maximum solidification time of 60 minutes,
d. LHTESS is required to have an energy storage capacity more than 100 kJ,
e. Achieve more than 5 °C of cooling for the HTF during melting.

1.5 Scope

The aim of this study is to investigate the thermal performance of a compact heat exchanger (CHX) and experimentally evaluate the efficacy of this CHX when used as a latent heat thermal energy storage system (LHTESS). The scope of the experiments will be limited to meet the program objectives of the sponsored research project from the ARPA-E ARID program. Based on the ambient temperature variation in typical arid regions, the range of operating temperatures is restricted to within 20 – 40 °C. For this reason, the inlet temperature values of the HTF during melting have been chosen to be 33 °C, 35 °C, and 37.4 °C. The inlet temperature of the HTF (deionized water) during solidification has been chosen to be 25 °C and 20 °C. “Cold Finger” technique was implemented for solid mass fractions of 90%, 70%, 50%, 30%, and 10% during melting (to test its efficacy in mitigating subcooling effects during the solidification process). A high degree of subcooling can be an impediment to the solidification of PCM, which also compromises the operational reliability of the system, and can lead to catastrophic system failure if the PCM does not solidify under ambient conditions

during nighttime. The PCM for this study is limited to lithium nitrate trihydrate. For real life applications, the PCM should be able to solidify overnight when temperatures are cooler. To deliver on the targets for this sponsored research project, the melting and solidification rates and times were recorded in these proposed experiments.

1.6 Overview

A description of the experimental apparatus and the experimental procedure are provided in section 2. The experimental data garnered in this study are reported in section 3 along with a discussion on the nuances and implications of these results. All experiments were performed using the "*Cold Finger*" technique. The specific tasks include:

(1) Melting rate and time, as a function of inlet temperature of HTF, flow rate, and flow direction;

(2) Solidification rate and time, as a function of inlet temperature of HTF, flow rate, and flow direction;

(3) Repeat of #1 and #2 above for different levels of insulation.

The conclusions derived and the suggestions for future work accruing from this study are discussed in section 4.

2 EXPERIMENTAL APPARATUS AND PROCEDURE

2.1 Experimental Setup

The experimental set up used in this study consists of a flow loop integrated with temperature-controlled water baths (a hot bath and a cold bath), while utilizing three-way valves (six each), flow-control needle valves (two each), and a compact heat exchanger filled with the chosen PCM, i.e., lithium nitrate trihydrate *($LiNO_3 \cdot 3H_2O$)*. The flow loop was designed for both co-current and counter-current configurations with the aid of the three-way valves. A schematic and the photographic images of the experimental apparatus is shown in Figure 3, Figure 4 and Figure 5, respectively. The flow direction of the valves for co-current and counter-current flow is provided in a schematic diagram in Appendix A.

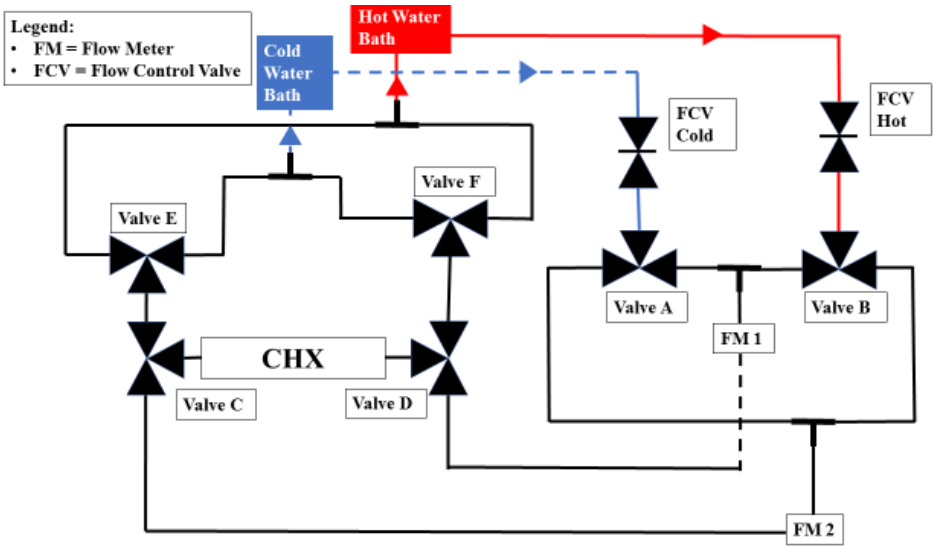

Figure 3: Schematic of Heat Exchanger Flow Loop Apparatus for Both Co-current and Counter-current Flow Configurations. The valve configurations for co-current and counter-current flows are listed in Appendix A.

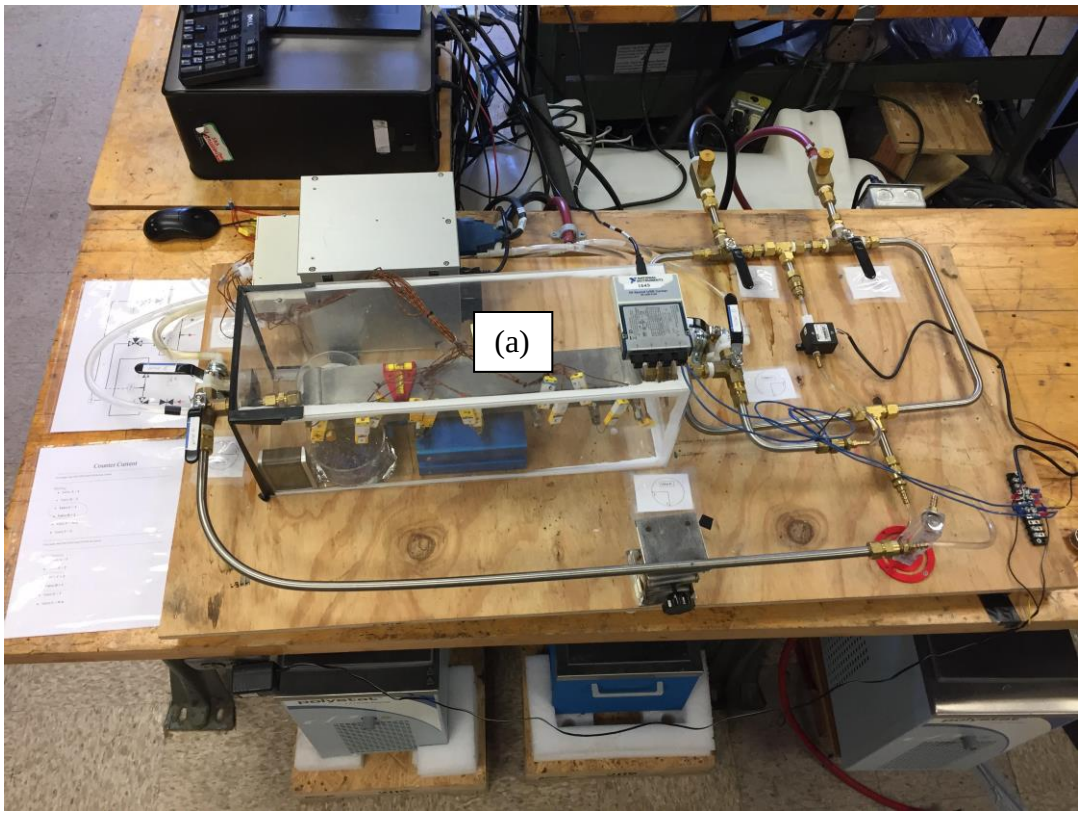

Figure 4: Image of the Experimental Apparatus—with Uninsulated Heat Exchanger (a). The heat exchanger is not insulated, for the purpose of measuring the heat loss to the ambient. The heat exchanger was enclosed in a plexi-glass chamber to reduce the exposure to ambient humidity. During the experiments, the humidity in the enclosure was measured to be ~16% and the ambient humidity was measured to be ~45%.

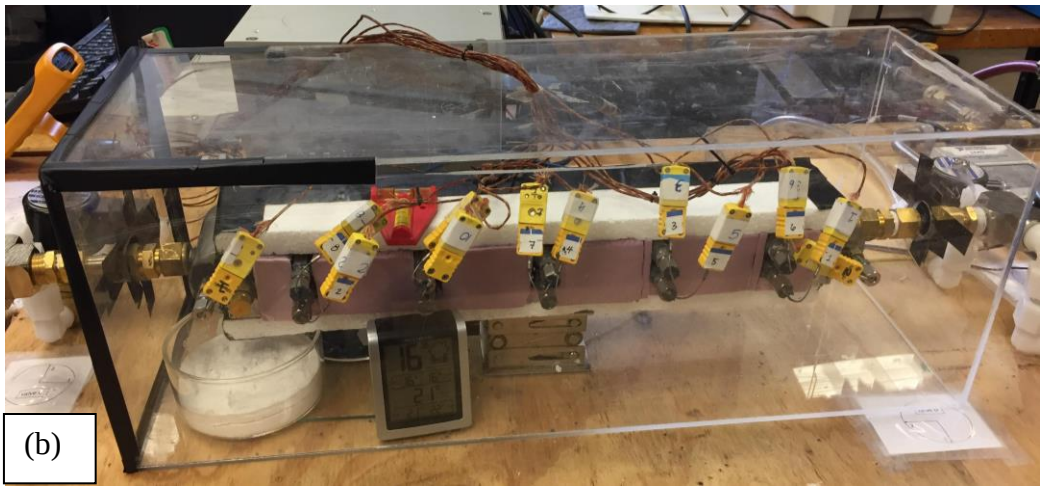

Figure 5: Image of the Experimental Apparatus—with Insulated Heat Exchanger (b). The heat exchanger was insulated to simulate an adiabatic boundary condition. During the experiments, the humidity in the enclosure was measured to be ~16% and the ambient humidity was measured to be ~45%.

2.1.1 Lithium Nitrate Trihydrate

The samples of PCM, i.e., lithium nitrate trihydrate *($LiNO_3 \cdot 3H_2O$)* were synthesized in-house, using anhydrous lithium nitrate salt powders that were procured commercially (Beantown Chemical, NH, Purtity > 99%). Due to the hygroscopic nature of lithium nitrate, a tedious hydration technique was used to minimize the effects of humidity on the sample. In the initial steps, the lithium nitrate powders were dried in an oven for 12 hours at 150 °C, to remove the moisture content completely from the lithium nitrate. Once the dehydration procedure was completed, the lithium nitrate samples were placed in a heated vacuum chamber overnight at 90 °C as shown in Figure 6.

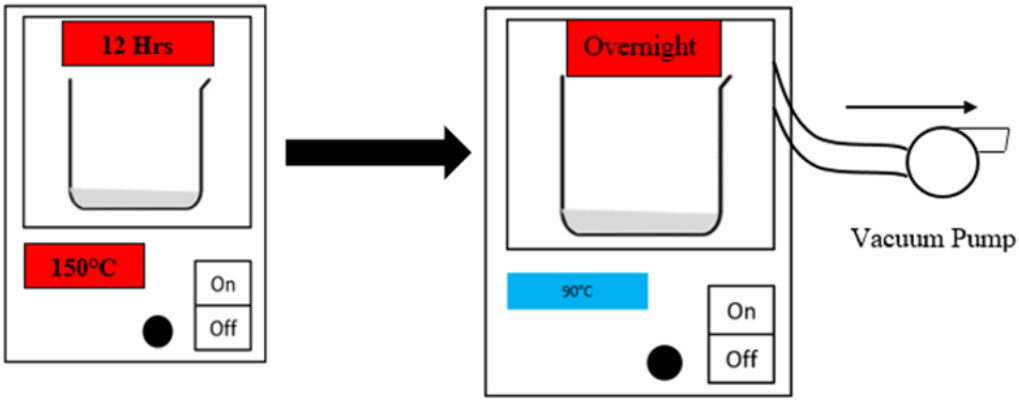

Figure 6: Drying Process for Lithium Nitrate.

For the hydration process, stoichiometric quantities of de-ionized water were added to the anhydrous lithium nitrate at 35 °C (above phase transition). The hydrated lithium nitrate (i.e lithium nitrate trihydrate) should contain 44% by mass of water and 56% by mass of lithium nitrate salt, as shown in Figure 7.

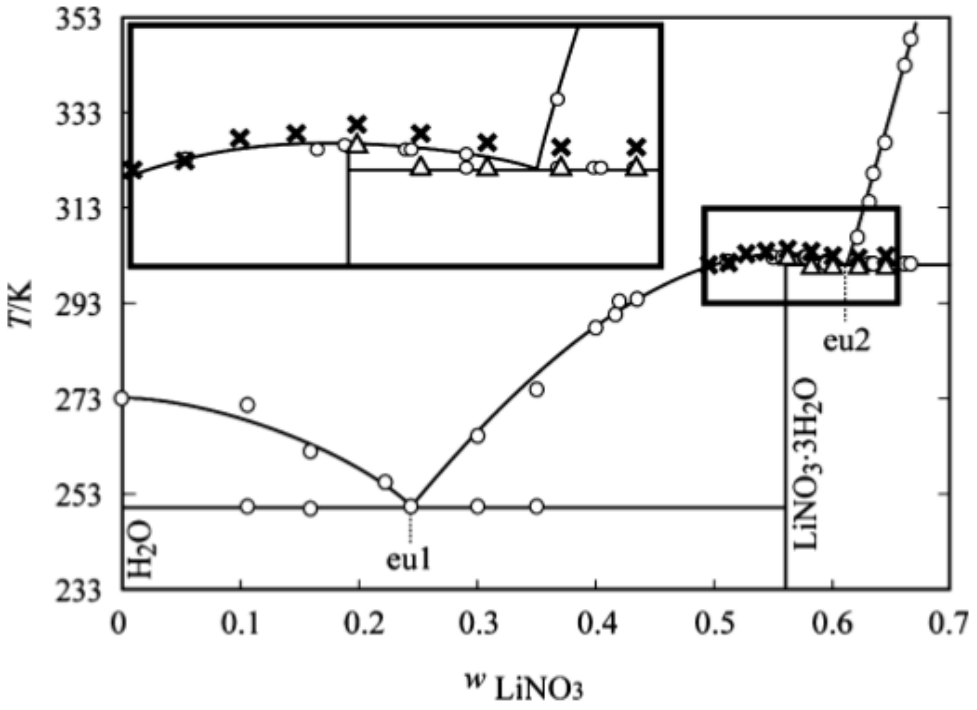

Figure 7: Phase Diagram for Lithium Nitrate [37].

Finally, a small quantity of the hydrated lithium nitrate is removed from the bulk mixture and dehydrated to validate the mole concentration of water. The thermal performance of the PCM (lithium nitrate trihydrate) tends to vary significantly for small changes in the hydration level (i.e., for a lack or excess of hydration).

The initial characterization of lithium nitrate trihydrate was performed using the T-History technique. The measurements were performed between 24 °C and 40 °C. As summarized in Table 1, the energy storage capacity of lithium nitrate trihydrate was ~273 J/g for endothermic process and ~234 J/g for exothermic process. These measurements were within 6% of the literature data and were obtained using the DSC measurement technique [37]. The difference in the energy storage capacity between

endothermic and exothermic processes is mainly due to effects of subcooling and measurement uncertainty. Measurement accuracy of the T-History technique was diminished during exothermic reaction, as the referenced heat transfer coefficient was higher than that of the PCM ($h_{ref} \neq h_{pcm}$) in subcooled cases. The phase transition occurred around 28.6 °C and required 5 °C subcooling to initiate solidification.

Table 1: Initial Characterization of Lithium Nitrate Trihydrate Without Additives using the T-History Technique.

	C_p Liquid (J/g k)	C_p Solid (J/g k)	MP (°C)	FP (°C)	Latent Heat (endothermic) (J/g)	Latent Heat (exothermic) (J/g)	ΔT °C
Initial Data	1.81	3.14	29.2	28.63	273	234	15
Uncertainty (Abs)	0.13	0.89	0.14	0.8	16	21	0.5

2.1.2 Compact Heat Exchanger

The compact heat exchanger has three channels for fluid flow and four hermetically sealed channels that encapsulates the PCM (i.e. lithium nitrate trihydrate). The fluid side of the heat exchanger has an offset fin configuration of 21 fins per inch; the offset fin configuration was selected because it yields a higher surface area compactness ratio and Reynolds number, which allows for a higher overall heat transfer performance in comparison to other heat exchangers that are designed for a given volumetric mass flow rate. The details of the offset fin configuration are shown in Figure 8 and Table 2.

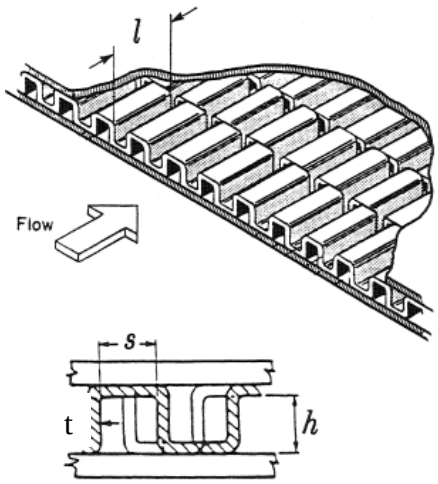

Figure 8: Schematic of Fin Configuration modified from [38].

Table 2: Specifications for Fin Configuration.

Parameter	Inches
h	.075
t	.006
l	.125
s	.040
α	.008
γ	.048
δ	.048

The PCM channels contain aluminum porous mesh as shown in Figure 9 (with an equivalent fin configuration of 100 fins per inch). The mesh was impregnated with the PCM (lithium nitrate trihydrate) to enhance its capacity and the mesh enabled the enhancement of the effective thermal conductivity. The heat exchanger design allowed the center PCM channels to be charged and discharged through both the top and bottom side, whereas the top and bottom PCM channels only allowed charging and discharging in one direction (i.e. bottom side) as shown in Figure 10. Therefore, this

resulted in faster charging and discharging in the center PCM channels in comparison to both the top and bottom PCM channels.

Figure 9: Image of Aluminum Wire Cloth. Material: Aluminum 5052, Mesh Size: 200×200, Porosity: 34%, Wire Diameter: 0.0021".

Based on the mass of PCM loaded into the CHX, the net energy storage capacity of the latent heat thermal energy storage system (LHTESS) was theoretically rated to be 130 kJ. Furthermore, the mass and latent heat of the PCM was measured to be 474 grams and 275 J/g, respectively. The PCM was assumed to be distributed evenly throughout each channel at 68.7 J/channel. A spirit level was placed on the top of the heat exchanger (at the center) to ensure an even mass flow rate as well as uniform melting and solidification of the PCM throughout each HTF channel. A schematic of the compact heat exchanger is shown in Figure 10. The melt front and freeze front of the PCM in the top and center plate were estimated and monitored by

embedding thermocouples at fixed locations (corresponding to melt fractions of 10%, 30%, 50%, 70%, and 90%) along the axial direction as shown in Figure 10.

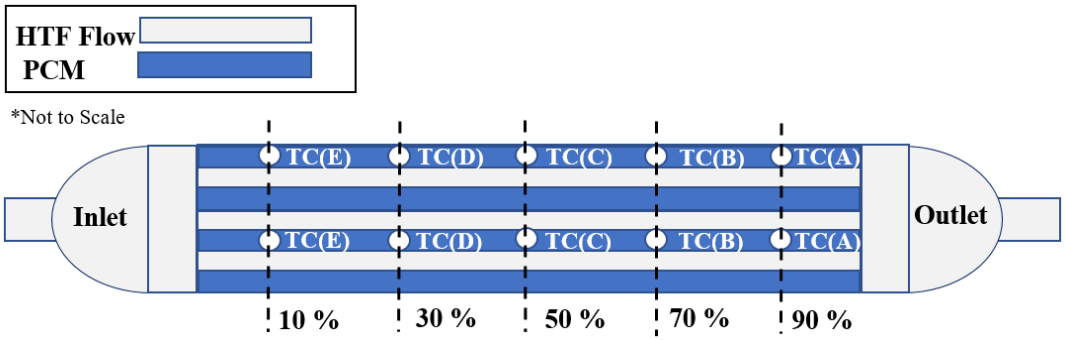

Figure 10: Schematic of Compact Heat Exchanger with PCM for marking the locations of the thermocouples.

The temperature of the HTF (i.e. DI water) was measured at the inlet and outlet of the heat exchanger. Lastly, due to the hygroscopic nature of lithium nitrate trihydrate, the compact heat exchanger apparatus was placed in a sealed plexiglass enclosure containing desiccants (i.e. calcium chloride and cobalt chloride) to maintain a low humidity environment. The humidity in the enclosure was maintained at ~15% compared to an ambient humidity of 40~45%.

2.1.3 Thermocouples and Data Acquisition System

The thermocouples utilized in the temperature measurements were K-Type (1/16” diameter) with hydro-thermic sheathed tips (Sheathing Material: SS 316, and Manufacturer: Tempel, Ohio). The thermocouples were calibrated in a water bath from 10 °C to 40 °C using an NIST Standard thermometer (Least Count: ± 0.25 °C and

calibration uncertainty of 0.8%). After calibration, the uncertainty of the thermocouples was determined to be ±0.25 °C ~ ±0.35 °C. A high-speed data acquisition (DAQ) system was used for recording the temperature values measured in the experiments. The DAQ consists of NI SCXI 1000 Chassis, and NI SCXI-1303 board. The temperature measurements were performed at 1 HZ frequency (i.e. 1 reading/second). The least count accuracy of DAQ system was 0.003 °C; therefore, the uncertainty from the DAQ can be considered negligible. Simultaneously, the voltage measurement from the flow meter was acquired using a NI USB 9162 DAQ at 1 HZ frequency. The HTF volumetric flow rate in the system was measured by an Omega FLR 1000 series flow meter (S/N 10981) which was calibrated for 0.2 L/ minute to 2 L/ minute. A sample of the calibration curves for the thermocouples and flow meters is shown in Figure 11 and Figure 12, respectively (additional information are provided in Appendix B).

It should be noted that the thermocouples were bent slightly while inserting them into the heat exchanger. The induced stresses and strains in the initially unbent thermocouples likely led to a change in the calibration constants for these thermocouples. The calibration curves obtained for these thermocouples, both: for the pre-experiment (unbent thermocouples) and the post-experiment (bent thermocouples) conditions are provided in Appendix B. The post-experiment calibration constants were observed to cause a minor change in the transient data for temperature transients recorded in these experiments, resulting in a deviation of 1~6% in the values of

capacity and power ratings from that of the results obtained using the pre-experiment calibration constants.

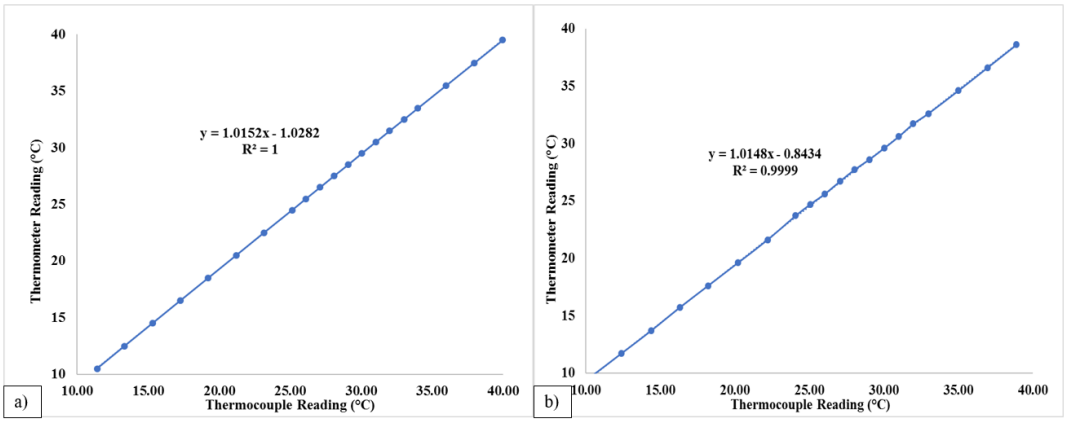

Figure 11: Calibration curve for thermocouple 1. a) pre-experiment b) post experiment.

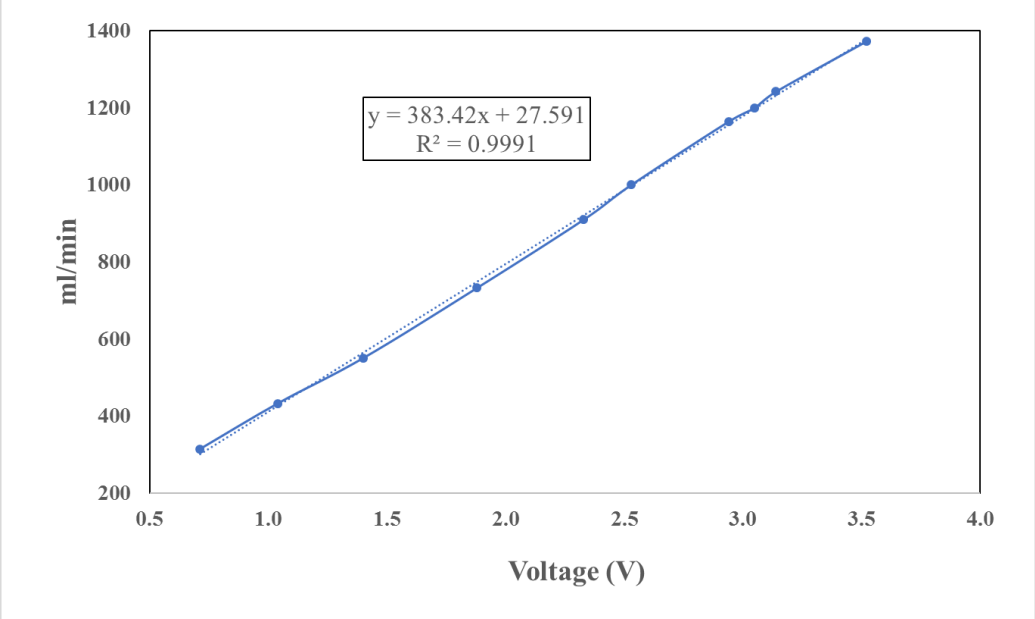

Figure 12: Calibration Curve for Flow Meter.

2.1.4 Constant Temperature Baths (Chillers)

A hot bath and cold bath were used (by Cole-Parmer Polystat cooling/ heating circulating baths) for supplying HTF to the CHX. The two chillers and their model numbers are shown in Figure 13. The flow direction for the co-current and counter-current configurations were manipulated using three-way valves. This allowed for the melting or solidification experiments to be performed in co-current or counter-current flow configurations. The flow control valves were implemented to control the flow rates and to maintain the desired flow direction.

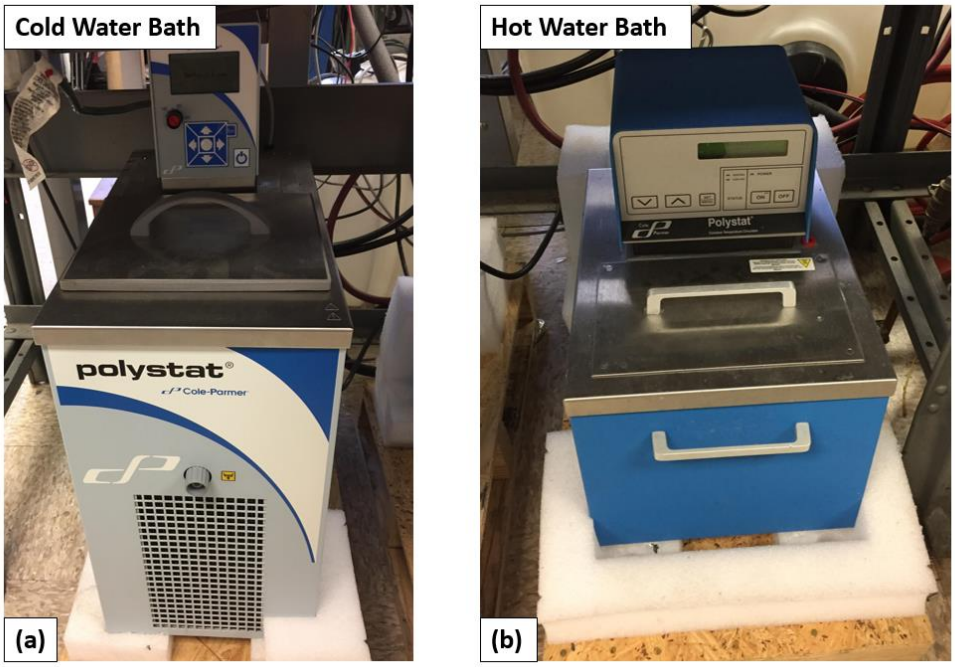

Figure 13: Water Baths. (A) Cold HTF, Cole-Parmer Polystat cooling/heating circulating bath (BOM# 212233800); (B) Hot HT, Cole-Parmer Polystat constant temperature controller (Model 12106-10).

2.2 Experimental Procedure

The melting and solidification of the PCM in the LHTESS was conducted using *Cold Finger* protocols. The *Cold Finger* technique is a localized cooling technique where a cold spot is created intentionally in the PCM to ensure that a portion of the PCM remained un-melted (during the thermal cycling procedure for melting) while also ensuring that there is partial or complete solidification of the PCM during the solidification step. In this study, the *Cold Finger* protocol consisted of 90% melting of PCM — leaving 10% of PCM as solid crystals (and followed by complete solidification of PCM).

Furthermore, the flow direction of the cold HTF is varied (co-current vs. counter-current) to observe the sensitivity of the LHTESS to subcooling. The experiments were performed by changing: (a) the percentage of the PCM that remained solidified at the end of the melting cycle, (b) the flow rate of the HTF, (c) the inlet temperature of the hot HTF for the incomplete melting process (i.e. the time for accomplishing the discharging cycle), and (d) the inlet temperature of the cold HTF for complete solidification (i.e. the time for accomplishing the charging cycle). The time required for melting and solidification therefore translates to the power rating of the heat exchanger during charging and discharging cycles. Additionally, for the 90% melt cases, the experiments were repeated with and without insulation. These experiments involving insulated CHX were designed to compare the parasitic heat loss to the environment during the melting and solidification process (and were compared to that of the experimental results involving no extraneous insulation).

The experimental procedure is listed as follows:

(1) Initially solidify PCM with HTF at cold inlet temperature;

(2) Close the cold HTF control valve and turn valves to direct the hot HTF;

(3) Open the hot HTF control valve and melt to the desired mass fraction of un-melted PCM (10 ~ 90%);

(4) Close hot HTF flow control valve and turn valves to direct the cold HTF;

(5) Completely solidify the PCM;

(6) Repeat steps (2) through (5) above for ensuring repeatability and other desired mass fractions;

In the co-current flow configuration, the direction of the HTF flow for melting and solidification remained same, as illustrated in Figure 14.

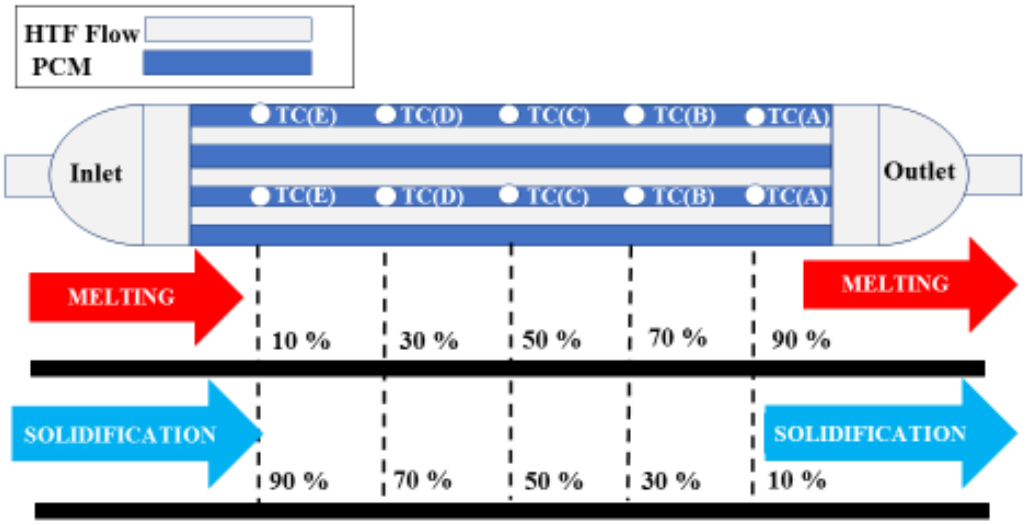

Figure 14: Co-Current Flow Direction for Melting and Solidification.

In the counter-current flow configuration, the direction of the HTF fluid during melting and solidification were reversed, as illustrated in Figure 15.

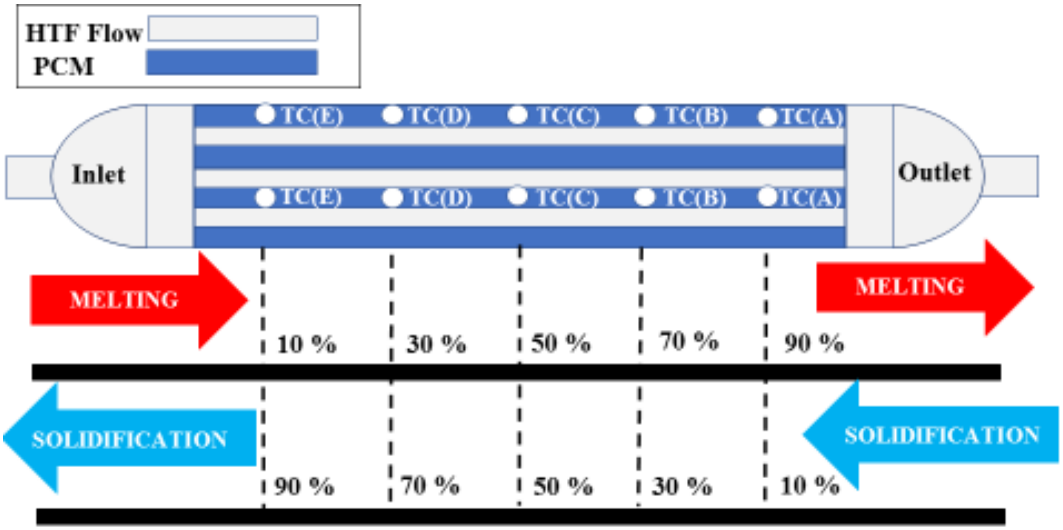

Figure 15: Counter-Current Flow Direction for Melting and Solidification.

This procedure was repeated for volumetric flow rates of 3 GPH and 5 GPH and the HTF inlet temperature (hot) was varied between 33 °C, 35 °C, and 37.4 °C. Similarly, the HTF inlet temperature (cold) was varied between 25 °C and 20 °C. The experiments were performed with and without insulation - in order to estimate the heat loss and for enabling more sophistication in the model predictions expected to be developed in the future – based on these experimental results.

2.3 Data Reduction

The following section summarizes the equations used for data analyses involving temperatures measured for the HTF, in order to derive the values for effectiveness, total energy storage capacity, and power rating. Measurement uncertainties were computed based on the Kline and McClintock Method [39]. The temperature difference of the HTF flowing within the heat exchanger was computed using the difference of the inlet and outlet temperatures:

$$\Delta T_{HTF} = T_{outlet} - T_{inlet} \quad (1)$$

where, T_{outlet} is the HTF temperature measured at the outlet port of the heat exchanger and T_{inlet} is the inlet temperature measured at the inlet port of the heat exchanger. The measurement uncertainty of the ΔT_{HTF} values were obtained at each instant and were estimated by using the following equation:

$$u_{\Delta T_{HTF}} = \left[\left(\frac{\partial \Delta T_{HTF}}{\partial T_{outlet}}\right)^2 \left(u_{T_{out}}\right)^2 + \left(\frac{\partial \Delta T_{HTF}}{\partial T_{inlet}}\right)^2 \left(u_{T_{inlet}}\right)^2\right]^{1/2} \quad (2)$$

where, u is the statistical uncertainty for each variable: ΔT_{HTF},T_{out}, and T_{inlet} . The calibrated uncertainty of thermocouples was determined to be ± 0.35 °C between 20 °C and 45 °C. The average uncertainty for ΔT_{HTF} is computed to be ± 0.49 °C.

The effectiveness (ε) of the heat exchanger is an important parameter for determining the thermal performance of the heat exchanger and was calculated in this study using Equation 3:

$$\varepsilon = \frac{T_{inlet} - T_{outlet}}{T_{inlet} - T_{PCM}} \tag{3}$$

where, T_{PCM} is the temperature of the of the PCM at the 90% melt point in the heat exchanger (i.e. thermocouple E in Figure 14 and Figure 15), T_{inlet} is the HTF inlet temperature, and T_{outlet} is the HTF outlet temperature. The uncertainty for the effectiveness was computed as shown:

$$u_\varepsilon = \left[\left(\frac{\partial \varepsilon}{\partial T_{inlet}}\right)^2 \left(u_{T_{inlet}}\right)^2 + \left(\frac{\partial \varepsilon}{\partial T_{outlet}}\right)^2 \left(u_{T_{outlet}}\right)^2 + \left(\frac{\partial \varepsilon}{\partial T_{PCM}}\right)^2 \left(u_{T_{PCM}}\right)^2\right]^{1/2} \tag{4}$$

where, u is the statistical uncertainty for each variable; ε, $u_{T_{out}}$, T_{PCM}, and T_{inlet} .

The specific heat capacity (C_p) of the HTF was calculated as shown:

$$C_p = \left[4 \times 10^{-13} T_{avg}^6 - 2 \times 10^{-10} T_{avg}^5 + 2 \times 10^{-8} T_{avg}^4 - 2 \times 10^{-6} T_{avg}^3 + 1 \times 10^{-4} T_{avg}^2 - 3.4 \times 10^{-3} T_{avg} + 4.2199\right] 1000 \tag{5}$$

The density (ρ) of the HTF was calculated as shown:

$$\rho = \left[1 \times 10^{-7} T_{avg}^{4} + 4 \times 10^{-5} T_{avg}^{3} + 7.5 \times 10^{-3} T_{avg}^{2} - 5.16 \times 10^{-2} T_{avg}\right] + 999.87 \quad (6)$$

The thermal storage capacity of the heat exchanger was calculated by using Equation 7, based on the measurements of the HTF temperature values and flow rates:

$$E = \Delta T_{HTF} C_{p_{avg}} \dot{m}_{avg} \quad (7)$$

where, ΔT_{HTF} is the difference between the temperature of the HTF at inlet and outlet, $C_{p_{avg}}$ is the average specific heat during each respective phase change, and $\dot{m}_{avg}$ is the average mass flow rate of the HTF. The uncertainty of the mass flow rate of the HTF is calculated as shown:

$$u_{\dot{m}} = \left[\left(\frac{\partial \dot{m}}{\partial \dot{V}}\right)^{2} (u_{\dot{V}})^{2} + \left(\frac{\partial \dot{m}}{\partial \rho}\right)^{2} (u_{\rho})^{2}\right]^{1/2} \quad (8)$$

where, $\dot{V}$ is the measured volumetric flow rate of the HTF and ρ is the density of the HTF. The uncertainty for the volumetric flow rate, $u_{\dot{V},}$ is determined to be 7.2×10^{-5} L/minute. The extremely small uncertainty is due to the quality of the calibration of the flow meter and is therefore neglected in the thermal performance calculations. The uncertainty for the thermal power ratings (heat transfer rates) is then calculated using Equation 9, as follows:

$$u_E = \left[\left(\frac{\partial E}{\partial \dot{m}}\right)^2 (u_{\dot{m}})^2 + \left(\frac{\partial E}{\partial c_p}\right)^2 \left(u_{c_p}\right)^2 + \left(\frac{\partial E}{\int \partial \Delta T_{HTF}}\right)^2 (u_{\Delta T})^2 + \left(\frac{\partial E}{\partial t}\right)^2 (u_t)^2\right]^{1/2} \quad (9)$$

where, t is time and u is the statistical uncertainty for each variable: $\dot{m}$, c_p, ΔT_{HTF} and t. For this experiment, u_{c_p} and u_t were considered to be negligible. The power rating (*P*) for the LHTESS was calculated using Equation 10, as follows:

$$P = \dot{m} C_p \Delta T_{HTF} \quad (10)$$

The measurement uncertainty for the estimates of the power rating of the LHTESS (for both melting and solidification) was calculated using Equation 11, as follows:

$$u_P = \left[\left(\frac{\partial P}{\partial \dot{m}}\right)^2 (u_{\dot{m}})^2 + \left(\frac{\partial P}{\partial C_p}\right)^2 \left(u_{C_p}\right)^2 + \left(\frac{\partial P}{\partial \Delta T_{HTF}}\right)^2 \left(u_{\Delta T_{HTF}}\right)^2\right]^{1/2} \quad (11)$$

Stefan number (*St*) is defined as the ratio of the sensible heat to the latent heat. Hence, the Stefan number was calculated using Equation 12, as follows:

$$St = \frac{sensible\ heat}{latent\ heat} = \frac{C_p \Delta T}{h_{fs}} \quad (12)$$

where, h_{fs} is the latent heat value of the PCM.

3 RESULTS AND DISCUSSION

The primary goal of the study was to experimentally determine the viability of using a compact heat exchanger (CHX) as a latent heat thermal energy storage system (LHTESS) with potential applications in providing supplemental cooling in power plants. Experiments were performed by varying the flow rates and inlet temperatures, and the different experimental configurations are listed in Appendix C. Case B (co-current) and case G (counter-current) were the cases corresponding to the desired design conditions. The following section provides in-depth thermal performance analyses of the design conditions in comparison to other cases (i.e. to determine the sensitivity of the thermal performance of the LHTESS to variations in flow rates and inlet temperatures).

The results show that for the *Cold Finger* technique and counter-current configurations, subcooling of less than 1 °C was achieved. This is a phenomenal result, as no results exist in the literature with less than 2 °C subcooling (even with nucleating additives) for this PCM. The set-back of the *Cold Finger* technique is that the energy storage capacity is sacrificed significantly (i.e., CHX needs to be oversized to meet the specifications for energy storage capacity: which in turn increases the cost due to additional material / PCM that needs to be loaded into the LHTESS).

The melting time and solidification time are very sensitive to variations in both the flow rates and HTF inlet temperature values. The times for both melting and solidification are more sensitive to the HTF inlet temperature than the flow rates. In real-life applications, increasing the temperature difference with respect to the HTF

inlet temperature (and the phase change temperature of the PCM) will therefore be more beneficial than increasing the flow rates due to Reynolds analogy (i.e. increase in pump penalty due to higher pressure drops is concomitant with increasing the flow rates with little added benefit to the marginal improvement in the power ratings of the LHTESS).

3.1 Effectiveness of *Cold Finger* Technique

The effectiveness of the *Cold Finger* technique was experimentally ascertained in both co-current (Case B) and counter-current (Case G) configurations. In the case of the co-current configuration, maximum subcooling during solidification was 3 °C as shown in Figure 16, whereas in the case of counter-current configuration the maximum subcooling during solidification was 0.5 °C as shown in Figure 17. In the case of counter-current configuration, the direction of nucleation (i.e. crystal growth) was in the same direction as the flow, thus creating a favorable orientation of the nucleation spot, as portrayed in Figure 18.

In the co-current configuration, due to lack of a cold spot in the flow direction, the effectiveness of the *Cold Finger* technique (i.e., in both minimizing subcooling while enhancing the power rating) was diminished. Therefore, based on the flow directions (in melting and solidification), the subcooling in the PCM (i.e. 90% freeze front location) is enhanced without the aid of cold spots and decreases when there is presence of a cold spot (i.e. at the 10 % freeze location), as shown in Table 3.

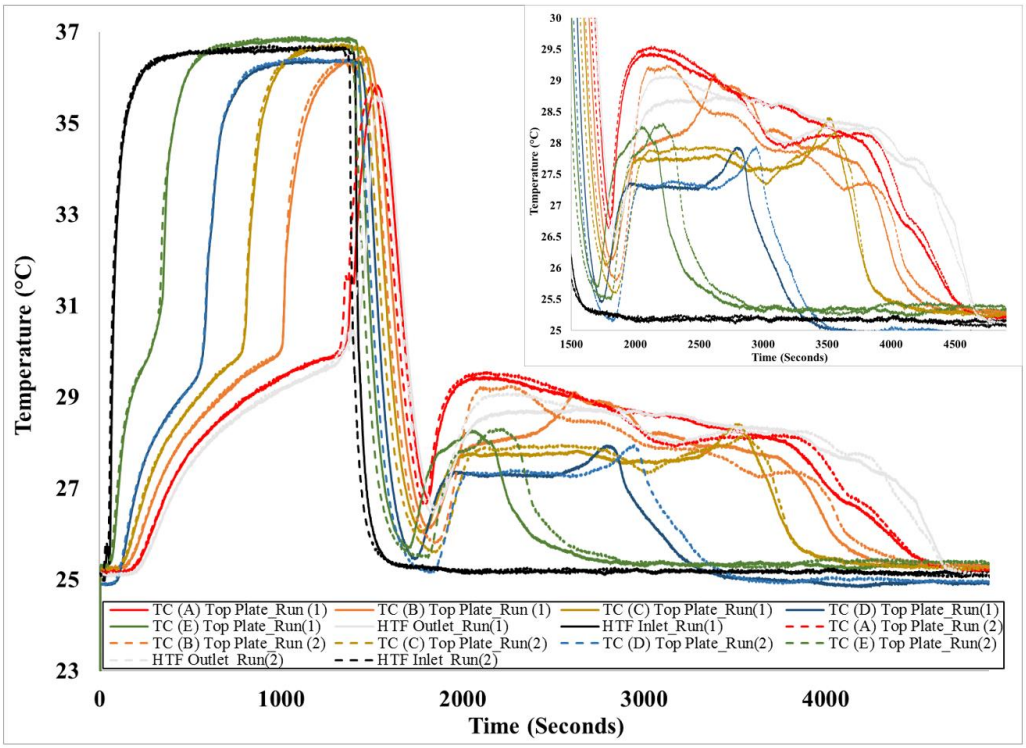

Figure 16: Temperature Profiles Recorded by Thermocouples at the Top Plate During Melting (90%) and Solidification at a Flow Rate of 3 GPH (Co-Current). Inlet temperature of HTF during melting is 37.4 °C and during solidification is 25 °C (Case B, Post-experiment calibration).

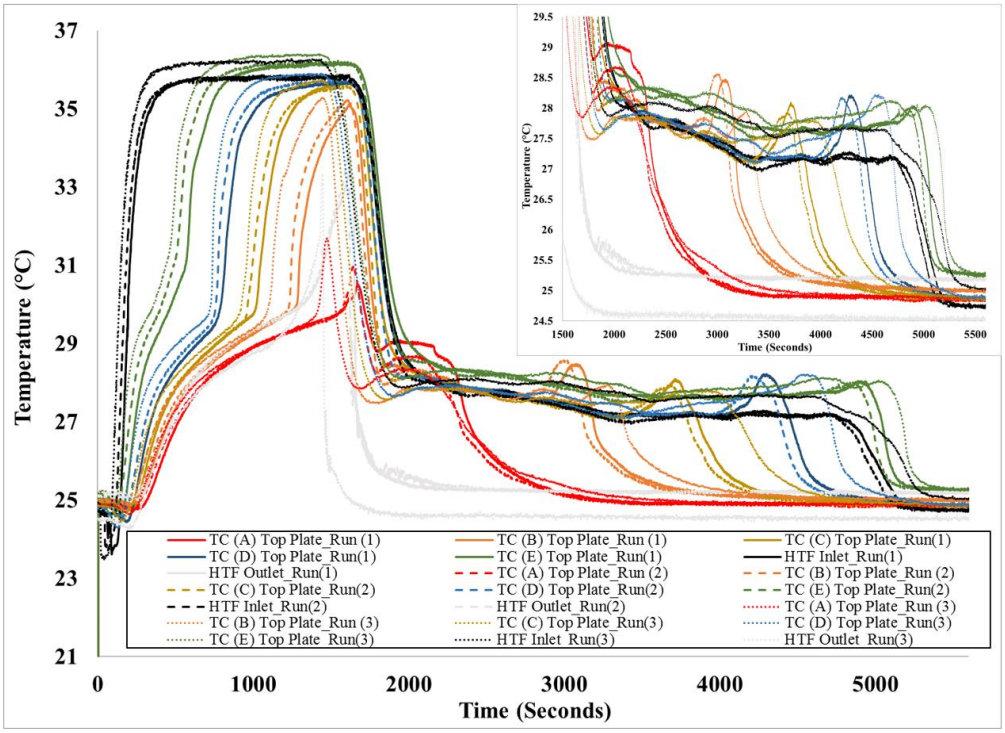

Figure 17: Temperature Profiles Recorded by Thermocouples at the Top Plate During Melting (90%) and Solidification at a Flow Rate of 3 GPH (Counter-Current). Inlet temperature of HTF during melting is 37.4 °C and during solidification is 25 °C (Case G, Post-experiment calibration).

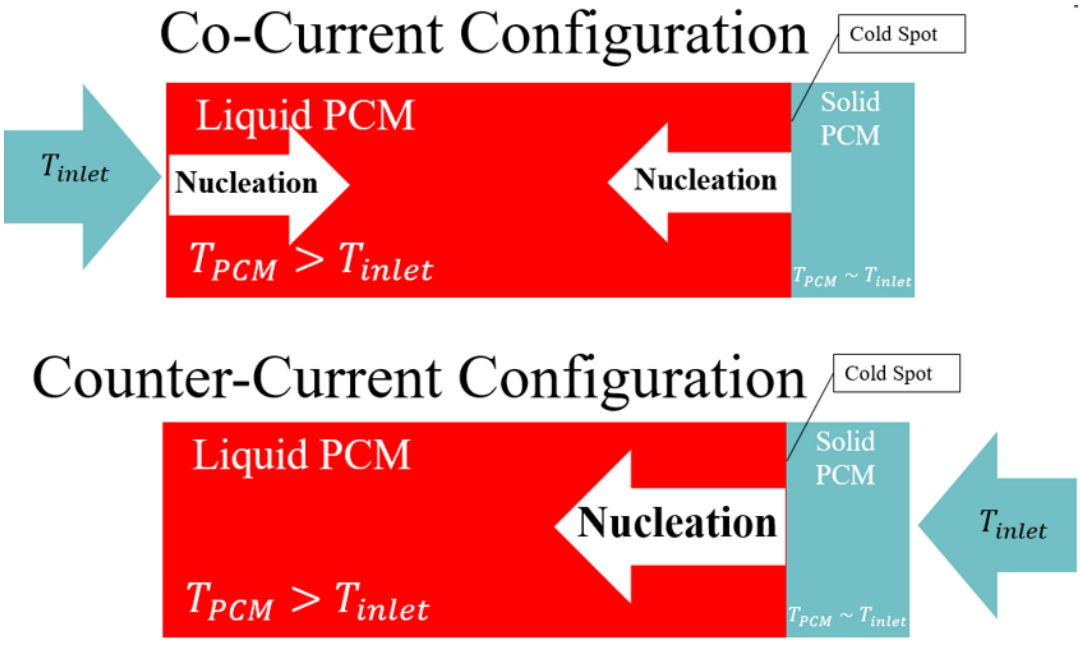

Figure 18: Schematic showing the effect on crystal growth process (for solidification) Co-current and Counter-current Configurations.

Another influence on the rate of nucleation and subcooling is the effect of ΔT_1 as shown in Equation 13; where, $T_{HTF,\ cold\ spot}$ is temperature of HTF at the cold spot location and $T_{PCM,\ cold\ spot}$ is the temperature of the cold spot (i.e. solid PCM). In both cases the cold spot is assumed to be in the range of 27 °C to 29 °C (i.e., at the 90% location). In the case of co-current experiments, the HTF temperature increases along the axial direction due to sensible cooling of PCM (and the parasitic energy loss to the heat exchanger mass) thus minimizing the values of ΔT_1 at the location of the cold spot. However, in the counter-current configuration maximum values of ΔT_1 is attained. Therefore, with counter-current configuration favorable conditions for

maximizing the rates of heat transfer and nucleation (solidification) rate are achieved at the locations of the cold spots.

$$\Delta T_1 = T_{HTF,cold\ Spot} - T_{PCM,cold\ Spot} \quad (13)$$

These effects can be further analyzed by monitoring the values of subcooling at different locations of the freeze front (i.e., locations corresponding to 70%, 50%, 30%, and 10% of the melt fractions) and are summarized in Table 3. In the case of counter-flow configuration, the degree of subcooling is less than 0.5 °C at varying freeze front locations compared to the co-current configuration (i.e., more than 1°C). This further demonstrates the importance on the direction of crystal growth (nucleation), flow direction, and heat transfer rate on subcooling.

As summarized in **Table 4**, the effects of varying the flow rates and inlet temperatures of the HTF were analyzed - for the counter-current configurations. The effect of flow rate and HTF inlet temperature during melting and solidification has negligible effect on subcooling as the results for varying flow rate and HTF inlet temperature is within the range of measurement uncertainty.

Table 3: The Degree of Subcooling Along the Freeze Front Locations in Both Co-current and Counter-current Configurations. The table summarizes the subcooling at the 70%, 50%, 30%, and 10% freeze front locations.

Freeze Front Location (%)	Co-Current Configuration (°C)	Counter-Current Configuration (°C)
70	3	0.3
50	1.5	0.1
30	2	0.4
10	2.5	0.4

Table 4: The Effect of Varying Flow Rate and HTF Inlet Temperature on Controlling Subcooling in the Counter Flow Configuration. The flow rate and HTF inlet temperature was varied between 3 and 5 GPH and 20 °C and 25 °C respectively.

Case	Flow rate (GPH)	T_{inlet} Melting (°C)	T_{inlet} Solidification (°C)	Nucleation Temperature (°C)	T_M (°C)	ΔT (°C)
E	3	33.0	25.0	27.3	27.2	0.1
F	3	35.0	25.0	26.8	27.0	0.2
G	3	37.4	25.0	27.0	26.9	0.1
H	5	33.0	25.0	27.0	27.2	0.2
I	5	35.0	25.0	26.3	26.5	0.2
J	5	37.4	25.0	25.7	26.2	0.5
H	3	35.0	20.0	26.3	26.4	0.1
I	3	37.4	20.0	26.5	26.5	0.0
J	5	35.0	20.0	25.2	25.7	0.5
K	5	37.4	20.0	25.1	25.6	0.5

In summary, a subcooling of 0.5 °C was achieved with counter-current configurations for the design case and less than 1 °C for all other counter-current configurations. Therefore, using a combination of *Cold Finger* technique with counter-current configuration was used to minimize subcooling while sacrificing approximately 10% of the energy storage capacity (i.e., by oversizing the heat

exchanger and at the expense of added material costs required for additional PCM that needs to be charged into the CHX to achieve the same energy storage capacity rating). Similar temperature profiles were also noticed in PCM center plates. The temperature profiles for center plates and other cases are summarized in Appendix D.

3.2 Melt and Freeze Front Propagation

The thermal profile for the 90% melt front locations (i.e., for case G with counter-current configuration) in the top plate is shown in Figure 17. The results for the center plates are provided in Appendix D, as their thermal profiles are similar to that of the top plate (with faster melting and freezing due to bi-directional heat transfer from both top and bottom side of the PCM contained in this layer). In case G, the melting was accomplished in 22.8 minutes (with ~90% of the PCM mass being melted) whereas complete solidification was accomplished in 53 minutes. In case B (co-current configuration), the melting was accomplished in 20.3 minutes whereas complete solidification was accomplished in 46.1 minutes. Therefore, in both cases, the time required for solidification is about twice as much as that of melting. During melting, the heat transfer in the PCM channel was enhanced by the onset of natural convection, whereas the heat transfer during freezing was dominated by conduction in the PCM channel. Counter-current configuration (case G) required 7 minutes longer to complete freezing in comparison to the co-current configuration (case B). This may be due to the thermal inertia of the heat exchanger. In the case of counter-current configuration, the heat transfer is occurring between the PCM (latent heat + sensible heat) and heat

exchanger at the same time. However, in the case of co-current configuration, there is enough delay in the onset of nucleation enabling the heat exchanger to already reach the steady state temperature (therefore, there are negligible parasitic losses to the mass of the CHX), and sensible heat gain by the PCM is therefore negligible as it has already attained subcooled condition. Therefore, during phase transition the heat transfer is occurring purely between the PCM and HTF, which accelerates the rate of solidification.

The times required for achieving the phase transition (to the desired melt fractions as well as for complete solidification) for the non-insulated cases; are summarized in Figure 19. The melting time was monitored as a function of both the variations in the values of the flow rate and the HTF inlet temperature. By comparing the results obtained from Case E (3 GPH) to that of the Case H (5 GPH); for fluid inlet temperature of 33 °C (for the HTF), it is observed that the melting time was reduced by 17.9% in Case H. In comparison, for Case E ($T_{in,HTF}$ = 33 °C), Case F ($T_{in,HTF}$ = 35 °C), and Case G ($T_{in,HTF}$ = 37.4 °C) at 3 GPH, the melting time was reduced by 34.7% with a 2 °C increase in inlet temperature ($T_{in,HTF}$) and 50% with a 4.4 °C increase in inlet temperature ($T_{in,HTF}$). In the solidification case, comparison of Case E (3 GPH) with Case H (5 GPH) for HTF inlet temperature of 25 °C shows that the freezing time was reduced by 20.6%, whereas by dropping the inlet temperature ($T_{in,HTF}$) by 5 °C the freezing time was reduced by 42% (Case G versus Case L).

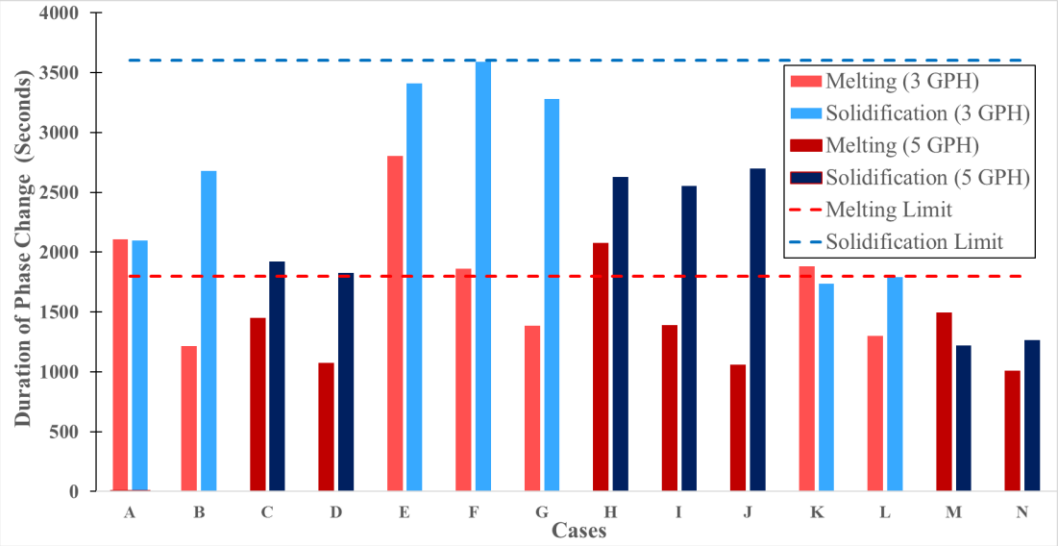

Figure 19: Duration of Phase Change for Non-insulated Cases at 90% Mass Fraction.

In summary, the time required for complete solidification is increased for the counter-current configurations. The melting time and solidification time is sensitive to both flow rate and HTF inlet temperature, but these values for time are more sensitive to the HTF inlet temperature. Therefore, in practical applications, increasing the HTF inlet temperature is more effective than increasing the flow rate, as increase in flow rate is associated with higher pressure drops and pump penalties that accrue from Reynolds analogy (i.e. increasing flowrate causes increase in pressure drop values with only marginal reduction in time required for phase change process).

3.3 Total Energy Storage Capacity

The experimental measurements for the total energy storage capacity are summarized in Figure 20. The experimental values for the energy storage capacity of

the LHTESS exceeds the theoretical value of 130 kJ for the non-insulated case, because the experimental measurements account for the combined values of the latent heat, sensible heat, and heat loss (while the theoretical estimate is based only on the values of latent heat). The calculations for Stefan number are shown in Appendix C and are always below a value of .06 (which shows that most of the thermal energy transfer accrues from the latent heat of the PCM). Furthermore, Case G (at a 90% melt fraction) shows that the Stefan number during the melting phase varies between .023 and .04. In contrast, the Stefan number is roughly double during the freezing process than that of the melting process. There is more sensible heat during freezing because the phase change happens at a slower rate due to the dominance of conduction.

From Figure 20 it can be observed that the total energy storage during the solidification process is typically higher than that of the melting process. This is largely due to the change in value of the specific heat of the PCM, which is 1.63 [J/(g·K)] in the liquid phase and 2.76 [J/(g·K)] in the solid phase. Overall, the energy storage is roughly the same throughout all the cases, but any variations are due to heat loss or heat gain.

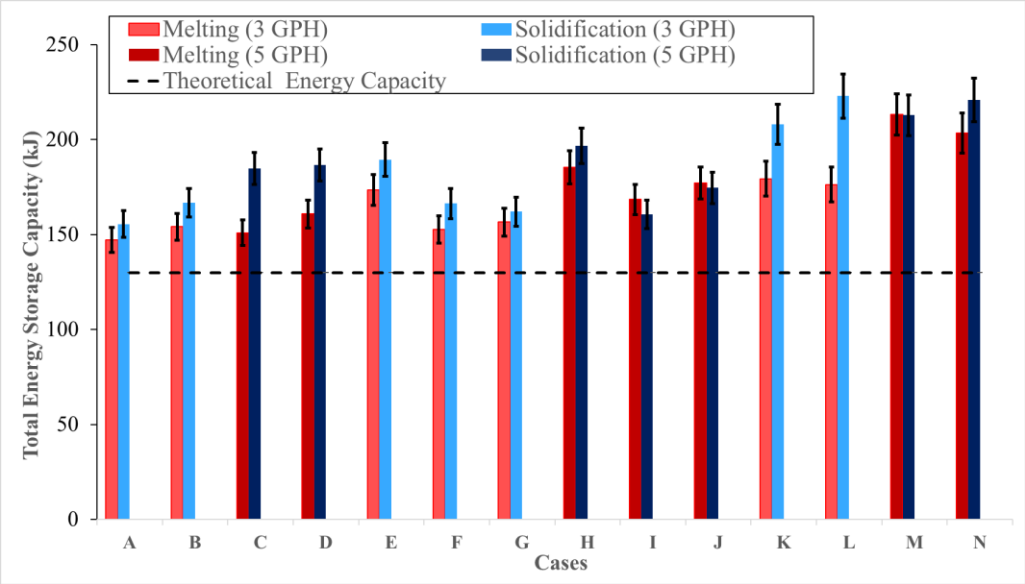

Figure 20: Total Energy Storage Capacity for Non-insulated Cases at 90% Melt Fraction.

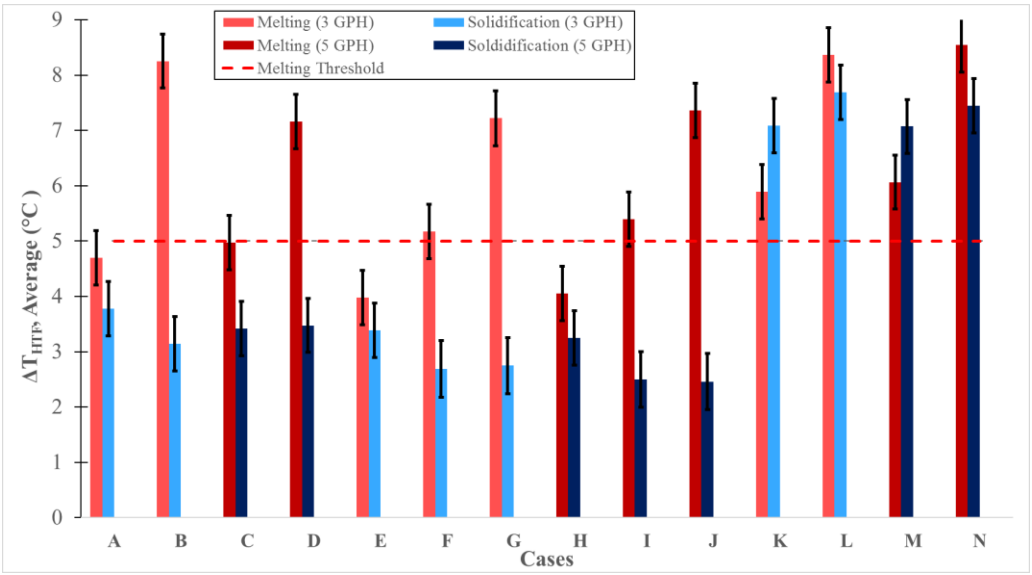

Figure 21: Average Temperature Difference of the Heat Transfer Fluid for all the Non-insulated Cases at 90 % Melting.

Comparing Case G to Case J (i.e., for variation in flow rates) the energy storage improvement is roughly 20.6 kJ and 12.5 kJ for melting and solidification, respectively. When Case G is compared to Case L (i.e., for variation of the inlet temperature during freezing), the improvement is roughly 19.8 kJ and 60.9 kJ for melting and solidification, respectively. For Case L, there is about five times improvement in the energy storage during the solidification process and about the same capacity during the melting process when compared to that of the improvements in Case J. Thus, the temperature drop (or gain) of the HTF is a more sensitive parameter than the mass flow rate, for the power rating of the LHTESS. The temperature difference for each case is summarized in Figure 21.

In summary, the uncertainty in the energy storage capacity of the heat exchanger is due to heat loss or gained from the ambient. The rate of heat loss is a function of flow rate and inlet temperature. The heat loss is magnified at a lower flow rate and higher ΔT ($\Delta T = T_{Heat\ Exchanger} - T_{ambient}$). Therefore values of ΔT_{HTF} during the melting process for the design condition was 7.2 °C (which exceeds the cooling condition specified by the ARID program).

3.4 Power Rating

The LHTESS is effectively a thermal battery (i.e., for delivering and storing heat at different duty cycles). Therefore, it is important to analyze the instantaneous values and average values of power during both the melting and solidification processes. In the case of an electric battery, power ratings are typically constant during both the

charging and discharging process. In contrast, for the thermal battery, as shown in Figure 22, the power ratings vary drastically at different periods of the charging and discharging process. For the thermal battery during melting, the power rating is not constant (unlike an electric battery). The power peaks initially due to the onset of melting (i.e. high release of latent heat energy) before reaching a stable outlet HTF temperature. The instantaneous values of power rating decrease gradually with time as the latent energy storage capacity is reduced. The average power rating for the design condition (Case G) is 180 watts, with a peak power of 200 watts (start of phase transition) and minimum power of 140 watts (end of phase transition). The instantaneous power rating during solidification is almost constant throughout the phase transition time except for the initial peak at the onset of nucleation. This effect is mainly due to the constant value of the effective thermal conductivity during solidification.

Figure 23 summarizes the values of the average power rating for variations in the values of flow rate and inlet temperature (for both melting and solidification cases). The power rating during melting and solidification are both plotted as a function of both flow rate and inlet temperature. As expected, higher flow rates and temperature differences lead to larger power ratings. From Equation 10, it is shown that the power rating is a function of mass flow rate, specific heat capacity of the HTF, and the temperature difference (for the HTF). Since there is marginal change in the specific heat capacity values of the HTF of this study is focused on the sensitivity of the experimental data to significant variations in the values of mass flow rate and inlet

temperature of the HTF. Comparing Case G to Case J (for exploring the variation in the flow rate from 3 GPH to 5 GPH), the average improvement in the power ratings for both melting and solidification is calculated to be about 51 W and 11.7 W, respectively. However, when comparing Case G to Case L, the improvement for melting and solidification are about 17.4 W and 73.3 W, respectively. This shows that the average power rating is more sensitive to the variation in the values of temperature difference (this arises from the "flat" portion of the plots for power ratings). The maximum power rating is more sensitive to the variations in the values of the mass flow rate. The plots for the power ratings for the other cases follow the same trends and are provided in Appendix F.

In summary, the instantaneous power during melting is not constant and varies with time. The power peaks initially due to the onset of melting (i.e. high release of latent energy) before reaching a stable outlet temperature of the HTF. The instantaneous power decreases gradually with time as the latent energy storage capacity decreases. The values of instantaneous power rating during solidification is almost constant throughout the duration of the phase transition (except for the initial peak at the onset of nucleation). This effect is mainly due to the constant values of effective thermal conductivity achieved during solidification. Therefore, the mass flow rate has larger influence on power output during solidification.

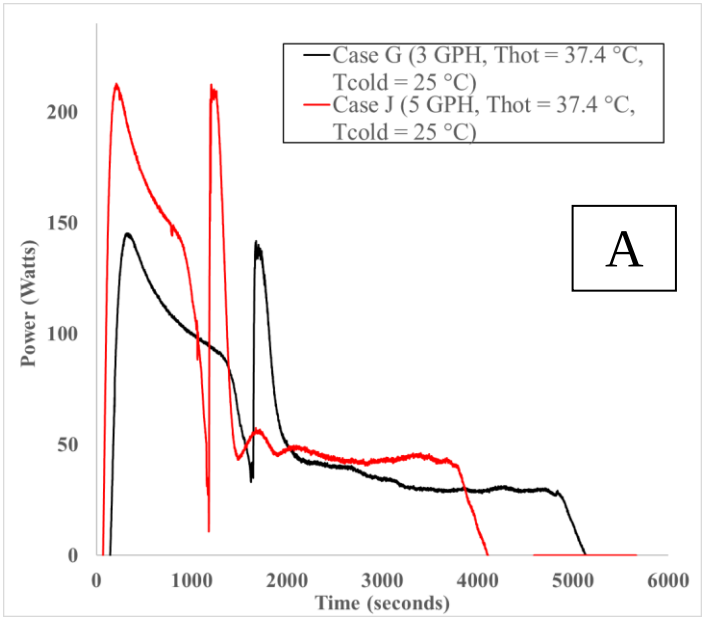

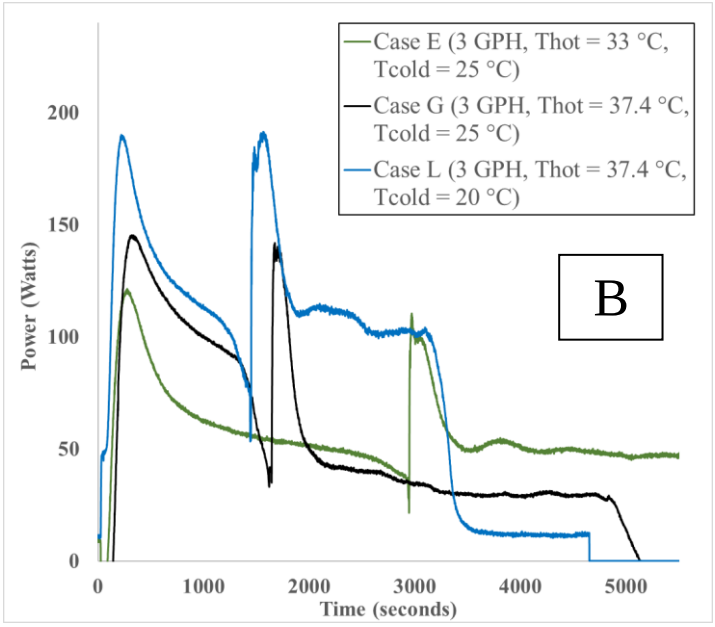

Figure 22: Instantaneous Power Ratings for variations in the Flow Rate and Inlet Temperature. (A) Varying volumetric flow rate from 3 GPH to 5 GPH with T_{hot} of 37.4 °C and T_{cold} of 25 °C; (B) Varying inlet temperature from T_{hot}: 33 °C to 37.4 °C and T_{cold}: 25 °C to 20 °C for a volumetric flow rate of 3 GPH.

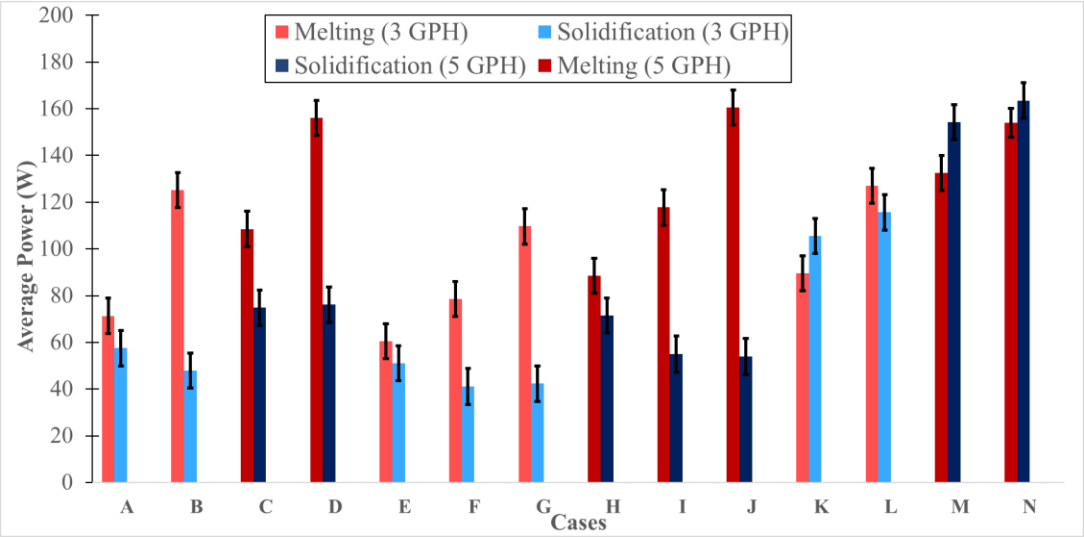

Figure 23: Average Power Rating for the Non-insulated Cases at 90% Mass Fraction.

3.5 Effectiveness

The effectiveness of the heat exchanger is ~0.8 for melting and ~1 for solidification as shown in Figure 24. Figure 24 also shows that the values of T_{PCM} during solidification is ~29 °C and $T_{HTF,OUTLET}$ is also ~29 °C (the curves in the plots for these two variables almost overlap). Therefore, the effectiveness during solidification is estimated to be ~1. Similarly for melting, T_{PCM} is ~27 °C and the value of $T_{HTF,OUTLET}$ is ~29 °C. Hence, the values of effectiveness during melting is ~0.8. However, the error in the effectiveness calculation is enormous (during certain portions of the phase change process) due to the manifold design. It takes more than 12 minutes to completely flush out the residual liquid (cold or hot fluid out) of the

manifold which affects the measured values for the overall ΔT, which in turn affects the estimated values of effectiveness (as the mixing of the fluid at the outlet with the residual fluid in the manifold causes the temperature of the mixture to be recorded by the thermocouple at exit; rather than the true values of the outlet temperature of the HTF). Therefore, to decrease the uncertainty in the effectiveness calculation during melting and solidification, the T_{PCM} values were considered only after 70% of the mass of the PCM was melted (which typically occurred at times exceeding 12 minutes).

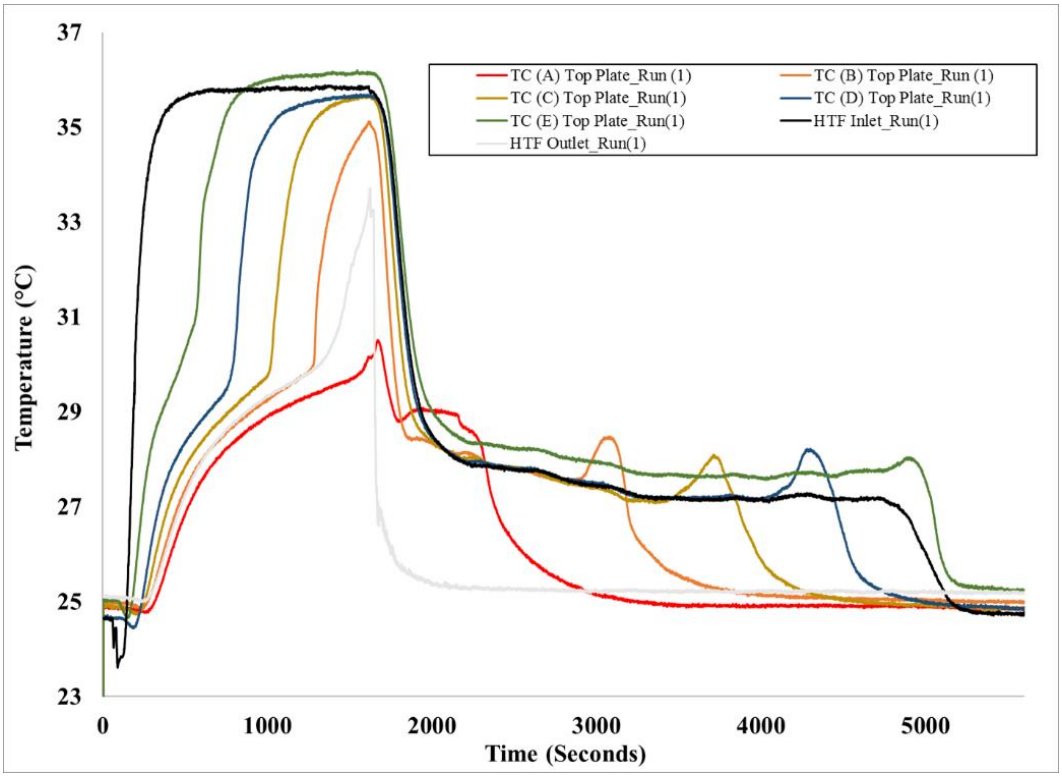

Figure 24: The Temperature Profile During Melting and Solidification During Design Condition (Case G, Post-experiment calibration).

3.6 Insulated Heat Exchanger

The duration of phase change for the experiments that were performed with and without insulation - are summarized in Figure 25. Comparing case G to R (design conditions), the melting time and solidification time reduce by ~10% and ~4%, respectively. The trend for melting are also similar for the other cases. However, the reduction in freezing time varies from 1% to 9% throughout all of the cases, with the exception of cases K and case O – for both melting and solidification time. When Comparing case K to case O, the melting time and solidification time reduce by ~3% and ~20%, respectively. These difference in the results are observed to vary with the variations in mass flow rates between the two cases, where cases O has the higher flow rate. Furthermore, the insulated system has less parasitic heat loss to the environment, which means there is more energy in system during the phase transition. The slight increases in energy in the system leads to a faster phase transition time.

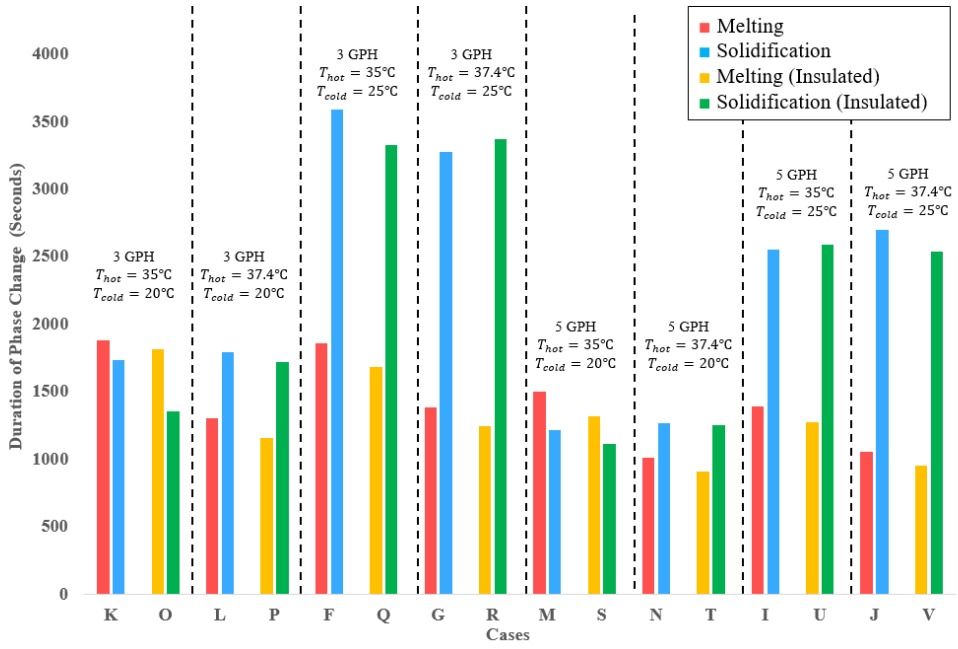

Figure 25: Duration of Phase Change for Non-insulated and Insulated Cases (at 90% Mass Fraction for melting).

The total energy storage capacity for the cases that were run with and without insulation are summarized in Figure 26. Comparing case G to case R, the melting phase shows ~3% reduction. Solidification, on the other hand, shows ~20% increase in total energy storage. The results for melting follow similar trends, and with less heat loss to the environment the total energy storage increases. The time required for solidification on the other hand, shows a slight increase. This increase can be attributed to two factors. The first being that the insulated melting phase now has a slight increase in its sensible energy. Secondly, when cooling around room temperature, the rate of heat loss to the ambient is also minimized (resulting in minimal difference between

the results for insulated versus non-insulated cases). Thus, with these two factors, there is a slight increase in the total energy storage of the insulated cases during freezing.

It should also be noted that the two reasons above explain the differences in total energy storage capacity between cases with inlet temperatures of $T_{Cold} = 25$ ℃ and $T_{Cold} = 20$ ℃, where $T_{Cold} = 25$ ℃ shows an increase and $T_{Cold} = 20$ ℃ shows a decrease. This is a result of the ΔT_{HTF}, as shown in Figure 27. The cases conducted with $T_{Cold} = 25$ ℃ show an increase in ΔT_{HTF} between the non-insulated and insulated cases. However, the ΔT_{HTF} values for cases corresponding to experiments conducted with $T_{Cold} = 20$ ℃ show almost no difference between the non-insulated and insulated cases.

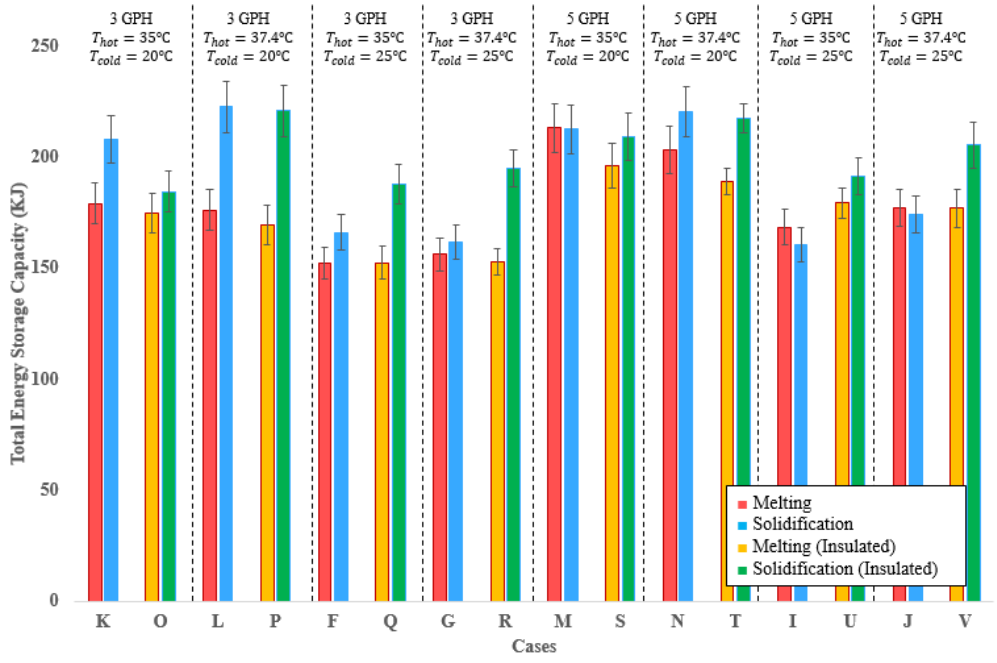

Figure 26: Total Energy Storage Capacity for Non-insulated and Insulated Cases at 90% Melt Fraction.

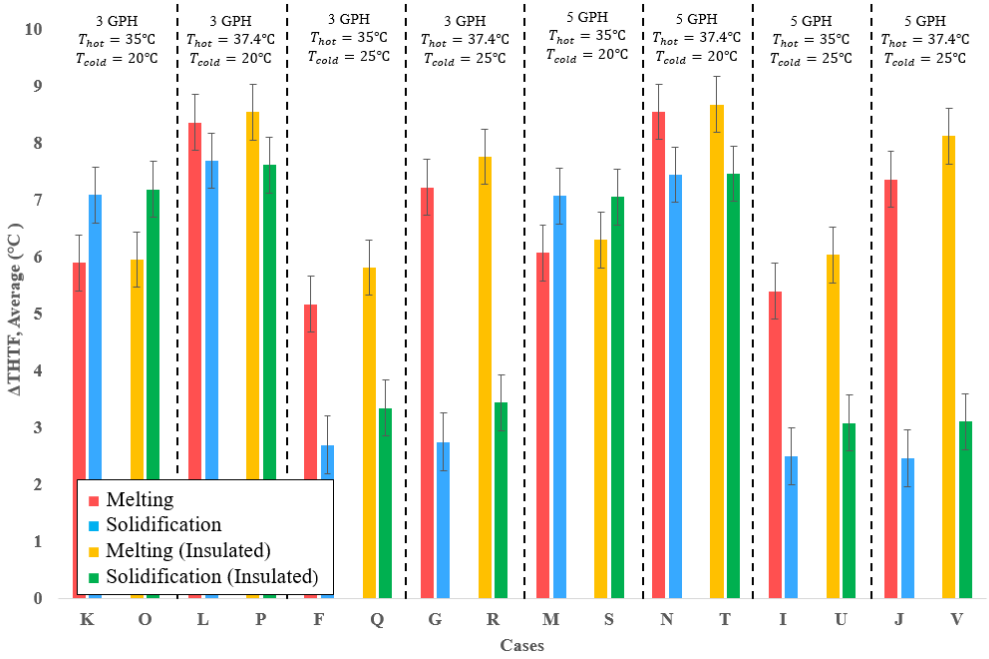

Figure 27: ΔT for Non-insulated and Insulated Cases at 90% Mass Fraction.

In summary, the insulation around the heat exchanger showed minimal effect, due to the melting and solidifying temperatures being close to the room temperature. The total energy storage for melting and freezing are also roughly the same for both the non-insulated and insulated cases. A summary of the results for the average power and Stefan number with the insulated heat exchanger are shown in Appendix G.

4 SUMMARY AND FUTURE DIRECTIONS

4.1 Summary of Results

In this study, the efficacy of a compact heat exchanger containing a PCM (lithium nitrate trihydrate) was explored for realizing a LHTESS; in applications involving supplemental cooling (e.g., for improving the operational efficiency and reliability of a thermoelectric power plants). The scope of this study was limited to evaluating the thermal performance of the compact heat exchanger to conditions that meet the program objectives and deliverables of the sponsored research project (i.e., to the specifications outlined in the ARPA-E ARID program).

The tests performed using the LHTESS in this study were implemented by varying the values of inlet temperature and by estimating the variations in the values for time (i.e., the values of the instantaneous power rating) for incomplete melting and complete solidification (i.e., for "Cold Finger" technique). The temperature ranges explored in this study correspond to the values of temperature ranges typically encountered in typical arid climates.

The values of the inlet temperatures of the HTF during melting were 33 °C, 35 °C, and 37.4 °C. The inlet temperature of the HTF (de-ionized water or "DI" water) during solidification were 25 °C and 20 °C. The *Cold Finger* technique was implemented for solid mass fractions of 90%, 70%, 50%, 30%, and 10% during melting (to test the efficacy in mitigating subcooling effects during the solidification process). A total of twenty different cases were implemented in this study (and tested for repeatability of the experimental data) in order to determine the thermal

performance and viability of the heat exchanger configuration for meeting the objectives of the sponsored research project (i.e., the ARPA-E ARID program).

A subcooling of 0.5 °C was achieved with counter-current configurations for the design case (and to less than 1 °C for all other counter-current configurations). Therefore, a combination of the *Cold Finger* technique along with the counter-current configuration can enable the subcooling issues to be obviated. This is achieved for a penalty associated with 10% reduction in the energy storage capacity (i.e., the improved reliability is achieved by oversizing the heat exchanger and results in higher material costs due to larger mass of PCM that needs to be loaded into the LHTESS).

The time required for complete solidification to be achieved is increased in the counter-current configurations (compared to that of the co-current configurations). The values of the melting time and solidification time are sensitive to variation in both flow rate and inlet temperature of the HTF. However, these values for the time are more sensitive to the variation in the inlet temperature of the HTF. In practical (engineering) applications, increasing the HTF inlet temperature is a more effective strategy for improving the power ratings of the LHTESS since increasing the flowrate to achieve the same level of power rating is typically associated with much higher values of pump penalty, that arise from Reynolds analogy (i.e. increasing flowrate causes dramatic increase in pressure drop and pump power consumed for achieving the same end-goal).

The uncertainty in the energy storage capacity of the heat exchanger arises from the parasitic heat loss or gain from the surroundings (ambient conditions). The

rate of heat loss is strongly affected by the flow rate and the values of inlet temperature of the HTF. The heat loss is magnified at lower flow rate and higher ΔT ($\Delta T = T_{Heat\ Exchanger} - T_{ambient}$). The values of ΔT_{HTF} achieved during the melting process for the design condition was 7.2 °C (which exceeds the amount of cooling required by the specifications in the ARID program).

The instantaneous power during melting is not constant and varies significantly with time. The power peaks initially due to the onset of melting (i.e. high release of latent energy) before reaching a stable value as the outlet HTF temperature reaches steady state conditions. The instantaneous power decreases gradually with time as the latent energy storage capacity decreases. The values of instantaneous power rating during solidification are almost constant throughout the phase transition process (except for the initial peak at the onset of nucleation). This accrues mainly from the constant values of the effective thermal conductivity of the liquid PCM during the solidification process. The mass flow rate is, therefore, observed to be a more sensitive parameter for the values of power rating during the solidification process.

The insulation around the heat exchanger showed minimal effect, due to the melting and solidifying temperatures being around room temperature. The total energy storage for melting and freezing are also roughly the same as between the non-insulated and insulated cases.

4.2 Conclusion

The conclusions gleaned from this study are summarized below:

- Subcooling of less than 1 °C was achieved by combining the *Cold Finger* technique with counter-flow configuration.
- Flow rate and inlet temperature do not significantly affect the level of subcooling.
- The melting and freezing time are sensitive to both flow rate and inlet temperature of the HTF.
    - The values for melting time and freezing time are more sensitive to the variations in the inlet temperature (than that of the flow rate of the HTF). Increasing the flow rate to achieve the same levels of instantaneous power ratings are associated with higher values of pump penalty to achieve the same goals.
    - Hence, varying the inlet temperature of the HTF is a more effective strategy for enhancing the power rating of the LHTESS explored in this study.
- The uncertainty in estimating the energy storage capacity rating of the LHTESS in this study increases due to parasitic heat transfer (heat loss or gain from the surroundings).
- For the design condition explored in this study, the achieved level of cooling exceeds 7 °C (which is more than the specified value of 5 °C in the ARPA-E ARID program).

The effectiveness during melting was ~0.8 and during solidification was ~1 for the design conditions explored in this study (which is deemed to be adequate for the program requirements of this ARID Project).

4.3 Future Directions and Recommendations

A recurring problem for heat exchangers is the unavoidable debilitating effects accruing from progressive corrosion and fouling. These issues can lead to major problems associated with the degradation in reliability and thermal performance. For this reason, parametric studies should be conducted to determine the sensitivity of the thermal performance of the LHTESS to variations in the level of corrosion (e.g., between the PCM and the heat exchanger material).

It is also recommended that the compact heat exchanger be tested for repeated thermal cycling; involving tests in excess of 1000 cycles (in order to ensure the long term reliability of the LHTESS). Salt hydrates are known to suffer from performance degradation due to phase segregation. Implementing these types of long term reliability testing protocols for the LHTESS will help determine their efficacy in commercial applications.

With the recent technological and commercial breakthroughs achieved in additive manufacturing, 3-D printed heat exchangers could also prove to be a viable option for manufacturing and wide spread commercial deployment of LHTESS in consumer applications (and therefore the results from this study are not just limited to power generation applications). One 3-D printed LHTESS has already been implemented by Texas A&M University during the AutoDrive Challenge, which is

sponsored by the Society of Automotive Engineers and General Motors [40]. The Texas A&M University team designed a 3-D printed shell-and-tube heat exchanger TES to cool the electronic systems in the car, where the team ended up placing 2nd in the competition [41]. Additionally, these heat exchanger designs would alleviate the need to perform corrosion studies, as corrosion is not expected to be a significant technical (or economic) issue for the 3-D printed materials and heat exchanger configurations.

Finally, the studied thermal energy storage system satisfies the requirements for the ARPA-E ARID program requirements, however, these requirements are limited to small scale prototypes and are just the initial steps to finding a viable supplemental cooling unit. In order to verify that this system is a viable option for large scale use (i.e subsequent integration in a thermal power plant supplemental cooling) the system should be scaled up and further analyzed.

REFERENCES

[1] Water Energy Technology Laboratory. (2018, May 21). *Water Usage in Coal To Power Applications*. Available: https://www.netl.doe.gov/research/Coal/energy-systems/gasification/gasifipedia/water-usage

[2] World Nuclear Association. (2018, February). *Cooling Power Plants*. Available: http://www.world-nuclear.org/information-library/current-and-future-generation/cooling-power-plants.aspx

[3] F. A. Kulacki, *Handbook of Thermal Science and Engineering*. Springer, 2018.

[4] A. Abhat, "Low temperature latent heat thermal energy storage: heat storage materials," *Solar energy*, vol. 30, no. 4, pp. 313-332, 1983.

[5] M. K. Rathod and J. Banerjee, "Thermal stability of phase change materials used in latent heat energy storage systems: a review," *Renewable and Sustainable Energy Reviews*, vol. 18, pp. 246-258, 2013.

[6] B. Zalba, J. M. Marın, L. F. Cabeza, and H. Mehling, "Review on thermal energy storage with phase change: materials, heat transfer analysis and applications," *Applied thermal engineering*, vol. 23, no. 3, pp. 251-283, 2003.

[7] A. Sharma, V. V. Tyagi, C. Chen, and D. Buddhi, "Review on thermal energy storage with phase change materials and applications," *Renewable and Sustainable energy reviews*, vol. 13, no. 2, pp. 318-345, 2009.

[8] R. K. Shah and D. P. Sekulic, *Fundamentals of heat exchanger design*. John Wiley & Sons, 2003.

[9] F. Agyenim, N. Hewitt, P. Eames, and M. Smyth, "A review of materials, heat transfer and phase change problem formulation for latent heat thermal energy storage systems (LHTESS)," *Renewable and sustainable energy reviews*, vol. 14, no. 2, pp. 615-628, 2010.

[10] A. F. Regin, S. C. Solanki, and J. S. Saini, "Heat transfer characteristics of thermal energy storage system using PCM capsules: A review," *Renewable and Sustainable Energy Reviews,* vol. 12, no. 9, pp. 2438-2458, 2008.

[11] M. K. Rathod and J. Banerjee, "Thermal Performance of a Phase Change Material-Based Latent Heat Thermal Storage Unit," *Heat Transfer—Asian Research,* vol. 43, no. 8, pp. 706-719, 2014.

[12] M. Hosseini, M. Rahimi, and R. Bahrampoury, "Experimental and computational evolution of a shell and tube heat exchanger as a PCM thermal storage system," *International Communications in Heat and Mass Transfer,* vol. 50, pp. 128-136, 2014.

[13] A. Agarwal and R. Sarviya, "An experimental investigation of shell and tube latent heat storage for solar dryer using paraffin wax as heat storage material," *Engineering Science and Technology, an International Journal,* vol. 19, no. 1, pp. 619-631, 2016.

[14] M. Avci and M. Y. Yazici, "Experimental study of thermal energy storage characteristics of a paraffin in a horizontal tube-in-shell storage unit," *Energy conversion and management,* vol. 73, pp. 271-277, 2013.

[15] N. Kousha, M. Hosseini, M. Aligoodarz, R. Pakrouh, and R. Bahrampoury, "Effect of inclination angle on the performance of a shell and tube heat storage unit–An experimental study," *Applied Thermal Engineering,* vol. 112, pp. 1497-1509, 2017.

[16] S. Seddegh, M. M. Joybari, X. Wang, and F. Haghighat, "Experimental and numerical characterization of natural convection in a vertical shell-and-tube latent thermal energy storage system," *Sustainable Cities and Society,* vol. 35, pp. 13-24, 2017.

[17] J. N. Chiu and V. Martin, "Submerged finned heat exchanger latent heat storage design and its experimental verification," *Applied Energy,* vol. 93, pp. 507-516, 2012.

[18] K. Merlin, D. Delaunay, J. Soto, and L. Traonvouez, "Heat transfer enhancement in latent heat thermal storage systems: comparative study of

different solutions and thermal contact investigation between the exchanger and the PCM," *Applied energy*, vol. 166, pp. 107-116, 2016.

[19] M. Hosseini, M. Rahimi, and R. Bahrampoury, "Thermal analysis of PCM containing heat exchanger enhanced with normal annular fines," *Mechanical Sciences*, vol. 6, no. 2, p. 221, 2015.

[20] A. A. Al-Abidi, S. Mat, K. Sopian, M. Sulaiman, and A. T. Mohammad, "Experimental study of melting and solidification of PCM in a triplex tube heat exchanger with fins," *Energy and Buildings*, vol. 68, pp. 33-41, 2014.

[21] J. Shon, H. Kim, and K. Lee, "Improved heat storage rate for an automobile coolant waste heat recovery system using phase-change material in a fin–tube heat exchanger," *Applied Energy*, vol. 113, pp. 680-689, 2014.

[22] J. García-Alonso, F. Aguilar, and E. Montero, "Heat transfer with phase change in a shell and tube latent heat storage unit," 2014: International Conference on Heat Transfer, Fluid Mechanics and Thermodynamics.

[23] Y. Tao, Y. Liu, and Y.-L. He, "Effects of PCM arrangement and natural convection on charging and discharging performance of shell-and-tube LHS unit," *International Journal of Heat and Mass Transfer*, vol. 115, pp. 99-107, 2017.

[24] M. Medrano, M. Yilmaz, M. Nogués, I. Martorell, J. Roca, and L. F. Cabeza, "Experimental evaluation of commercial heat exchangers for use as PCM thermal storage systems," *Applied energy*, vol. 86, no. 10, pp. 2047-2055, 2009.

[25] T. Pirasaci and D. Y. Goswami, "Influence of design on performance of a latent heat storage system for a direct steam generation power plant," *Applied energy*, vol. 162, pp. 644-652, 2016.

[26] N. I. Ibrahim, F. A. Al-Sulaiman, S. Rahman, B. S. Yilbas, and A. Z. Sahin, "Heat transfer enhancement of phase change materials for thermal energy storage applications: A critical review," *Renewable and Sustainable Energy Reviews*, vol. 74, pp. 26-50, 2017.

[27] M. E. H. Amagour, A. Rachek, M. Bennajah, and M. E. Touhami, "Experimental investigation and comparative performance analysis of a compact finned-tube heat exchanger uniformly filled with a phase change material for thermal energy storage," *Energy Conversion and Management*, vol. 165, pp. 137-151, 2018.

[28] Z. Khan and Z. A. Khan, "An experimental investigation of discharge/solidification cycle of paraffin in novel shell and tube with longitudinal fins based latent heat storage system," *Energy Conversion and Management*, vol. 154, pp. 157-167, 2017.

[29] A. M. Abdulateef, J. Abdulateef, S. Mat, K. Sopian, B. Elhub, and M. A. Mussa, "Experimental and numerical study of solidifying phase-change material in a triplex-tube heat exchanger with longitudinal/triangular fins," *International Communications in Heat and Mass Transfer*, vol. 90, pp. 73-84, 2018.

[30] M. Kenisarin and K. Mahkamov, "Passive thermal control in residential buildings using phase change materials," *Renewable and sustainable energy reviews*, vol. 55, pp. 371-398, 2016.

[31] A. Lazaro, P. Dolado, J. M. Marín, and B. Zalba, "PCM–air heat exchangers for free-cooling applications in buildings: Experimental results of two real-scale prototypes," *Energy Conversion and Management*, vol. 50, no. 3, pp. 439-443, 2009.

[32] J. Lei, J. Yang, and E.-H. Yang, "Energy performance of building envelopes integrated with phase change materials for cooling load reduction in tropical Singapore," *Applied Energy*, vol. 162, pp. 207-217, 2016.

[33] Y. Zhang, G. Zhou, K. Lin, Q. Zhang, and H. Di, "Application of latent heat thermal energy storage in buildings: State-of-the-art and outlook," *Building and Environment*, vol. 42, no. 6, pp. 2197-2209, 2007.

[34] S. M. Vakilaltojjar, "Phase change thermal storage system for space heating and cooling," University of South Australia, 2000.

[35] S. Sharma, A. Tahir, K. Reddy, and T. K. Mallick, "Performance enhancement of a Building-Integrated Concentrating Photovoltaic system using phase change material," *Solar Energy Materials and Solar Cells*, vol. 149, pp. 29-39, 2016.

[36] ARPA-E ARID. *ARID Program Overview*. Available: https://arpa-e.energy.gov/sites/default/files/documents/files/ARID_ProgramOverview.pdf

[37] P. J. Shamberger and T. Reid, "Thermophysical properties of lithium nitrate trihydrate from (253 to 353) K," *Journal of Chemical & Engineering Data*, vol. 57, no. 5, pp. 1404-1411, 2012.

[38] R. K. Shah, "Extended surface heat transfer," *Thermopedia, Feb*, vol. 14, pp. 1-8, 2011.

[39] (2008, June 11). *Kline-McClintock Method (Experimental Uncertianity)*. Available: https://www.scribd.com/document/242477924/Kline-Mcclintock-Uncertainty

[40] J. Reiley, R. Rose, and C. Scoggins. (2018, 2 June). *Texas A&M AutoDrive Challenge team shares experience before showcase*. Available: https://tees.tamu.edu/news/2018/04/25/texas-am-autodrive-challenge-team-shares-experience-before-showcase/

[41] SAE International. (2018, 2 June). *SAE International and General Motors Announce Winners of Year One of the AutoDrive Challenge Competition*. Available: https://www.sae.org/news/press-room/2018/05/sae-international-and-general-motors-announce-winners-of-year-one-of-the-autodrive-challenge-competition

APPENDIX A

This section provides additional information on the flow configurations for the compact heat exchanger flow loop.

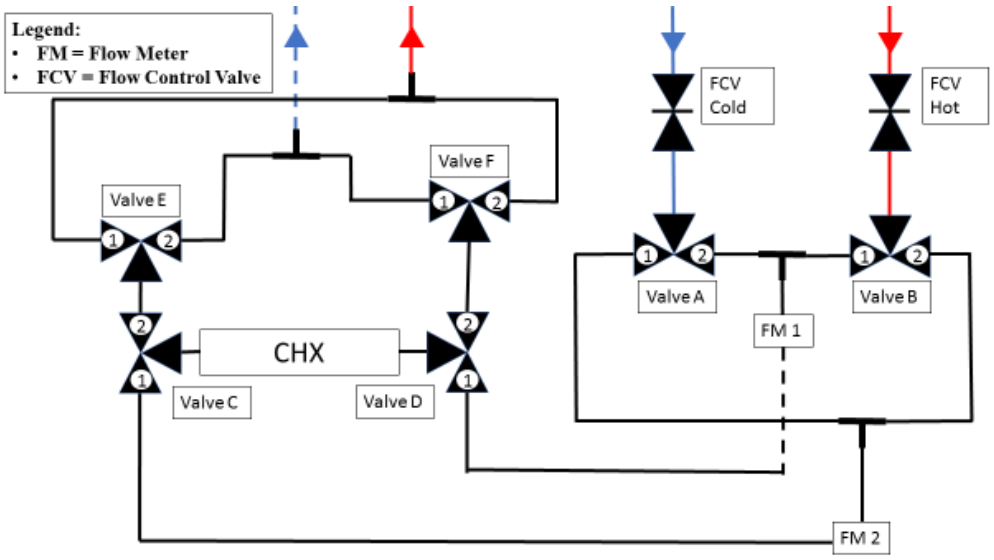

Figure 28: Schematic of Heat Exchanger Flow Loop for both co-current and counter current configuration; showing the valve configurations for achieving both co-current and counter-current arrangements.

Counter-Current

Table 5: Valve configurations for melting and solidification in counter-current flow configuration.

Valve	Location for Melting	Location for Solidification
A	2	2
B	2	2
C	1	2
D	2	1
E	N/A	1
F	2	N/A

Co-Current

Table 6: Valve locations for melting and solidification in co-current flow configuration.

Valve	Location for Melting	Location for Solidification
A	2	1
B	2	2
C	1	1
D	2	2
E	N/A	N/A
F	2	1

APPENDIX B

The section provides the thermocouple calibrations that were done before (pre-experiment) and after (post-experiment) the experiment.

Table 7: Summary of Calibration curves for each thermocouple before and after the experiment

Thermocouples	Location	Calibration Coefficient (Pre-experiment)	Calibration Coefficient (Post-experiment)
11	HTF Inlet	Y= 1.0142x – 0.6269	y = 1.02x - 1.4297
12	HTF Outlet	Y= 1.0162x – 0.7106	y = 1.0209x - 1.3023
6	10% Top Plate	Y= 1.0165x - 1.0185	y = 1.0175x - 0.8497
3	30% Top Plate	Y=1.0151x - 0.9547	y = 1.0163x - 0.6955
7	50% Top Plate	Y=1.0156x - 1.073	y = 1.0192x - 0.7798
9	70% Top Plate	Y=1.0123x - 0.5428	y = 1.0195x - 1.4931
8	90% Top Plate	Y=1.0160x - 1.1462	y = 1.0196x - 1.3791
1	10% Center Plate	Y=1.0152x - 1.0282	y = 1.0148x - 0.8434
5	30% Center Plate	Y=1.0000x – 0.0000	y = 1.0183x - 0.4943
4	50% Center Plate	Y=1.0221x - 1.3752	y = 1.0162x - 0.7505
10	70% Center Plate	Y=1.0142x – 0.7036	y = 1.018x - 1.3416
2	90% Center Plate	Y=1.015x – 1.1444	y = 1.0177x - 0.6686

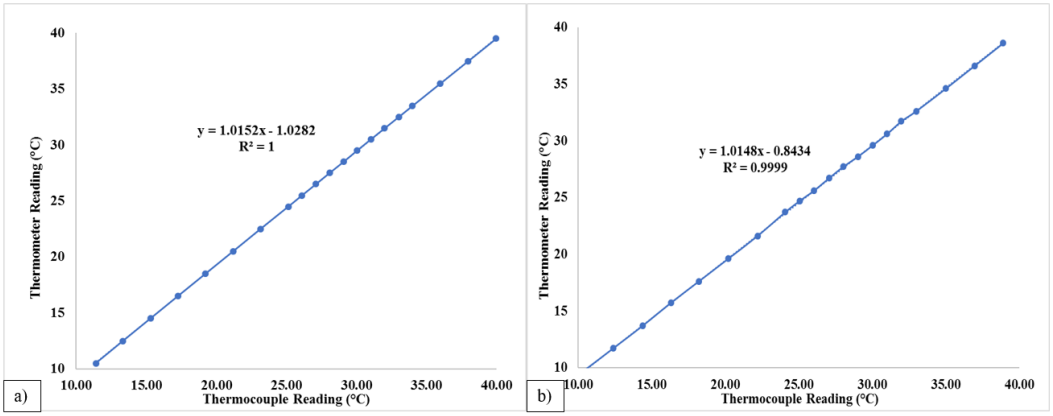

Figure 29: Calibration curve for thermocouple 1. a) pre-experiment b) post experiment.

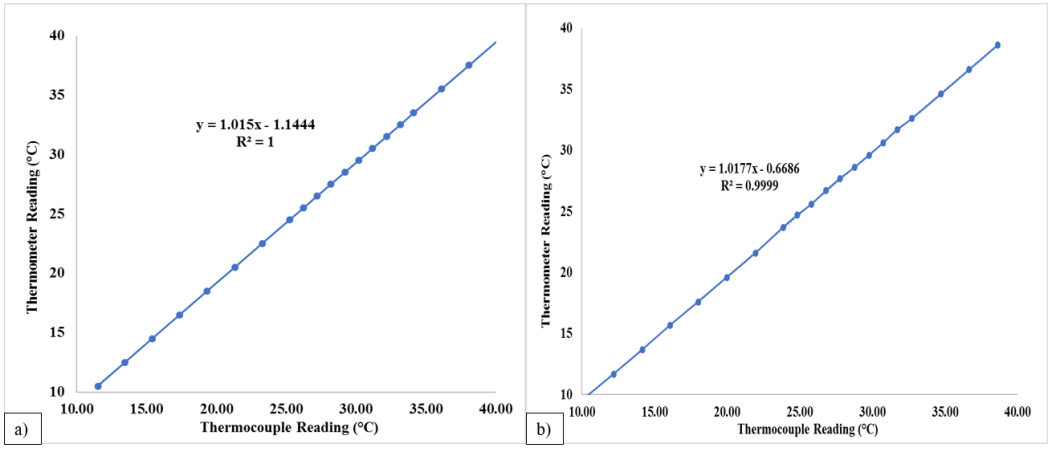

Figure 30: Calibration curve for thermocouple 2. a) pre-experiment b) post experiment.

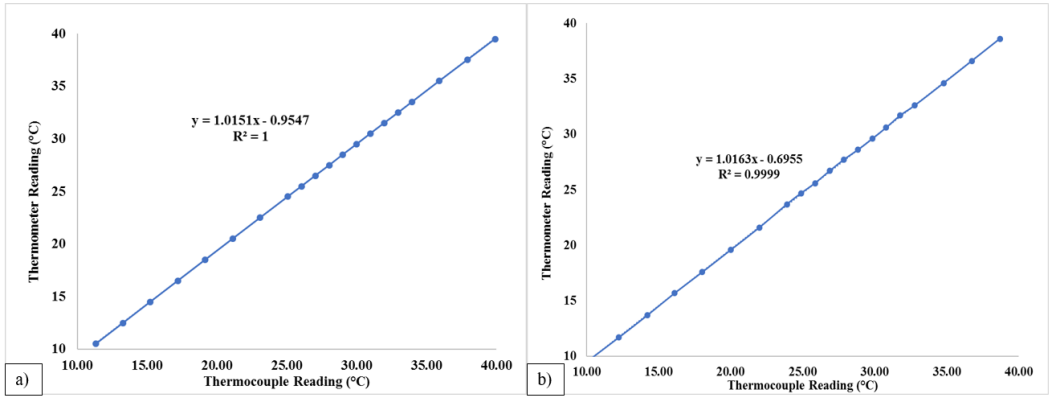

Figure 31: Calibration curve for thermocouple 3. a) pre-experiment b) post experiment.

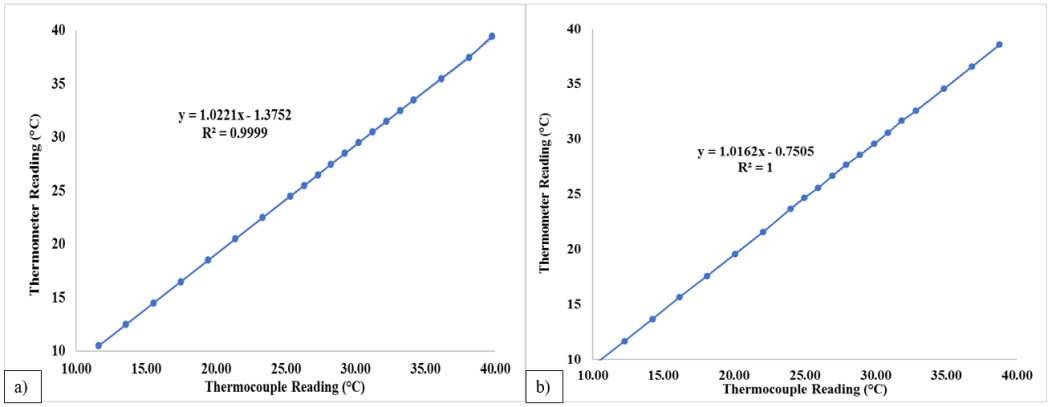

Figure 32: Calibration curve for thermocouple 4. a) pre-experiment b) post experiment.

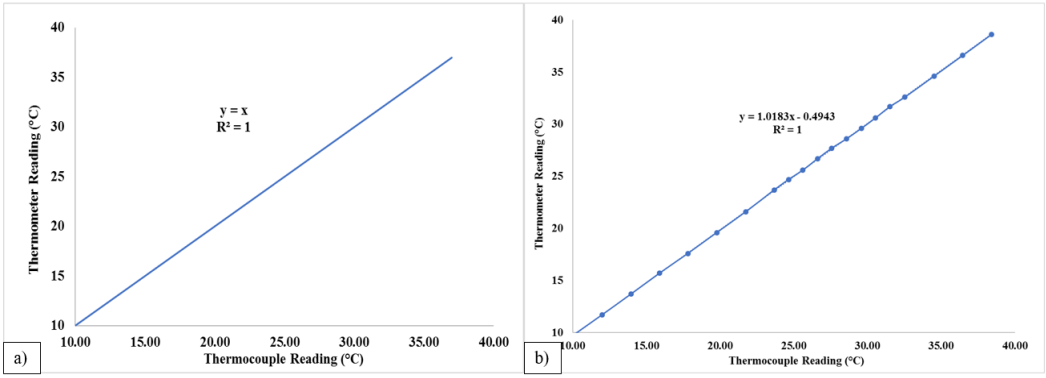

Figure 33: Calibration curve for thermocouple 5. a) pre-experiment b) post experiment.

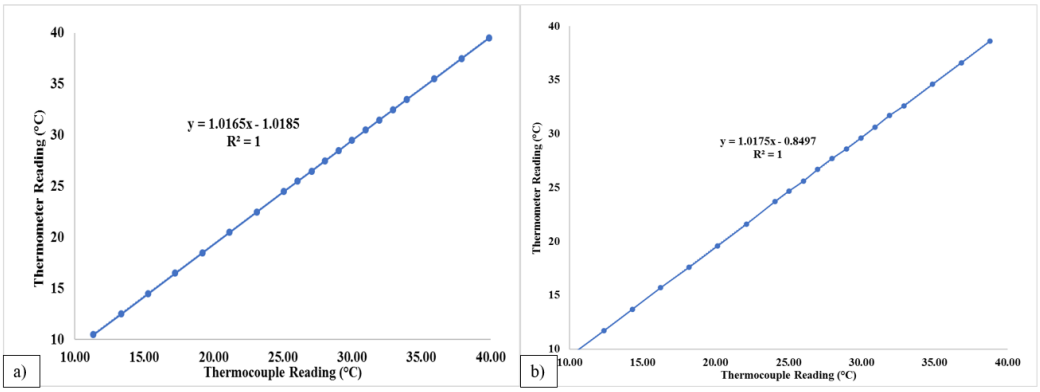

Figure 34: Calibration curve for thermocouple 6. a) pre-experiment b) post experiment.

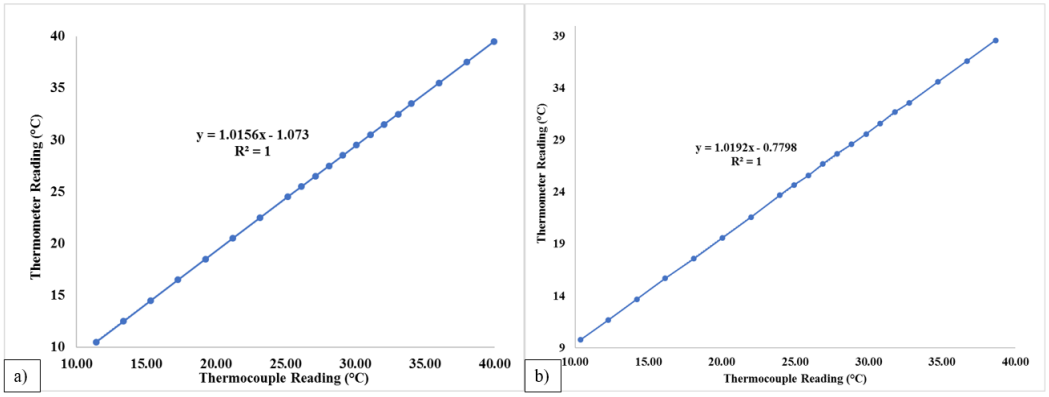

Figure 35: Calibration curve for thermocouple 7. a) pre-experiment b) post experiment.

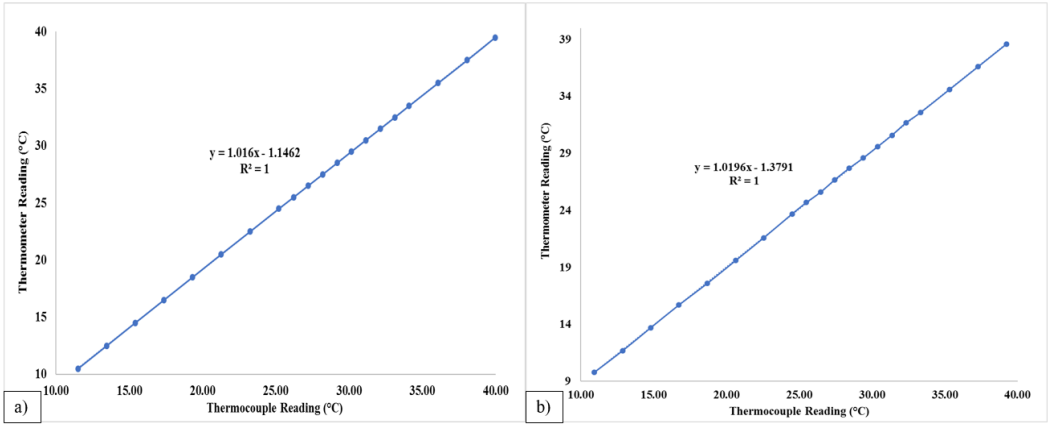

Figure 36: Calibration curve for thermocouple 8. a) pre-experiment b) post experiment.

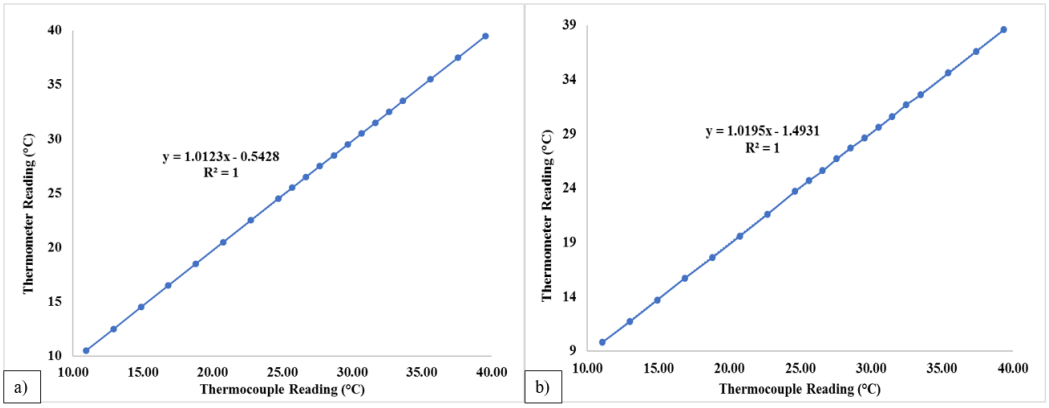

Figure 37: Calibration curve for thermocouple 9 a) pre-experiment b) post experiment.

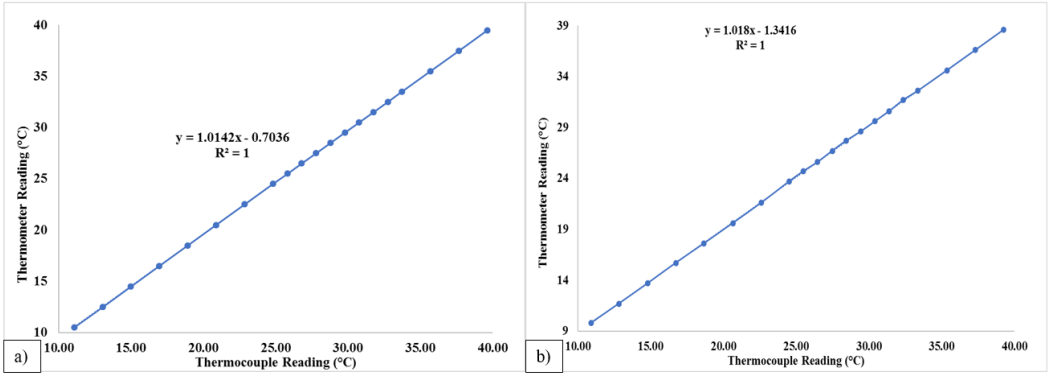

Figure 38: Calibration curve for thermocouple 10 a) pre-experiment b) post experiment.

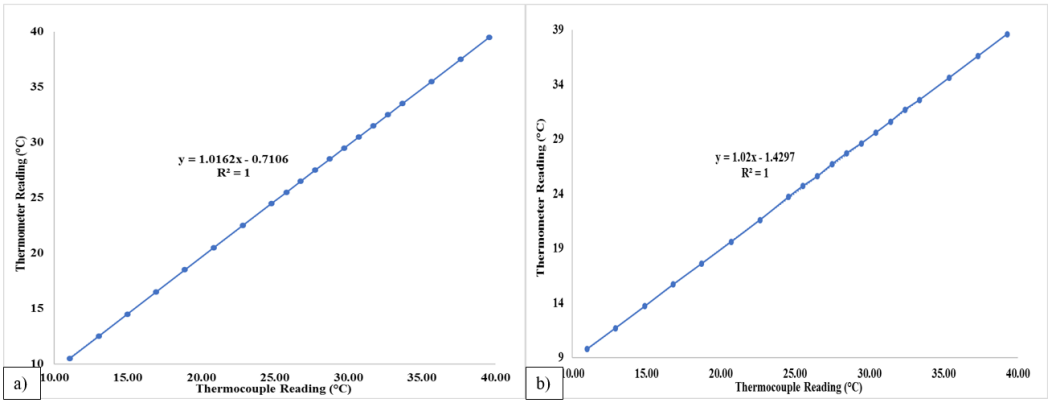

Figure 39: Calibration curve for thermocouple 11 a) pre-experiment b) post experiment.

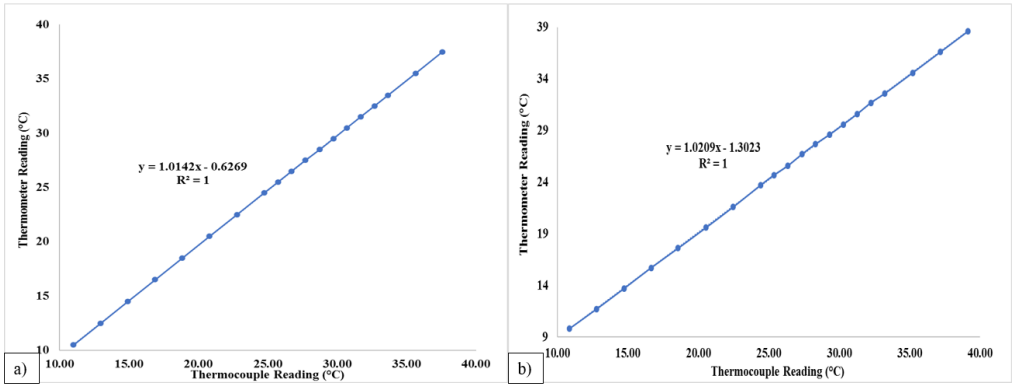

Figure 40: Calibration curve for thermocouple 12 a) pre-experiment b) post experiment.

APPENDIX C

This section has the tables with all the calculations (pre-experiment calibration) for each case.

Table 8: Summary of experimental validation of compact heat exchanger with varying flow arrangement, flow rate, melting and solidification temperatures.

	nu.	Case	Flow Type	Flow Rate (GPH)	Melt Temperature (°C)	Solidification Temperature (°C)
Non - Insulated	1	Case A	Co - Current	3	35	25
	2	Case B	Co - Current	3	37.4	25
	3	Case C	Co - Current	5	35	25
	4	Case D	Co - Current	5	37.4	25
	5	Case E	Counter - Current	3	33	25
	6	Case F	Counter - Current	3	35	25
	7	Case G	Counter - Current	3	37.4	25
	8	Case H	Counter - Current	5	33	25
	9	Case I	Counter - Current	5	35	25
	10	Case J	Counter - Current	5	37.4	25
	11	Case K	Counter - Current	3	35	20
	12	Case L	Counter - Current	3	37.4	20
	13	Case M	Counter - Current	5	35	20
	14	Case N	Counter - Current	5	37.4	20
Insulated	15	Case O	Counter - Current	3	35	20
	16	Case P	Counter - Current	3	37.4	20
	17	Case Q	Counter - Current	3	35	25
	18	Case R	Counter - Current	3	37.4	25
	19	Case S	Counter - Current	5	35	20
	20	Case T	Counter - Current	5	37.4	20
	21	Case U	Counter - Current	5	35	25
	22	Case V	Counter - Current	5	37.4	25

Table 9: Summary of experimental measurements and calculations for 90%, 70 %, 50%, 30%, and 10% melts. At a flow rate of 3 GPH (co-current), inlet temperature of HTF during melting is 35 °C and during solidification is 25 °C (Case A).

Melt Fraction	90 %		70 %		50 %		30 %		10%	
Case A	Melting	Solidification	Melting	Solidification	Melting	Solidification	Melting	Solidification	Melting	Solidification
Inlet Temperature (°C)	35	25	35	25	35	25	35	25	35	25
Average Mass Flowrate (kg/sec)	0.0036	0.0037	0.0036	0.0037	0.0036	0.0037	0.0036	0.0037	0.0037	0.0037
ΔT_{HTF}, Average (°C)	4.70 (± 10.4 %)	3.78 (± 13 %)	5.30 (± 9.3 %)	3.69 (± 13.3 %)	5.67 (± 8.6 %)	3.76 (± 13 %)	6.14 (± 8 %)	3.78 (± 13 %)	6.58 (± 7.5 %)	3.90 (± 12.6 %)
Total Energy Storage Capacity (kJ)	147.33 (± 4.5 %)	155.61 (± 4.5 %)	100.92 (± 4.5 %)	143.62 (± 4.5 %)	64.19 (± 4.5 %)	107.97 (± 4.5 %)	50.32 (± 4.6 %)	87.19 (± 4.6 %)	28.80 (± 4.6 %)	67.29 (± 4.6 %)
Duration of Phase Change (Seconds)	2107	2099	1390	2060	1003	1447	701	1074	467	747
Duration of Phase Change (Minutes)	35.11	34.98	23.17	34.33	16.72	24.12	11.68	17.90	7.78	12.44
Average Power (W)	71.35 (± 10.5 %)	57.52 (± 13 %)	80.49 (± 9.3 %)	56.19 (± 13.3 %)	86.15 (± 8.7 %)	57.26 (± 13.1 %)	93.34 (± 8 %)	57.64 (± 13 %)	100.04 (± 7.5 %)	59.40 (± 12.6 %)
Effectiveness	.8	1	.8	1	.8	1	.8	1	.8	1
Stefan Number	0.022	0.038	0.020	0.036	0.018	0.031	0.015	0.027	0.011	0.022

Table 10: Summary of experimental measurements and calculations for 90%, 70 %, 50%, 30%, and 10% melts. At a flow rate of 3 GPH (co-current), inlet temperature of HTF during melting is 37.4 °C and during solidification is 25 °C (Case B).

Melt Fraction	90 %		70 %		50 %		30 %		10%	
Case B	**Melting**	**Solidification**	**Melting**	**Solidification**	**Melting**	**Solidification**	**Melting**	**Solidification**	**Melting**	**Solidification**
Inlet Temperature (°C)	37.4	25	37.4	25	37.4	25	37.4	25	37.4	25
Average Mass Flowrate (kg/sec)	0.0036	0.0037	0.0036	0.0037	0.0036	0.0037	0.0036	0.0037	0.0036	0.0037
ΔT_{HTF}, Average (°C)	8.25 (± 5.9%)	3.14 (± 15.6 %)	8.75 (± 5.6 %)	3.69 (± 13.3 %)	9.30 (± 5.3 %)	3.34 (± 14.7 %)	9.70 (± 5.1 %)	3.30 (± 14.8 %)	10.22 (± 4.8 %)	3.27 (± 15 %)
Total Energy Storage Capacity (kJ)	154.19 (± 4.6 %)	166.74 (± 4.6 %)	112.89 (± 4.6 %)	133.83 (± 4.6 %)	80.09 (± 4.6 %)	101.30 (± 4.6 %)	60.89 (± 4.6 %)	76.99 (± 4.6 %)	28.20 (± 4.6 %)	45.82 (± 4.6 %)
Duration of Phase Change (Seconds)	1216	2678	918	1915	644	1550	446	1108	231	644
Duration of Phase Change (Minutes)	20.27	44.63	15.29	31.91	10.73	25.83	7.43	18.46	3.84	10.73
Average Power (W)	125.29 (± 6 %)	47.85 (± 15.7 %)	132.80 (± 5.6 %)	56.19 (± 13.3 %)	141.22 (± 5.3 %)	50.93 (± 14.7 %)	147.26 (± 5.1 %)	50.30 (± 14.9 %)	155.36 (± 4.8 %)	49.86 (± 15 %)
Effectiveness	.8	1	.8	1	.8	1	.8	1	.8	1
Stefan Number	.028	.047	.022	.041	.024	.033	.020	.028	.016	.020

Table 11: Summary of experimental measurements and calculations for 90%, 70 %, 50%, 30%, and 10% melts. At a flow rate of 5 GPH (co-current), inlet temperature of HTF during melting is 35 °C and during solidification is 25 °C (Case C).

Melt Fraction	90 %		70 %		50 %		30 %		10%	
Case C	Melting	Solidification	Melting	Solidification	Melting	Solidification	Melting	Solidification	Melting	Solidification
Inlet Temperature (°C)	35	25	35	25	35	25	35	25	35	25
Average Mass Flowrate (kg/sec)	0.0052	0.0052	0.0052	0.0052	0.0052	0.0052	0.0052	0.0052	0.0052	0.0052
ΔT_{HTF}, Average (°C)	4.98 (± 9.9 %)	3.42 (± 14.3 %)	5.55 (± 8.8 %)	3.71 (± 13.2 %)	5.85 (± 8.4 %)	3.80 (± 12.9 %)	6.07 (± 8.1 %)	3.99 (± 12.3 %)	6.64 (± 7.4 %)	4.18 (± 11.7 %)
Total Energy Storage Capacity (kJ)	150.99 (± 4.5 %)	184.85 (± 4.5 %)	118.28 (± 4.5 %)	161.80 (± 4.5 %)	89.39 (± 4.5 %)	133.90 (± 4.5 %)	69.13 (± 4.6 %)	112.95 (± 4.6 %)	35.27 (± 4.6 %)	82.40 (± 4.6 %)
Duration of Phase Change (Seconds)	1449	1922	1083	1632	861	1263	703	1024	426	686
Duration of Phase Change (Minutes)	24.15	32.03	18.04	27.19	14.34	21.04	11.72	17.07	7.09	11.43
Average Power (W)	108.56 (± 6.9 %)	74.78 (± 10 %)	121.03 (± 6.2 %)	81.15 (± 9.2 %)	127.57 (± 5.9 %)	83.07 (± 9 %)	132.43 (± 5.7 %)	87.30 (± 8.6 %)	144.91 (± 5.2 %)	91.55 (± 8.2 %)
Effectiveness	.8	1	.8	1	.8	1	.8	1	.8	1
Stefan Number	0.022	0.042	0.021	0.038	0.018	0.034	0.016	0.030	0.014	0.023

Table 12: Summary of experimental measurements and calculations for 90%, 70 %, 50%, 30%, and 10% melts. At a flow rate of 5 GPH (co-current), inlet temperature of HTF during melting is 37.4 °C and during solidification is 25 °C (Case D).

Melt Fraction	90 %		70 %		50 %		30 %		10%	
Case D	**Melting**	**Solidification**	**Melting**	**Solidification**	**Melting**	**Solidification**	**Melting**	**Solidification**	**Melting**	**Solidification**
Inlet Temperature (°C)	37.4	25	37.4	25	37.4	25	37.4	25	37.4	25
Average Mass Flowrate (kg/sec)	0.0052	0.0052	0.0052	0.0052	0.0052	0.0052	0.0052	0.0052	0.0052	0.0052
ΔT_{HTF}, Average (°C)	7.16 (± 6.8 %)	3.48 (± 14.1 %)	7.81 (± 6.3 %)	3.30 (± 14.8 %)	8.01 (± 6.1 %)	3.90 (± 12.6 %)	8.47 (± 5.8 %)	3.71 (± 13.2 %)	8.88 (± 5.5 %)	3.99 (± 12.3 %)
Total Energy Storage Capacity (kJ)	160.86 (± 4.5 %)	186.67 (± 4.5 %)	125.27 (± 4.5 %)	160.00 (± 4.5 %)	87.31 (± 4.5 %)	131.01 (± 4.5 %)	71.91 (± 4.6 %)	110.23 (± 4.6 %)	39.75 (± 4.6 %)	76.87 (± 4.6 %)
Duration of Phase Change (Seconds)	1074	1826	807	1820	623	1209	467	1058	277	692
Duration of Phase Change (Minutes)	17.89	30.43	13.44	30.33	10.38	20.14	7.78	17.63	4.62	11.53
Average Power (kW)	156.19 (± 4.8 %)	76.09 (± 9.8 %)	170.38 (± 4.4 %)	72.31 (± 10.4 %)	174.63 (± 4.3 %)	85.25 (± 8.8 %)	184.81 (± 4.1 %)	81.26 (± 9.2 %)	193.90 (± 3.9 %)	87.28 (± 8.6 %)
Effectiveness	.8	1	.8	1	.8	1	.8	1	.8	1
Stefan Number	0.028	0.048	0.026	0.044	0.022	0.036	0.020	0.032	0.015	0.022

Table 13: Summary of experimental measurements and calculations for 90%, 70 %, and 50% melts. At a flow rate of 3 GPH (counter-current), inlet temperature of HTF during melting is 33 °C and during solidification is 25 °C (Case E).

Melt Fraction	90 %		70 %		50 %	
Case E	**Melting**	**Solidification**	**Melting**	**Solidification**	**Melting**	**Solidification**
Inlet Temperature (°C)	33	25	33	25	33	25
Average Mass Flowrate (kg/sec)	0.0036	0.0036	0.0036	0.0036	0.0036	0.0036
ΔT_{HTF}, Average (°C)	3.98 (± 12.3 %)	3.38 (± 14.5 %)	4.38 (± 11.2 %)	3.45 (± 14.2 %)	4.65 (± 10.5 %)	3.47 (± 14.1 %)
Total Energy Storage Capacity (kJ)	173.57 (± 4.7 %)	189.52 (± 4.7 %)	142.99 (± 4.7 %)	162.47 (± 4.7 %)	131.79 (± 4.8 %)	139.09 (± 4.8 %)
Duration of Phase Change (Seconds)	2802	3412	1971	2987	1721	2490
Duration of Phase Change (Minutes)	46.69	56.86	32.84	49.78	28.68	41.51
Average Power (W)	60.52 (± 12.4 %)	50.96 (± 14.7 %)	66.64 (± 11.2 %)	51.60 (± 14.5 %)	70.62 (± 10.6 %)	51.75 (± 14.5 %)
Effectiveness	.8	1	.8	1	.8	1
Stefan Number	0.016	0.031	0.013	0.024	0.009	0.018

Table 14: Summary of experimental measurements and calculations for 90%, 70 %, 50%, 30%, and 10% melts. At a flow rate of 3 GPH (counter-current), inlet temperature of HTF during melting is 35 °C and during solidification is 25 °C (Case F).

Melt Fraction	90 %		70 %		50 %		30 %		10%	
Case F	Melting	Solidification	Melting	Solidification	Melting	Solidification	Melting	Solidification	Melting	Solidification
Inlet Temperature (°C)	35	25	35	25	35	25	35	25	35	25
Average Mass Flowrate (kg/sec)	0.0036	0.0037	0.0036	0.0037	0.0036	0.0037	0.0036	0.0037	0.0037	0.0037
ΔT_{HTF}, Average (°C)	5.17 (± 9.5 %)	2.69 (± 18.9 %)	5.66 (± 8.7 %)	2.79 (± 18.3 %)	5.96 (± 8.3 %)	2.86 (± 17.8 %)	6.20 (± 7.9 %)	2.87 (± 17.8 %)	6.81 (± 7.2 %)	3.31 (± 15.1 %)
Total Energy Storage Capacity (kJ)	152.63 (± 4.7 %)	166.33 (± 4.7 %)	135.01 (± 4.7 %)	138.14 (± 4.7 %)	120.16 (± 4.8 %)	118.99 (± 4.8 %)	99.51 (± 4.8 %)	96.95 (± 4.8 %)	63.27 (± 4.8 %)	61.90 (± 4.8 %)
Duration of Phase Change (Seconds)	1861	3590	1405	3210	1085	2636	820	2069	458	1041
Duration of Phase Change (Minutes)	31.01	59.83	23.41	53.51	18.08	43.93	13.67	34.49	7.63	17.36
Average Power (W)	78.56 (± 9.6 %)	41.05 (± 18.9 %)	86.02 (± 8.8 %)	42.55 (± 18.3 %)	90.57 (± 8.3 %)	43.71 (± 17.7 %)	94.24 (± 8 %)	44.06 (± 17.7 %)	103.62 (± 7.3 %)	50.91 (± 15 %)
Effectiveness	.8	1	.8	1	.8	1	.8	1	.8	1
Stefan Number	0.019	0.035	0.015	0.030	0.014	0.028	0.012	0.025	0.008	0.021

Table 15: Summary of experimental measurements and calculations for 90%, 70 %, 50%, 30%, and 10% melts. At a flow rate of 3 GPH (counter-current), inlet temperature of HTF during melting is 37.4 °C and during solidification is 25 °C (Case G).

Melt Fraction	90 %		70 %		50 %		30 %		10%	
Case G	Melting	Solidification	Melting	Solidification	Melting	Solidification	Melting	Solidification	Melting	Solidification
Inlet Temperature (°C)	37.4	25	37.4	25	37.4	25	37.4	25	37.4	25
Average Mass Flowrate (kg/sec)	0.0036	0.0037	0.0036	0.0037	0.0036	0.0037	0.0036	0.0037	0.0036	0.0037
ΔT_{HTF}, Average (°C)	7.22 (± 6.8 %)	2.75 (± 18.3 %)	7.82 (± 6.3 %)	2.98 (± 16.9 %)	8.21 (± 6 %)	3.02 (± 16.6 %)	8.49 (± 5.8 %)	3.08 (± 16.2 %)	8.86 (± 5.5 %)	3.32 (± 15.2 %)
Total Energy Storage Capacity (kJ)	156.56 (± 4.7 %)	162.13 (± 4.7 %)	140.61 (± 4.8 %)	146.64 (± 4.8 %)	121.21 (± 4.8 %)	120.57 (± 4.8 %)	96.16 (± 4.8 %)	96.58 (± 4.8 %)	62.25 (± 4.8 %)	60.62 (± 4.8 %)
Duration of Phase Change (Seconds)	1385	3278	1039	3111	802	2484	585	1881	327	983
Duration of Phase Change (Minutes)	23.09	54.63	17.31	51.84	13.37	41.40	9.75	31.36	5.45	16.38
Average Power (W)	109.62 (± 6.9 %)	42.30 (± 18.2 %)	118.78 (± 6.3 %)	45.75 (± 16.8 %)	124.73 (± 6 %)	46.40 (± 16.6 %)	128.91 (± 5.8 %)	47.66 (± 16 %)	134.72 (± 5.6 %)	50.75 (± 15.2 %)
Effectiveness	.8	1	.8	1	.8	1	.8	1	.8	1
Stefan Number	0.023	0.040	0.020	0.035	0.015	0.031	0.012	0.023	0.010	0.022

Table 16: Summary of experimental measurements and calculations for 90%, 70 %, and 50% melts. At a flow rate of 5 GPH (counter-current), inlet temperature of HTF during melting is 33 °C and during solidification is 25 °C (Case H).

Melt Fraction	90 %		70 %		50 %	
Case H	Melting	Solidification	Melting	Solidification	Melting	Solidification
Inlet Temperature (°C)	33	25	33	25	33	25
Average Mass Flowrate (kg/sec)	0.0052	0.0053	0.0052	0.0053	0.0052	0.0053
ΔT_{HTF}, Average (°C)	4.06 (± 12.1 %)	3.25 (± 15.1 %)	4.36 (± 11.2 %)	3.21 (± 15.3 %)	4.73 (± 10.4 %)	3.28 (± 14.9 %)
Total Energy Storage Capacity (kJ)	185.48 (± 4.7 %)	196.88 (± 4.7 %)	160.26 (± 4.8 %)	181.64 (± 4.8 %)	140.30 (± 4.8 %)	152.54 (± 4.8 %)
Duration of Phase Change (Seconds)	2077	2627	1595	2470	1136	1986
Duration of Phase Change (Minutes)	34.62	43.78	26.58	41.16	18.94	33.10
Average Power (W)	88.57 (± 8.5 %)	71.44 (± 10.5 %)	95.27 (± 7.9 %)	70.51 (± 10.6 %)	103.31 (± 7.2 %)	72.57 (± 10.3 %)
Effectiveness	.8	1	.8	1	.8	1
Stefan Number	0.011	0.030	0.013	0.029	0.012	0.028

Table 17: Summary of experimental measurements and calculations for 90%, 70 %, 50%, 30%, and 10% melts. At a flow rate of 5 GPH (counter-current), inlet temperature of HTF during melting is 35 °C and during solidification is 25 °C (Case I).

Melt Fraction	90 %		70 %		50 %		30 %		10%	
Case I	**Melting**	**Solidification**	**Melting**	**Solidification**	**Melting**	**Solidification**	**Melting**	**Solidification**	**Melting**	**Solidification**
Inlet Temperature (°C)	35	25	35	25	35	25	35	25	35	25
Average Mass Flowrate (kg/sec)	0.0052	0.0053	0.0052	0.0053	0.0052	0.0053	0.0052	0.0053	0.0052	0.0053
ΔT_{HTF}, Average (°C)	5.40 (± 9.1 %)	2.50 (± 20 %)	5.87 (± 8.4 %)	2.72 (± 18.4 %)	6.18 (± 8 %)	2.69 (± 18.6 %)	6.46 (± 7.6 %)	2.85 (± 17.6 %)	6.91 (± 7.1 %)	3.25 (± 15.3 %)
Total Energy Storage Capacity (kJ)	168.56 (± 4.7 %)	160.63 (± 4.7 %)	152.00 (± 4.7 %)	143.10 (± 4.7 %)	137.94 (± 4.8 %)	124.32 (± 4.8 %)	119.14 (± 4.8 %)	105.67 (± 4.8 %)	78.37 (± 4.8 %)	70.23 (± 4.8 %)
Duration of Phase Change (Seconds)	1391	2550	1100	2371	853	2075	665	1639	394	863
Duration of Phase Change (Minutes)	23.18	42.51	18.33	39.51	14.22	34.58	11.08	27.32	6.56	14.38
Average Power (W)	117.74 (± 6.4 %)	54.99 (± 13.9 %)	128.09 (± 5.9 %)	59.79 (± 12.8 %)	134.92 (± 5.6 %)	59.37 (± 12.9 %)	140.98 (± 5.3 %)	62.44 (± 12.2 %)	150.81 (± 5 %)	71.34 (± 10.7 %)
Effectiveness	.8	1	.8	1	.8	1	.8	1	.8	1
Stefan Number	0.020	0.035	0.018	0.033	0.016	0.031	0.015	0.029	0.012	0.024

Table 18: Summary of experimental measurements and calculations for 90%, 70 %, 50%, 30%, and 10% melts. At a flow rate of 5 GPH (counter-current), inlet temperature of HTF during melting is 37.4 °C and during solidification is 25 °C (Case J).

Melt Fraction	90 %		70 %		50 %		30 %		10%	
Case J	Melting	Solidification	Melting	Solidification	Melting	Solidification	Melting	Solidification	Melting	Solidification
Inlet Temperature (°C)	37.4	25	37.4	25	37.4	25	37.4	25	37.4	25
Average Mass Flowrate (kg/sec)	0.0052	0.0053	0.0052	0.0053	0.0052	0.0053	0.0052	0.0053	0.0052	0.0053
ΔT_{HTF}, Average (°C)	7.36 (± 6.7 %)	2.46 (± 20.6 %)	8.16 (± 6 %)	2.81 (± 17.9 %)	8.12 (± 6 %)	2.45 (± 20 %)	8.71 (± 5.6 %)	2.89 (± 17.4 %)	8.90 (± 5.5 %)	2.91 (± 16.8 %)
Total Energy Storage Capacity (kJ)	177.18 (± 4.7 %)	174.59 (± 4.7 %)	160.52 (± 4.8 %)	152.50 (± 4.8 %)	137.95 (± 4.8 %)	110.71 (± 4.8 %)	122.80 (± 4.8 %)	106.00 (± 4.8 %)	83.17 (± 4.8 %)	64.17 (± 4.8 %)
Duration of Phase Change (Seconds)	1058	2700	785	2422	645	2057	502	1634	323	909
Duration of Phase Change (Minutes)	17.63	45.01	13.09	40.37	10.75	34.28	8.37	27.23	5.38	15.14
Average Power (W)	160.60 (± 4.7 %)	53.97 (± 14.4 %)	177.92 (± 4.2 %)	61.65 (± 12.5 %)	177.06 (± 4.2 %)	53.60 (± 14 %)	190.10 (± 4 %)	63.20 (± 12.2 %)	193.86 (± 3.9 %)	63.72 (± 11.8 %)
Effectiveness	.8	1	.8	1	.8	1	.8	1	.8	1
Stefan Number	0.028	0.043	0.024	0.039	0.023	0.036	0.018	0.032	0.015	0.024

Table 19: Summary of experimental measurements and calculations for 90%, 70 %, and 50% melts. At a flow rate of 3 GPH (counter-current), inlet temperature of HTF during melting is 35 °C and during solidification is 20 °C (Case K).

Melt Fraction	90 %		70 %		50 %	
Case K	Melting	Solidification	Melting	Solidification	Melting	Solidification
Inlet Temperature (°C)	35	20	35	20	35	20
Average Mass Flowrate (kg/sec)	0.0036	0.0036	0.0036	0.0036	0.0037	0.0036
ΔT_{HTF}, Average (°C)	5.89 (± 8.3 %)	7.09 (± 6.9 %)	6.45 (± 7.2 %)	7.23 (± 6.8 %)	7.04 (± 7 %)	7.23 (± 6.8 %)
Total Energy Storage Capacity (kJ)	179.46 (± 5.1 %)	208.21 (± 5.1 %)	175.39 (± 5.1 %)	183.50 (± 5.1 %)	155.79 (± 5.2 %)	158.00 (± 5.2 %)
Duration of Phase Change (Seconds)	1881	1736	1487	1711	1093	1345
Duration of Phase Change (Minutes)	31.34	28.93	24.78	28.52	18.21	22.41
Average Power (W)	89.57 (± 8.4 %)	105.55 (± 7.1 %)	97.98 (± 7.6 %)	108.22 (± 6.9 %)	107.15 (± 7 %)	108.00 (± 6.9 %)
Effectiveness	.8	1	.8	1	.8	1
Stefan Number	0.034	0.055	0.034	0.052	0.031	0.053

Table 20: Summary of experimental measurements and calculations for 90%, 70 %, and 50% melts. At a flow rate of 3 GPH (counter-current), inlet temperature of HTF during melting is 37.4 °C and during solidification is 20 °C (Case L).

Melt Fraction	90 %		70 %		50 %	
Case L	**Melting**	**Solidification**	**Melting**	**Solidification**	**Melting**	**Solidification**
Inlet Temperature (°C)	37.4	20	37.4	20	37.4	20
Average Mass Flowrate (kg/sec)	0.0036	0.0036	0.0036	0.0036	0.0036	0.0036
ΔT_{HTF}, Average (°C)	8.36 (± 5.9 %)	7.69 (± 6.4 %)	8.99 (± 5.4 %)	7.55 (± 6.5 %)	9.47 (± 5.2 %)	7.37 (± 6.7 %)
Total Energy Storage Capacity (kJ)	176.37 (± 5.2 %)	223.00 (± 5.2 %)	171.95 (± 5.2 %)	199.82 (± 5.2 %)	152.66 (± 5.3 %)	161.79 (± 5.3 %)
Duration of Phase Change (Seconds)	1301	1793	1058	1647	786	1360
Duration of Phase Change (Minutes)	21.68	29.88	17.63	27.45	13.09	22.66
Average Power (W)	127.04 (± 5.9 %)	115.64 (± 6.5 %)	136.52 (± 5.5 %)	113.69 (± 6.6 %)	143.68 (± 5.2 %)	110.10 (± 6.8 %)
Effectiveness	.8	1	.8	1	.8	1
Stefan Number	0.042	0.062	0.039	0.057	0.035	0.055

Table 21: Summary of experimental measurements and calculations for 90%, 70 %, and 50% melts. At a flow rate of 5 GPH (counter-current), inlet temperature of HTF during melting is 35 °C and during solidification is 20 °C (Case M).

Melt Fraction	90 %		70 %		50 %	
Case M	**Melting**	**Solidification**	**Melting**	**Solidification**	**Melting**	**Solidification**
Inlet Temperature (°C)	35	20	35	20	35	20
Average Mass Flowrate (kg/sec)	0.0052	0.0052	0.0052	0.0053	0.0052	0.0053
ΔT_{HTF}, Average (°C)	6.07 (± 8.1 %)	7.07 (± 6.9 %)	6.54 (± 7.5 %)	7.23 (± 6.8 %)	7.09 (± 6.9 %)	7.17 (± 6.8 %)
Total Energy Storage Capacity (kJ)	213.40 (± 5.1 %)	212.85 (± 5.1 %)	191.37 (± 5.1 %)	195.74 (± 5.1 %)	176.53 (± 5.2 %)	174.08 (± 5.2 %)
Duration of Phase Change (Seconds)	1497	1218	1151	1129	851	973
Duration of Phase Change (Minutes)	24.95	20.29	19.18	18.81	14.18	16.21
Average Power (W)	132.45 (± 5.7 %)	154.24 (± 4.9 %)	142.67 (± 5.3 %)	159.28 (± 4.7 %)	154.64 (± 4.8 %)	158.65 (± 4.7 %)
Effectiveness	.8	1	.8	1	.8	1
Stefan Number	0.037	0.058	0.036	0.055	0.034	0.054

Table 22: Summary of experimental measurements and calculations for 90%, 70 %, and 50% melts. At a flow rate of 5 GPH (counter-current), inlet temperature of HTF during melting is 37.4 °C and during solidification is 20 °C (Case N).

Melt Fraction	90 %		70 %		50 %	
Case N	Melting	Solidification	Melting	Solidification	Melting	Solidification
Inlet Temperature (°C)	37.4	20	37.4	20	37.4	20
Average Mass Flowrate (kg/sec)	0.0052	0.0053	0.0052	0.0052	0.0052	0.0053
ΔT_{HTF}, Average (°C)	8.55 (± 5.7 %)	7.44 (± 6.6 %)	9.03 (± 5.4 %)	7.33 (± 6.7 %)	9.35 (± 5.2 %)	7.48 (± 6.5 %)
Total Energy Storage Capacity (kJ)	203.51 (± 5.2 %)	220.81 (± 5.2 %)	199.94 (± 5.3 %)	202.65 (± 5.3 %)	176.40 (± 5.3 %)	167.72 (± 5.3 %)
Duration of Phase Change (Seconds)	1010	1268	864	1128	641	934
Duration of Phase Change (Minutes)	16.83	21.13	14.39	18.79	10.68	15.56
Average Power (W)	186.46 (± 4 %)	163.55 (± 4.6%)	196.91 (± 3.8 %)	160.63 (± 4.7 %)	203.96 (± 3.7 %)	164.87 (± 4.5 %)
Effectiveness	.8	1	.8	1	.8	1
Stefan Number	0.044	0.065	0.044	0.061	0.038	0.057

Table 23: Summary of experimental measurements and calculations for 90 melt with insulated heat exchanger. At a flow rate of 3 GPH (counter-current), inlet temperature of HTF during melting is 35 °C and during solidification is 20 °C (Case O).

Melt Fraction	90 %	
Case O	Melting	Solidification
Inlet Temperature (°C)	35	20
Average Mass Flowrate (kg/sec)	0.0036	0.0037
ΔT_{HTF}, Average (°C)	5.95	7.18
Total Energy Storage Capacity (kJ)	175.19	184.78
Duration of Phase Change (Seconds)	1817	1356
Duration of Phase Change (Minutes)	30.28	22.60
Average Power (W)	90.39	111.37
Effectiveness	.8	1
Stefan Number	0.035	0.058

Table 24: Summary of experimental measurements and calculations for 90 melt with insulated heat exchanger. At a flow rate of 3 GPH (counter-current), inlet temperature of HTF during melting is 37.4 °C and during solidification is 20 °C (Case P).

Melt Fraction	90 %	
Case P	Melting	Solidification
Inlet Temperature (°C)	37.4	20
Average Mass Flowrate (kg/sec)	0.0036	0.0036
ΔT_{HTF}, Average (°C)	8.55	7.62
Total Energy Storage Capacity (kJ)	169.80	221.20
Duration of Phase Change (Seconds)	1158	1722
Duration of Phase Change (Minutes)	19.29	28.70
Average Power (W)	129.82	115.72
Effectiveness	.8	1
Stefan Number	0.044	0.065

Table 25: Summary of experimental measurements and calculations for 90 melt with insulated heat exchanger. At a flow rate of 3 GPH (counter-current), inlet temperature of HTF during melting is 35 °C and during solidification is 25 °C (Case Q).

Melt Fraction	90 %	
Case Q	Melting	Solidification
Inlet Temperature (°C)	35	25
Average Mass Flowrate (kg/sec)	0.0036	0.0037
ΔT_{HTF}, Average (°C)	5.81	3.34
Total Energy Storage Capacity (kJ)	152.66	187.90
Duration of Phase Change (Seconds)	1681	3327
Duration of Phase Change (Minutes)	28.02	55.46
Average Power (W)	88.31	51.30
Effectiveness	.8	1
Stefan Number	0.018	0.037

Table 26: Summary of experimental measurements and calculations for 90 melt with insulated heat exchanger. At a flow rate of 3 GPH (counter-current), inlet temperature of HTF during melting is 37.4 °C and during solidification is 25 °C (Case R).

Melt Fraction	90 %	
Case R	Melting	Solidification
Inlet Temperature (°C)	37.4	25
Average Mass Flowrate (kg/sec)	0.0036	0.0037
ΔT_{HTF}, Average (°C)	7.76	3.44
Total Energy Storage Capacity (kJ)	152.79	195.23
Duration of Phase Change (Seconds)	1245	3372
Duration of Phase Change (Minutes)	20.74	56.21
Average Power (W)	117.83	53.52
Effectiveness	.8	1
Stefan Number	0.024	0.042

Table 27: Summary of experimental measurements and calculations for 90 melt with insulated heat exchanger. At a flow rate of 5 GPH (counter-current), inlet temperature of HTF during melting is 35 °C and during solidification is 20 °C (Case S).

Melt Fraction	90 %	
Case S	Melting	Solidification
Inlet Temperature (°C)	35	20
Average Mass Flowrate (kg/sec)	0.0052	0.0053
ΔT_{HTF}, Average (°C)	6.30	7.06
Total Energy Storage Capacity (kJ)	196.64	209.53
Duration of Phase Change (Seconds)	1316	1110
Duration of Phase Change (Minutes)	21.93	18.51
Average Power (W)	137.53	156.39
Effectiveness	.8	1
Stefan Number	0.038	0.060

Table 28: Summary of experimental measurements and calculations for 90 melt with insulated heat exchanger. At a flow rate of 5 GPH (counter-current), inlet temperature of HTF during melting is 37.4 °C and during solidification is 20 °C (Case T).

Melt Fraction	90 %	
Case T	Melting	Solidification
Inlet Temperature (°C)	37.4	20
Average Mass Flowrate (kg/sec)	0.0052	0.0053
ΔT_{HTF}, Average (°C)	8.68	7.46
Total Energy Storage Capacity (kJ)	189.42	217.73
Duration of Phase Change (Seconds)	910	1251
Duration of Phase Change (Minutes)	15.17	20.86
Average Power (W)	189.26	164.17
Effectiveness	.8	1
Stefan Number	0.045	0.068

Table 29: Summary of experimental measurements and calculations for 90 melt with insulated heat exchanger. At a flow rate of 5 GPH (counter-current), inlet temperature of HTF during melting is 35 °C and during solidification is 25 °C (Case U).

Melt Fraction	90 %	
Case U	Melting	Solidification
Inlet Temperature (°C)	35	25
Average Mass Flowrate (kg/sec)	0.0052	0.0053
ΔT_{HTF}, Average (°C)	6.04	3.08
Total Energy Storage Capacity (kJ)	179.63	191.63
Duration of Phase Change (Seconds)	1275	2590
Duration of Phase Change (Minutes)	21.25	43.16
Average Power (W)	131.77	68.12
Effectiveness	.8	1
Stefan Number	0.020	0.040

Table 30: Summary of experimental measurements and calculations for 90 melt with insulated heat exchanger. At a flow rate of 5 GPH (counter-current), inlet temperature of HTF during melting is 37.4 °C and during solidification is 25 °C (Case V).

Melt Fraction	90 %	
Case V	Melting	Solidification
Inlet Temperature (°C)	37.4	25
Average Mass Flowrate (kg/sec)	0.0052	0.0053
ΔT_{HTF}, Average (°C)	8.13	3.10
Total Energy Storage Capacity (kJ)	177.18	205.73
Duration of Phase Change (Seconds)	951	2540
Duration of Phase Change (Minutes)	15.85	42.34
Average Power (W)	177.22	68.71
Effectiveness	.8	1
Stefan Number	0.028	0.045

APPENDIX D

This section provides thermal profile graphs (pre-experiment and post experiment calibrations) for the cases at a 90 % melt and complete freeze.

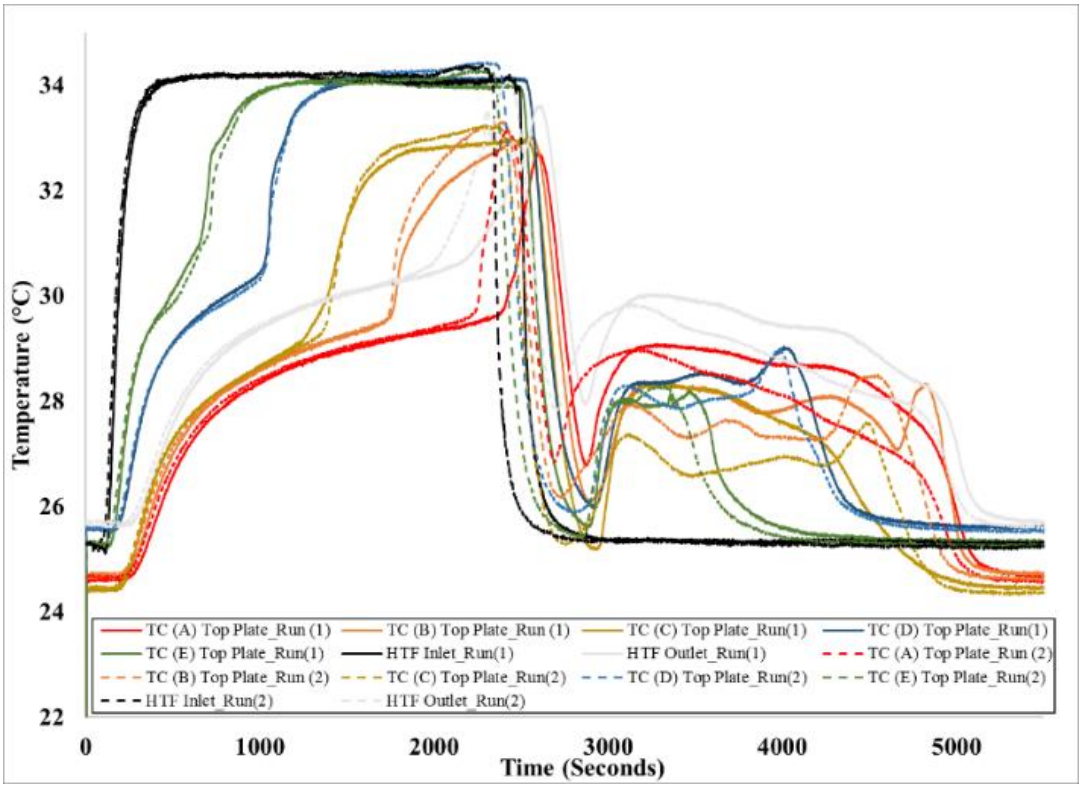

Figure 41: Temperature profiles recorded by thermocouples at the top plate during melting (90%) and solidification at a flow rate of 3 GPH (co-current). Inlet temperature of HTF during melting is 35 °C and during solidification is 25 °C (Case A, Pre-experiment calibration).

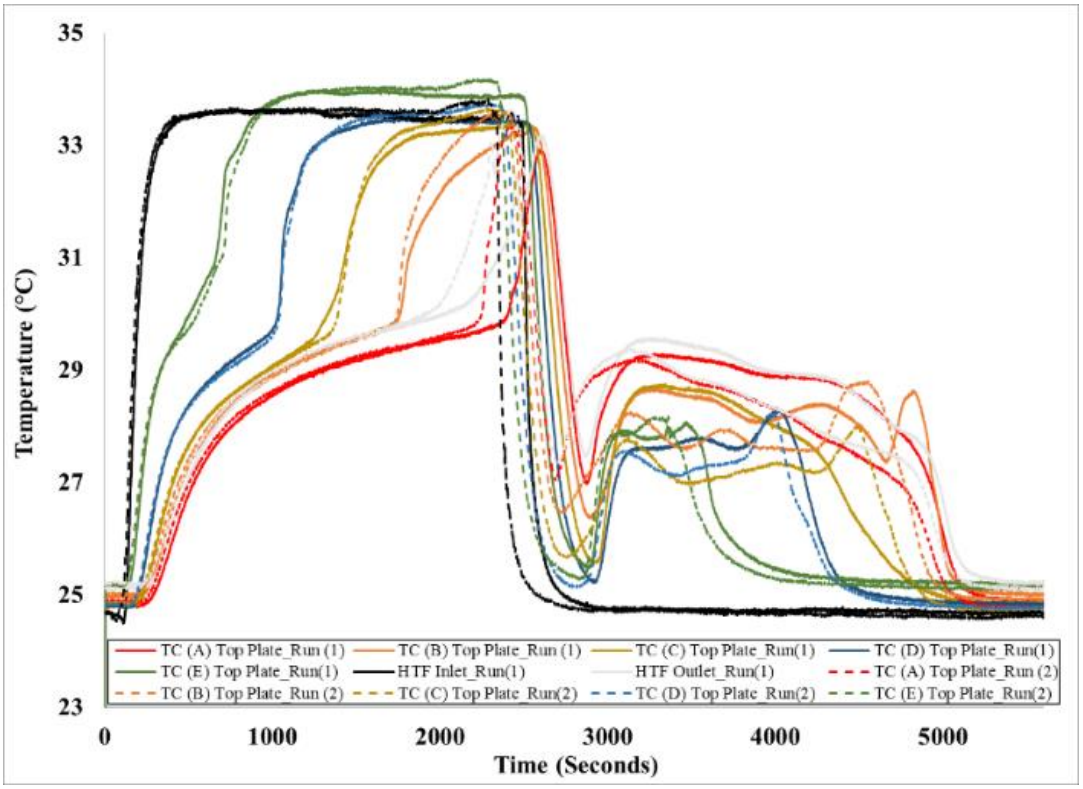

Figure 42: Temperature profiles recorded by thermocouples at the top plate during melting (90%) and solidification at a flow rate of 3 GPH (co-current). Inlet temperature of HTF during melting is 35 °C and during solidification is 25 °C (Case A, Post-experiment calibration).

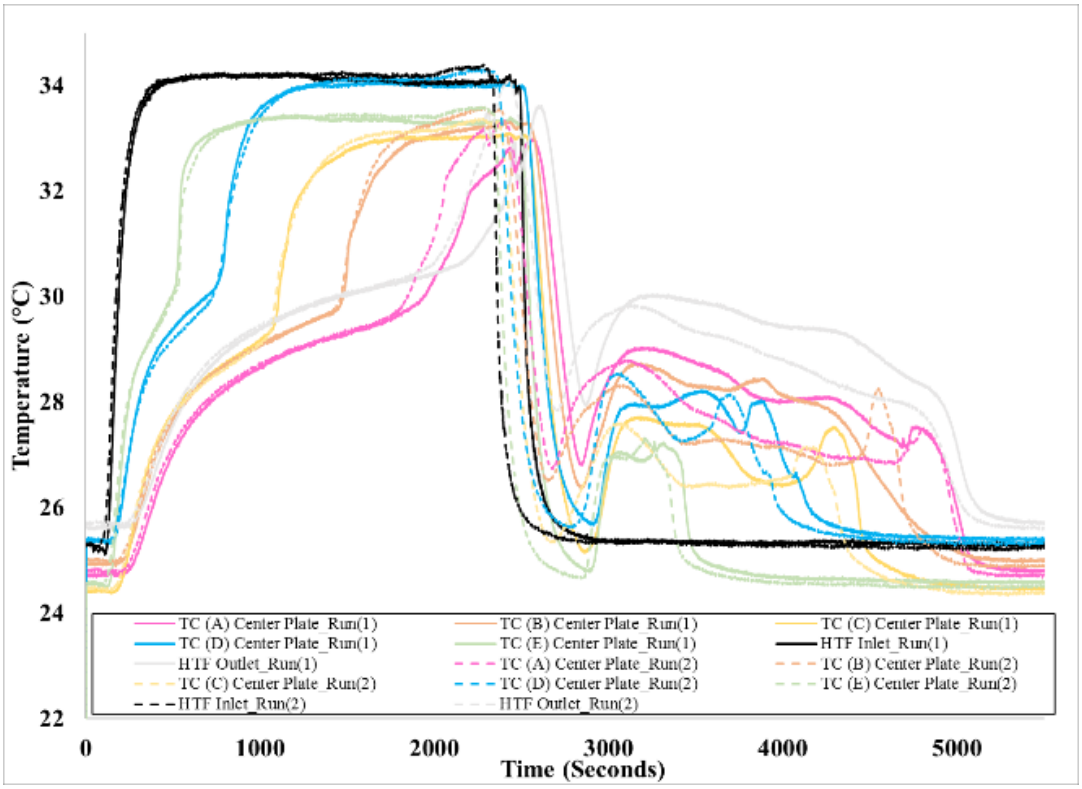

Figure 43: Temperature profiles recorded by thermocouples at the center plate during melting (90%) and solidification at a flow rate of 3 GPH (co-current). Inlet temperature of HTF during melting is 35 °C and during solidification is 25 °C (Case A, Pre-experiment calibration).

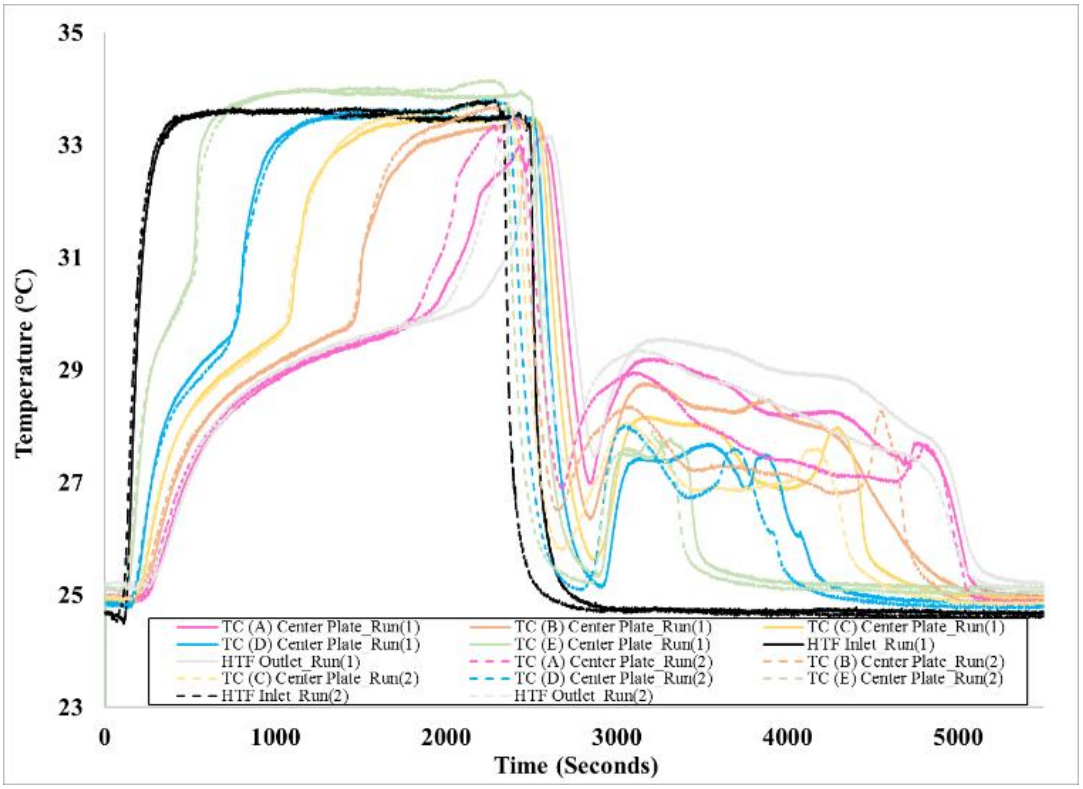

Figure 44: Temperature profiles recorded by thermocouples at the top plate during melting (90%) and solidification at a flow rate of 3 GPH (co-current). Inlet temperature of HTF during melting is 35 °C and during solidification is 25 °C (Case A, Post-experiment calibration).

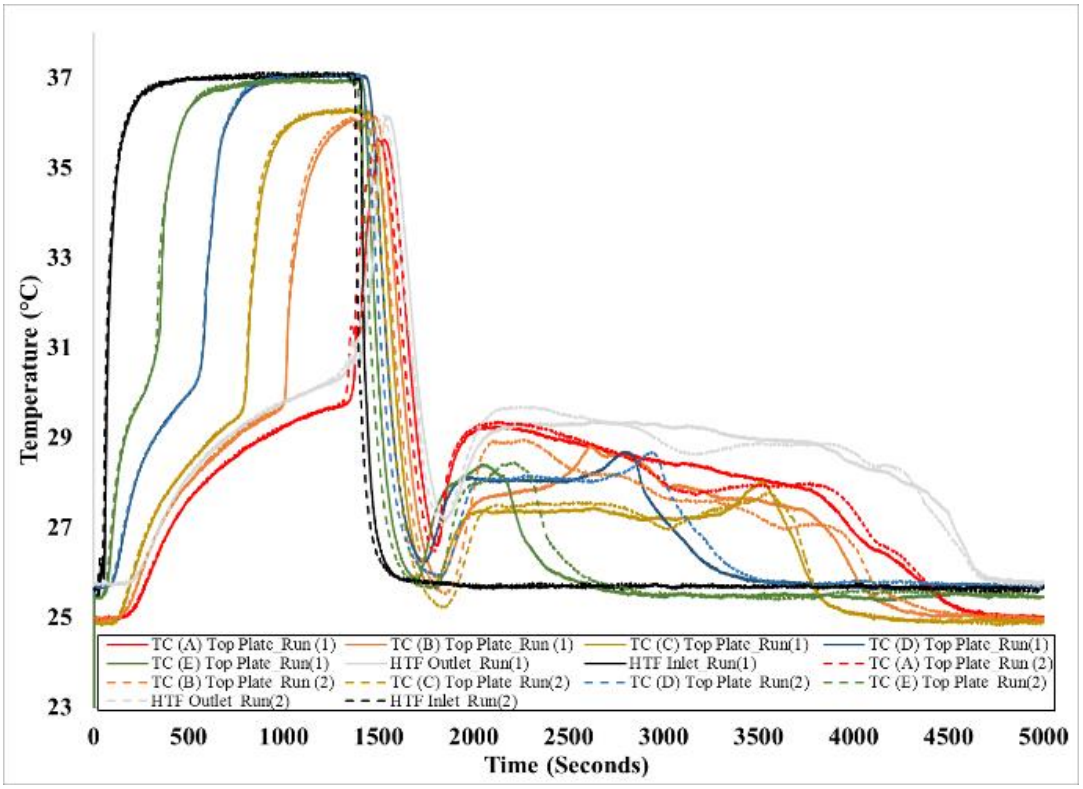

Figure 45: Temperature profiles recorded by thermocouples at the top plate during melting (90%) and solidification at a flow rate of 3 GPH (co-current). Inlet temperature of HTF during melting is 37.4 °C and during solidification is 25 °C (Case B, Pre-experiment calibration).

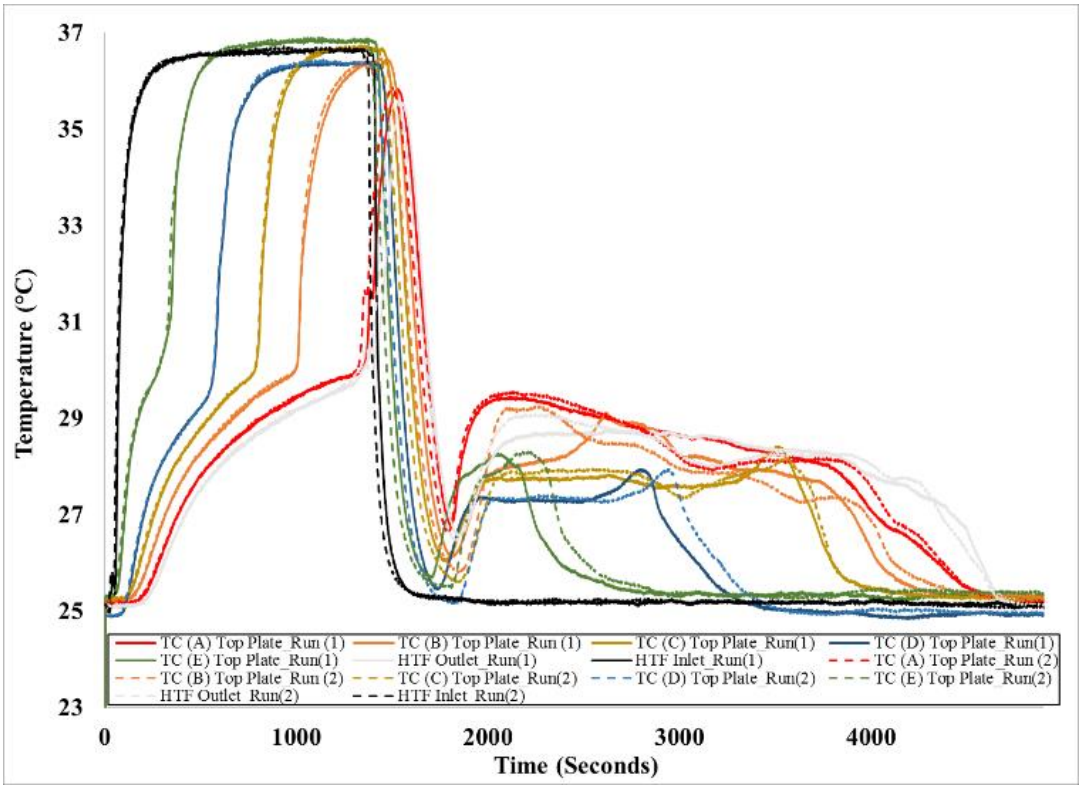

Figure 46: Temperature profiles recorded by thermocouples at the top plate during melting (90%) and solidification at a flow rate of 3 GPH (co-current). Inlet temperature of HTF during melting is 37.4 °C and during solidification is 25 °C (Case B, Post-experiment calibration).

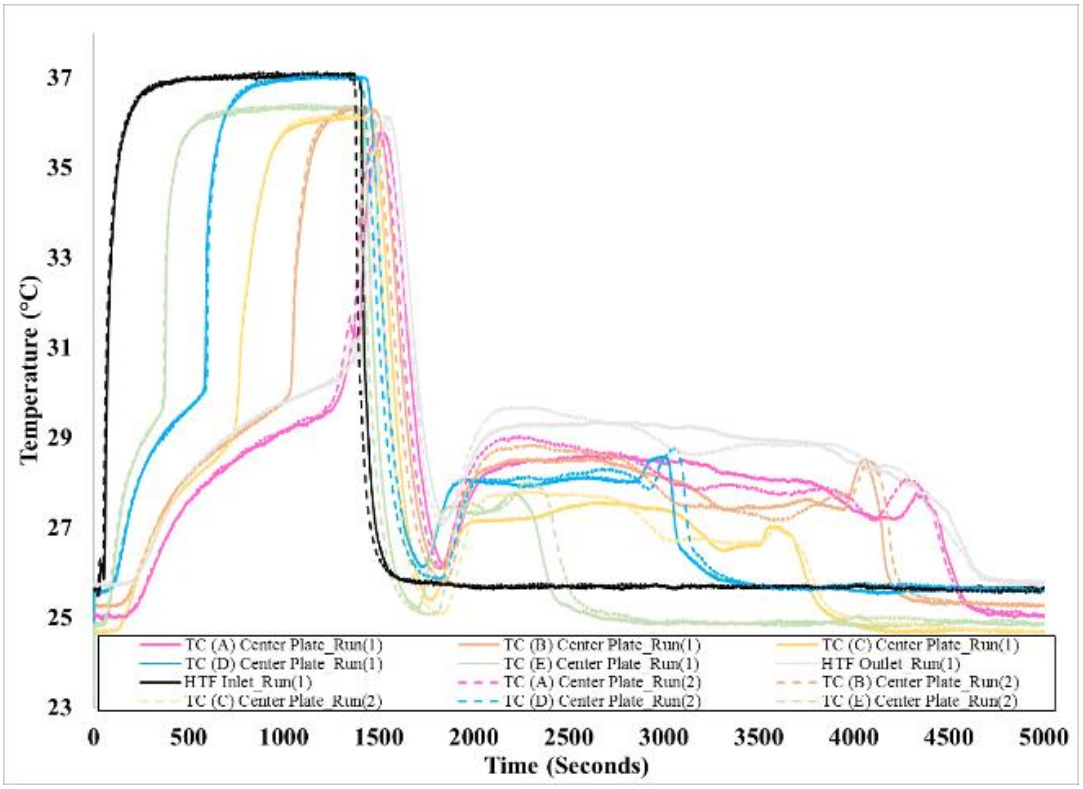

Figure 47: Temperature profiles recorded by thermocouples at the center plate during melting (90%) and solidification at a flow rate of 3 GPH (co-current). Inlet temperature of HTF during melting is 37.4 °C and during solidification is 25 °C (Case B, Pre-experiment calibration).

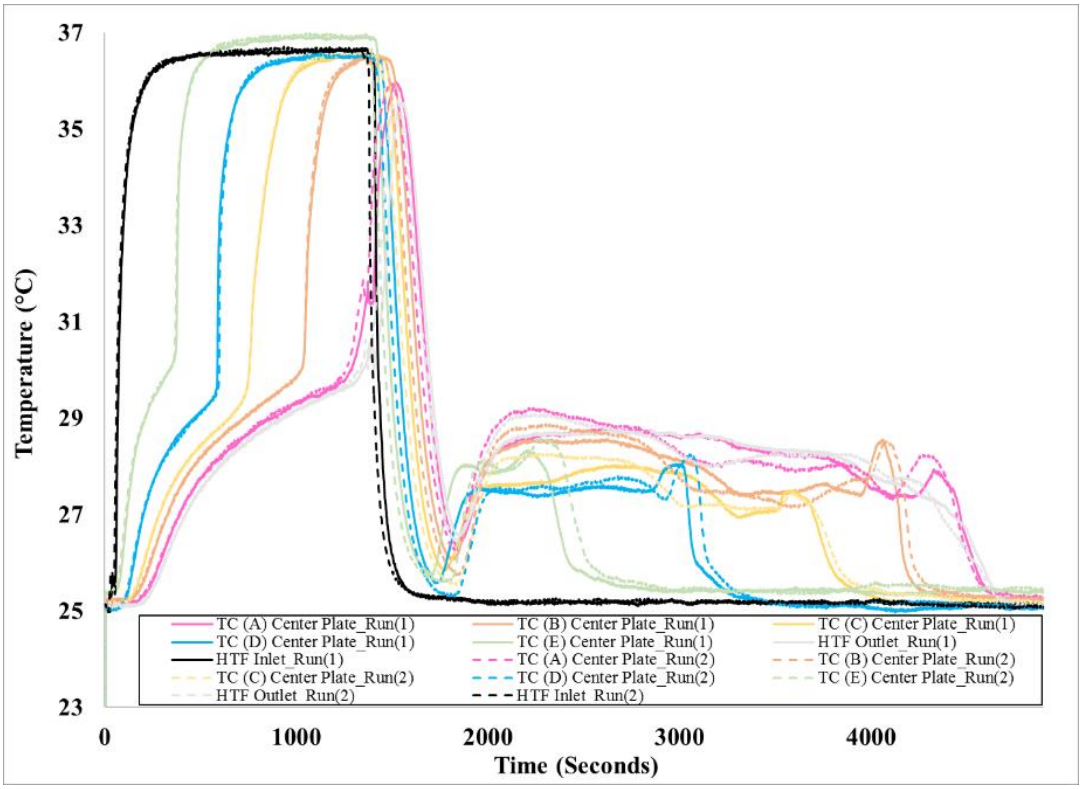

Figure 48: Temperature profiles recorded by thermocouples at the center plate during melting (90%) and solidification at a flow rate of 3 GPH (co-current). Inlet temperature of HTF during melting is 37.4 °C and during solidification is 25 °C (Case B, Post-experiment calibration).

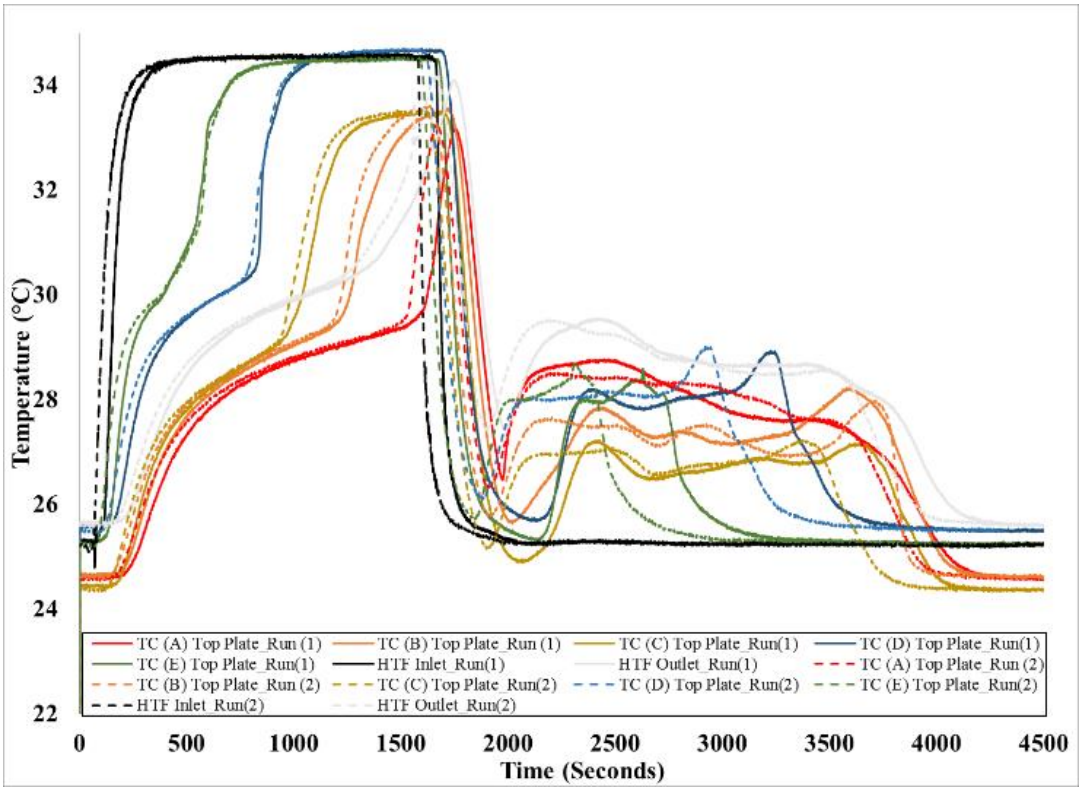

Figure 49: Temperature profiles recorded by thermocouples at the top plate during melting (90%) and solidification at a flow rate of 5 GPH (co-current). Inlet temperature of HTF during melting is 35 °C and during solidification is 25 °C (Case C, Pre-experiment calibration).

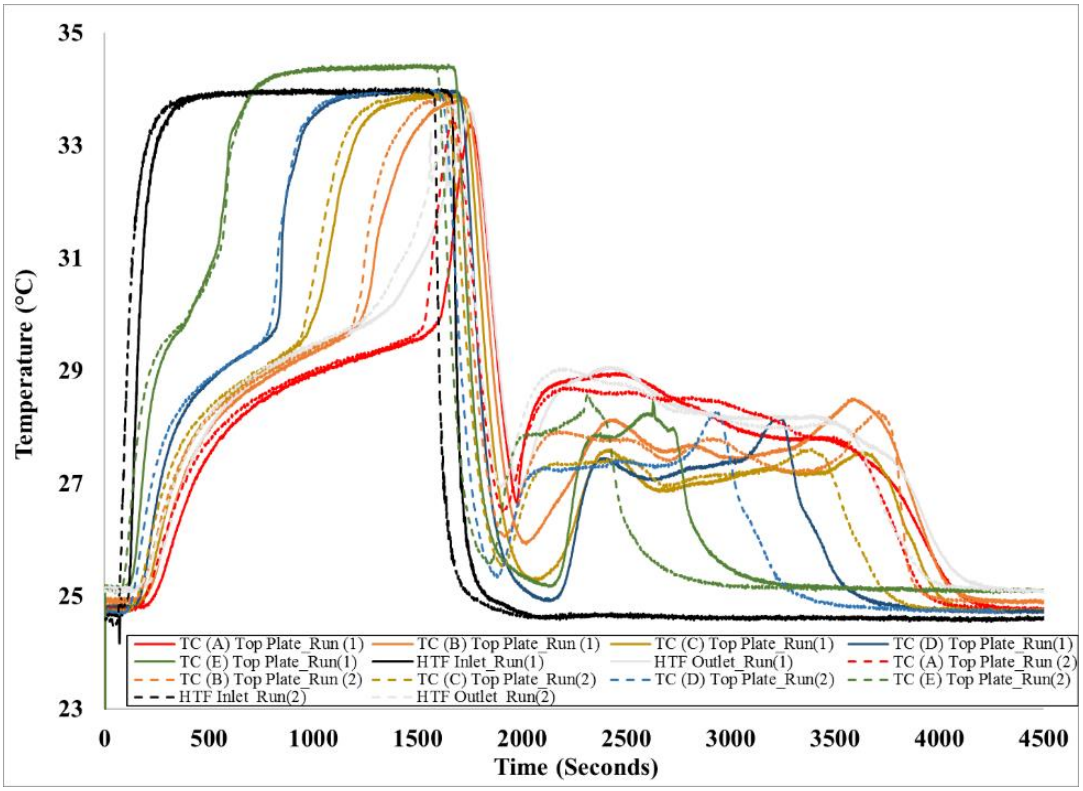

Figure 50: Temperature profiles recorded by thermocouples at the top plate during melting (90%) and solidification at a flow rate of 5 GPH (co-current). Inlet temperature of HTF during melting is 35 °C and during solidification is 25 °C (Case C, Post-experiment calibration).

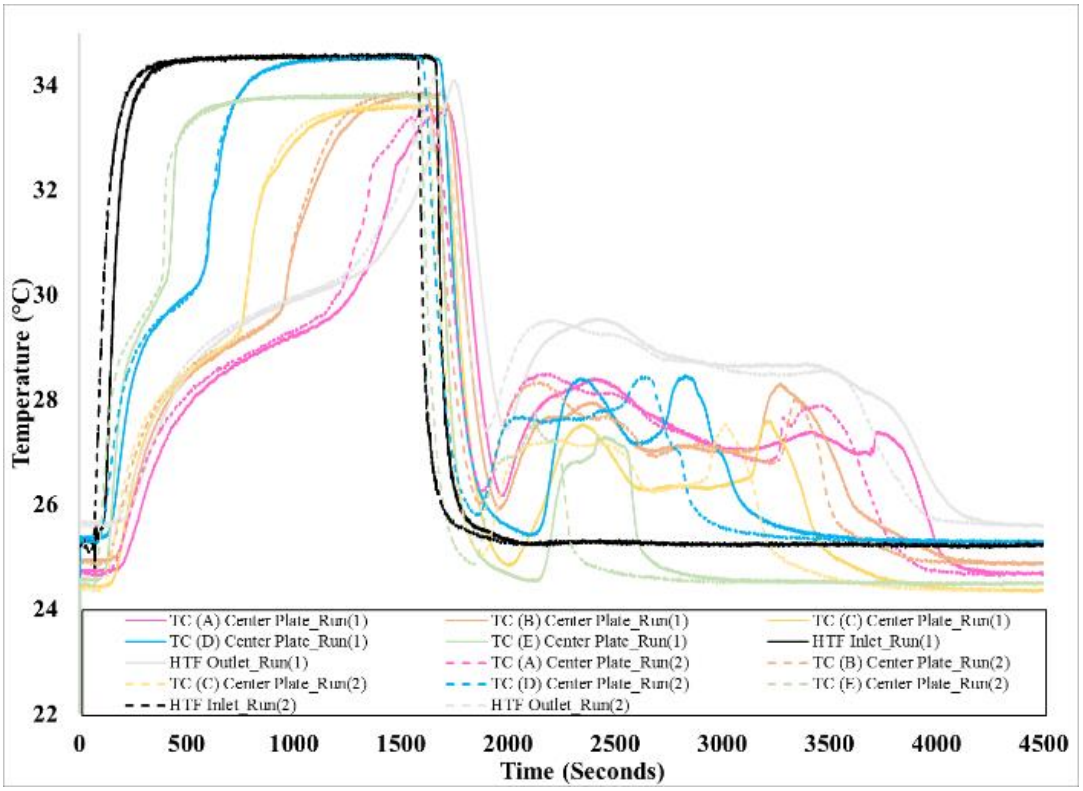

Figure 51: Temperature profiles recorded by thermocouples at the center plate during melting (90%) and solidification at a flow rate of 5 GPH (co-current). Inlet temperature of HTF during melting is 35 °C and during solidification is 25 °C (Case C, Pre-experiment calibration).

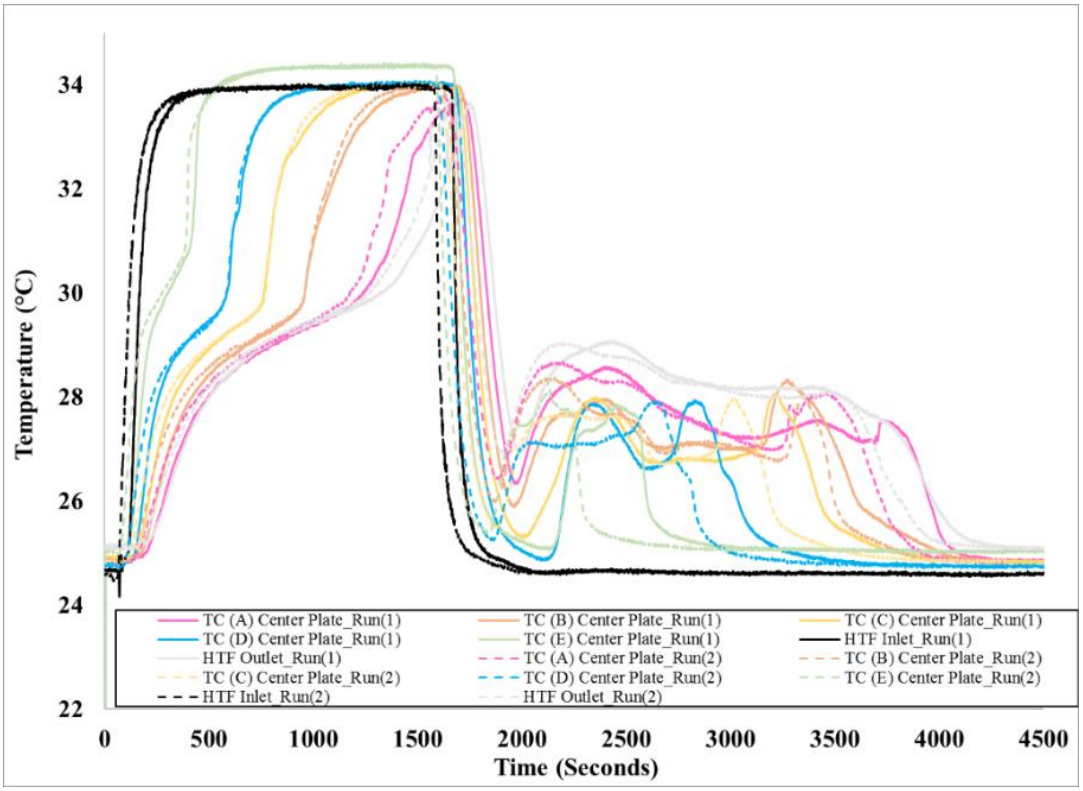

Figure 52: Temperature profiles recorded by thermocouples at the center plate during melting (90%) and solidification at a flow rate of 5 GPH (co-current). Inlet temperature of HTF during melting is 35 °C and during solidification is 25 °C (Case C, Post-experiment calibration).

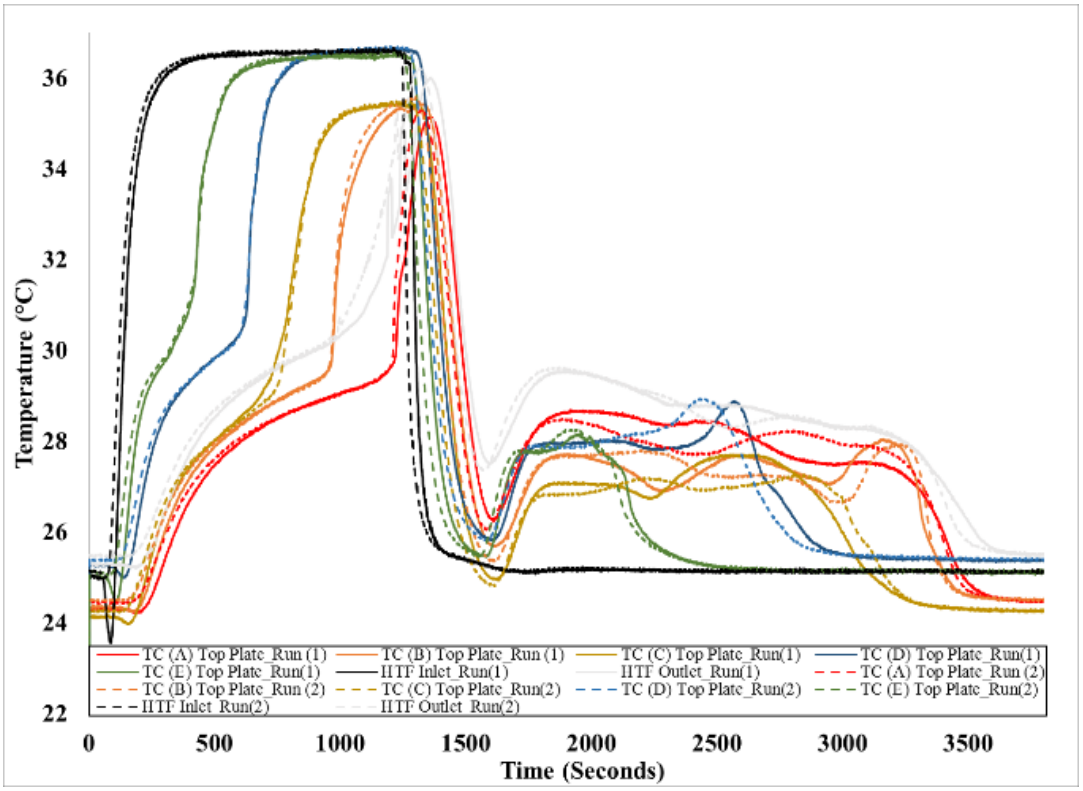

Figure 53: Temperature profiles recorded by thermocouples at the top plate during melting (90%) and solidification at a flow rate of 5 GPH (co-current). Inlet temperature of HTF during melting is 37.4 °C and during solidification is 25 °C (Case D, Pre-experiment calibration).

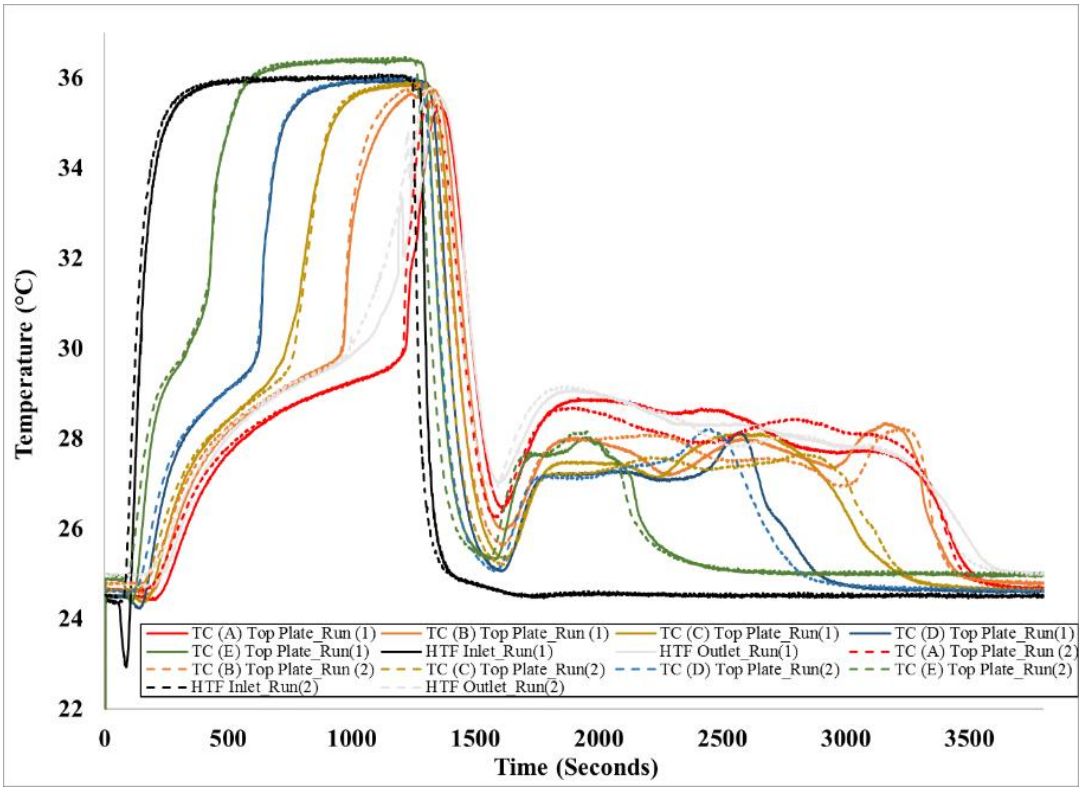

Figure 54: Temperature profiles recorded by thermocouples at the top plate during melting (90%) and solidification at a flow rate of 5 GPH (co-current). Inlet temperature of HTF during melting is 37.4 °C and during solidification is 25 °C (Case D, Post-experiment calibration).

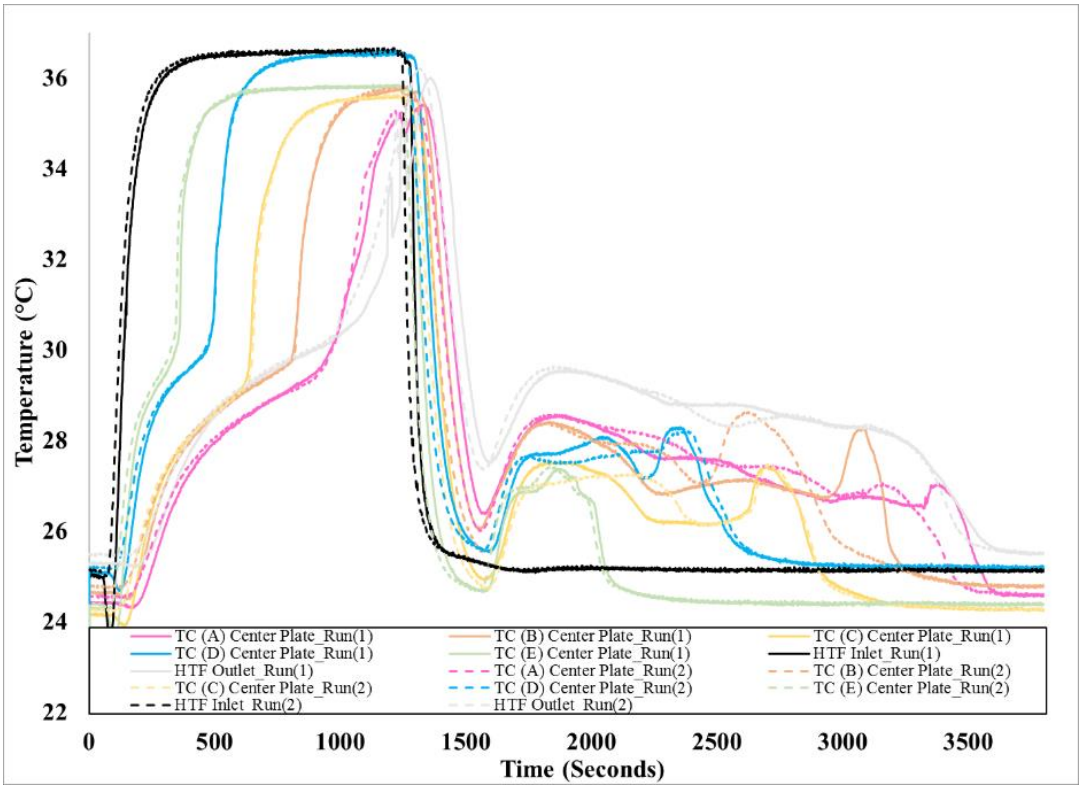

Figure 55: Temperature profiles recorded by thermocouples at the center plate during melting (90%) and solidification at a flow rate of 5 GPH (co-current). Inlet temperature of HTF during melting is 37.4 °C and during solidification is 25 °C (Case D, Pre-experiment calibration).

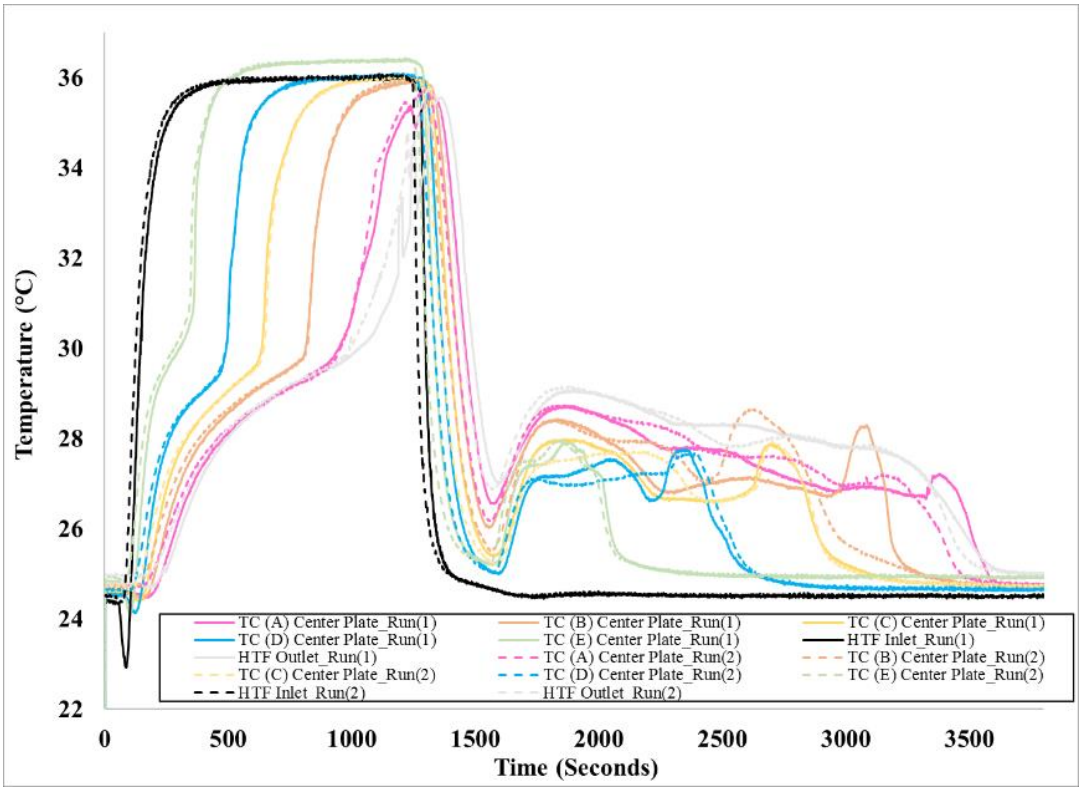

Figure 56: Temperature profiles recorded by thermocouples at the center plate during melting (90%) and solidification at a flow rate of 5 GPH (co-current). Inlet temperature of HTF during melting is 37.4 °C and during solidification is 25 °C (Case D, Post-experiment calibration).

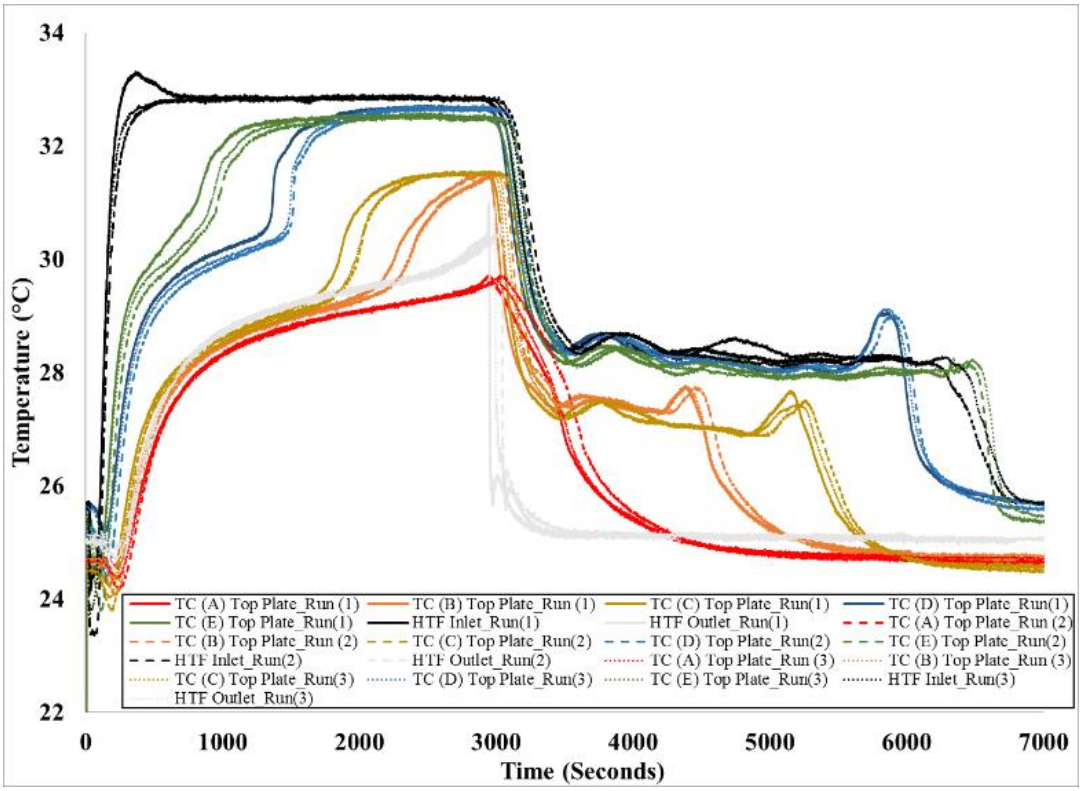

Figure 57: Temperature profiles recorded by thermocouples at the top plate during melting (90%) and solidification at a flow rate of 3 GPH (counter-current). Inlet temperature of HTF during melting is 33 °C and during solidification is 25 °C (Case E, Pre-experiment calibration).

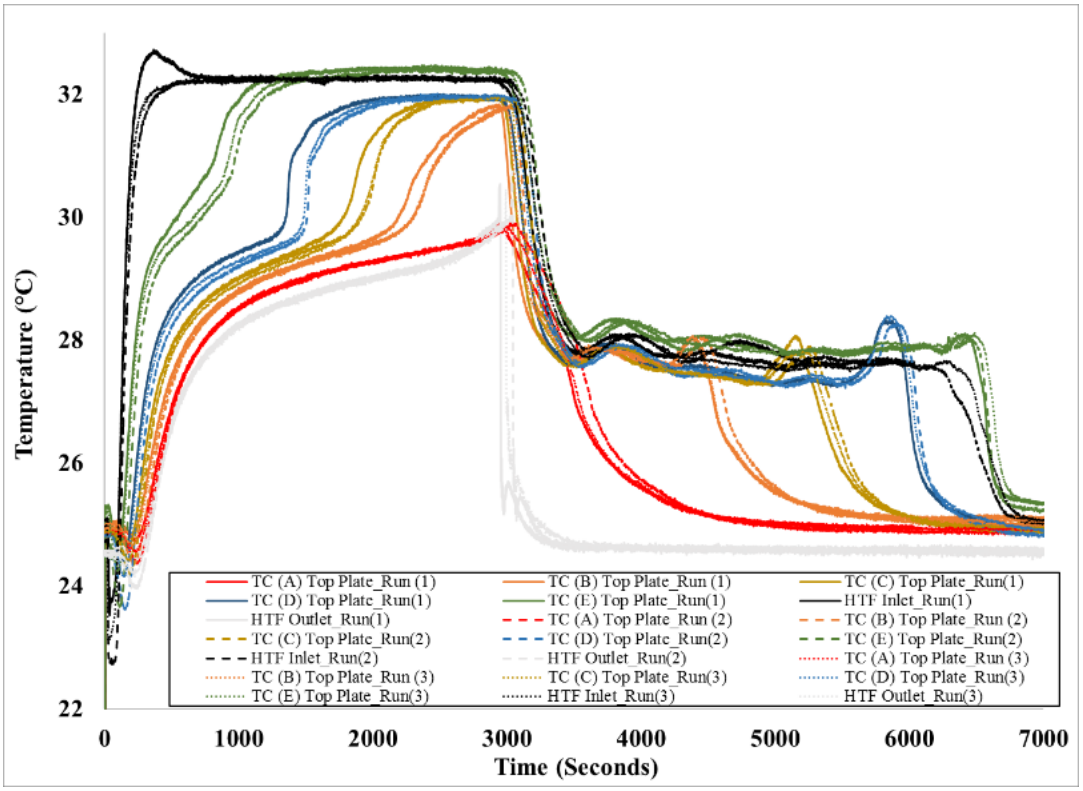

Figure 58: Temperature profiles recorded by thermocouples at the top plate during melting (90%) and solidification at a flow rate of 3 GPH (counter-current). Inlet temperature of HTF during melting is 33 °C and during solidification is 25 °C (Case E, Post-experiment calibration).

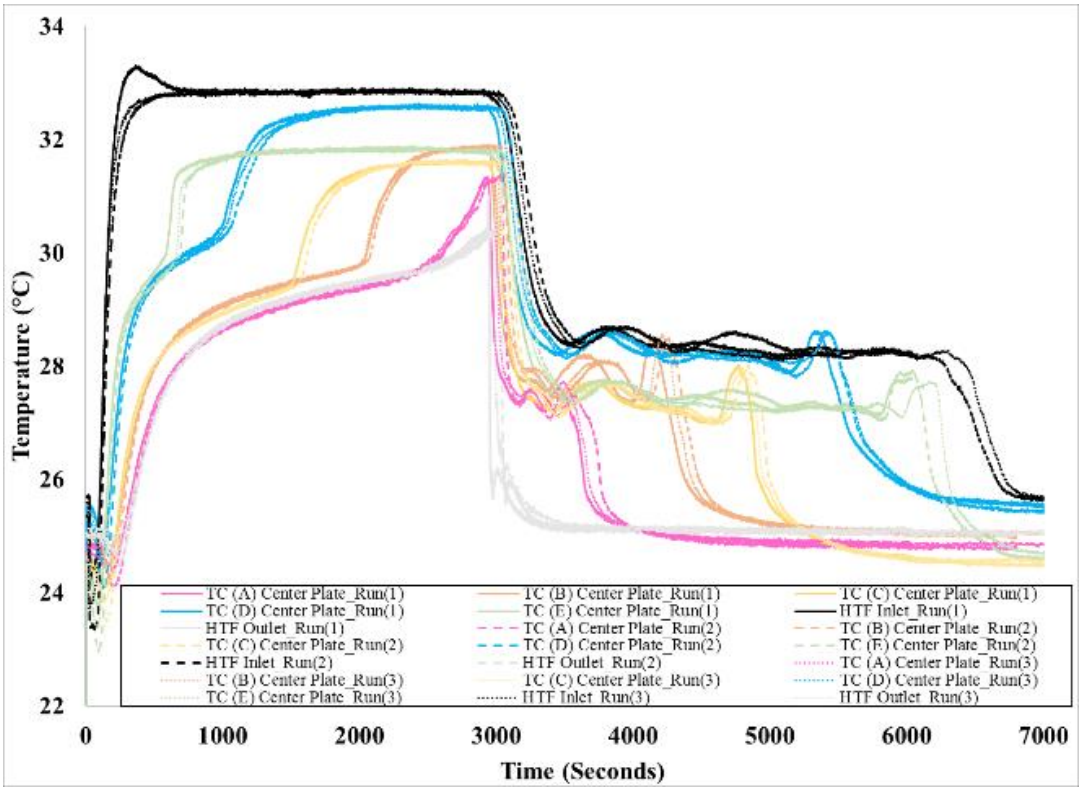

Figure 59: Temperature profiles recorded by thermocouples at the center plate during melting (90%) and solidification at a flow rate of 3 GPH (counter-current). Inlet temperature of HTF during melting is 33 °C and during solidification is 25 °C (Case E, Pre-experiment calibration).

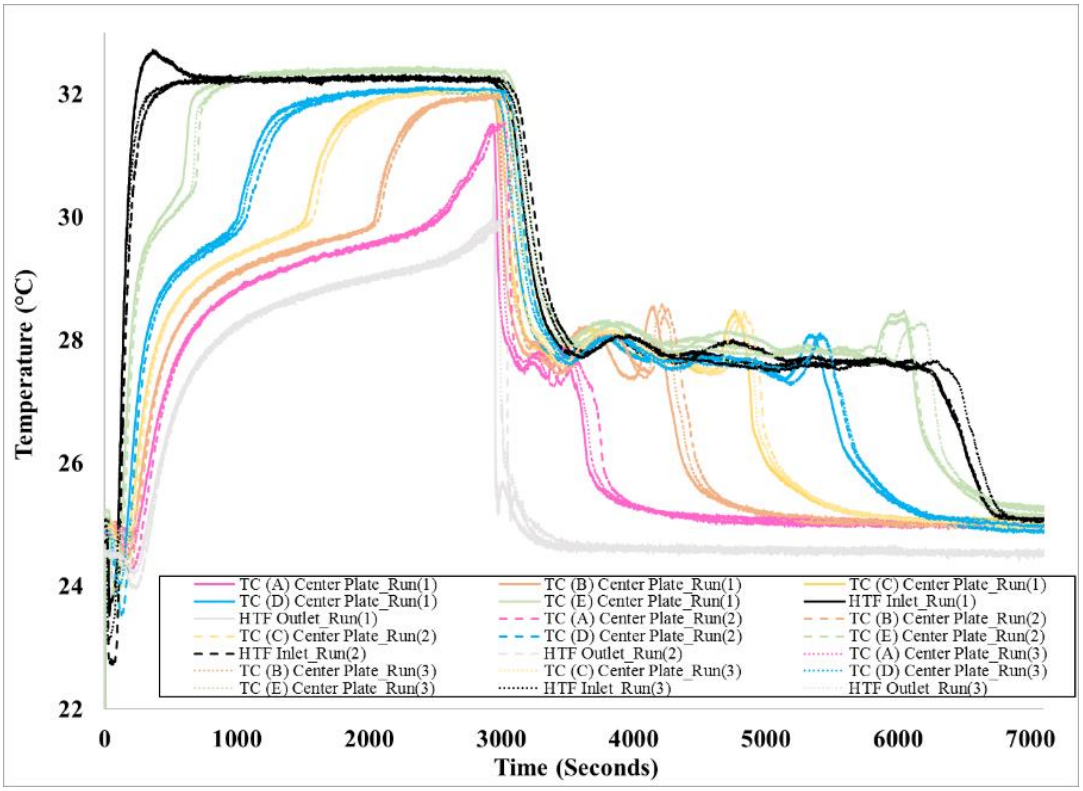

Figure 60: Temperature profiles recorded by thermocouples at the center plate during melting (90%) and solidification at a flow rate of 3 GPH (counter-current). Inlet temperature of HTF during melting is 33 °C and during solidification is 25 °C (Case E, Post-experiment calibration).

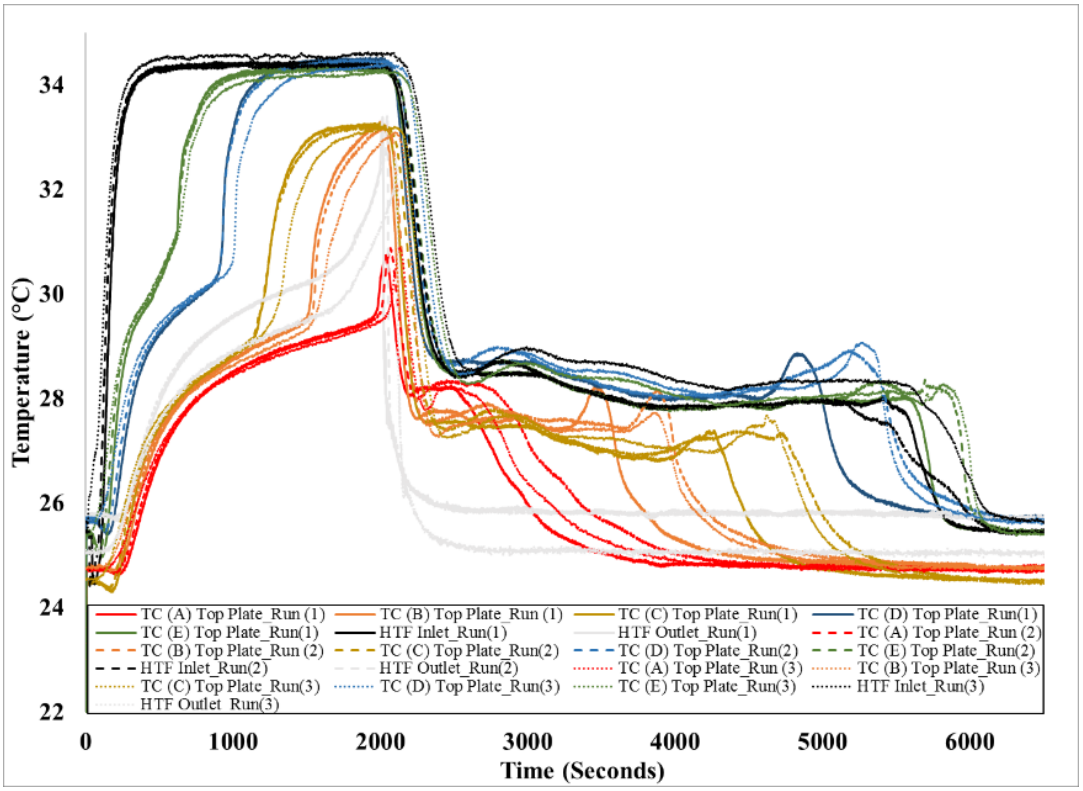

Figure 61: Temperature profiles recorded by thermocouples at the top plate during melting (90%) and solidification at a flow rate of 3 GPH (counter-current). Inlet temperature of HTF during melting is 35 °C and during solidification is 25 °C (Case F, Pre-experiment calibration).

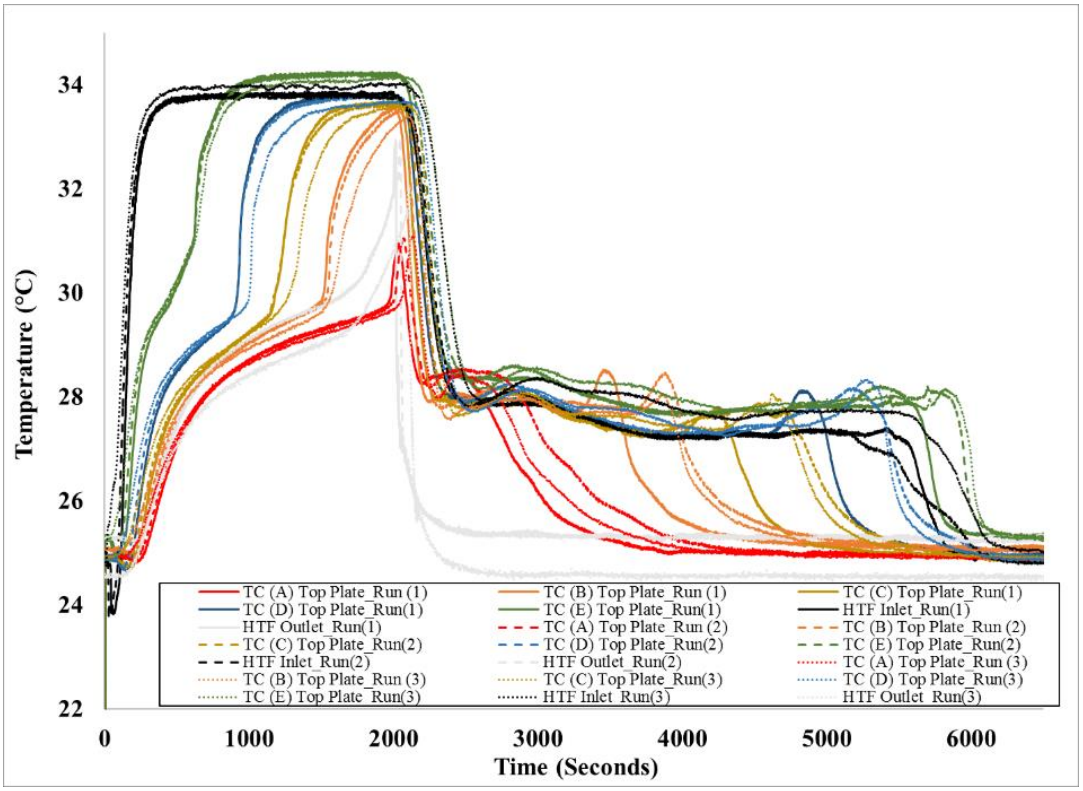

Figure 62: Temperature profiles recorded by thermocouples at the top plate during melting (90%) and solidification at a flow rate of 3 GPH (counter-current). Inlet temperature of HTF during melting is 35 °C and during solidification is 25 °C (Case F, Post-experiment calibration).

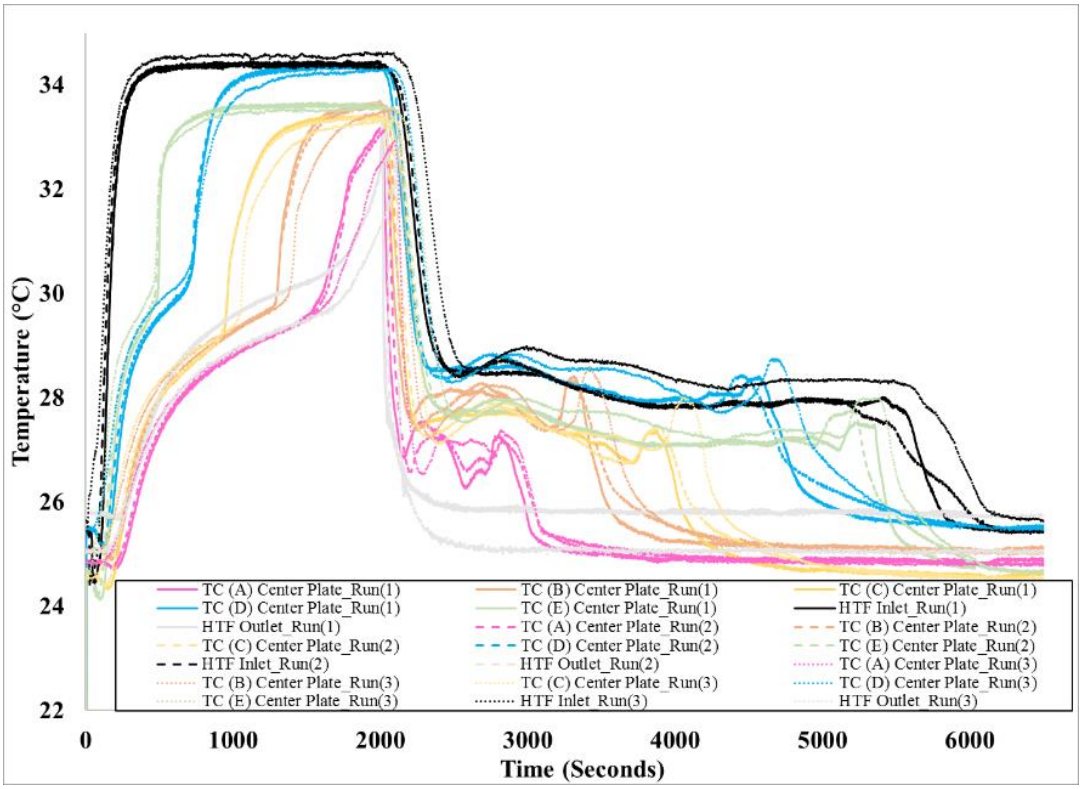

Figure 63: Temperature profiles recorded by thermocouples at the center plate during melting (90%) and solidification at a flow rate of 3 GPH (counter-current). Inlet temperature of HTF during melting is 35 °C and during solidification is 25 °C (Case F, Pre-experiment calibration).

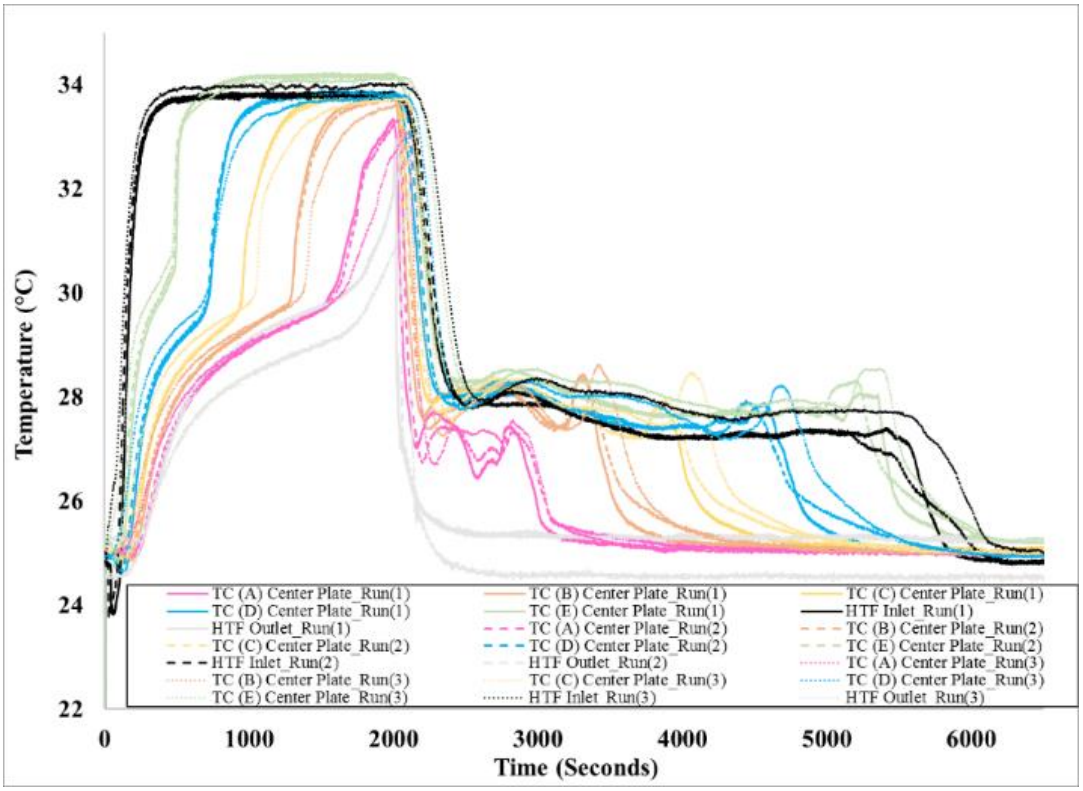

Figure 64: Temperature profiles recorded by thermocouples at the center plate during melting (90%) and solidification at a flow rate of 3 GPH (counter-current). Inlet temperature of HTF during melting is 35 °C and during solidification is 25 °C (Case F, Post-experiment calibration).

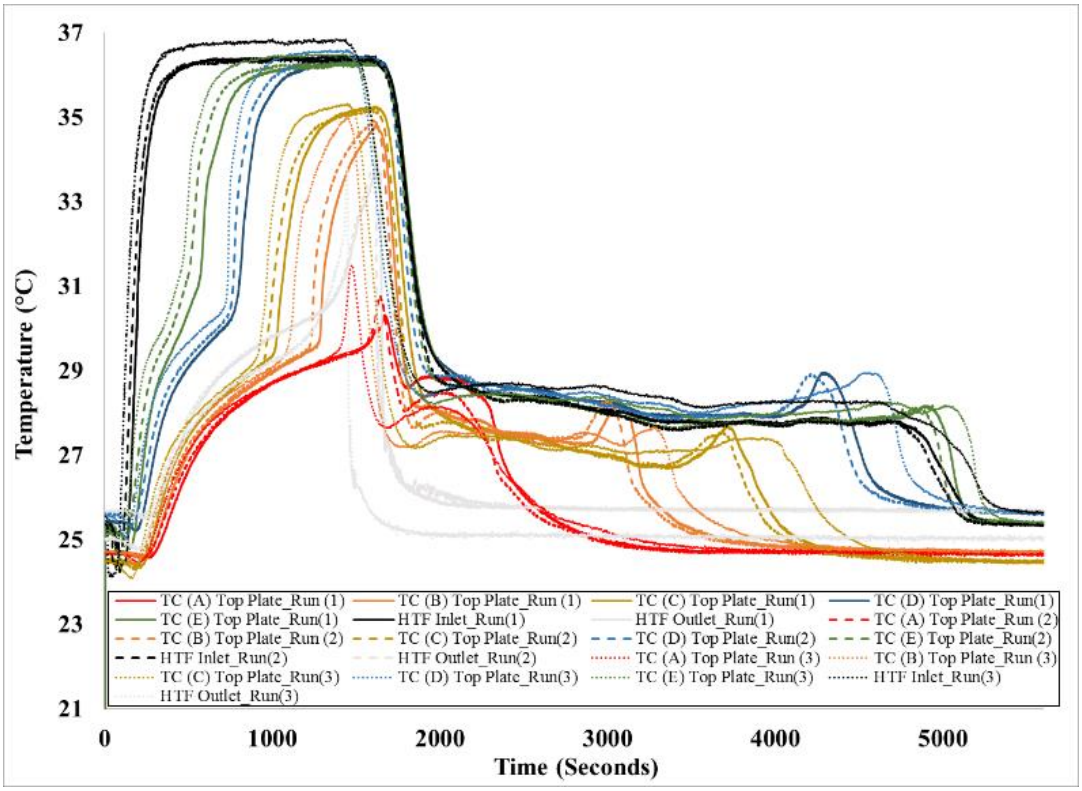

Figure 65: Temperature profiles recorded by thermocouples at the top plate during melting (90%) and solidification at a flow rate of 3 GPH (counter-current). Inlet temperature of HTF during melting is 37.4 °C and during solidification is 25 °C (Case G, Pre-experiment calibration).

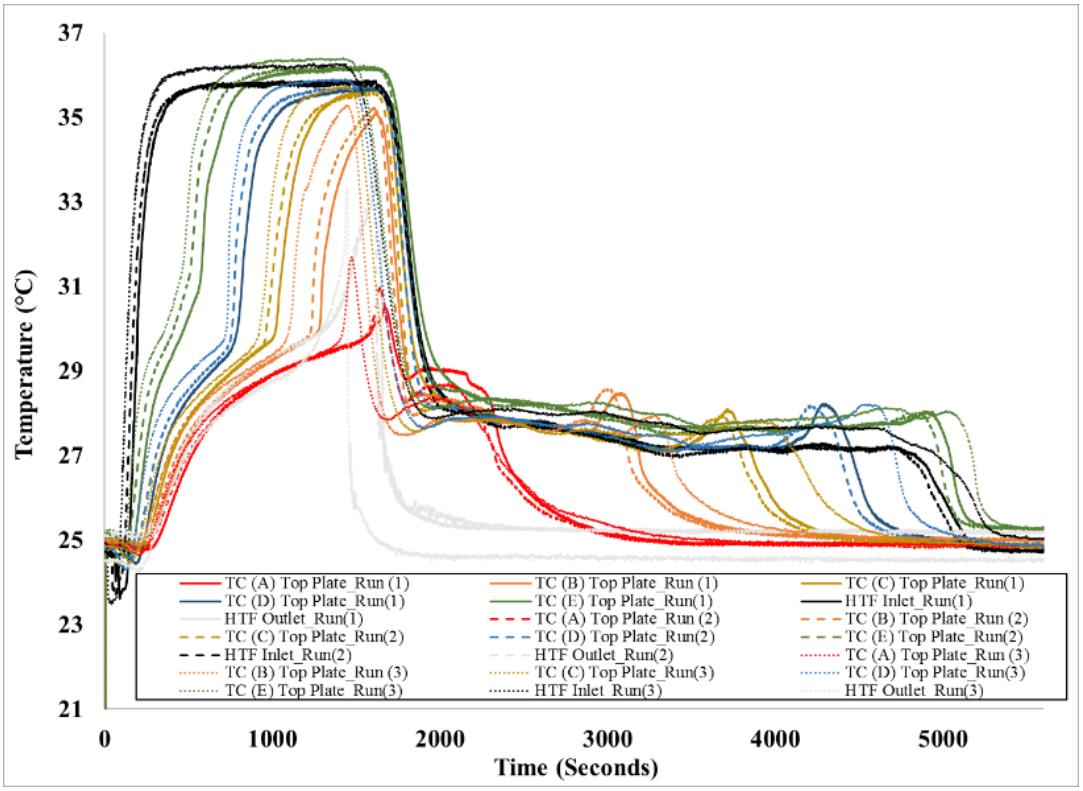

Figure 66: Temperature profiles recorded by thermocouples at the top plate during melting (90%) and solidification at a flow rate of 3 GPH (counter-current). Inlet temperature of HTF during melting is 37.4 °C and during solidification is 25 °C (Case G, Post-experiment calibration).

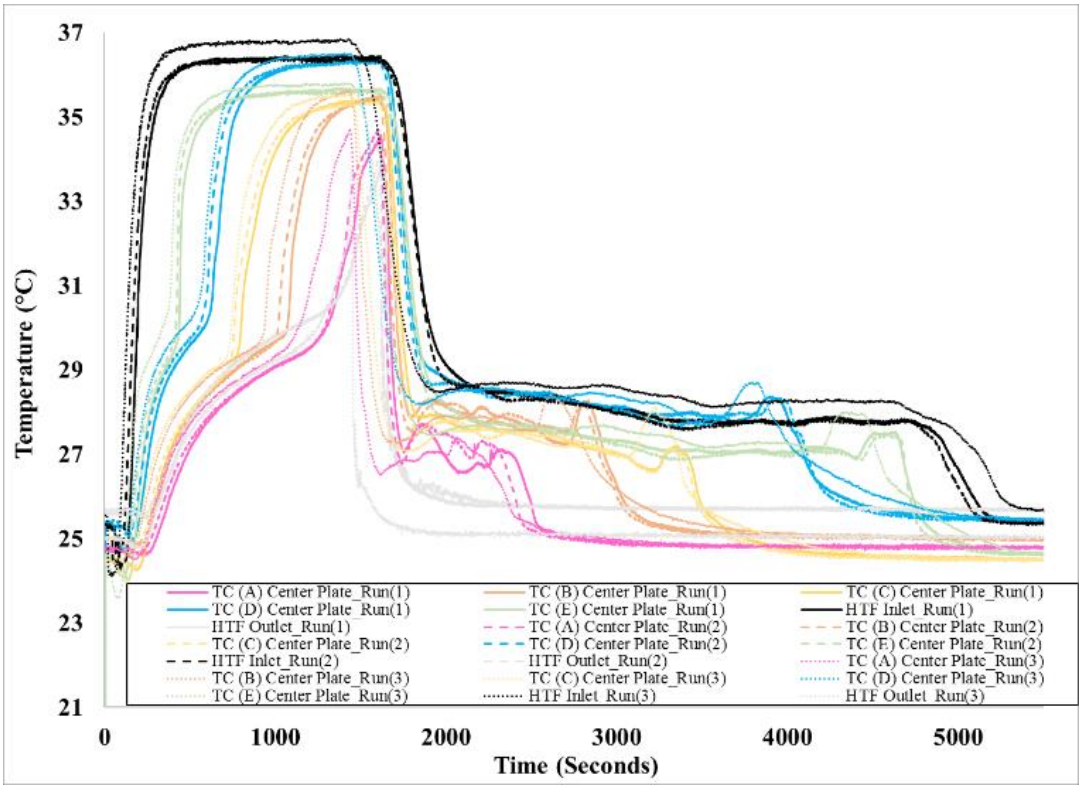

Figure 67: Temperature profiles recorded by thermocouples at the center plate during melting (90%) and solidification at a flow rate of 3 GPH (counter-current). Inlet temperature of HTF during melting is 37.4 °C and during solidification is 25 °C (Case G, Pre-experiment calibration).

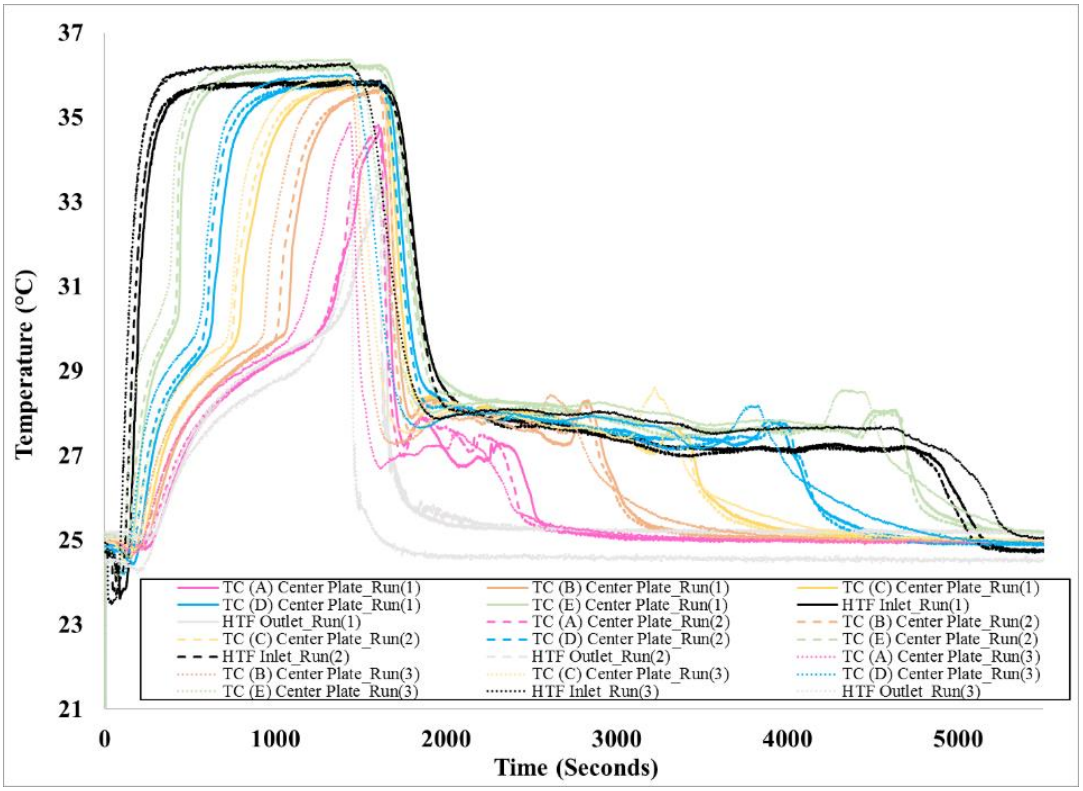

Figure 68: Temperature profiles recorded by thermocouples at the center plate during melting (90%) and solidification at a flow rate of 3 GPH (counter-current). Inlet temperature of HTF during melting is 37.4 °C and during solidification is 25 °C (Case G, Post-experiment calibration).

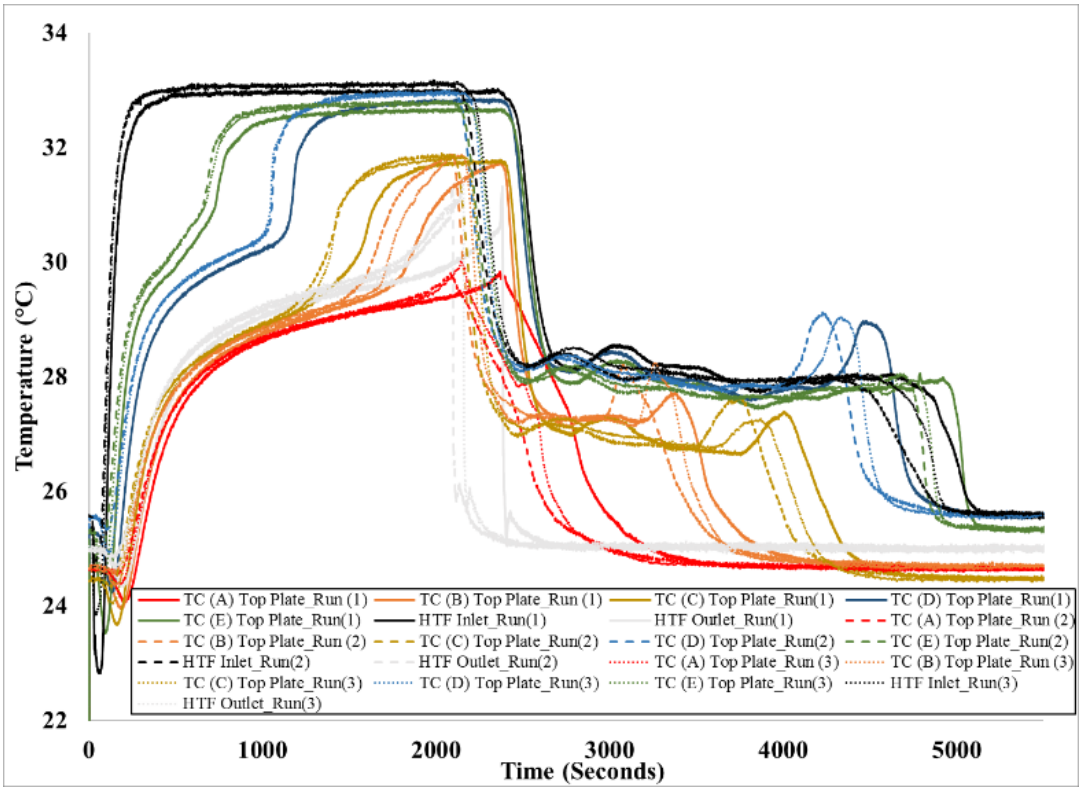

Figure 69: Temperature profiles recorded by thermocouples at the top plate during melting (90%) and solidification at a flow rate of 5 GPH (counter-current). Inlet temperature of HTF during melting is 33 °C and during solidification is 25 °C (Case H, Pre-experiment calibration).

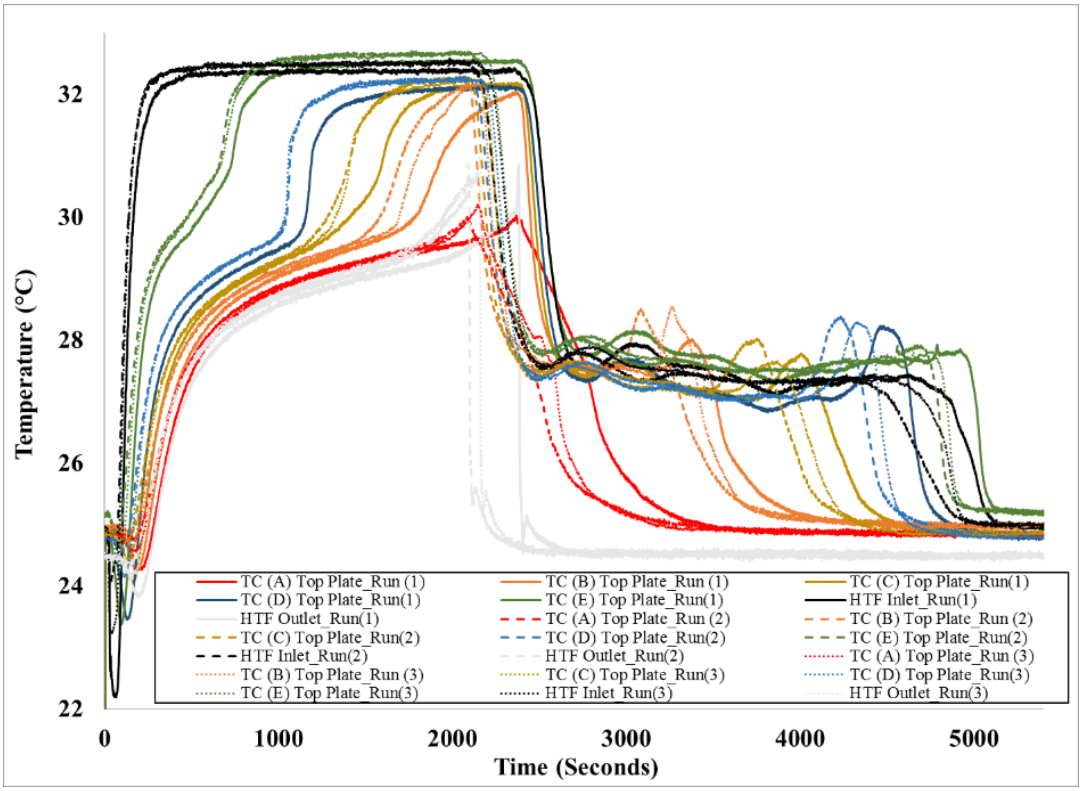

Figure 70: Temperature profiles recorded by thermocouples at the top plate during melting (90%) and solidification at a flow rate of 5 GPH (counter-current). Inlet temperature of HTF during melting is 33 °C and during solidification is 25 °C (Case H, Post-experiment calibration).

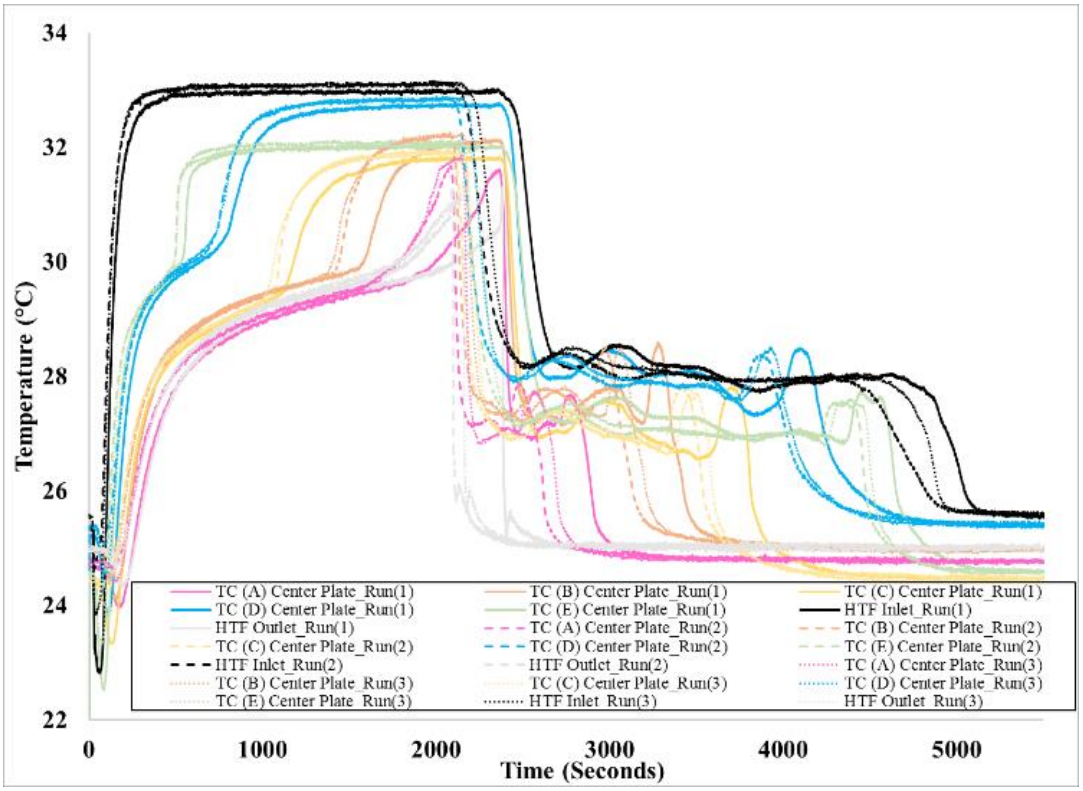

Figure 71: Temperature profiles recorded by thermocouples at the center plate during melting (90%) and solidification at a flow rate of 5 GPH (counter-current). Inlet temperature of HTF during melting is 33 °C and during solidification is 25 °C (Case H, Pre-experiment calibration).

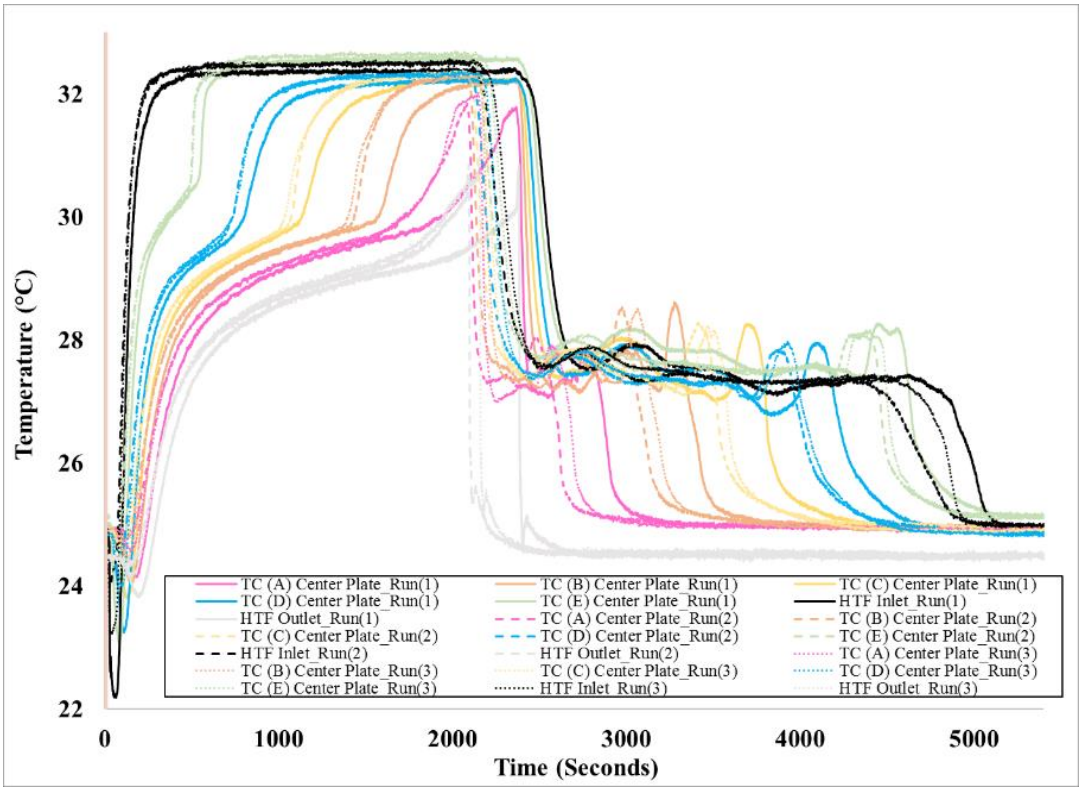

Figure 72: Temperature profiles recorded by thermocouples at the center plate during melting (90%) and solidification at a flow rate of 5 GPH (counter-current). Inlet temperature of HTF during melting is 33 °C and during solidification is 25 °C (Case H, Pre-experiment calibration).

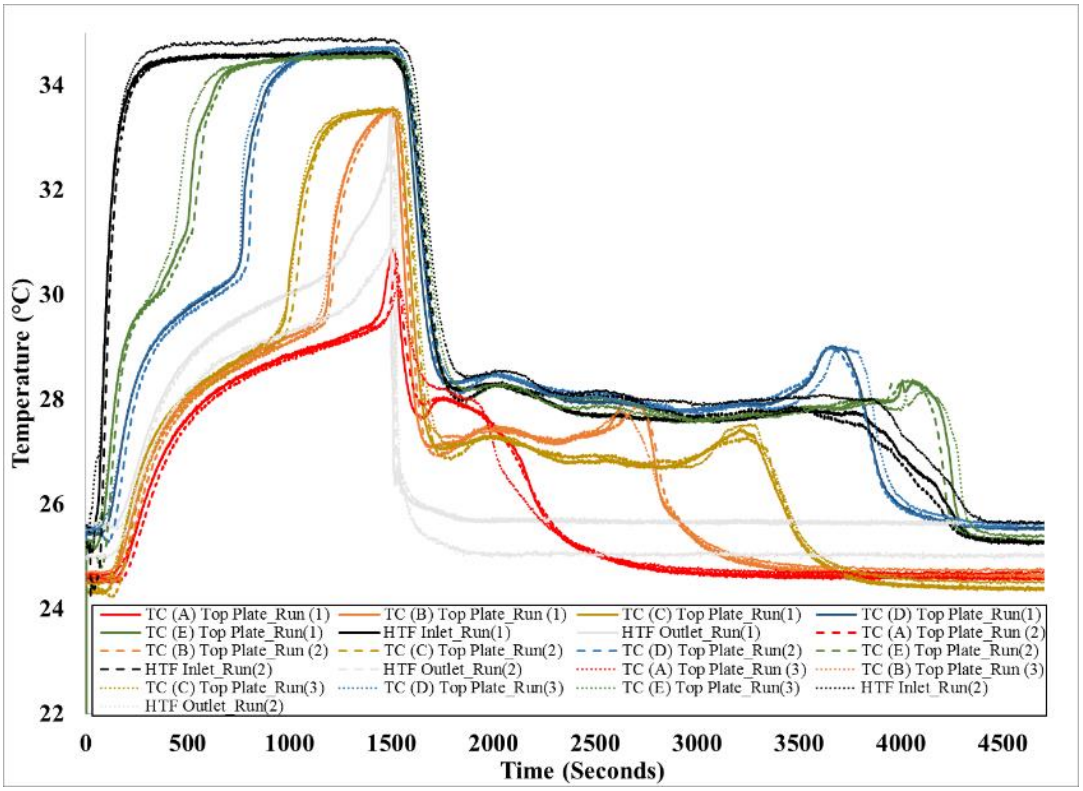

Figure 73: Temperature profiles recorded by thermocouples at the top plate during melting (90%) and solidification at a flow rate of 5 GPH (counter-current). Inlet temperature of HTF during melting is 35 °C and during solidification is 25 °C (Case I, Pre-experiment calibration).

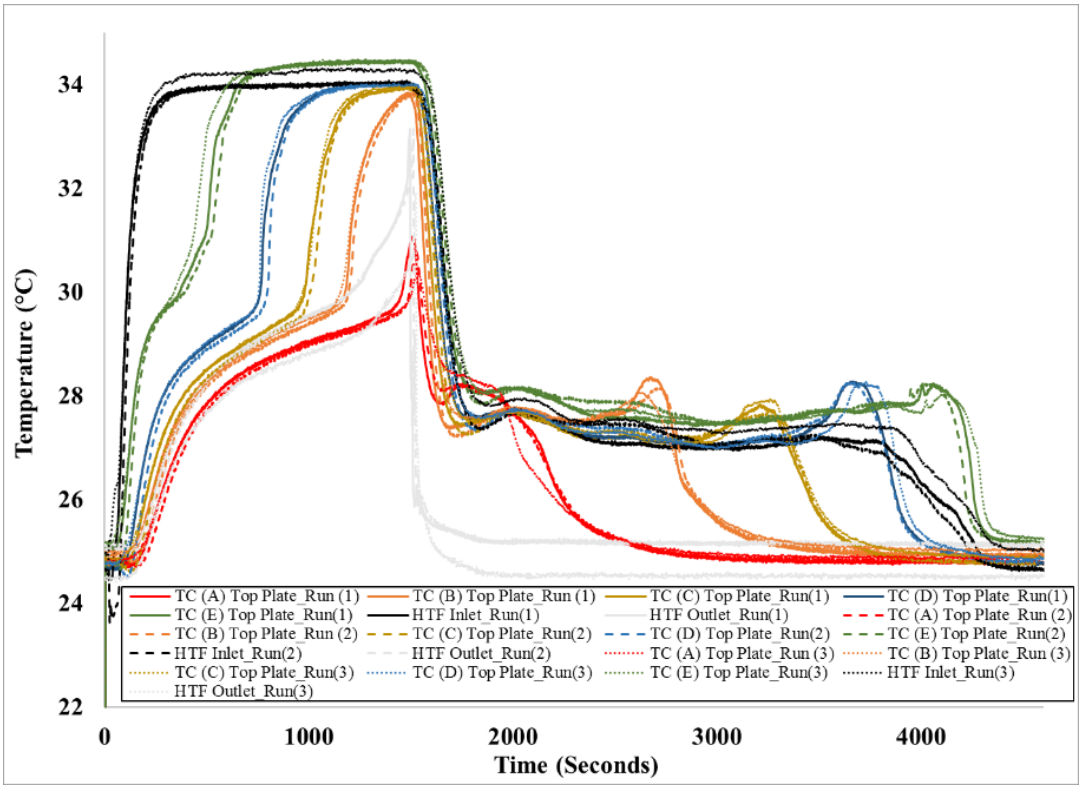

Figure 74: Temperature profiles recorded by thermocouples at the top plate during melting (90%) and solidification at a flow rate of 5 GPH (counter-current). Inlet temperature of HTF during melting is 35 °C and during solidification is 25 °C (Case I, Post-experiment calibration).

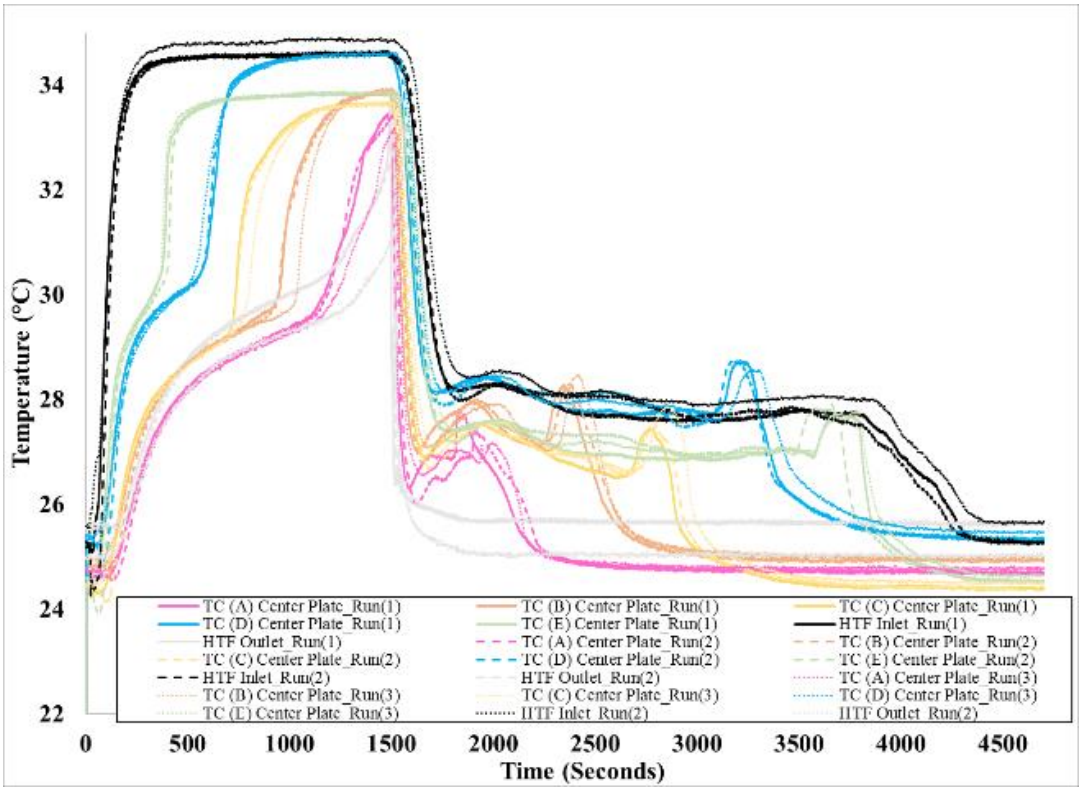

Figure 75: Temperature profiles recorded by thermocouples at the center plate during melting (90%) and solidification at a flow rate of 5 GPH (counter-current). Inlet temperature of HTF during melting is 35 °C and during solidification is 25 °C (Case I, Pre-experiment calibration).

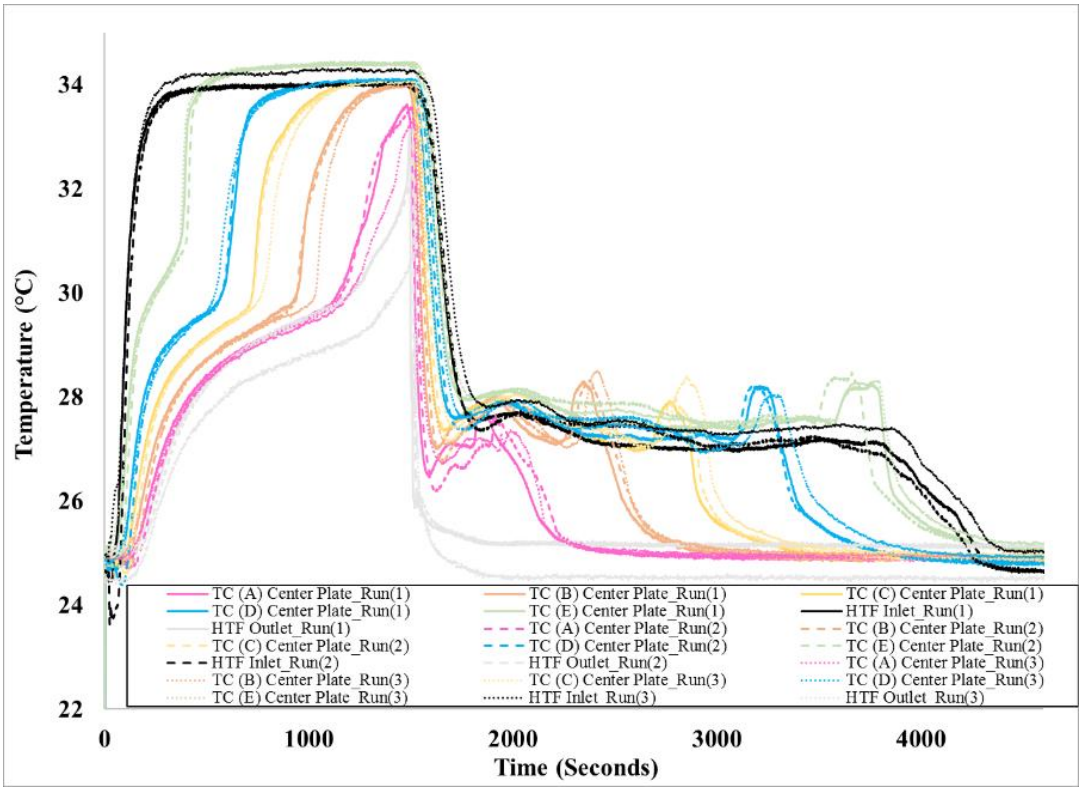

Figure 76: Temperature profiles recorded by thermocouples at the center plate during melting (90%) and solidification at a flow rate of 5 GPH (counter-current). Inlet temperature of HTF during melting is 35 °C and during solidification is 25 °C (Case I, Post-experiment calibration).

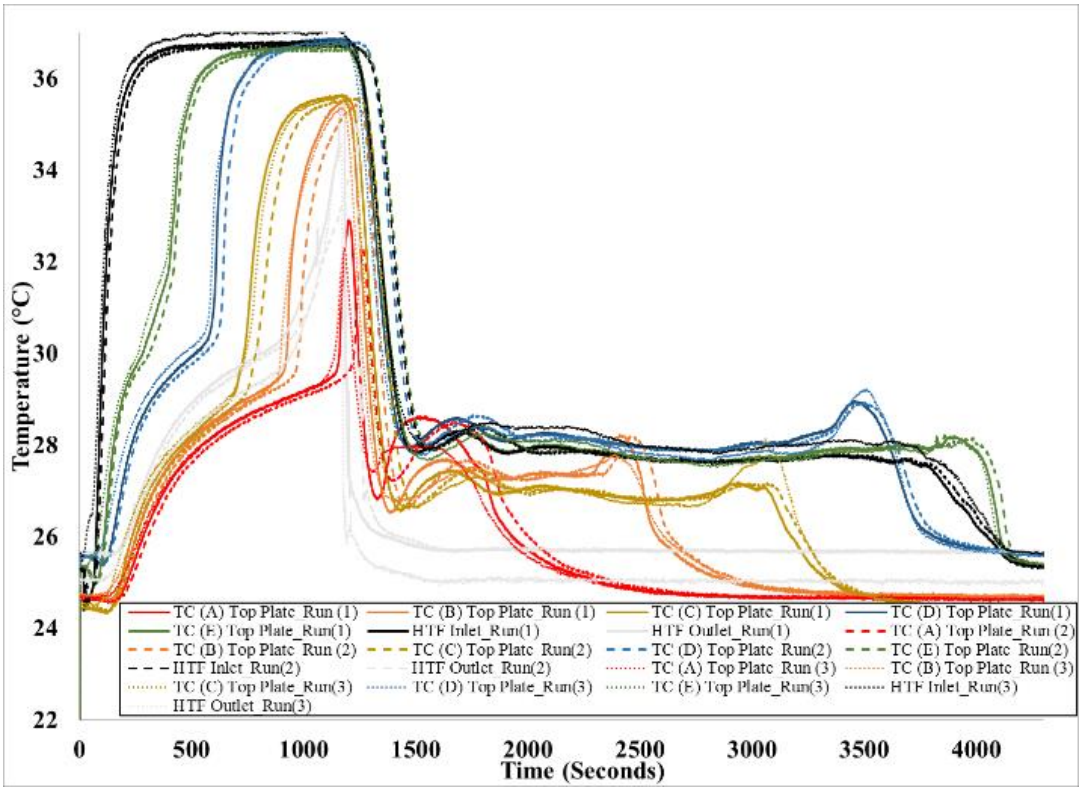

Figure 77: Temperature profiles recorded by thermocouples at the top plate during melting (90%) and solidification at a flow rate of 5 GPH (counter-current). Inlet temperature of HTF during melting is 37.4 °C and during solidification is 25 °C (Case J, Pre-experiment calibration).

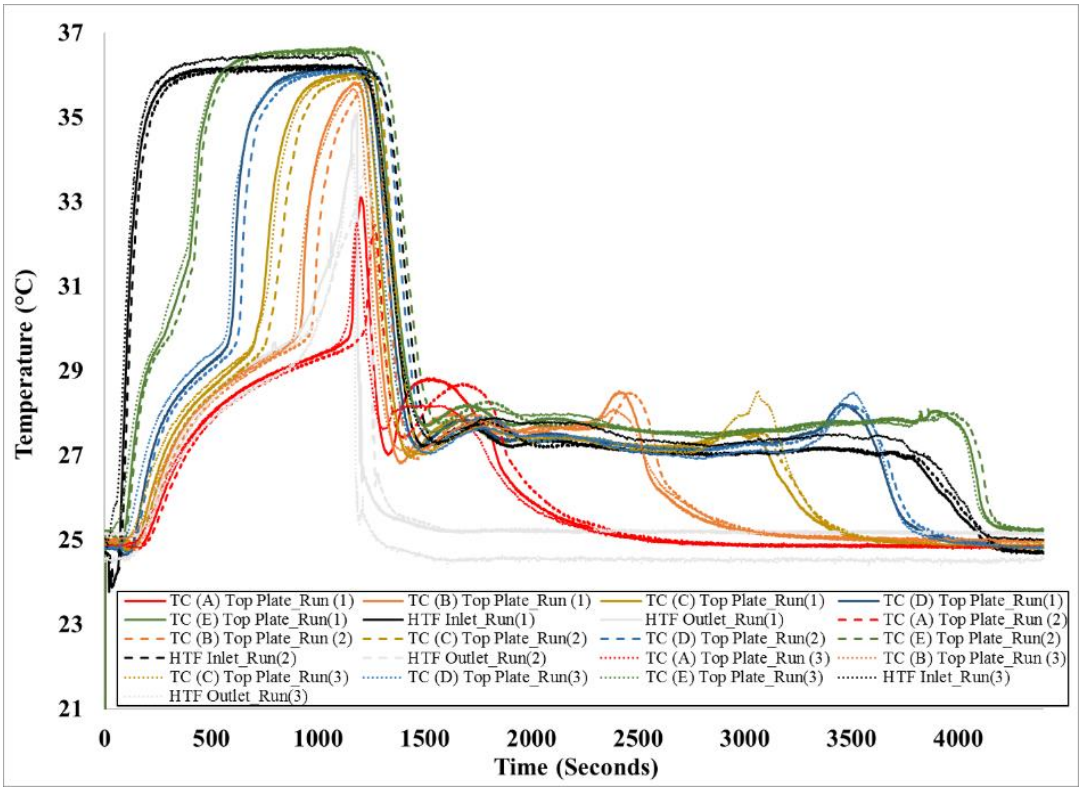

Figure 78: Temperature profiles recorded by thermocouples at the top plate during melting (90%) and solidification at a flow rate of 5 GPH (counter-current). Inlet temperature of HTF during melting is 37.4 °C and during solidification is 25 °C (Case J, Post-experiment calibration).

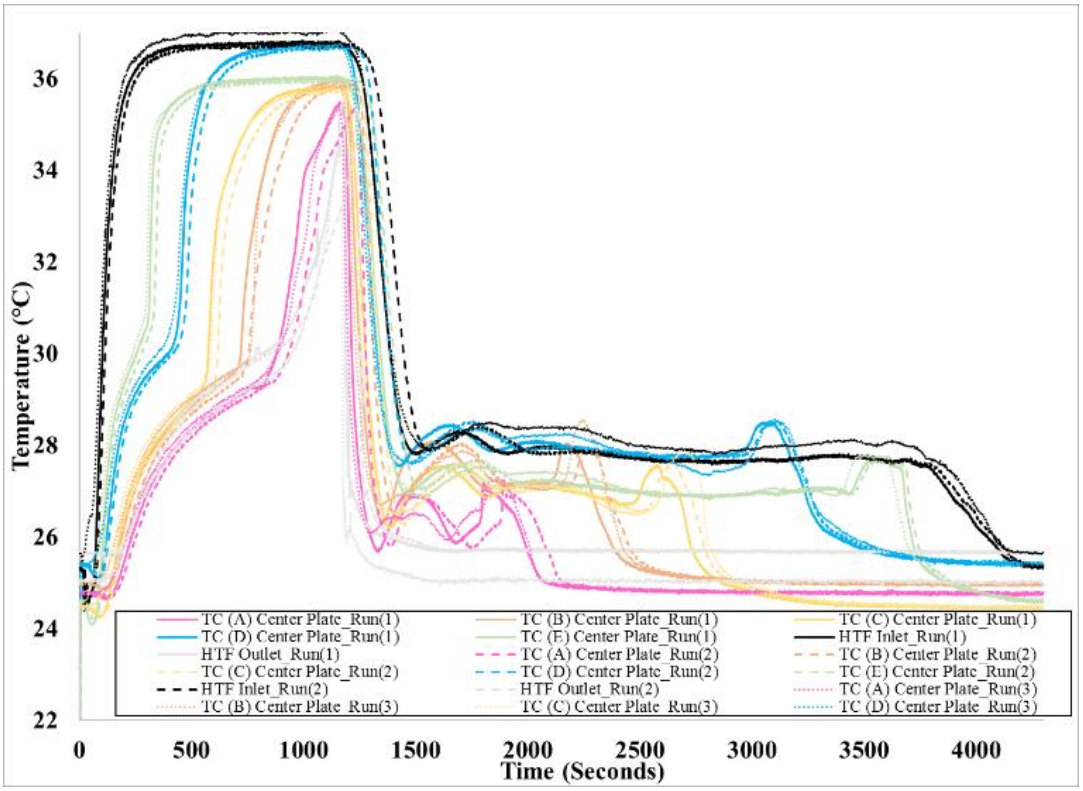

Figure 79: Temperature profiles recorded by thermocouples at the center plate during melting (90%) and solidification at a flow rate of 5 GPH (counter-current). Inlet temperature of HTF during melting is 37.4 °C and during solidification is 25 °C (Case J, Pre-experiment calibration).

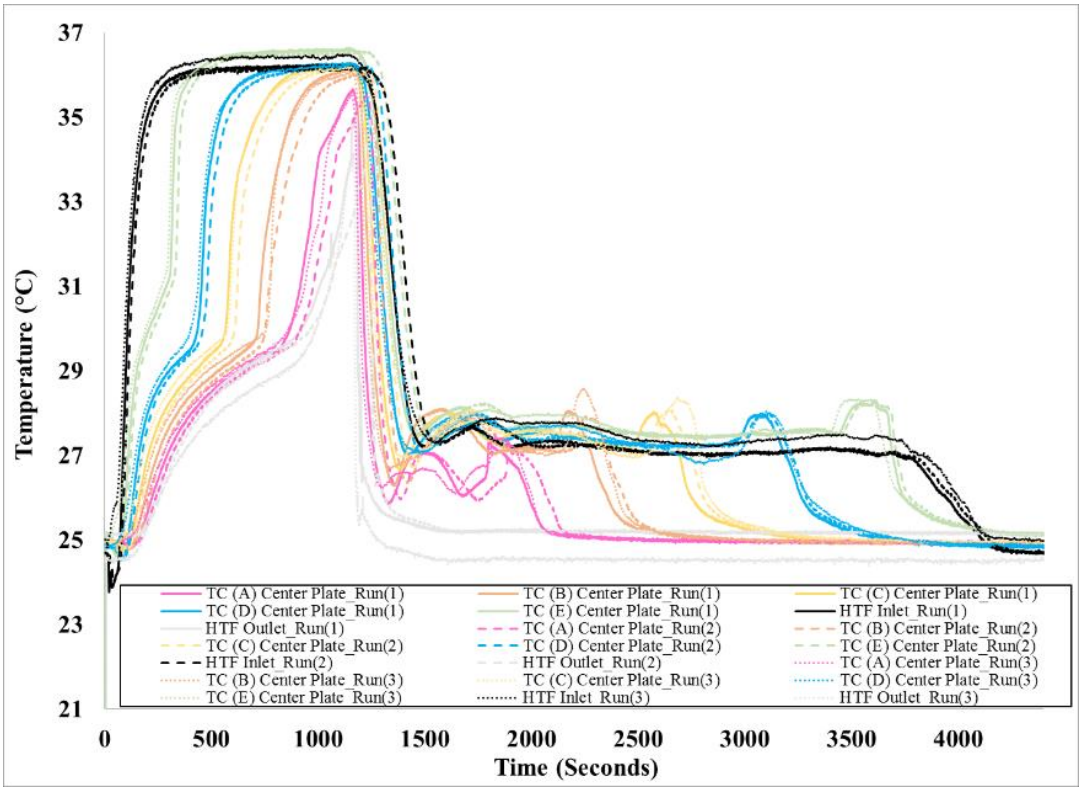

Figure 80: Temperature profiles recorded by thermocouples at the center plate during melting (90%) and solidification at a flow rate of 5 GPH (counter-current). Inlet temperature of HTF during melting is 37.4 °C and during solidification is 25 °C (Case J, Post-experiment calibration).

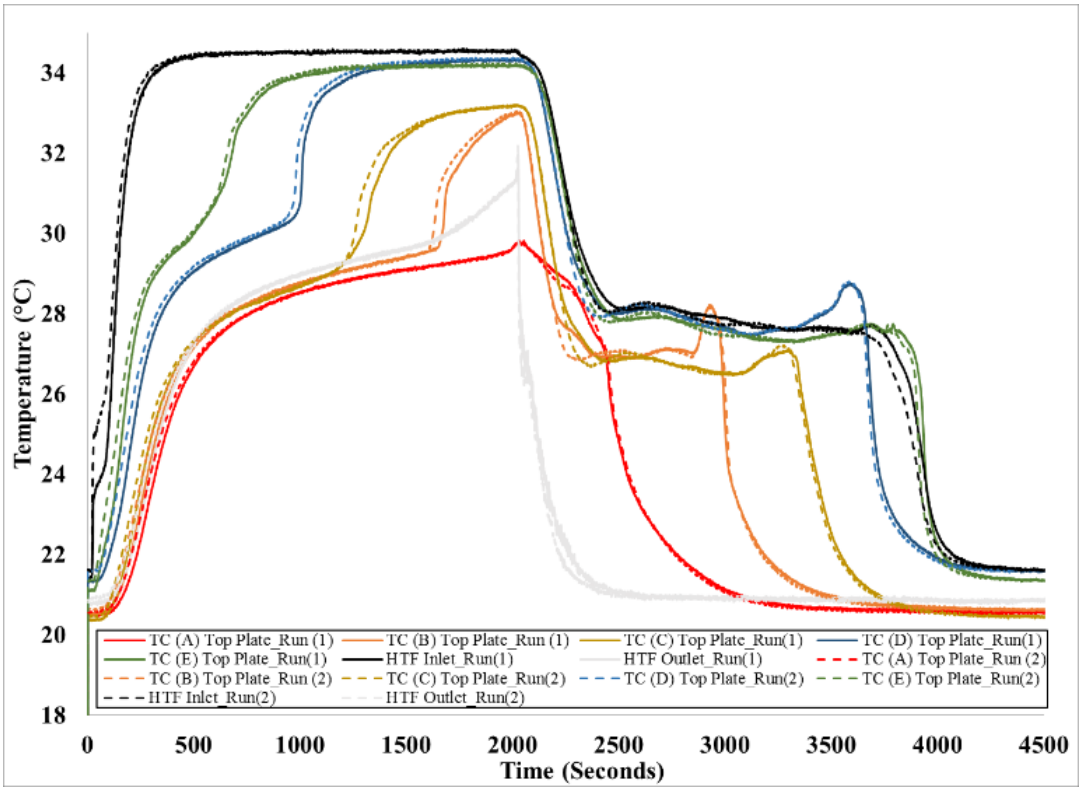

Figure 81: Temperature profiles recorded by thermocouples at the top plate during melting (90%) and solidification at a flow rate of 3 GPH (counter-current). Inlet temperature of HTF during melting is 35 °C and during solidification is 20 °C (Case K, Pre-experiment calibration).

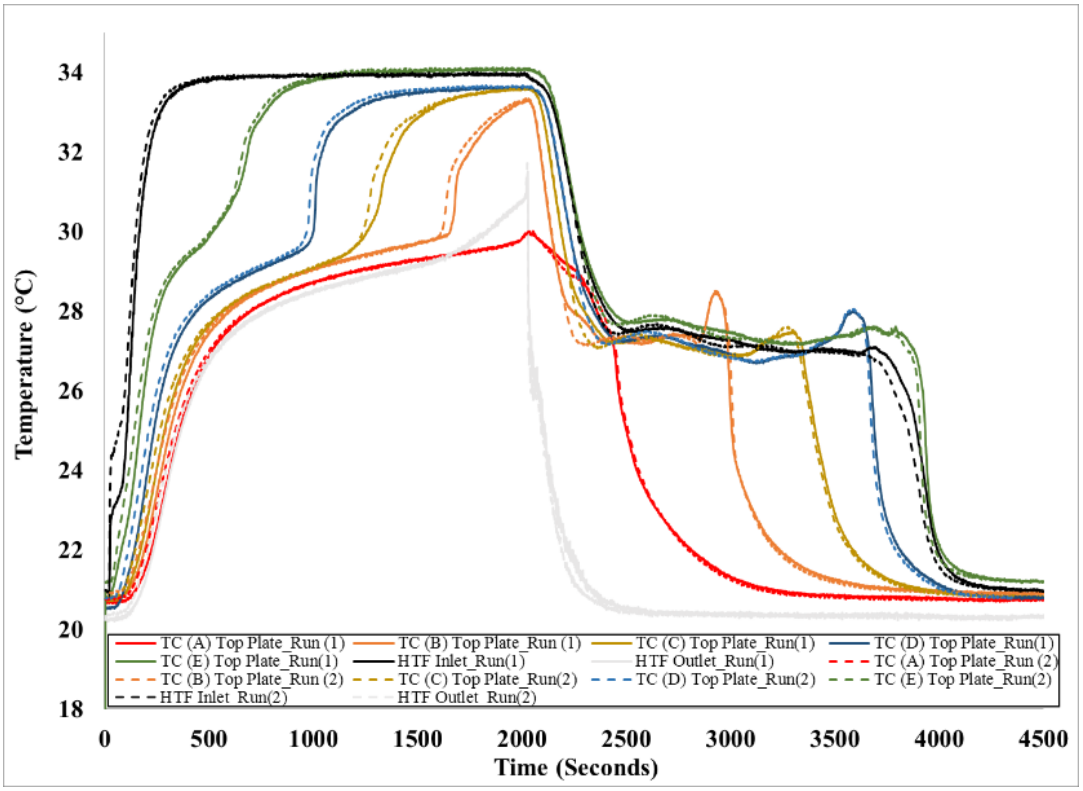

Figure 82: Temperature profiles recorded by thermocouples at the top plate during melting (90%) and solidification at a flow rate of 3 GPH (counter-current). Inlet temperature of HTF during melting is 35 °C and during solidification is 20 °C (Case K, Pre-experiment calibration).

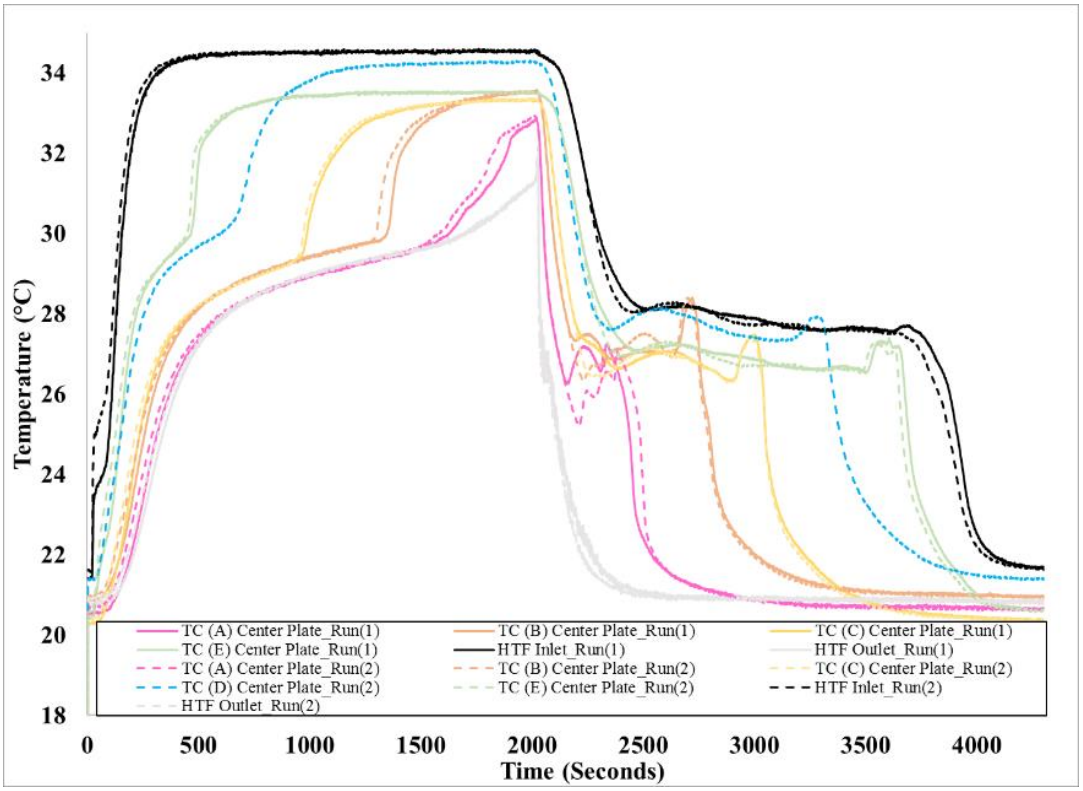

Figure 83: Temperature profiles recorded by thermocouples at the center plate during melting (90%) and solidification at a flow rate of 3 GPH (counter-current). Inlet temperature of HTF during melting is 35 °C and during solidification is 20 °C (Case K, Pre-experiment calibration).

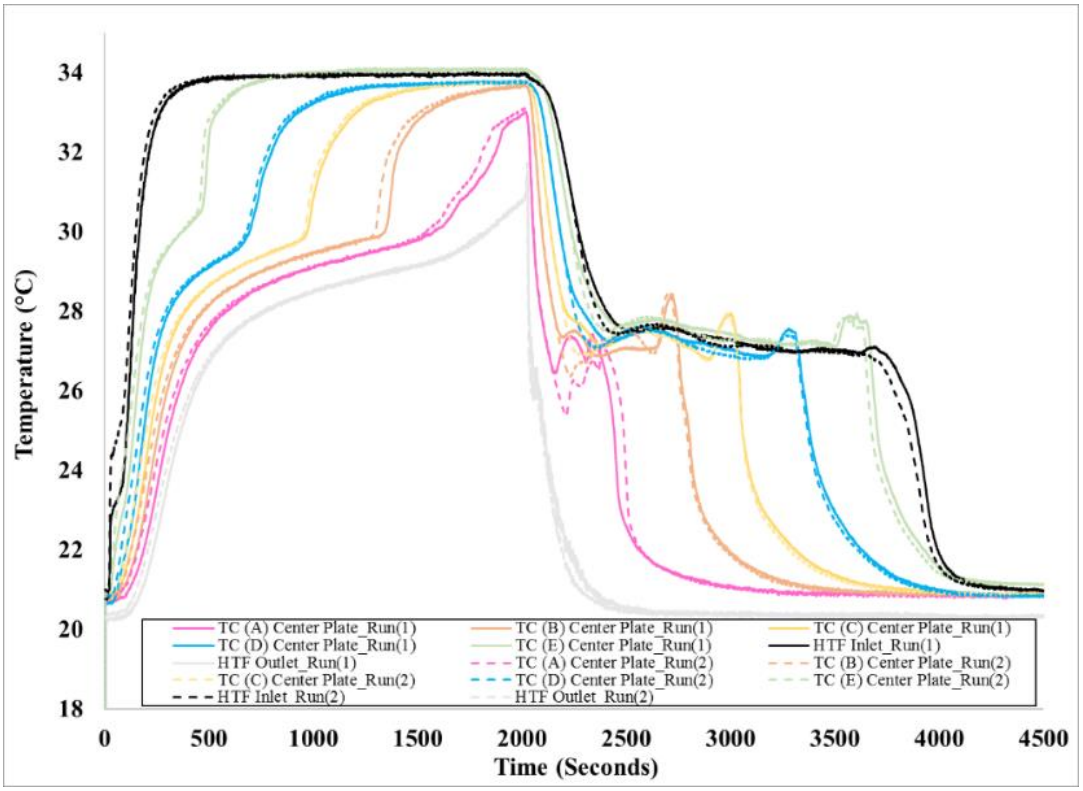

Figure 84: Temperature profiles recorded by thermocouples at the center plate during melting (90%) and solidification at a flow rate of 3 GPH (counter-current). Inlet temperature of HTF during melting is 35 °C and during solidification is 20 °C (Case K, Post-experiment calibration).

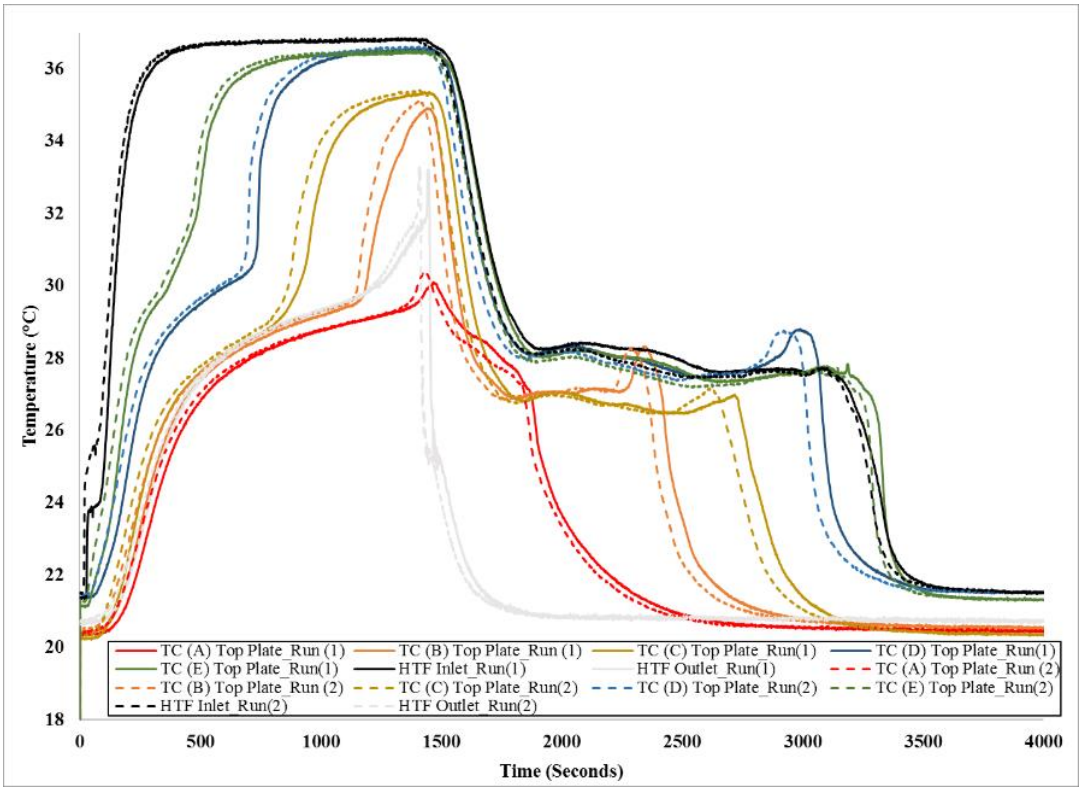

Figure 85: Temperature profiles recorded by thermocouples at the top plate during melting (90%) and solidification at a flow rate of 3 GPH (counter-current). Inlet temperature of HTF during melting is 37.4 °C and during solidification is 20 °C (Case L, Pre-experiment calibration).

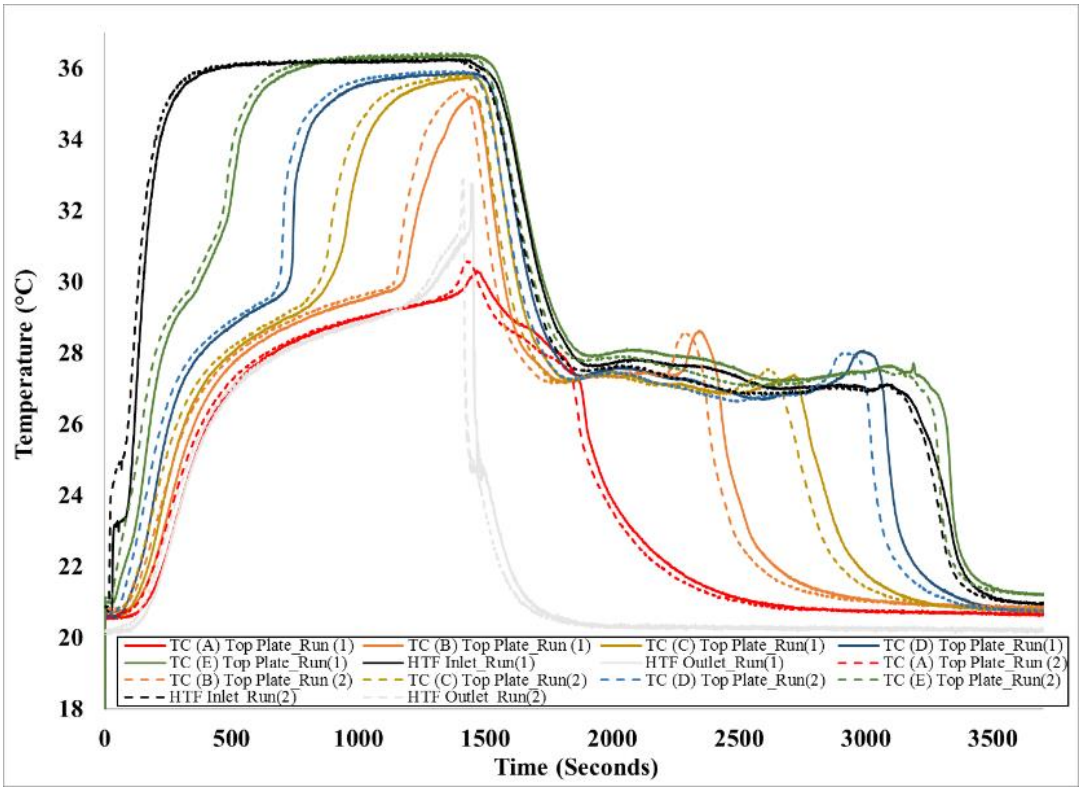

Figure 86: Temperature profiles recorded by thermocouples at the top plate during melting (90%) and solidification at a flow rate of 3 GPH (counter-current). Inlet temperature of HTF during melting is 37.4 °C and during solidification is 20 °C (Case L, Post-experiment calibration).

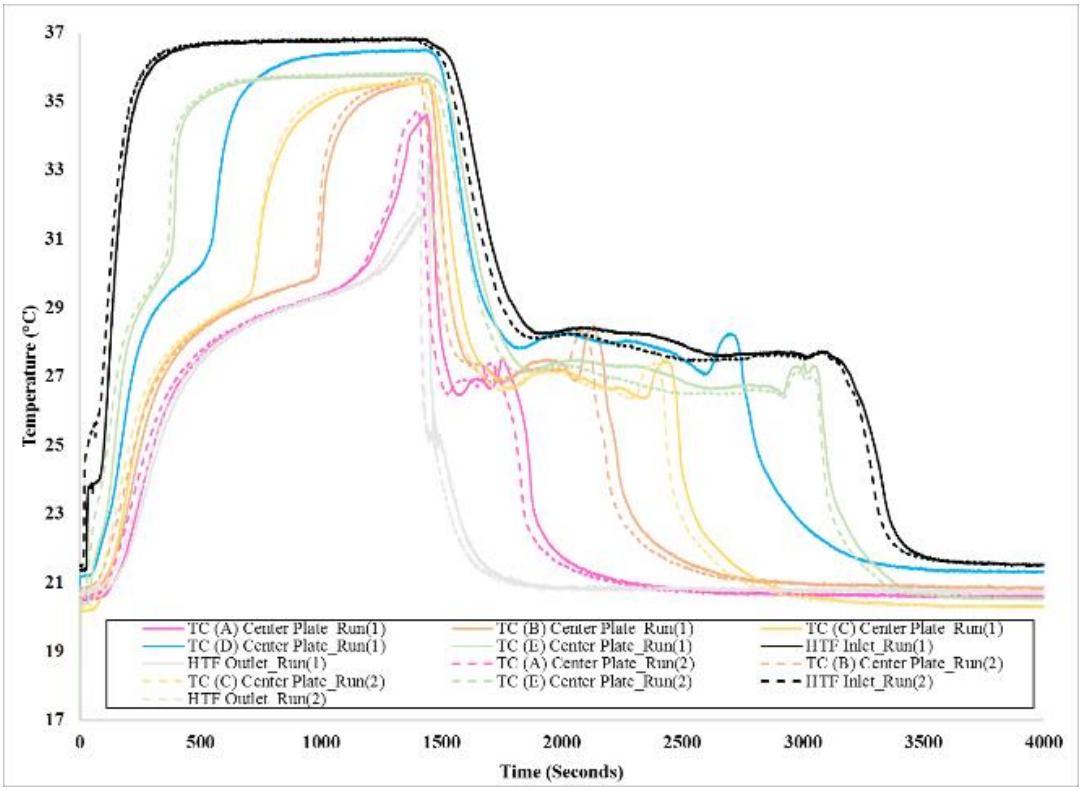

Figure 87: Temperature profiles recorded by thermocouples at the center plate during melting (90%) and solidification at a flow rate of 3 GPH (counter-current). Inlet temperature of HTF during melting is 37.4 °C and during solidification is 20 °C (Case L, Pre-experiment calibration).

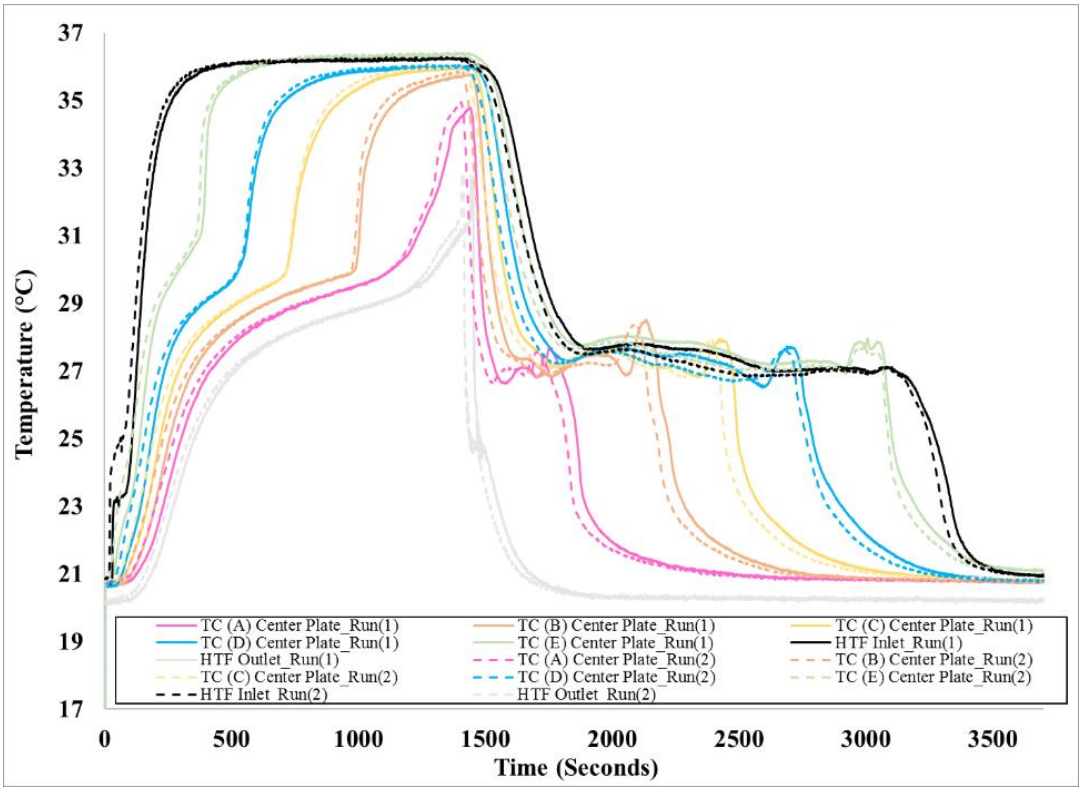

Figure 88: Temperature profiles recorded by thermocouples at the center plate during melting (90%) and solidification at a flow rate of 3 GPH (counter-current). Inlet temperature of HTF during melting is 37.4 °C and during solidification is 20 °C (Case L, Post-experiment calibration).

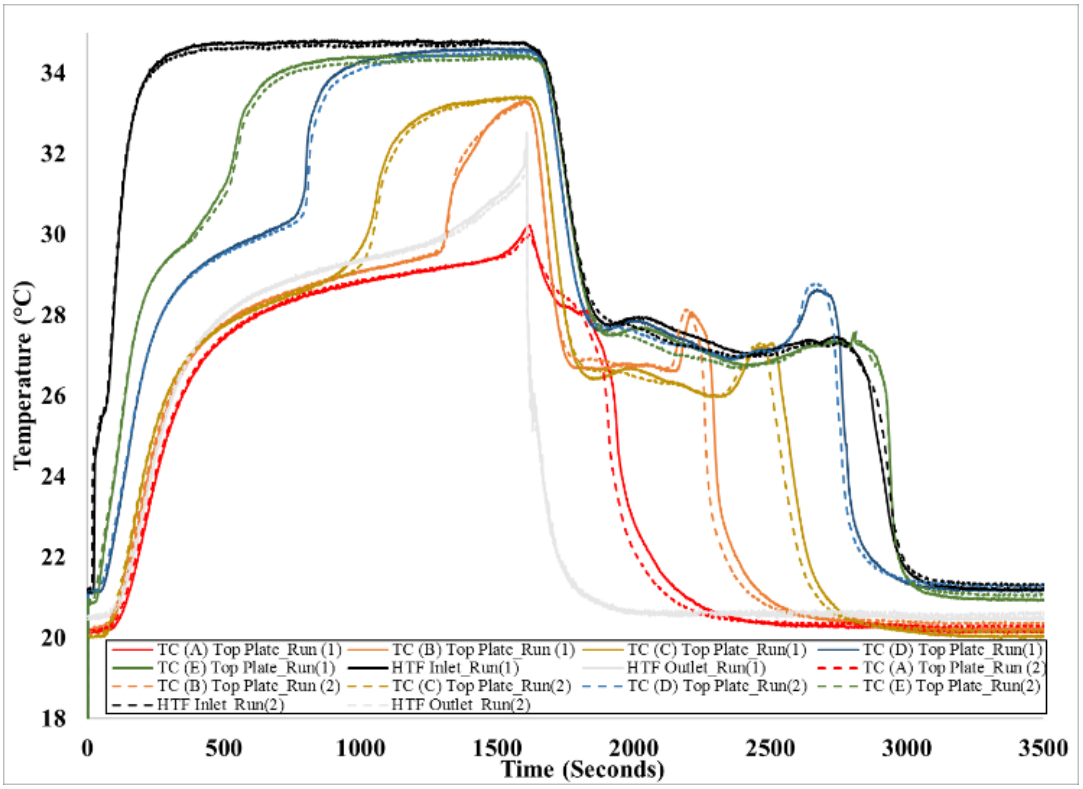

Figure 89: Temperature profiles recorded by thermocouples at the top plate during melting (90%) and solidification at a flow rate of 5 GPH (counter-current). Inlet temperature of HTF during melting is 35 °C and during solidification is 20 °C (Case M, Pre-experiment calibration).

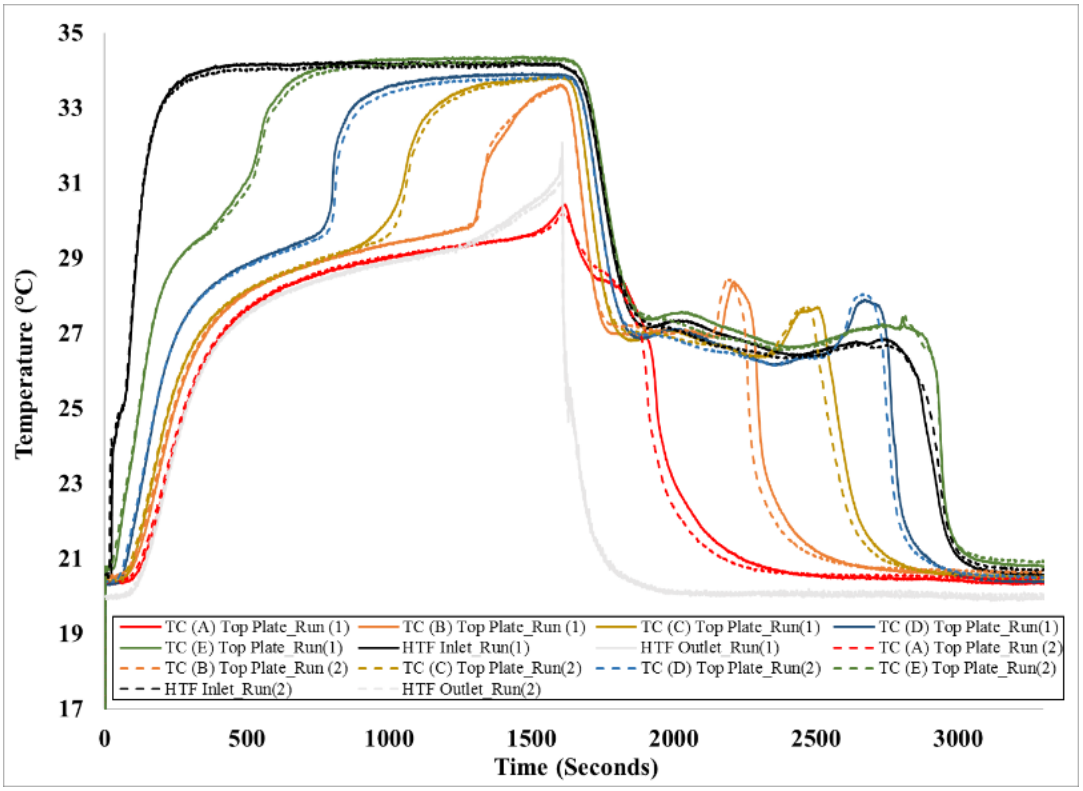

Figure 90: Temperature profiles recorded by thermocouples at the top plate during melting (90%) and solidification at a flow rate of 5 GPH (counter-current). Inlet temperature of HTF during melting is 35 °C and during solidification is 20 °C (Case M, Post-experiment calibration).

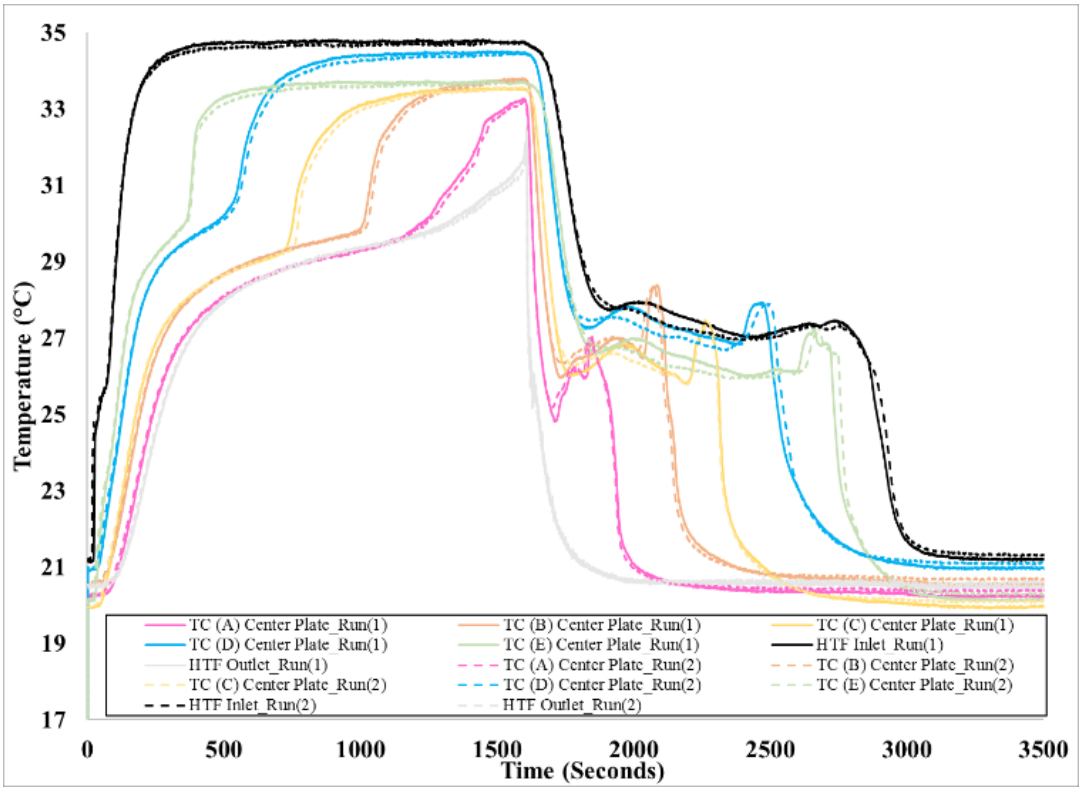

Figure 91: Temperature profiles recorded by thermocouples at the center plate during melting (90%) and solidification at a flow rate of 5 GPH (counter-current). Inlet temperature of HTF during melting is 35 °C and during solidification is 20 °C (Case M, Pre-experiment calibration).

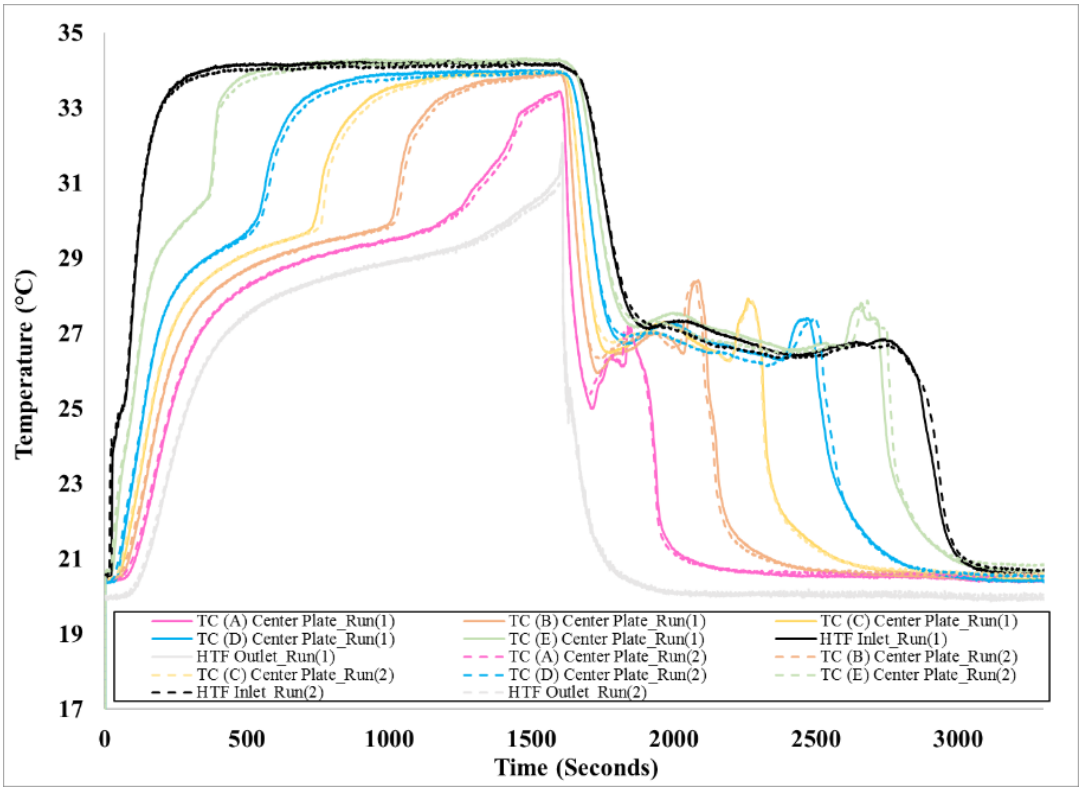

Figure 92: Temperature profiles recorded by thermocouples at the center plate during melting (90%) and solidification at a flow rate of 5 GPH (counter-current). Inlet temperature of HTF during melting is 35 °C and during solidification is 20 °C (Case M, Post-experiment calibration).

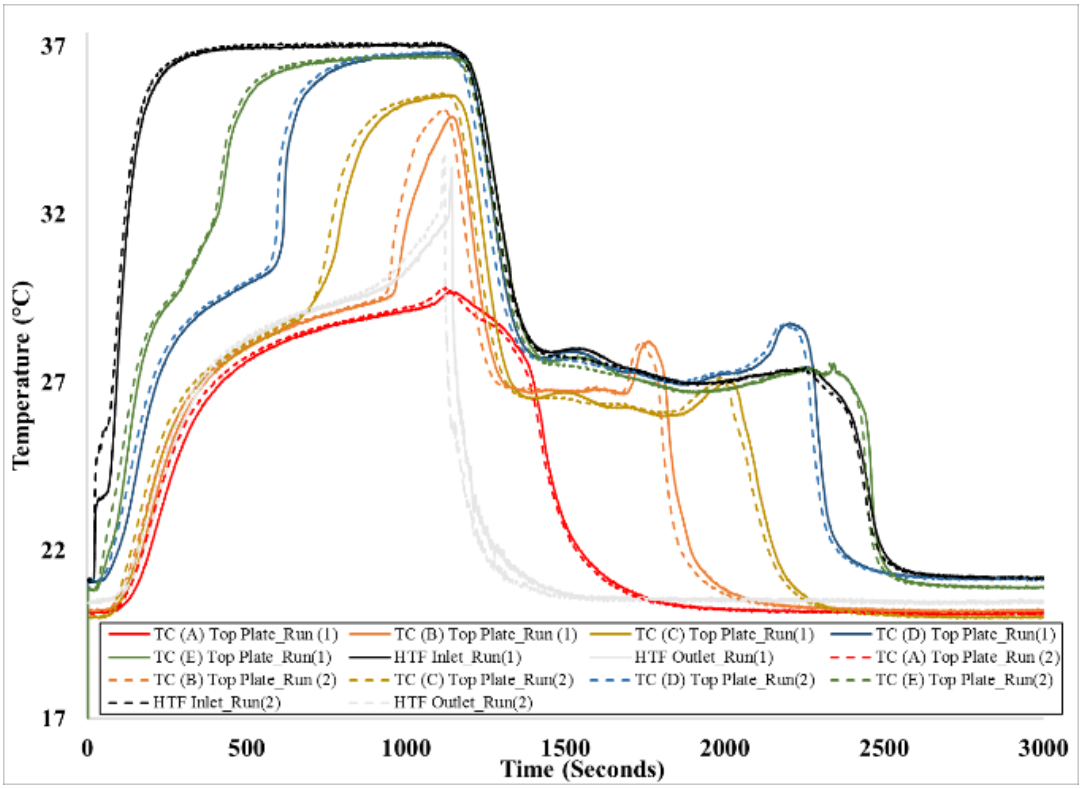

Figure 93: Temperature profiles recorded by thermocouples at the top plate during melting (90%) and solidification at a flow rate of 5 GPH (counter-current). Inlet temperature of HTF during melting is 37.4 °C and during solidification is 20 °C (Case N, Pre-experiment calibration).

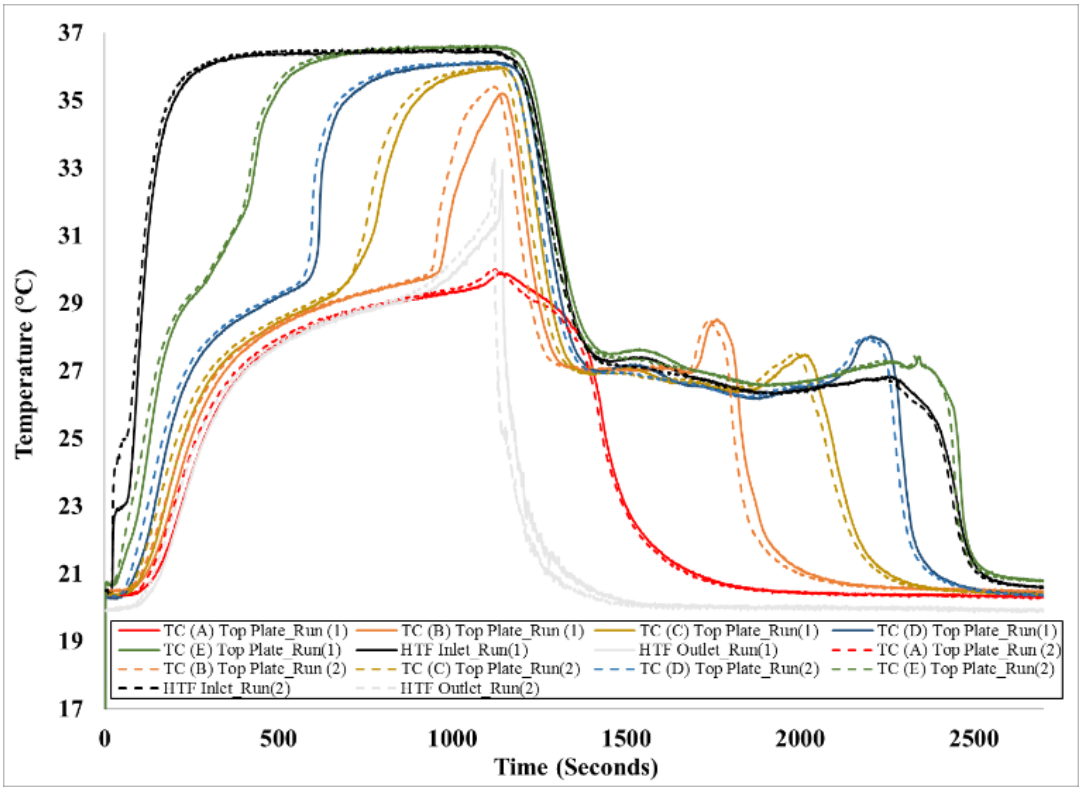

Figure 94: Temperature profiles recorded by thermocouples at the center plate during melting (90%) and solidification at a flow rate of 5 GPH (counter-current). Inlet temperature of HTF during melting is 37.4 °C and during solidification is 20 °C (Case N, Post-experiment calibration).

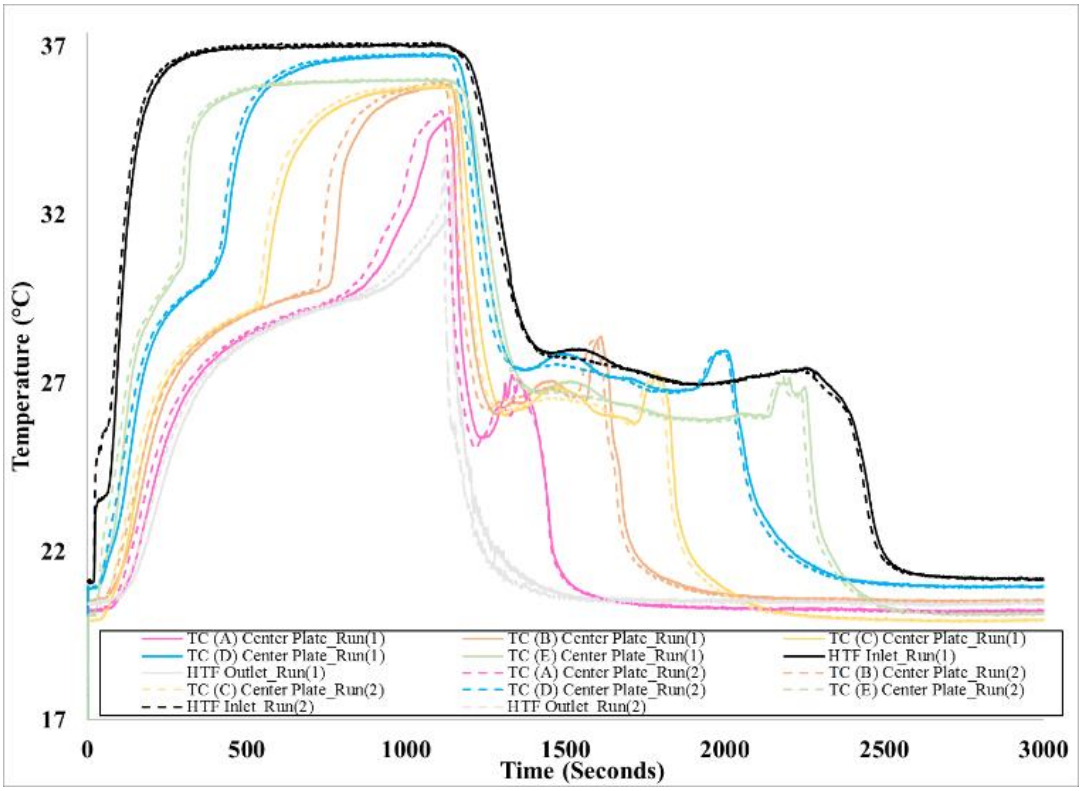

Figure 95: Temperature profiles recorded by thermocouples at the top plate during melting (90%) and solidification at a flow rate of 5 GPH (counter-current). Inlet temperature of HTF during melting is 37.4 °C and during solidification is 20 °C (Case N, Pre-experiment calibration).

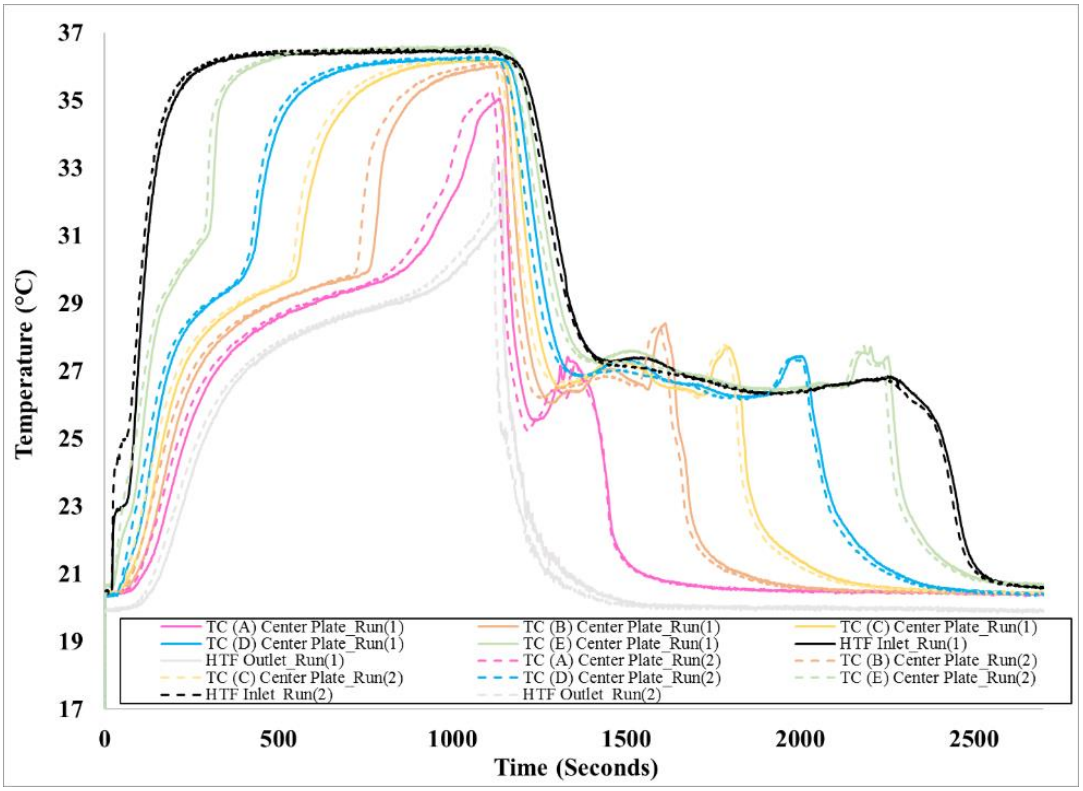

Figure 96: Temperature profiles recorded by thermocouples at the top plate during melting (90%) and solidification at a flow rate of 5 GPH (counter-current). Inlet temperature of HTF during melting is 37.4 °C and during solidification is 20 °C (Case N, Post-experiment calibration).

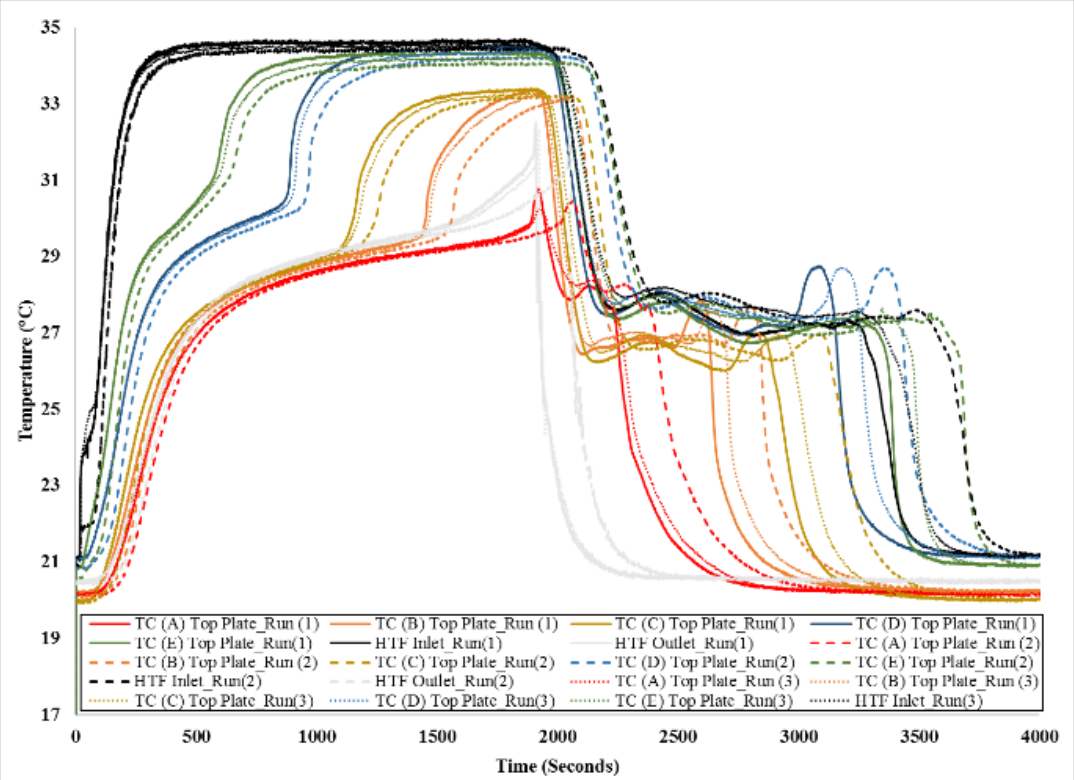

Figure 97: Temperature profiles recorded by thermocouples at the top plate during melting (90%) and solidification at a flow rate of 3 GPH (counter-current). Inlet temperature of HTF during melting is 35 °C and during solidification is 20 °C (Case O, Pre-experiment calibration, insulated).

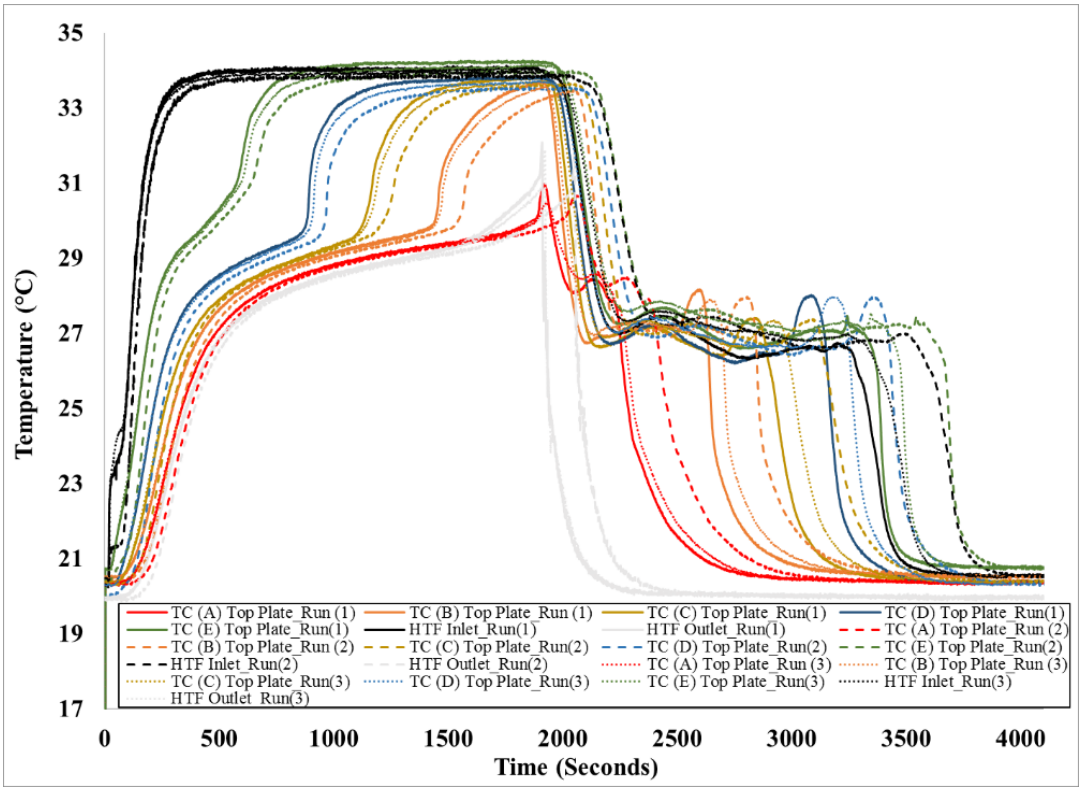

Figure 98: Temperature profiles recorded by thermocouples at the top plate during melting (90%) and solidification at a flow rate of 3 GPH (counter-current). Inlet temperature of HTF during melting is 35 °C and during solidification is 20 °C (Case O, Post-experiment calibration, insulated).

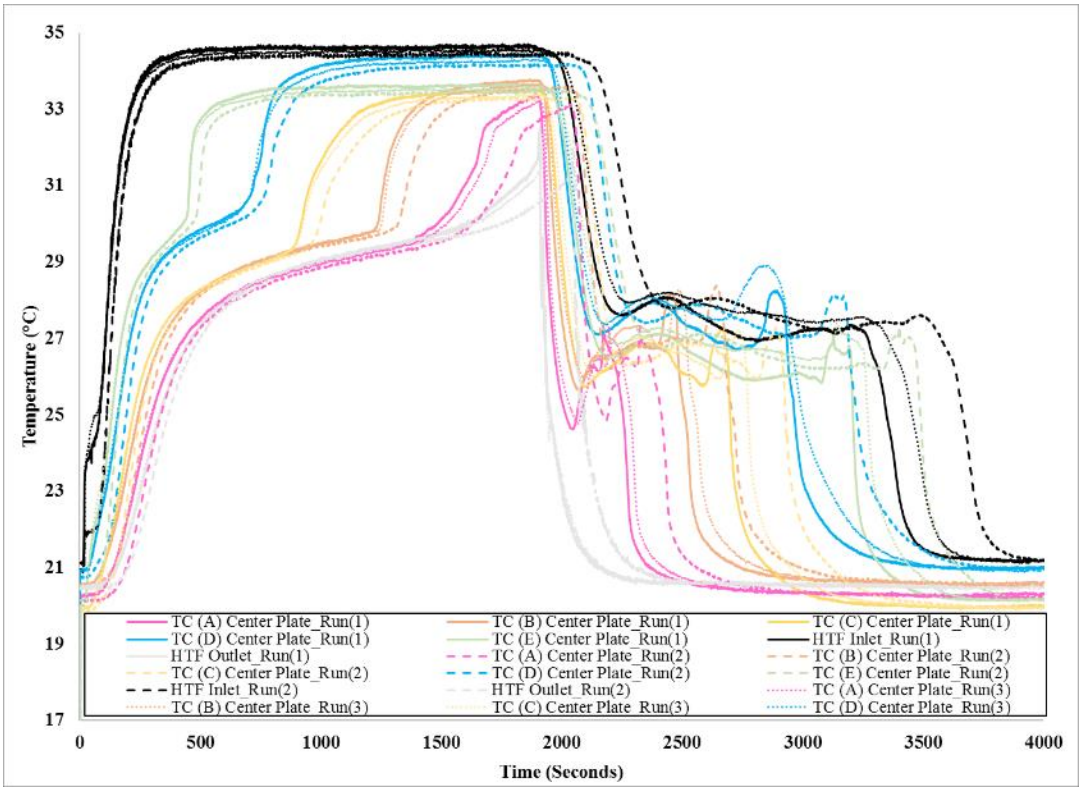

Figure 99: Temperature profiles recorded by thermocouples at the center plate during melting (90%) and solidification at a flow rate of 3 GPH (counter-current). Inlet temperature of HTF during melting is 35 °C and during solidification is 20 °C (Case O, Pre-experiment calibration, insulated).

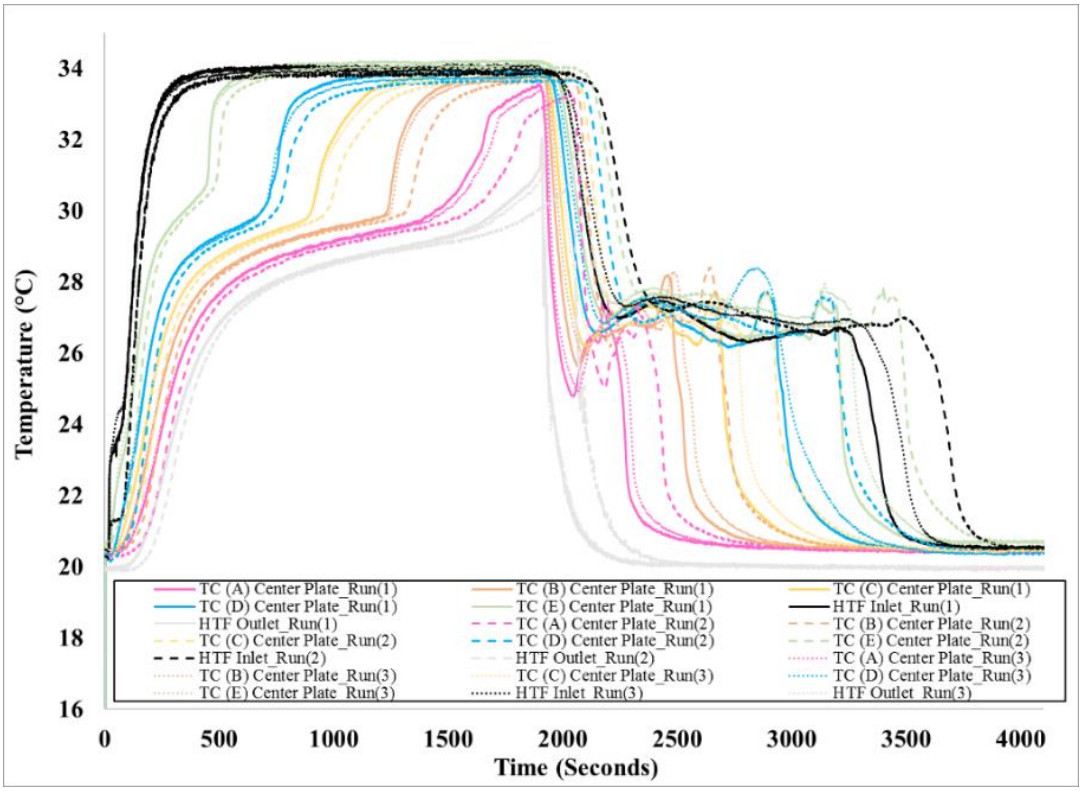

Figure 100: Temperature profiles recorded by thermocouples at the center plate during melting (90%) and solidification at a flow rate of 3 GPH (counter-current). Inlet temperature of HTF during melting is 35 °C and during solidification is 20 °C (Case O, Post-experiment calibration, insulated).

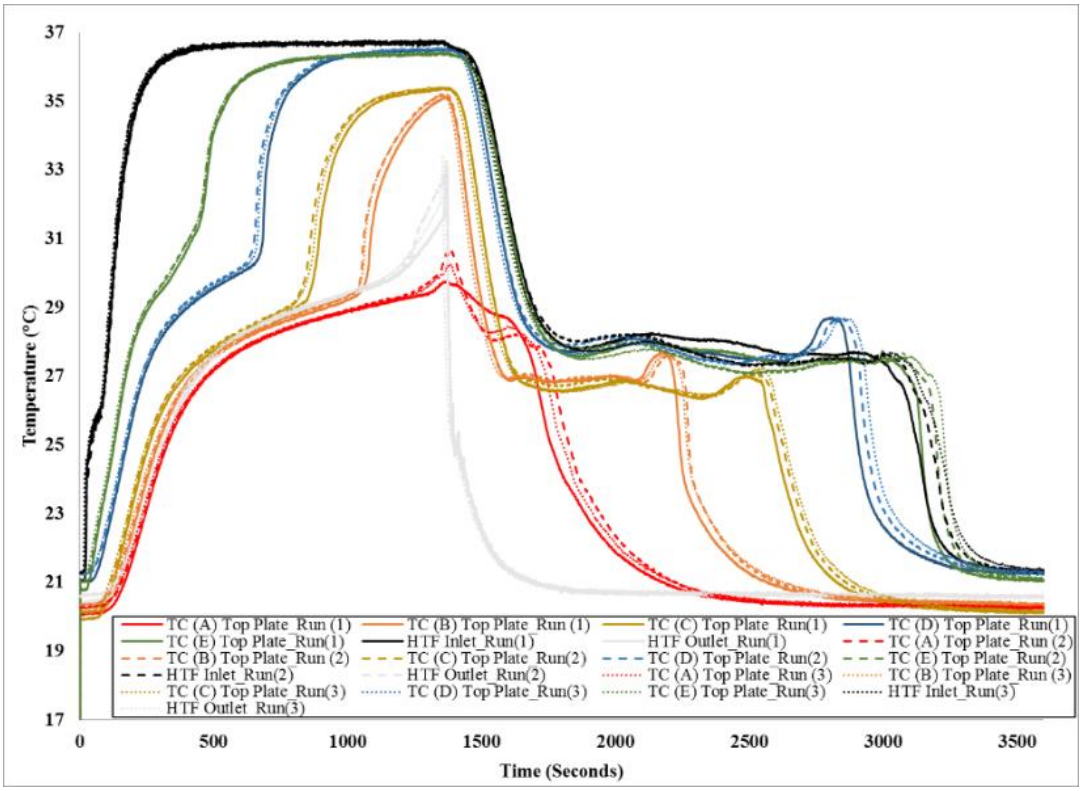

Figure 101: Temperature profiles recorded by thermocouples at the top plate during melting (90%) and solidification at a flow rate of 3 GPH (counter-current). Inlet temperature of HTF during melting is 37.4 °C and during solidification is 20 °C (Case P, Pre-experiment calibration, insulated).

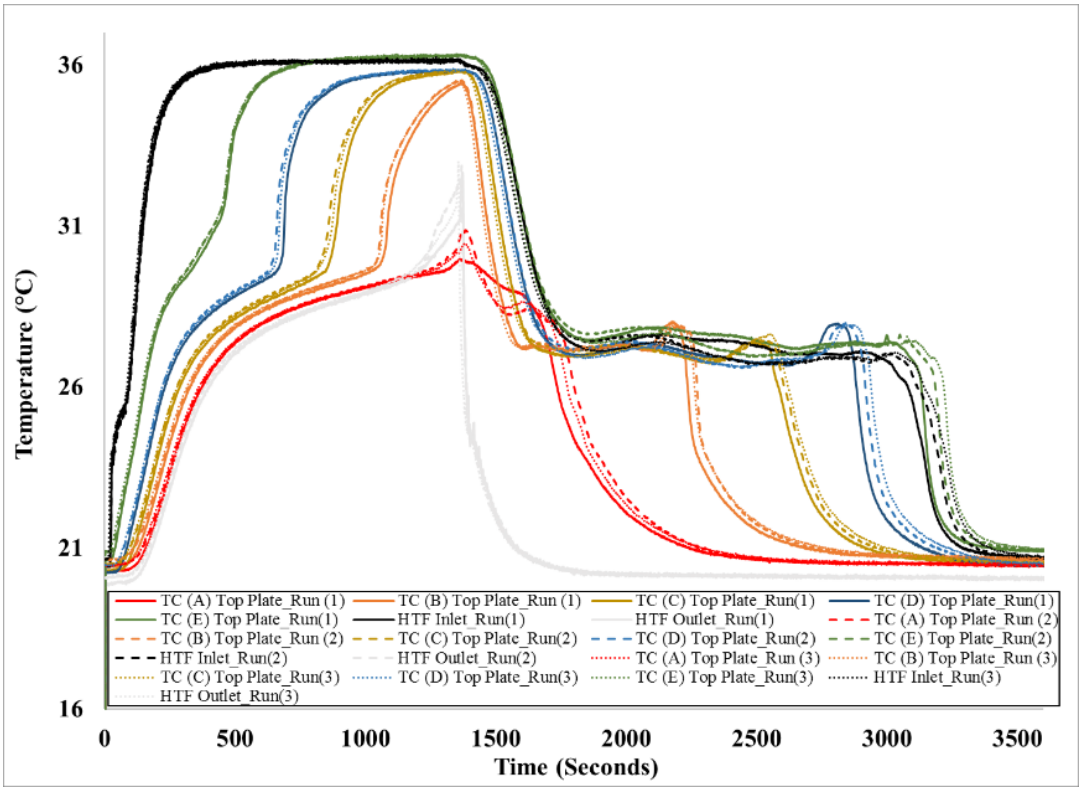

Figure 102: Temperature profiles recorded by thermocouples at the top plate during melting (90%) and solidification at a flow rate of 3 GPH (counter-current). Inlet temperature of HTF during melting is 37.4 °C and during solidification is 20 °C (Case P, Post-experiment calibration, insulated).

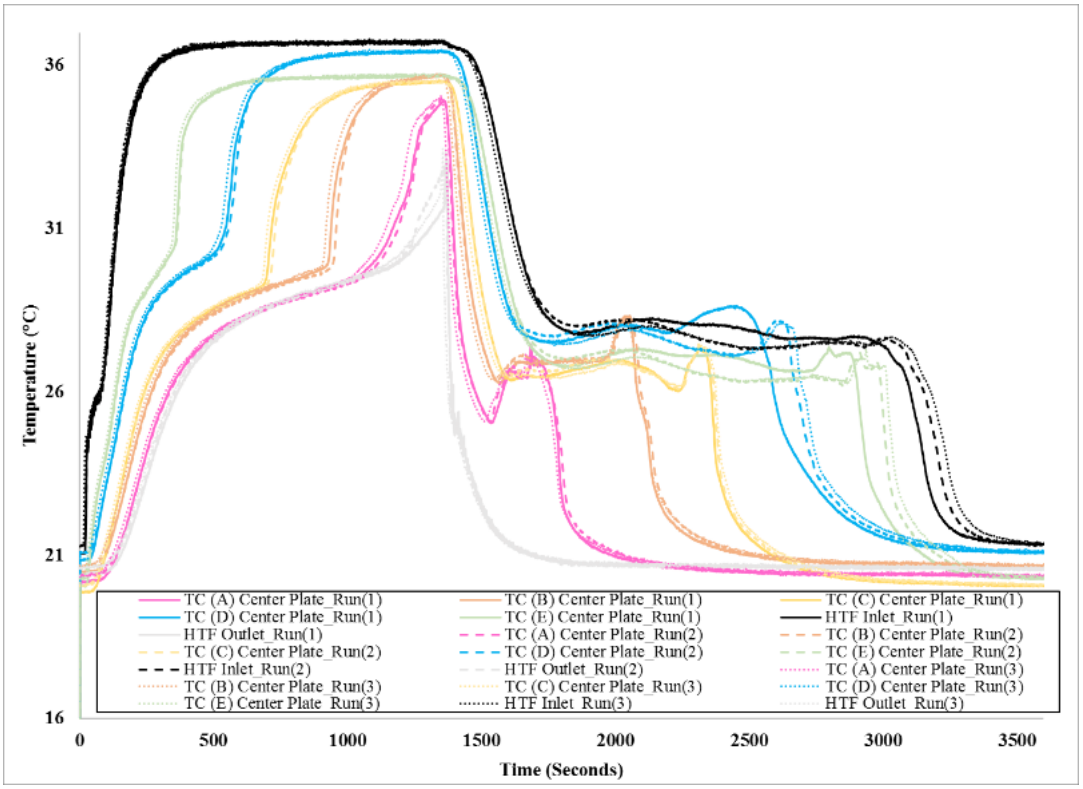

Figure 103: Temperature profiles recorded by thermocouples at the center plate during melting (90%) and solidification at a flow rate of 3 GPH (counter-current). Inlet temperature of HTF during melting is 37.4 °C and during solidification is 20 °C (Case P, Pre-experiment calibration, insulated).

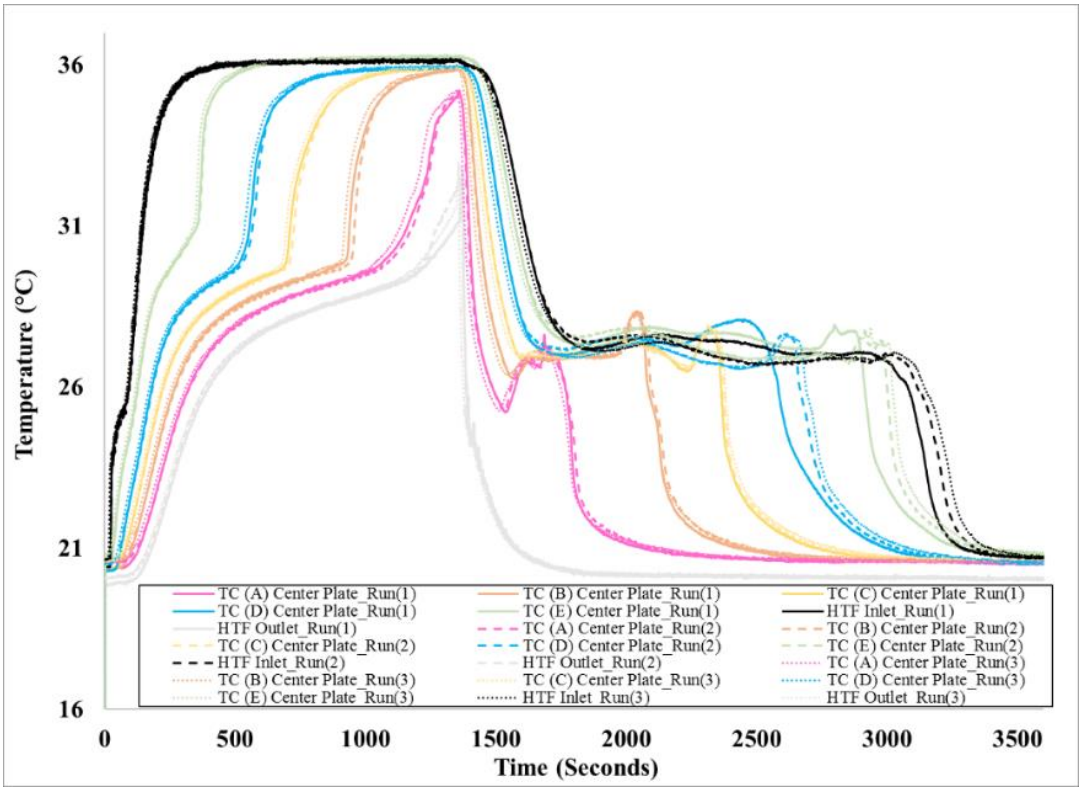

Figure 104: Temperature profiles recorded by thermocouples at the center plate during melting (90%) and solidification at a flow rate of 3 GPH (counter-current). Inlet temperature of HTF during melting is 37.4 °C and during solidification is 20 °C (Case P, Post-experiment calibration, insulated).

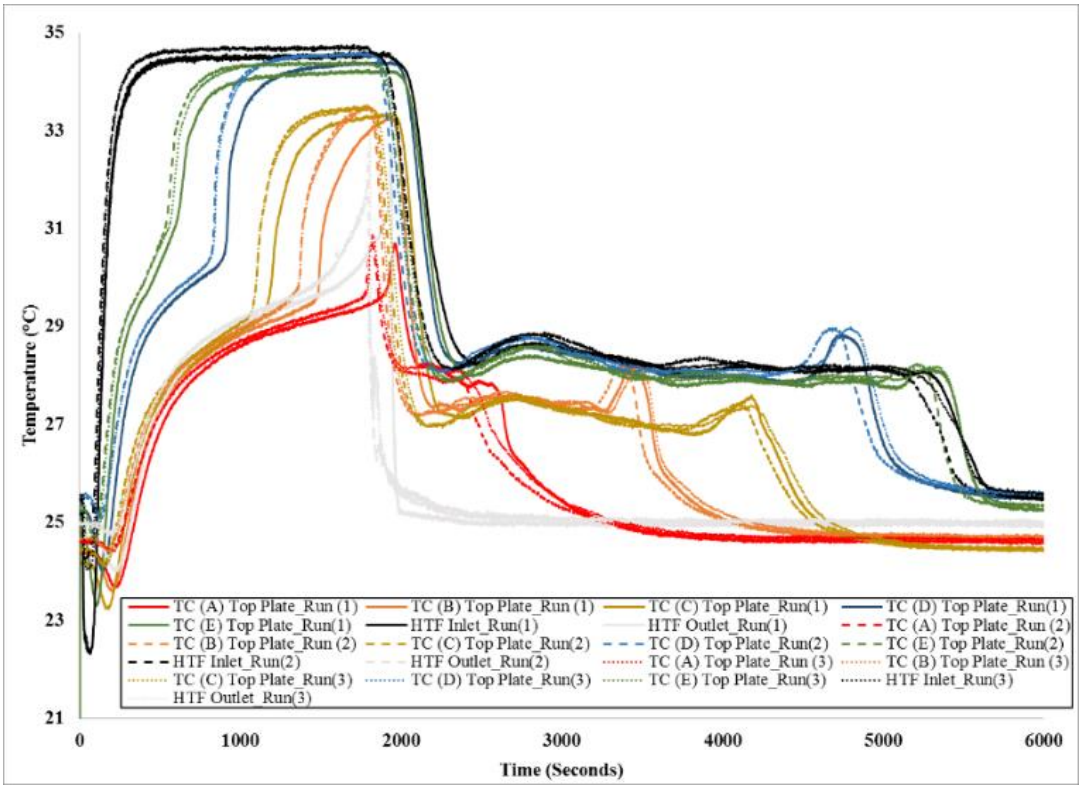

Figure 105: Temperature profiles recorded by thermocouples at the top plate during melting (90%) and solidification at a flow rate of 3 GPH (counter-current). Inlet temperature of HTF during melting is 35 °C and during solidification is 25 °C (Case Q, Pre-experiment calibration, insulated).

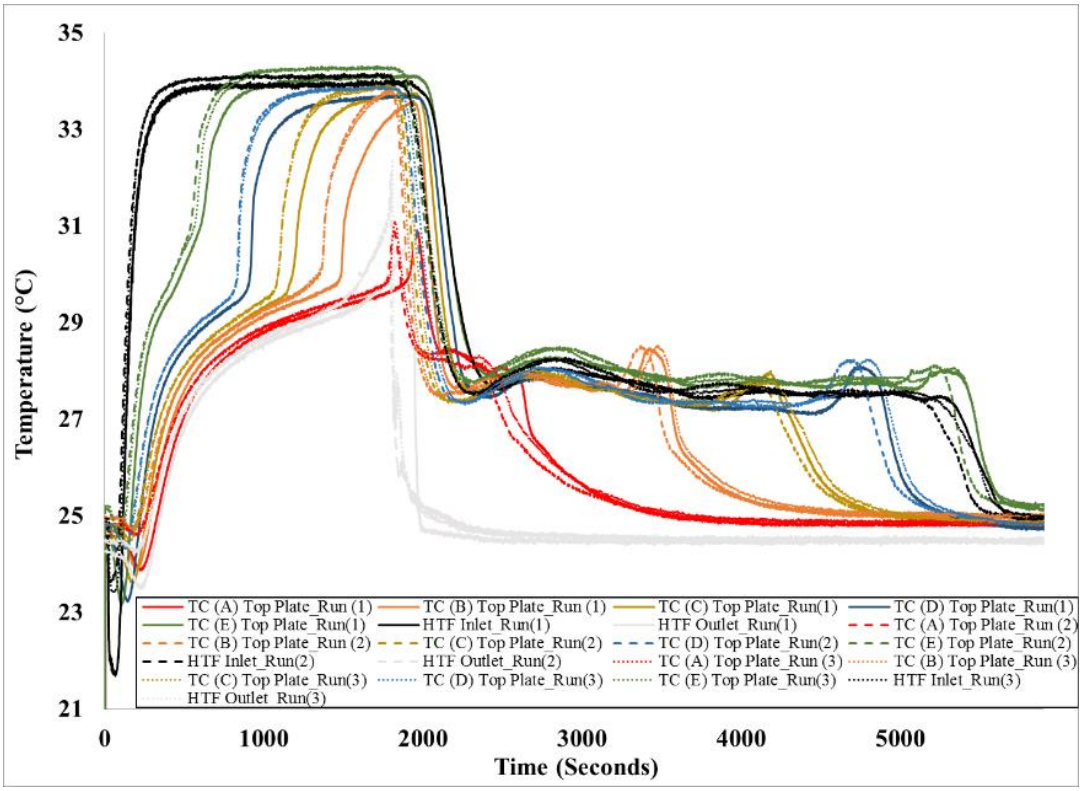

Figure 106: Temperature profiles recorded by thermocouples at the top plate during melting (90%) and solidification at a flow rate of 3 GPH (counter-current). Inlet temperature of HTF during melting is 35 °C and during solidification is 25 °C (Case Q, Post-experiment calibration, insulated).

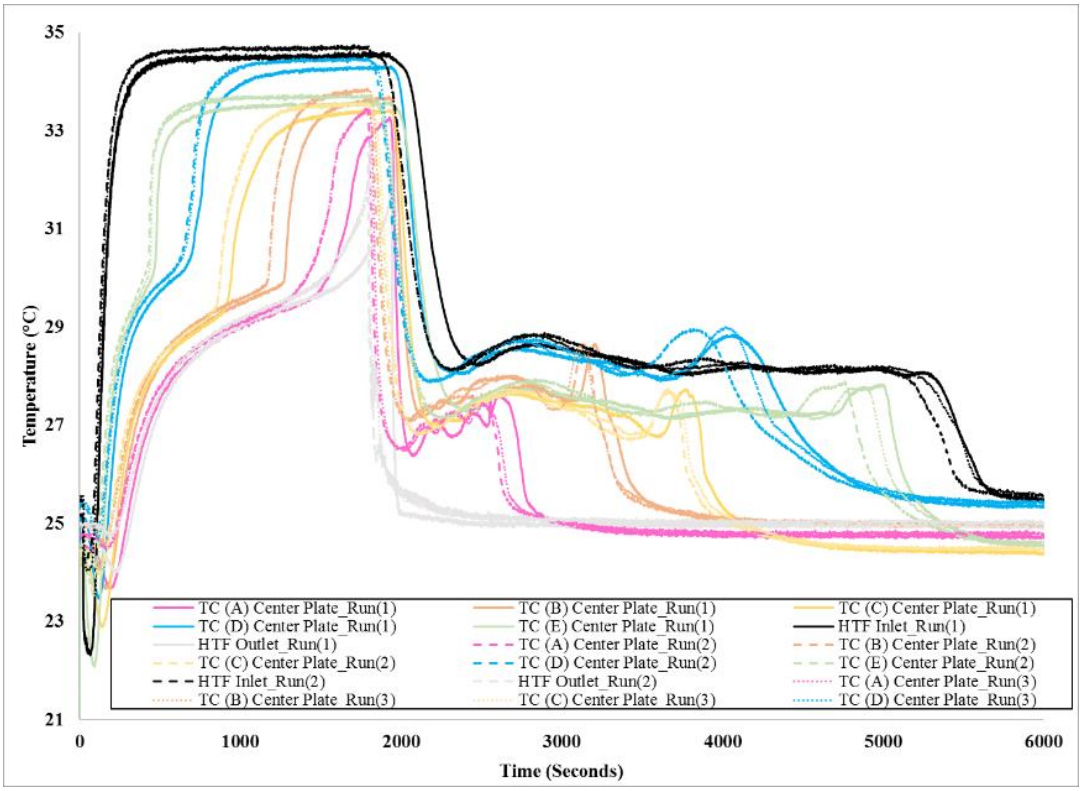

Figure 107: Temperature profiles recorded by thermocouples at the center plate during melting (90%) and solidification at a flow rate of 3 GPH (counter-current). Inlet temperature of HTF during melting is 35 °C and during solidification is 25 °C (Case Q, Pre-experiment calibration, insulated).

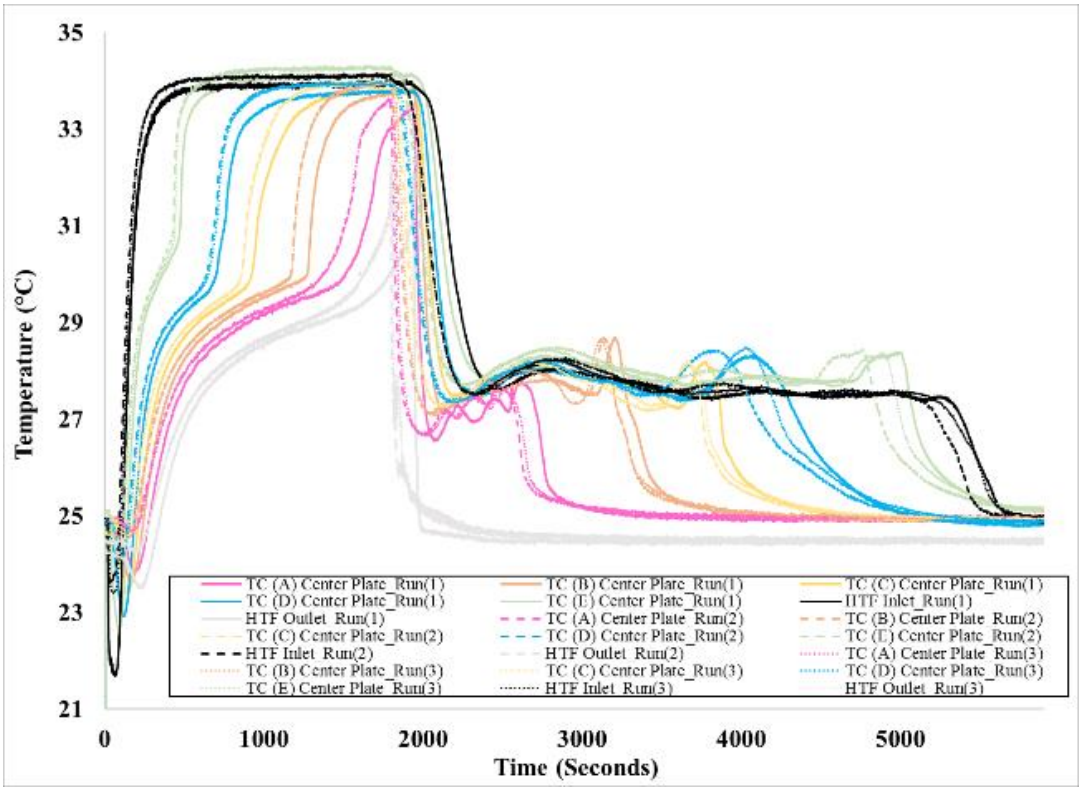

Figure 108: Temperature profiles recorded by thermocouples at the center plate during melting (90%) and solidification at a flow rate of 3 GPH (counter-current). Inlet temperature of HTF during melting is 35 °C and during solidification is 25 °C (Case Q, Post-experiment calibration, insulated).

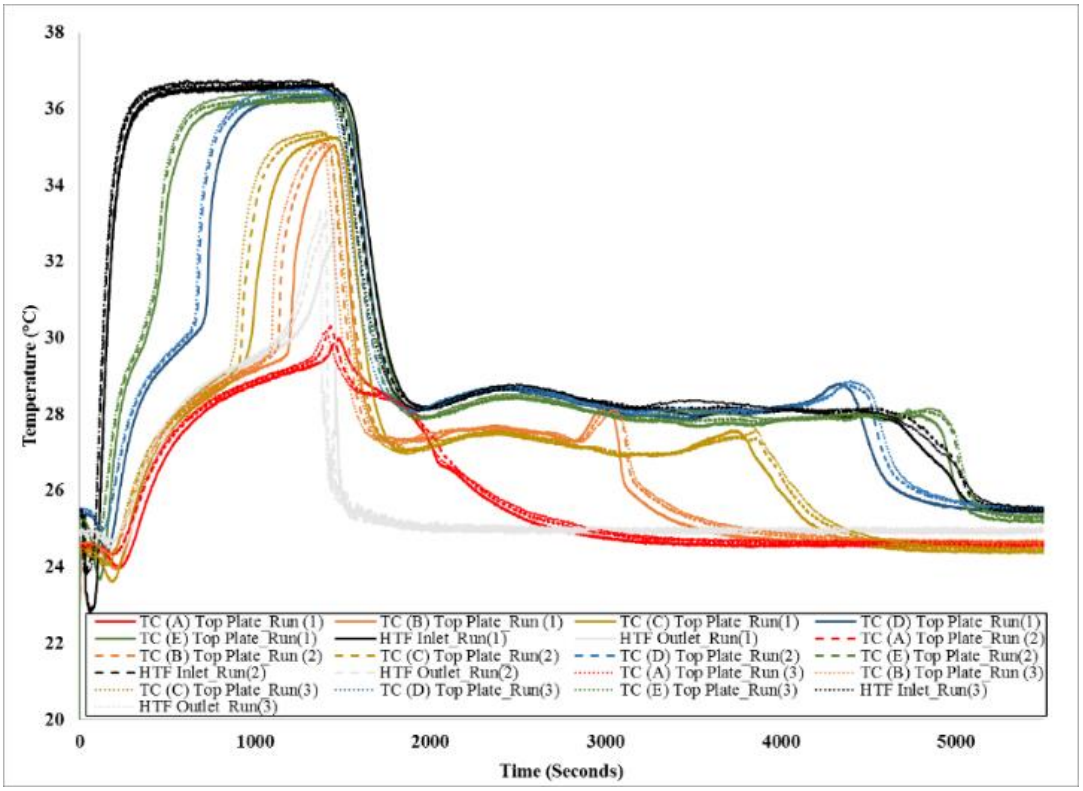

Figure 109: Temperature profiles recorded by thermocouples at the top plate during melting (90%) and solidification at a flow rate of 3 GPH (counter-current). Inlet temperature of HTF during melting is 37.4 °C and during solidification is 25 °C (Case R, Pre-experiment calibration, insulated).

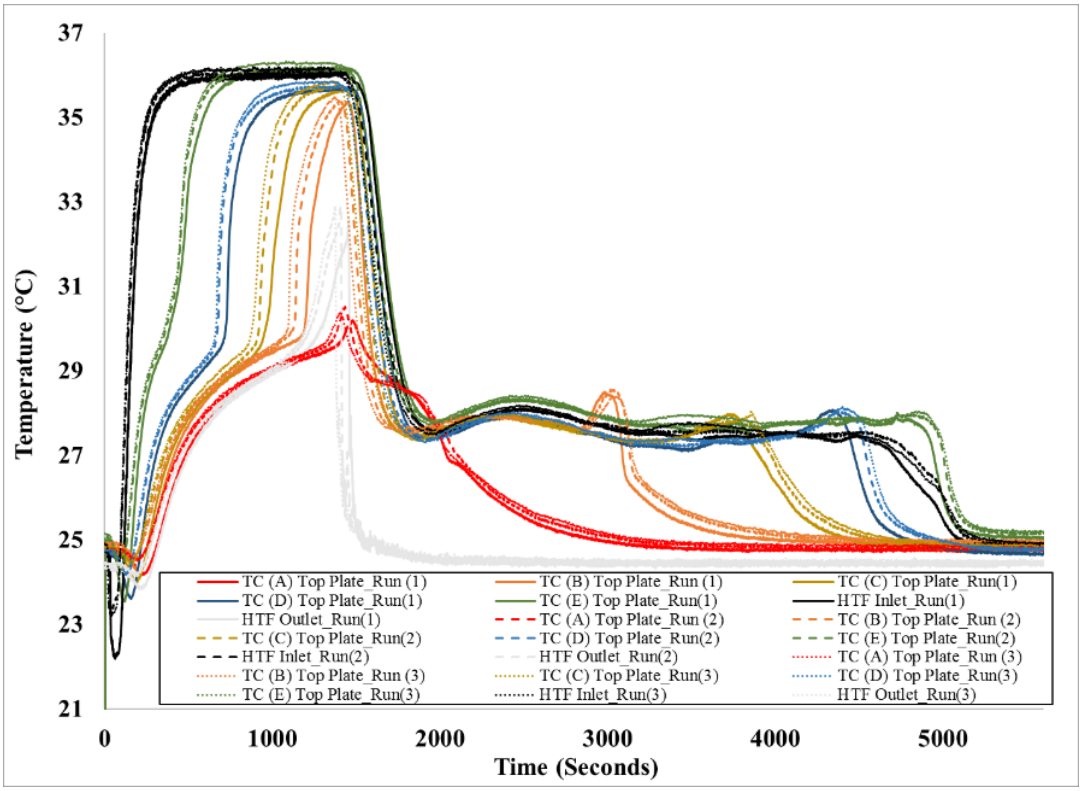

Figure 110: Temperature profiles recorded by thermocouples at the top plate during melting (90%) and solidification at a flow rate of 3 GPH (counter-current). Inlet temperature of HTF during melting is 37.4 °C and during solidification is 25 °C (Case R, Post-experiment calibration, insulated).

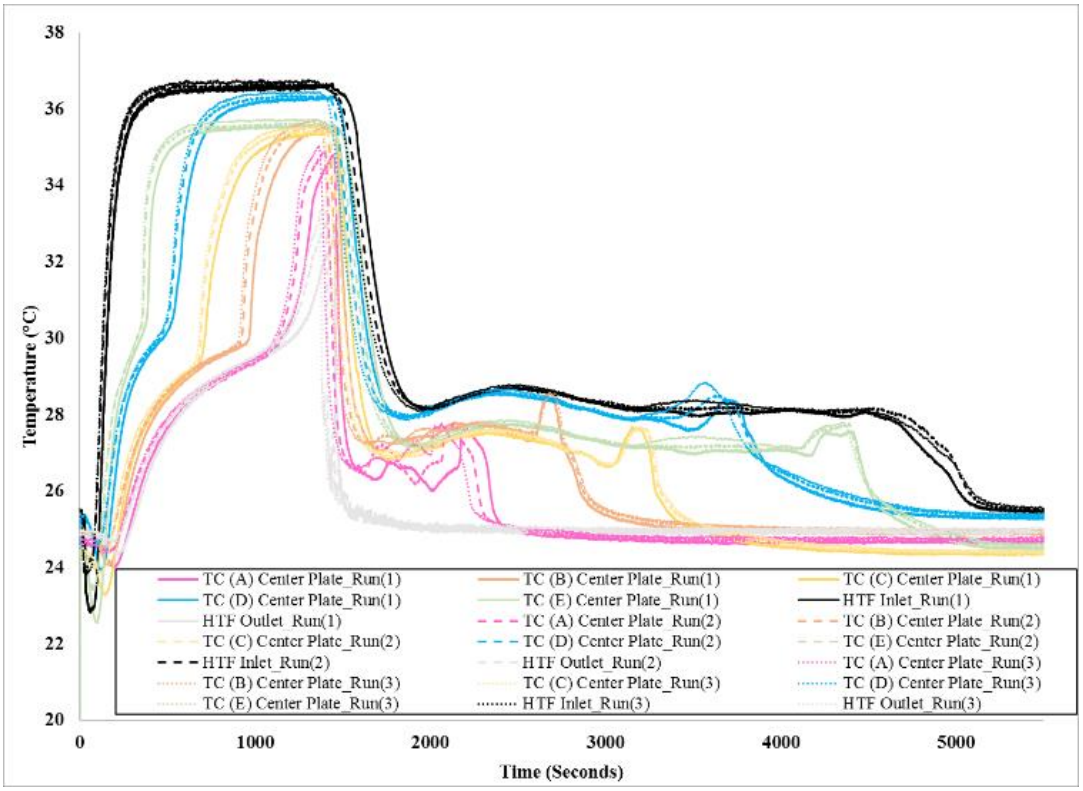

Figure 111: Temperature profiles recorded by thermocouples at the center plate during melting (90%) and solidification at a flow rate of 3 GPH (counter-current). Inlet temperature of HTF during melting is 37.4 °C and during solidification is 25 °C (Case R, Pre-experiment calibration, insulated).

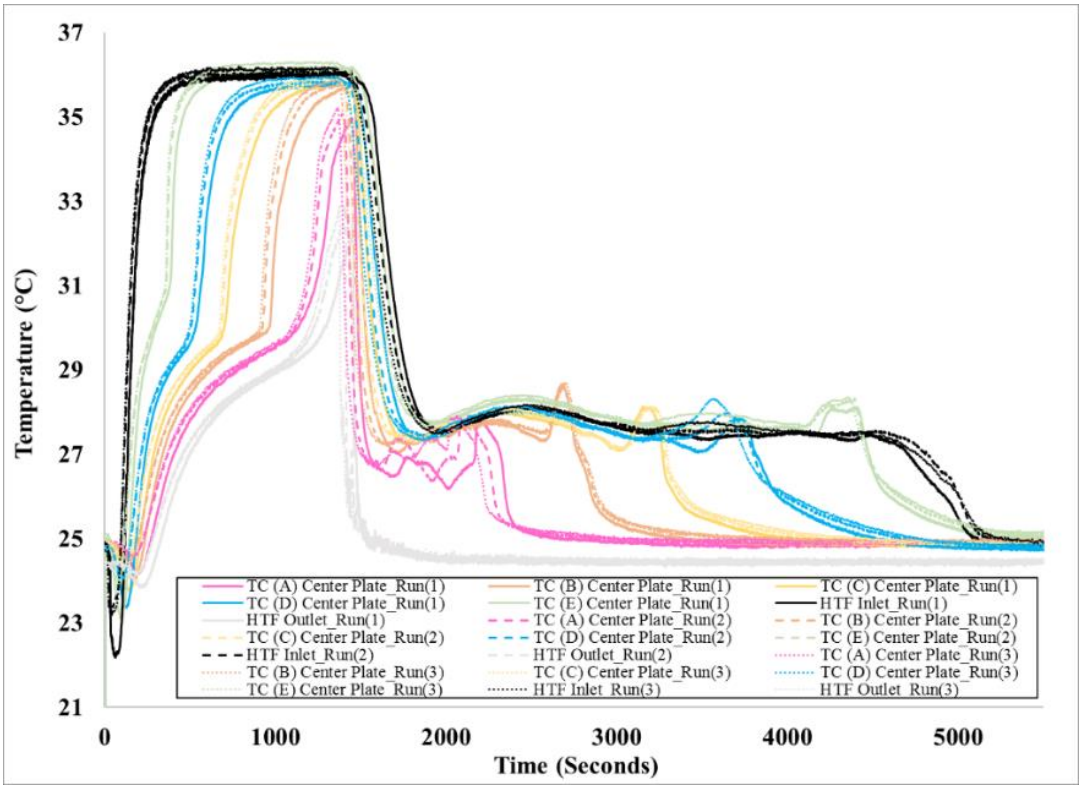

Figure 112: Temperature profiles recorded by thermocouples at the center plate during melting (90%) and solidification at a flow rate of 3 GPH (counter-current). Inlet temperature of HTF during melting is 37.4 °C and during solidification is 25 °C (Case R, Post-experiment calibration, insulated).

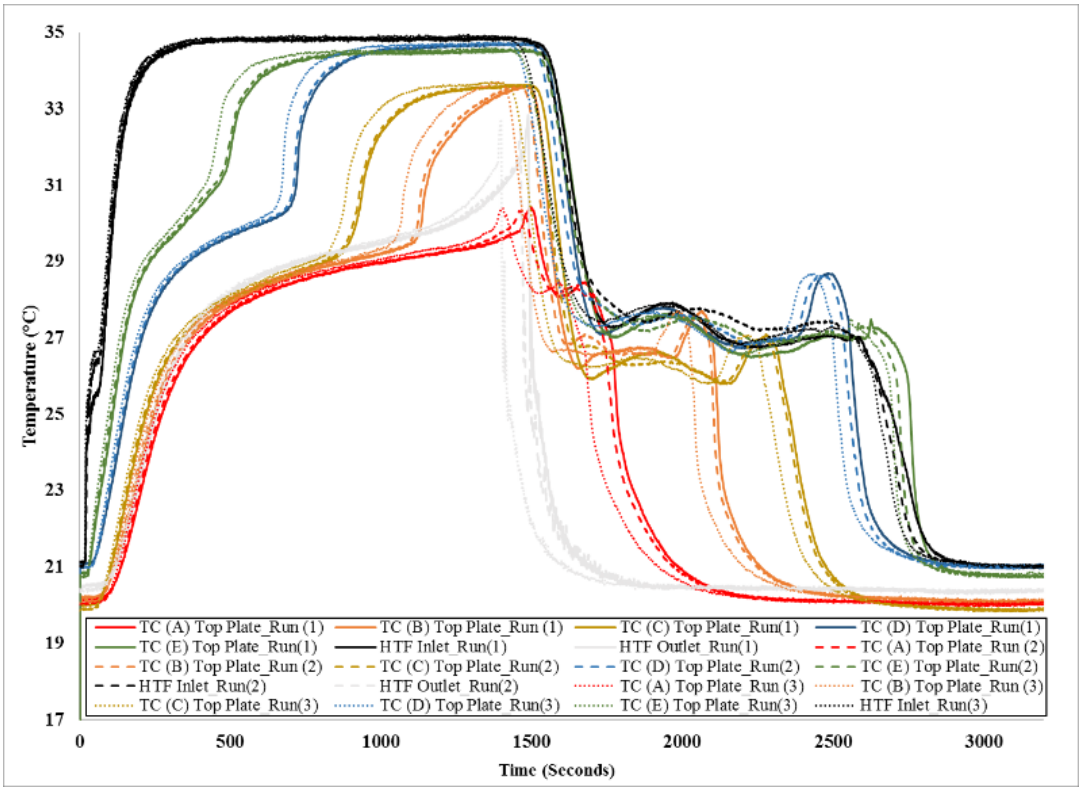

Figure 113: Temperature profiles recorded by thermocouples at the top plate during melting (90%) and solidification at a flow rate of 5 GPH (counter-current). Inlet temperature of HTF during melting is 35 °C and during solidification is 20 °C (Case S, Pre-experiment calibration, insulated).

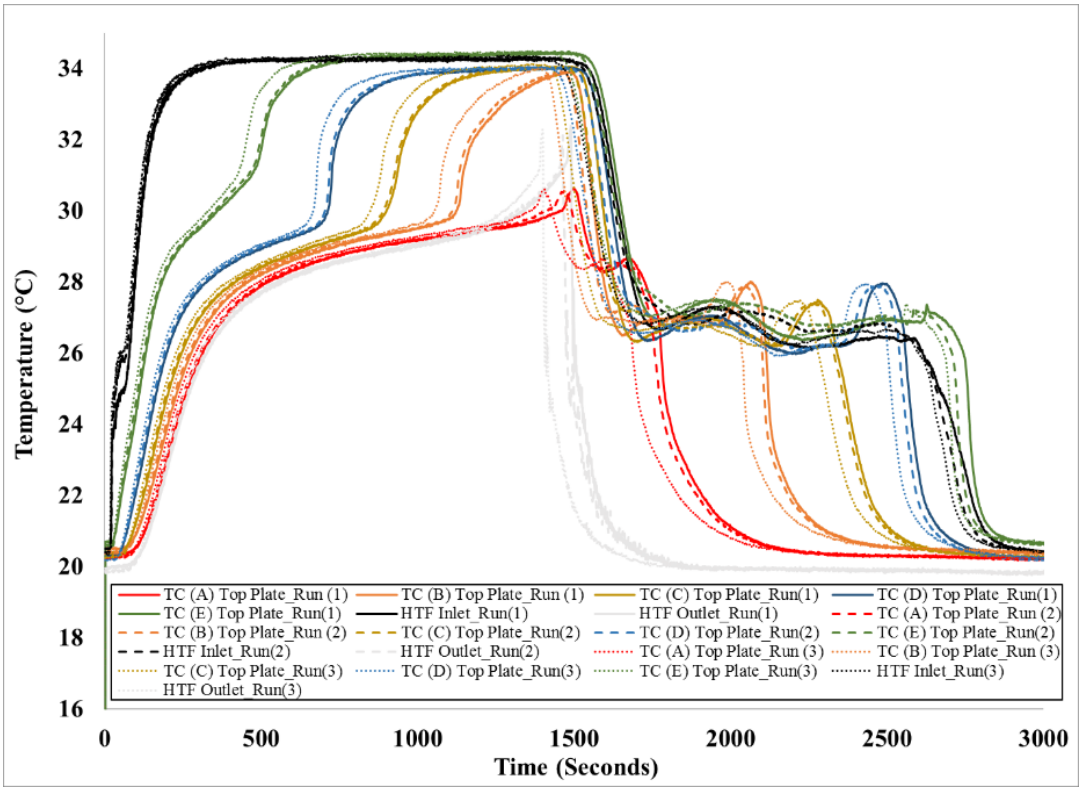

Figure 114: Temperature profiles recorded by thermocouples at the top plate during melting (90%) and solidification at a flow rate of 5 GPH (counter-current). Inlet temperature of HTF during melting is 35 °C and during solidification is 20 °C (Case S, Post-experiment calibration, insulated).

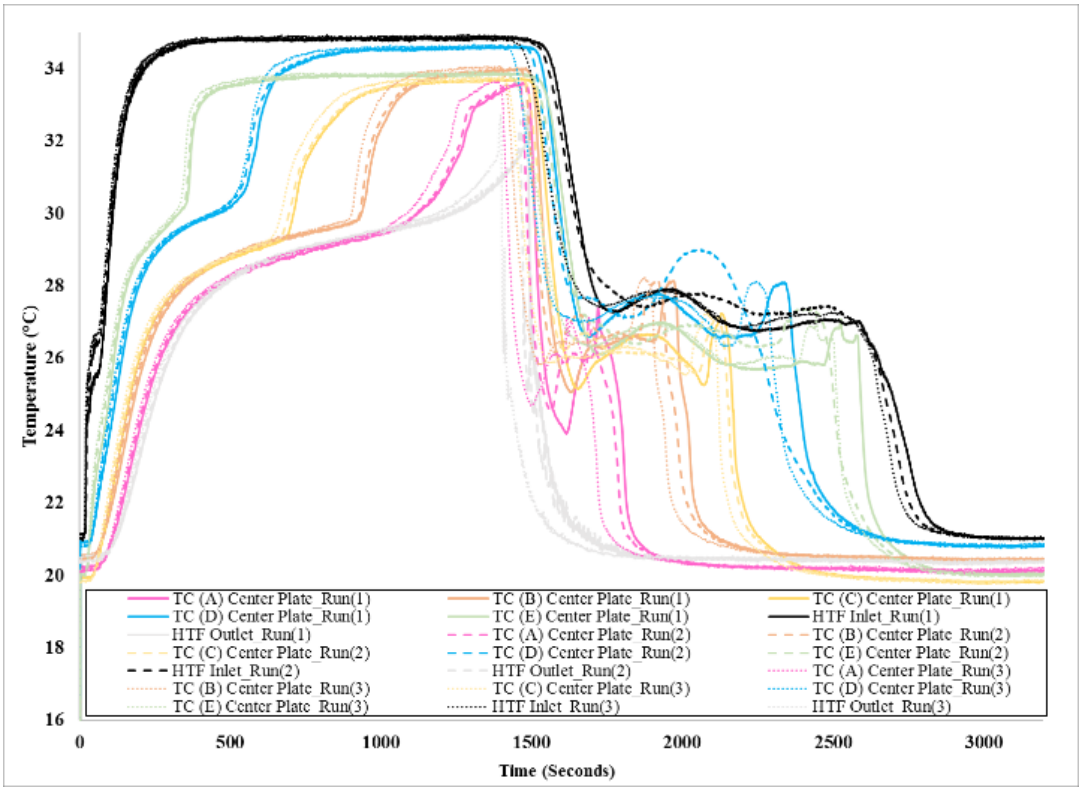

Figure 115: Temperature profiles recorded by thermocouples at the center plate during melting (90%) and solidification at a flow rate of 5 GPH (counter-current). Inlet temperature of HTF during melting is 35 °C and during solidification is 20 °C (Case S, Pre-experiment calibration, insulated).

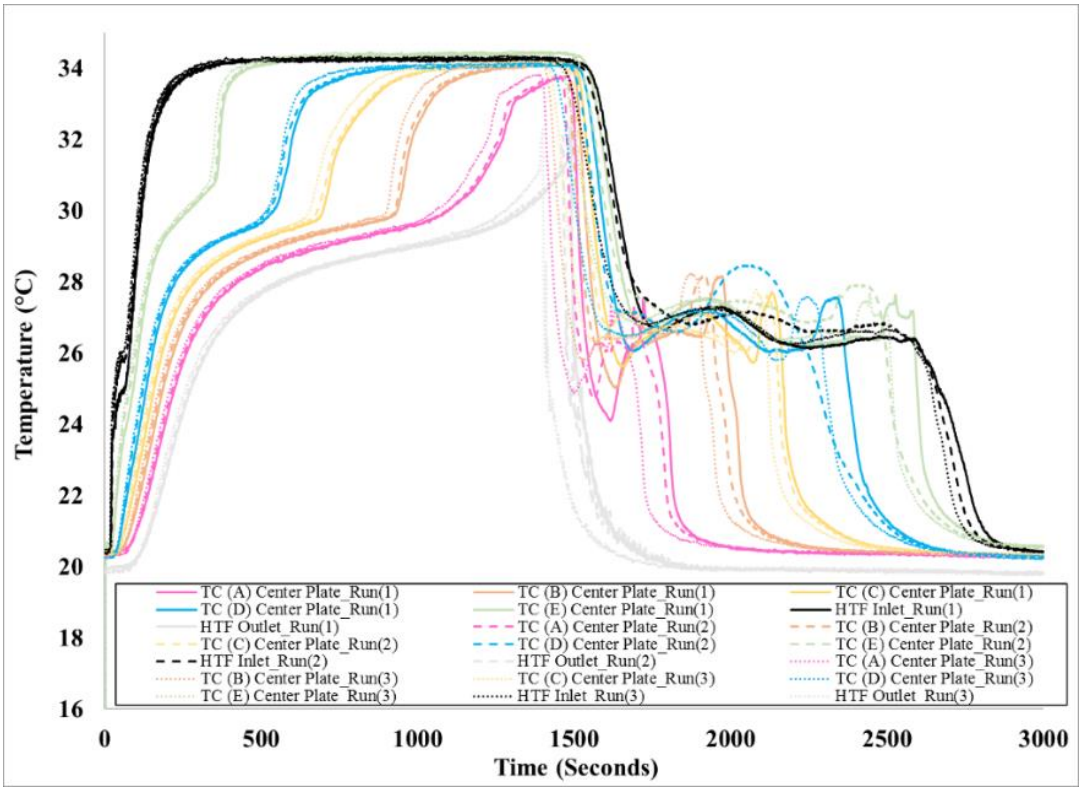

Figure 116: Temperature profiles recorded by thermocouples at the center plate during melting (90%) and solidification at a flow rate of 5 GPH (counter-current). Inlet temperature of HTF during melting is 35 °C and during solidification is 20 °C (Case S, Post-experiment calibration, insulated).

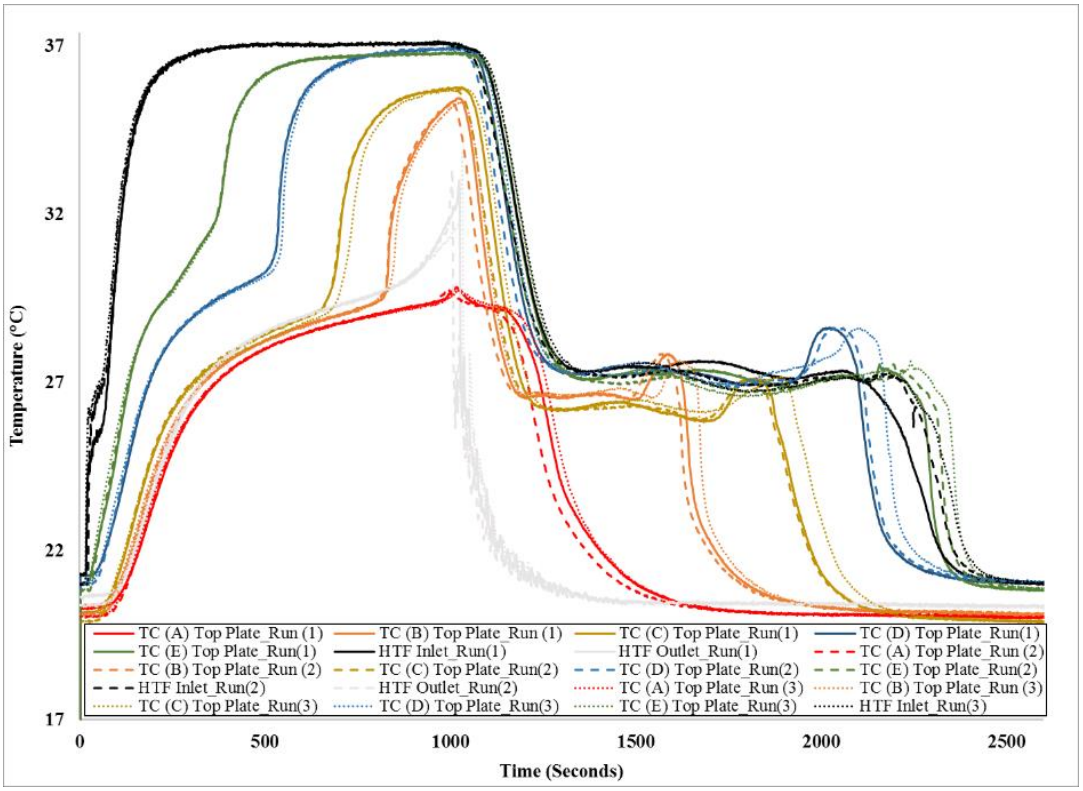

Figure 117: Temperature profiles recorded by thermocouples at the top plate during melting (90%) and solidification at a flow rate of 5 GPH (counter-current). Inlet temperature of HTF during melting is 37.4 °C and during solidification is 20 °C (Case T, Pre-experiment calibration, insulated).

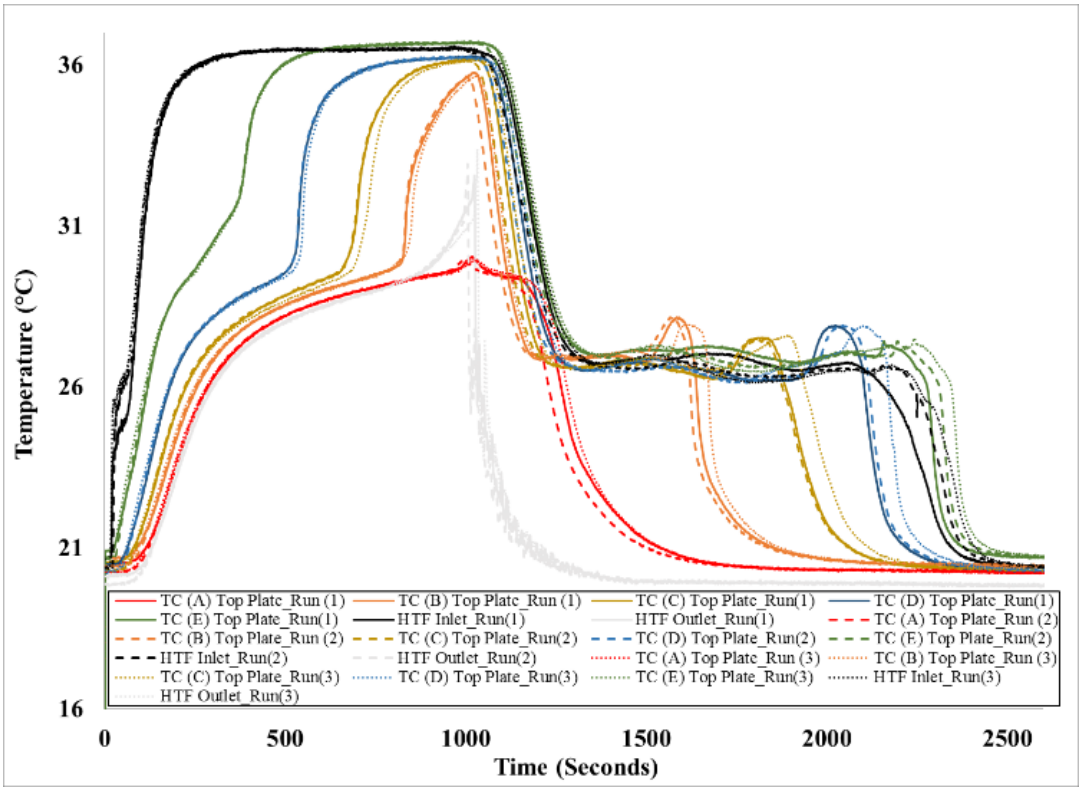

Figure 118: Temperature profiles recorded by thermocouples at the top plate during melting (90%) and solidification at a flow rate of 5 GPH (counter-current). Inlet temperature of HTF during melting is 37.4 °C and during solidification is 20 °C (Case T, Post-experiment calibration, insulated).

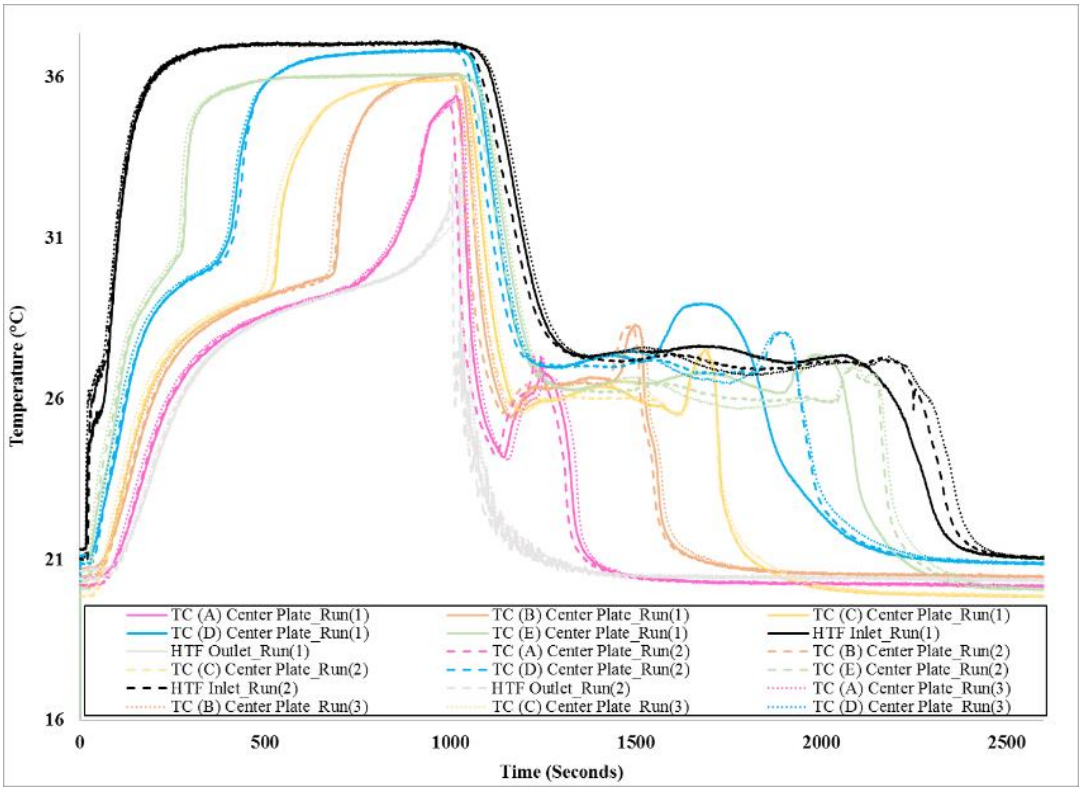

Figure 119: Temperature profiles recorded by thermocouples at the center plate during melting (90%) and solidification at a flow rate of 5 GPH (counter-current). Inlet temperature of HTF during melting is 37.4 °C and during solidification is 20 °C (Case T, Pre-experiment calibration, insulated).

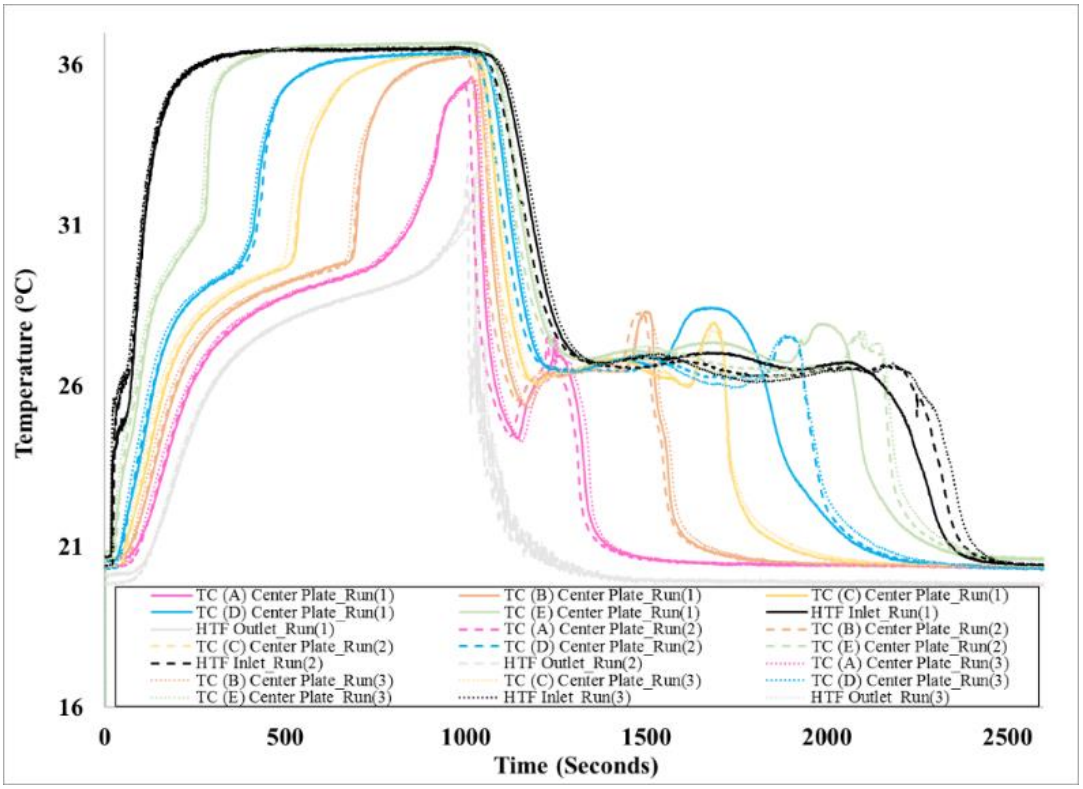

Figure 120: Temperature profiles recorded by thermocouples at the center plate during melting (90%) and solidification at a flow rate of 5 GPH (counter-current). Inlet temperature of HTF during melting is 37.4 °C and during solidification is 20 °C (Case T, Post-experiment calibration, insulated).

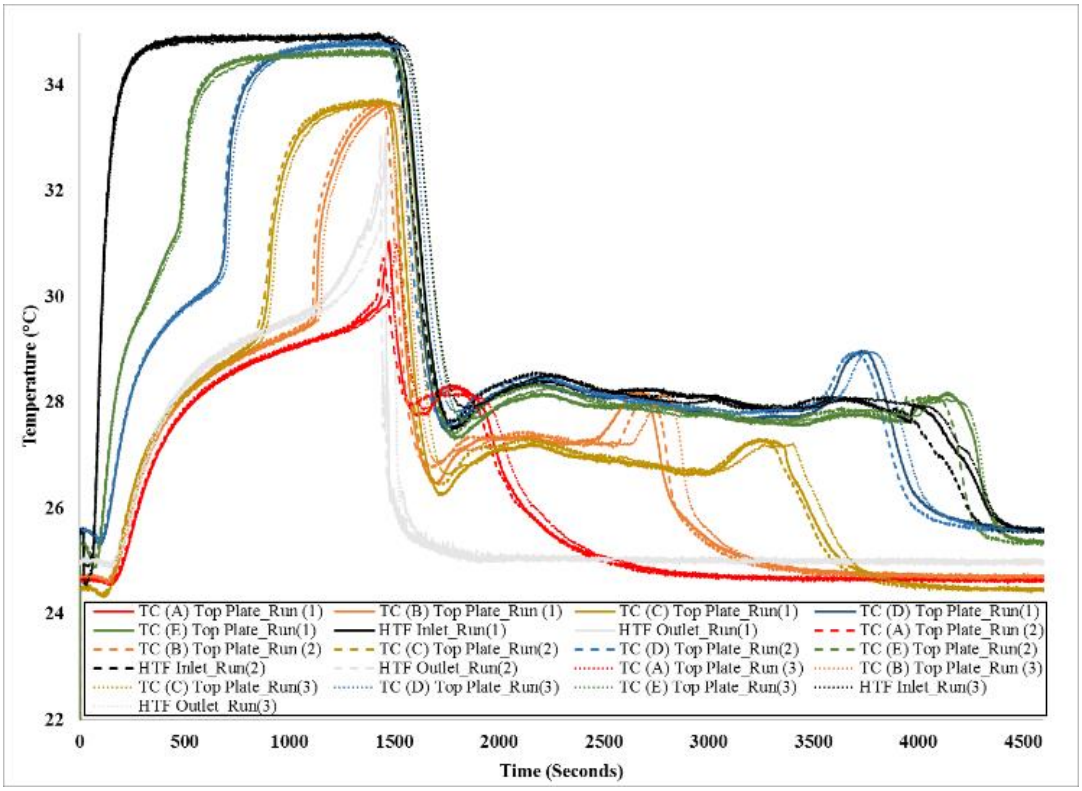

Figure 121: Temperature profiles recorded by thermocouples at the top plate during melting (90%) and solidification at a flow rate of 5 GPH (counter-current). Inlet temperature of HTF during melting is 35 °C and during solidification is 25 °C (Case U, Pre-experiment calibration, insulated).

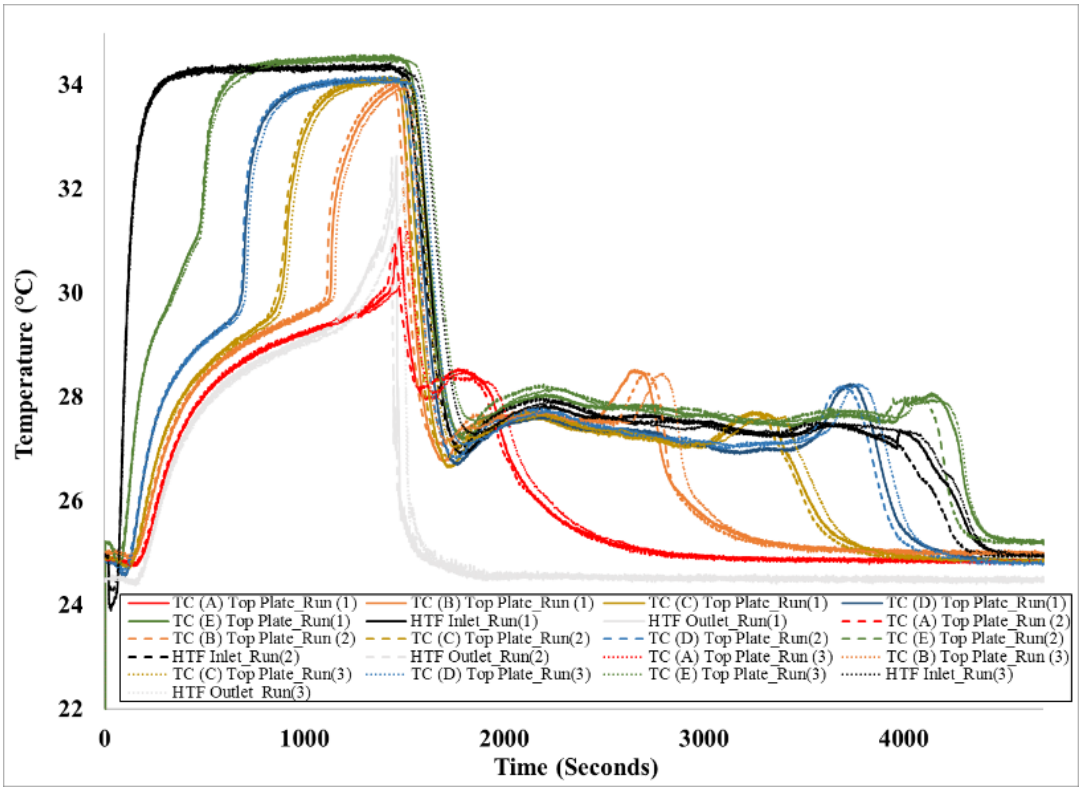

Figure 122: Temperature profiles recorded by thermocouples at the top plate during melting (90%) and solidification at a flow rate of 5 GPH (counter-current). Inlet temperature of HTF during melting is 35 °C and during solidification is 25 °C (Case U, Post-experiment calibration, insulated).

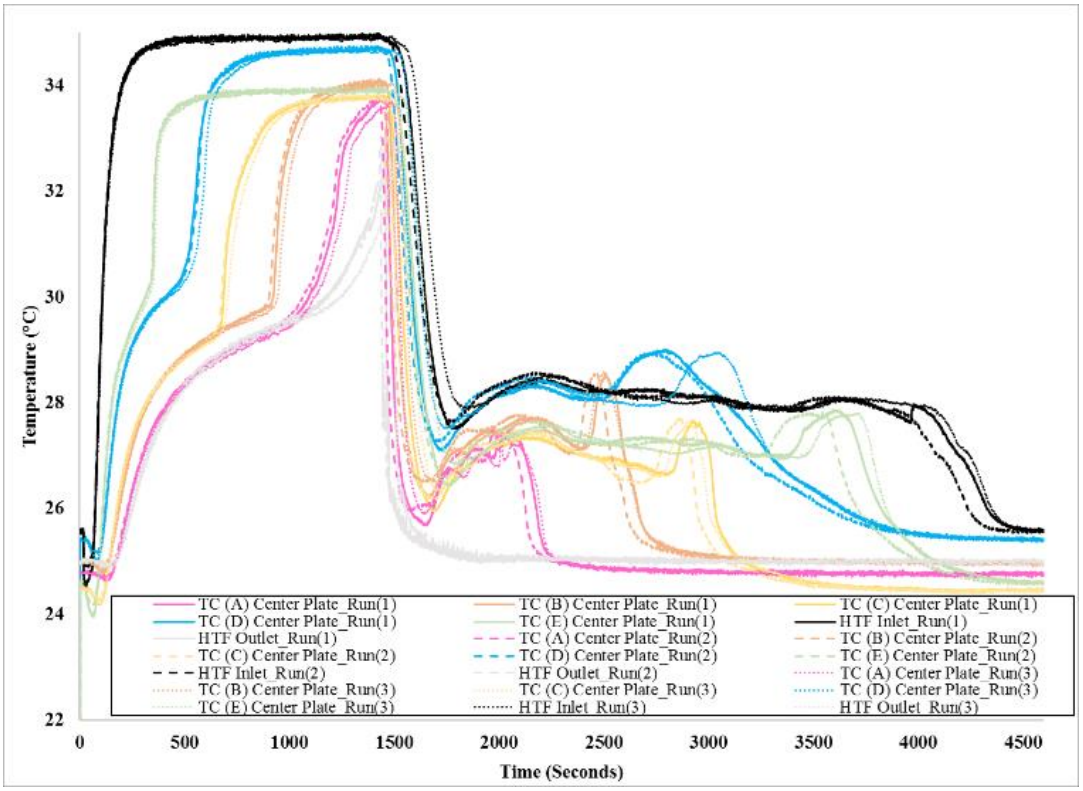

Figure 123: Temperature profiles recorded by thermocouples at the center plate during melting (90%) and solidification at a flow rate of 5 GPH (counter-current). Inlet temperature of HTF during melting is 35 °C and during solidification is 25 °C (Case U, Pre-experiment calibration, insulated).

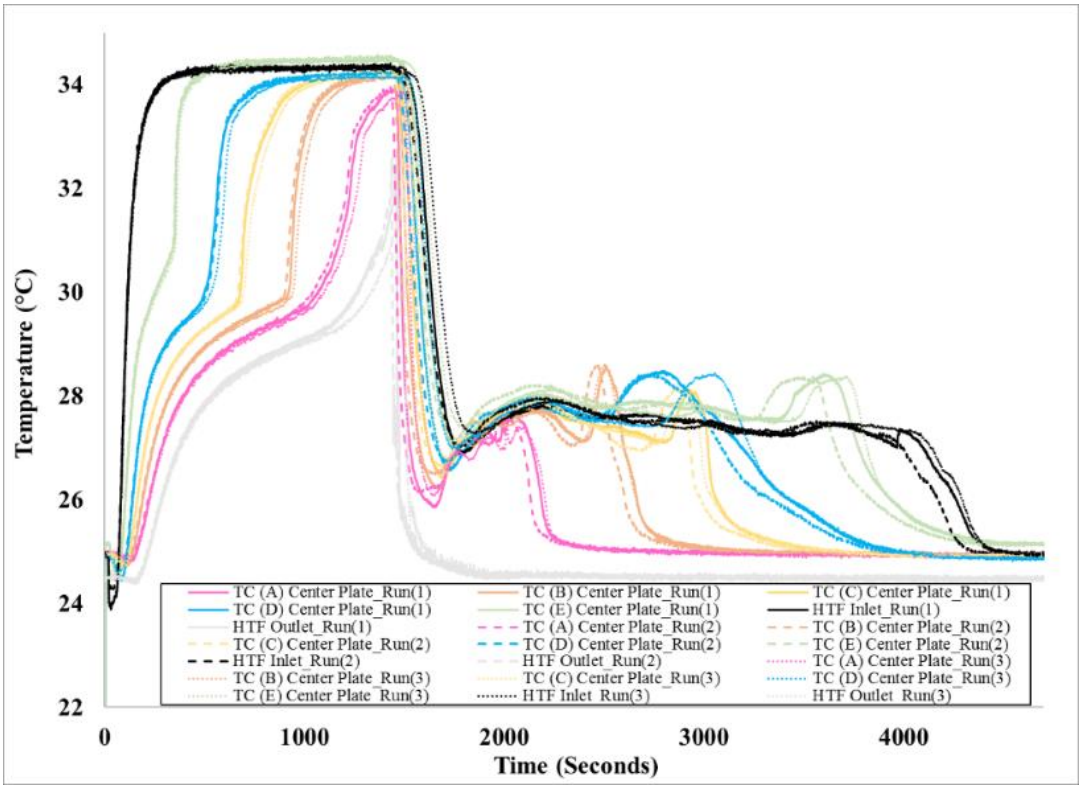

Figure 124: Temperature profiles recorded by thermocouples at the center plate during melting (90%) and solidification at a flow rate of 5 GPH (counter-current). Inlet temperature of HTF during melting is 35 °C and during solidification is 25 °C (Case U, Post-experiment calibration, insulated).

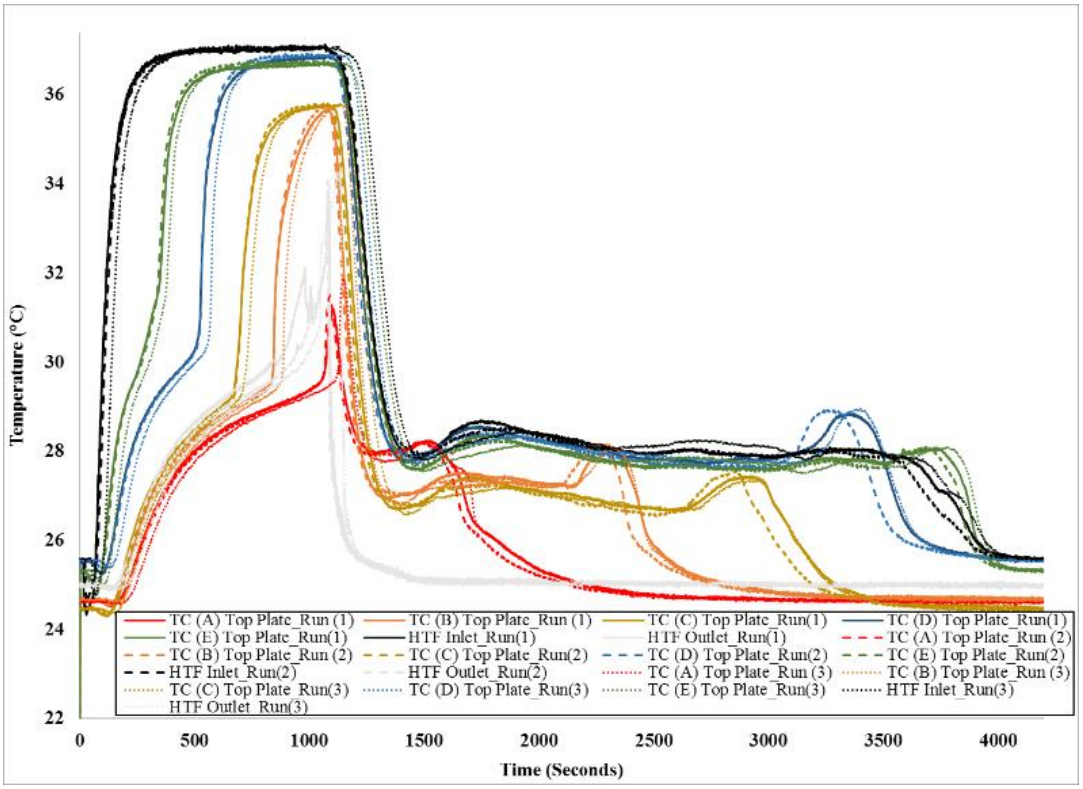

Figure 125: Temperature profiles recorded by thermocouples at the top plate during melting (90%) and solidification at a flow rate of 5 GPH (counter-current). Inlet temperature of HTF during melting is 37.4 °C and during solidification is 25 °C (Case V, Pre-experiment calibration, insulated).

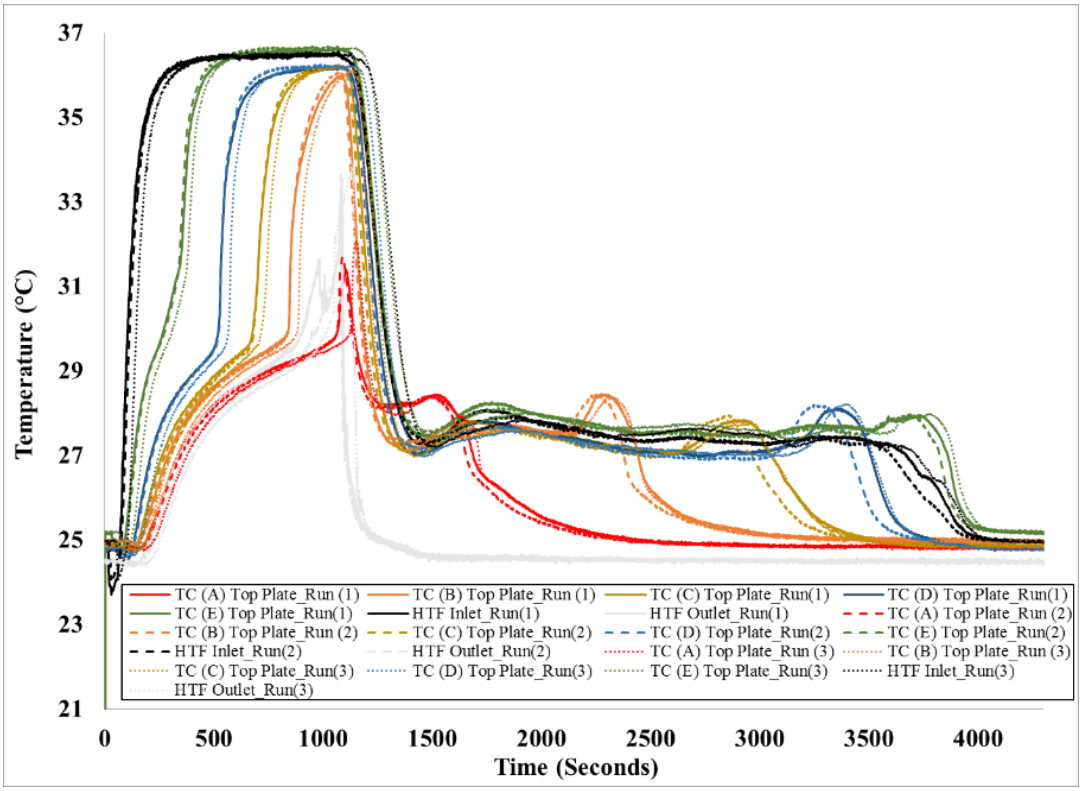

Figure 126: Temperature profiles recorded by thermocouples at the top plate during melting (90%) and solidification at a flow rate of 5 GPH (counter-current). Inlet temperature of HTF during melting is 37.4 °C and during solidification is 25 °C (Case V, Post-experiment calibration, insulated).

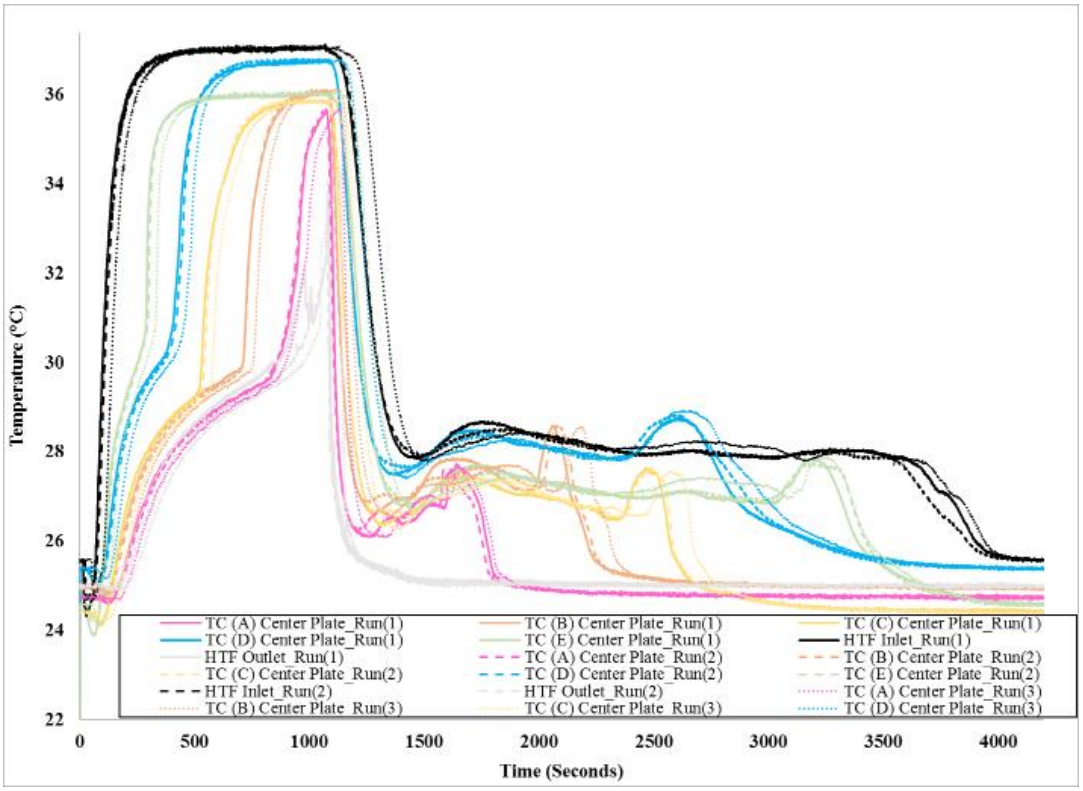

Figure 127: Temperature profiles recorded by thermocouples at the center plate during melting (90%) and solidification at a flow rate of 5 GPH (counter-current). Inlet temperature of HTF during melting is 37.4 °C and during solidification is 25 °C (Case V, Pre-experiment calibration, insulated).

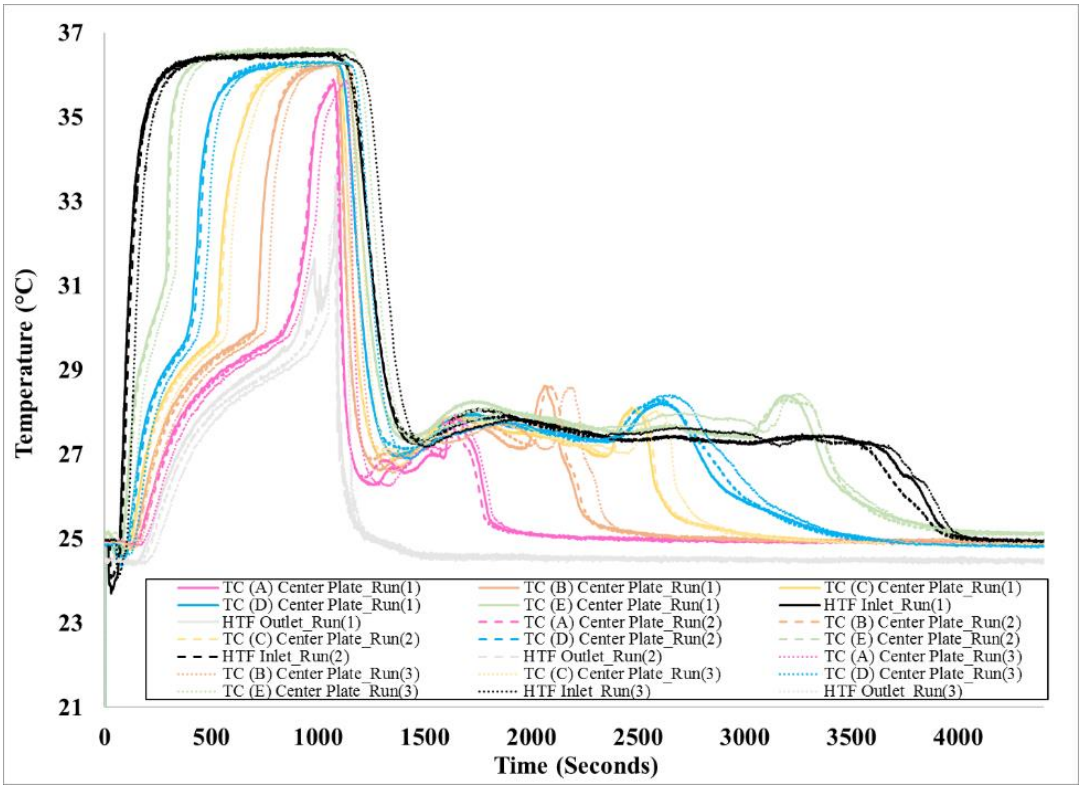

Figure 128: Temperature profiles recorded by thermocouples at the center plate during melting (90%) and solidification at a flow rate of 5 GPH (counter-current). Inlet temperature of HTF during melting is 37.4 °C and during solidification is 25 °C (Case V, Post-experiment calibration, insulated).

APPENDIX E

This section provides additional details on the repeatability and reproducibility (i.e., using post-experiment calibration constants). A minimum of two trials and a maximum of three trials were run for each case to ensure repeatability. The minimum was set to two trials to reduce the overall time spent on gathering data. For cases of greater interest (such as at design conditions), three trials were run to ensure greater repeatability. The repeatability is as shown in Figure 129, where the two trials are nearly identical.

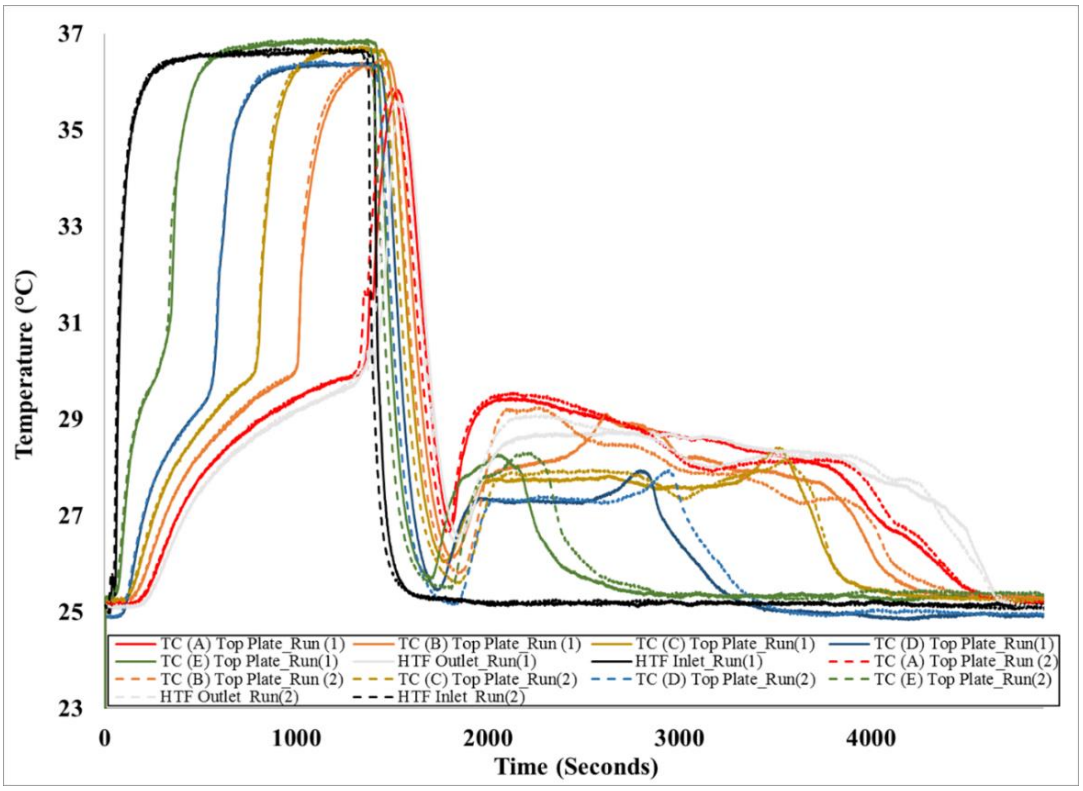

Figure 129: Temperature profiles recorded by thermocouples at the top plate during melting (90%) and solidification at a flow rate of 3 GPH (co-current). Inlet temperature of HTF during melting is 37.4 °C and during solidification is 25 °C (Case B, Post-experiment calibration).

Furthermore, the third trials for case F, Case G, Case I and Case J, were run on a different day from the first and second trial. Case G is as shown in Figure 130, where good reproducibility is observed.

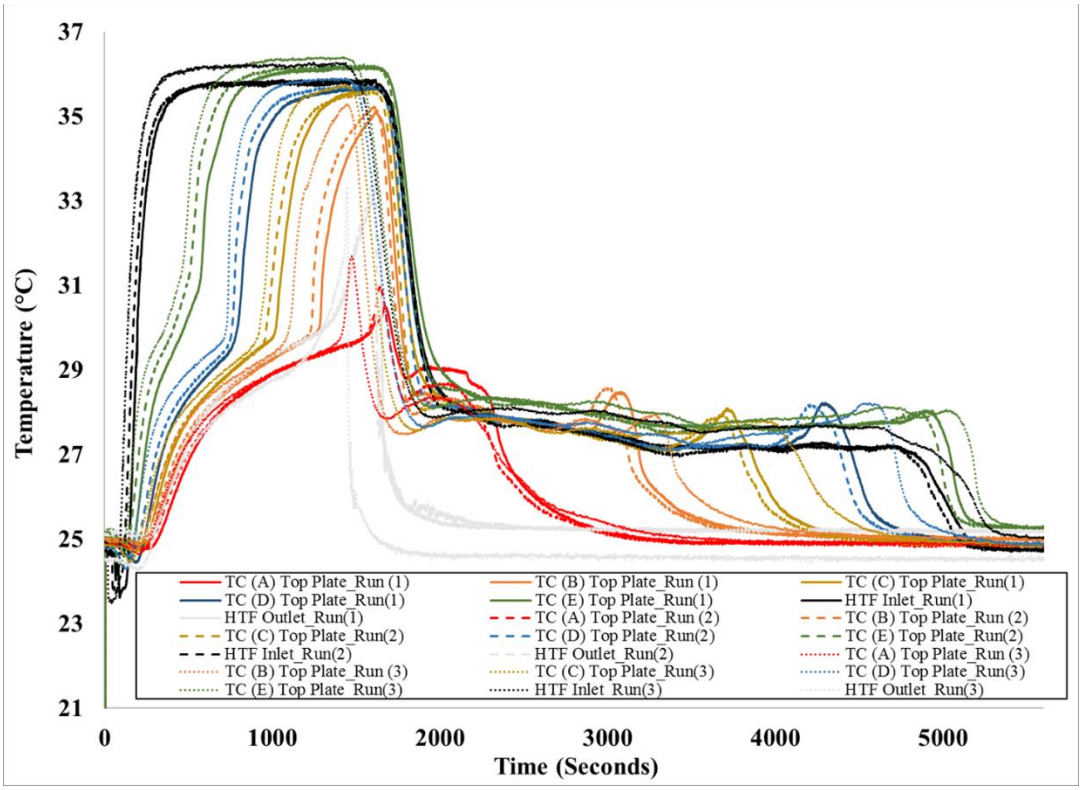

Figure 130: Temperature profiles recorded by thermocouples at the top plate during melting (90%) and solidification at a flow rate of 3 GPH (counter-current). Inlet temperature of HTF during melting is 37.4 °C and during solidification is 25 °C (Case G, Post experiment calibration).

APPENDIX F

This section provides instantaneous power curves for the different cases (using pre-experiment calibration constants).

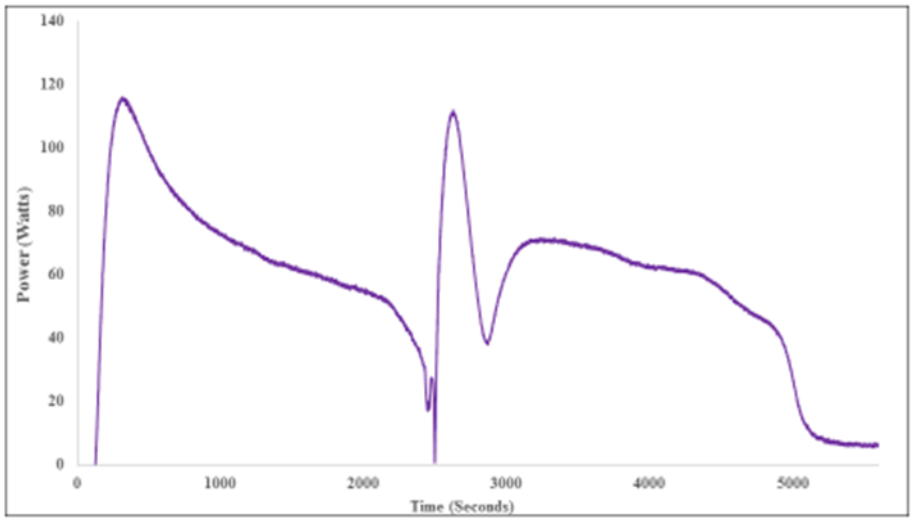

Figure 131: Co-current, Instantaneous Power Rating for volumetric flow rate of 3 GPH with T_{hot} of 35 °C and T_{cold} of 25 °C (Case A).

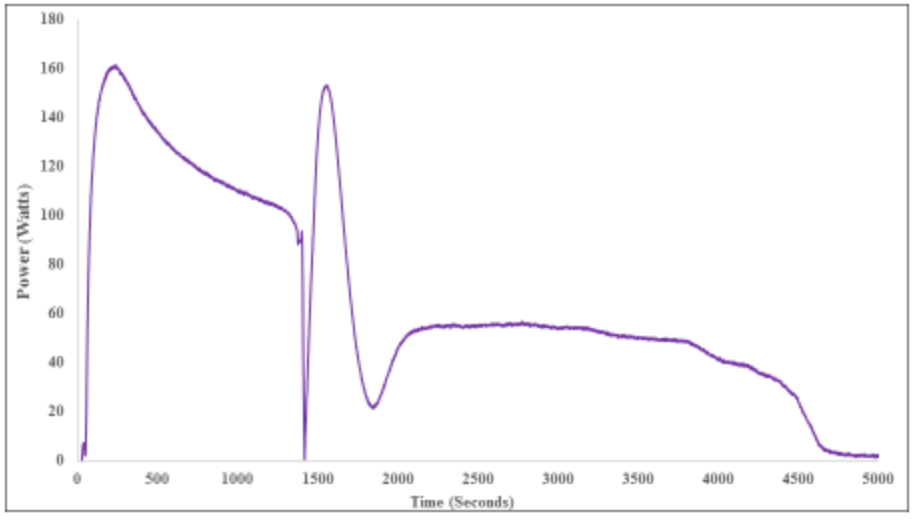

Figure 132: Co-current, Instantaneous Power Rating for volumetric flow rate of 3 GPH with T_{hot} of 37.4 °C and T_{cold} of 25 °C (Case B).

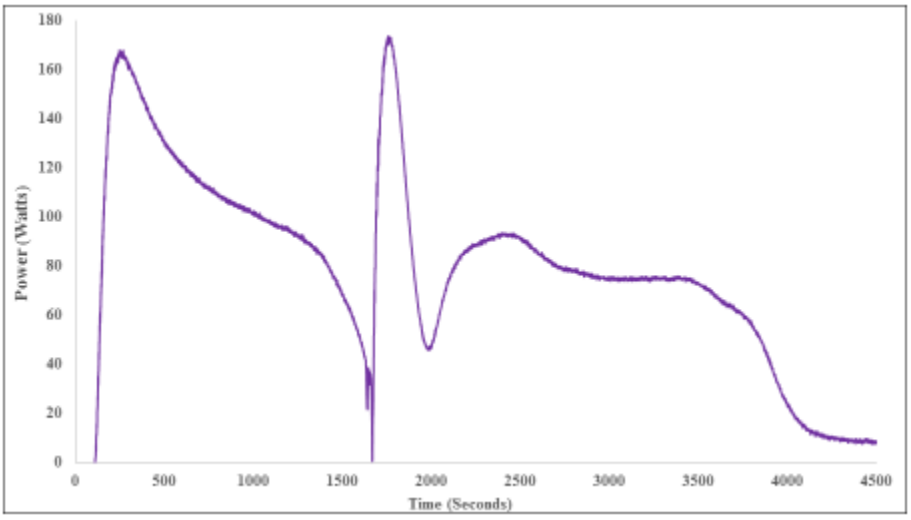

Figure 133: Co-current, Instantaneous Power Rating for volumetric flow rate of 5 GPH with T_{hot} of 35 °C and T_{cold} of 25 °C (Case C).

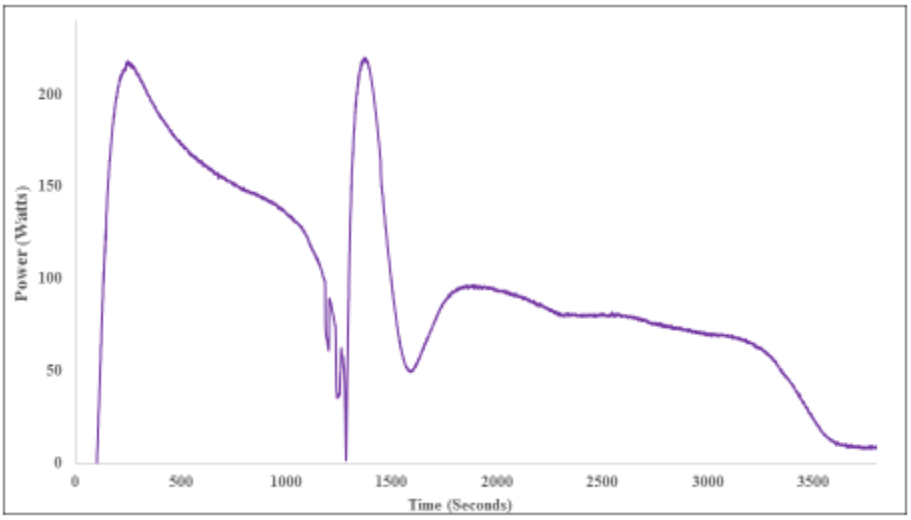

Figure 134: Co-current, Instantaneous Power Rating for volumetric flow rate of 5 GPH with T_{hot} of 37.4 °C and T_{cold} of 25 °C (Case D).

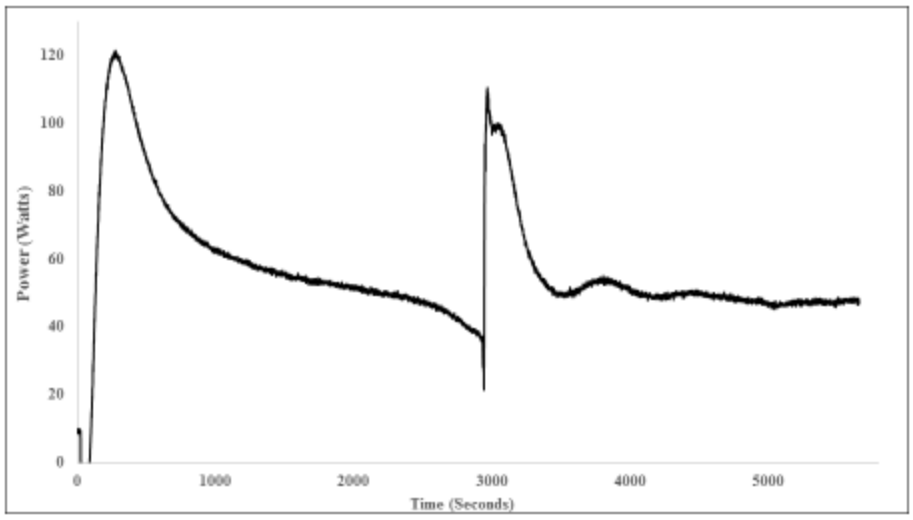

Figure 135: Counter-current, Instantaneous Power Rating for volumetric flow rate of 3 GPH with T_{hot} of 33 °C and T_{cold} of 25 °C (Case E).

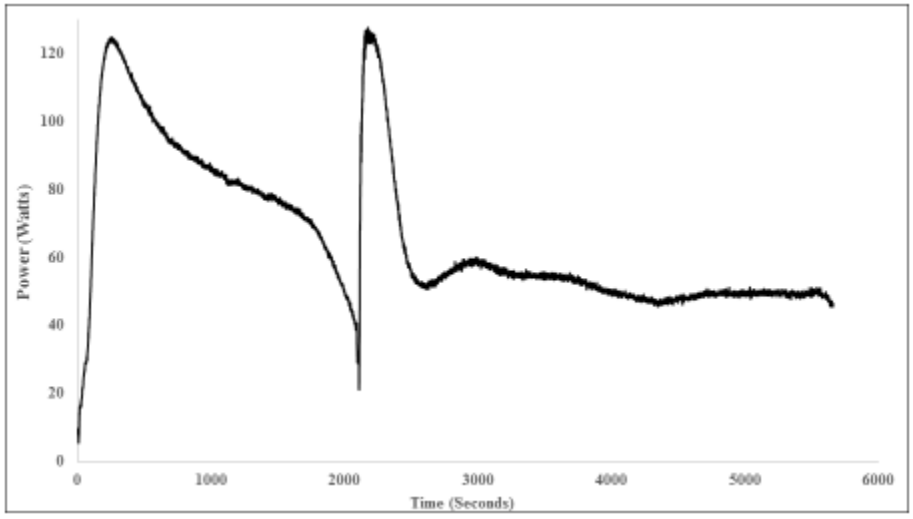

Figure 136: Counter-current, Instantaneous Power Rating for volumetric flow rate of 3 GPH with T_{hot} of 35 °C and T_{cold} of 25 °C (Case F).

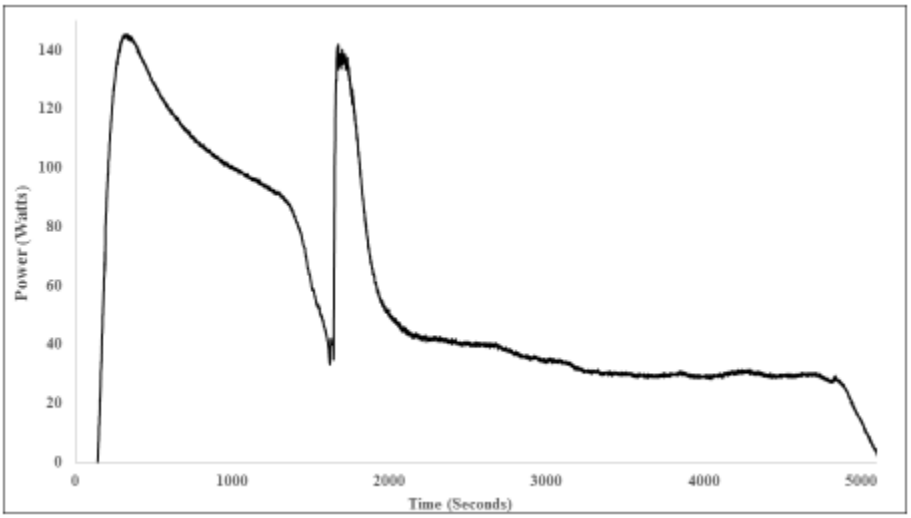

Figure 137: Counter-current, Instantaneous Power Rating for volumetric flow rate of 3 GPH with T_{hot} of 37.4 °C and T_{cold} of 25 °C (Case G).

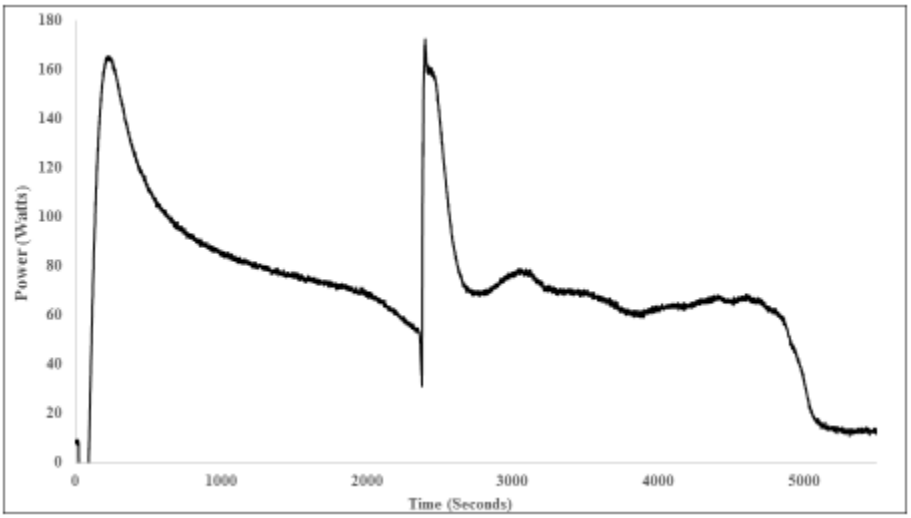

Figure 138: Counter-current, Instantaneous Power Rating for volumetric flow rate of 5 GPH with T_{hot} of 33 °C and T_{cold} of 25 °C (Case H).

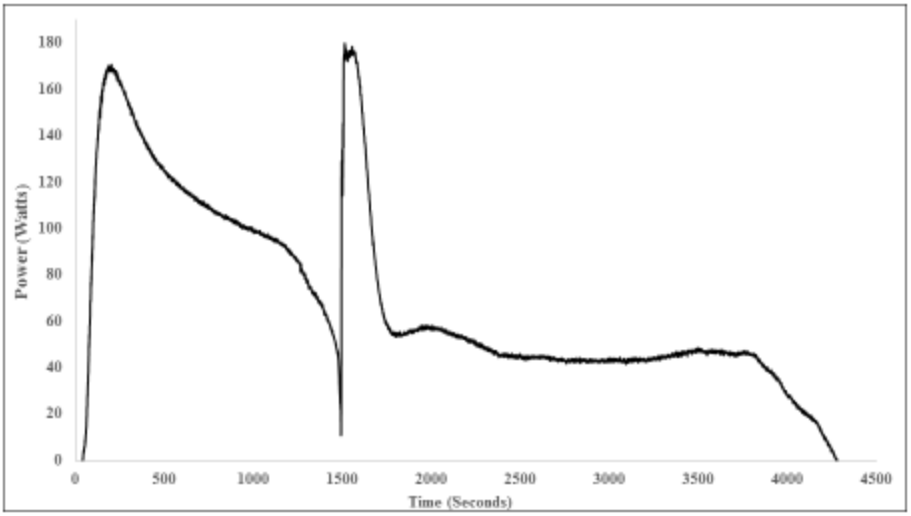

Figure 139: Counter-current, Instantaneous Power Rating for volumetric flow rate of 5 GPH with T_{hot} of 35 °C and T_{cold} of 25 °C (Case I).

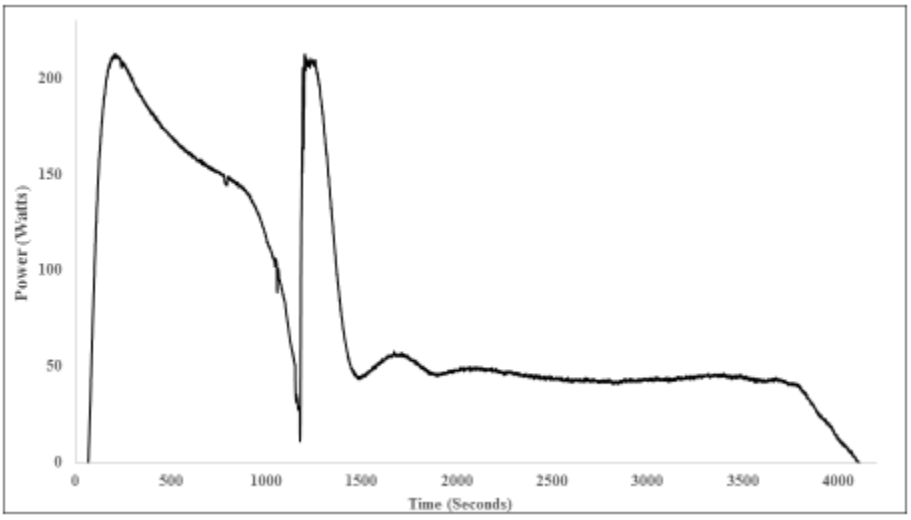

Figure 140: Counter-current, Instantaneous Power Rating for volumetric flow rate of 5 GPH with T_{hot} of 37.4 °C and T_{cold} of 25 °C (Case J).

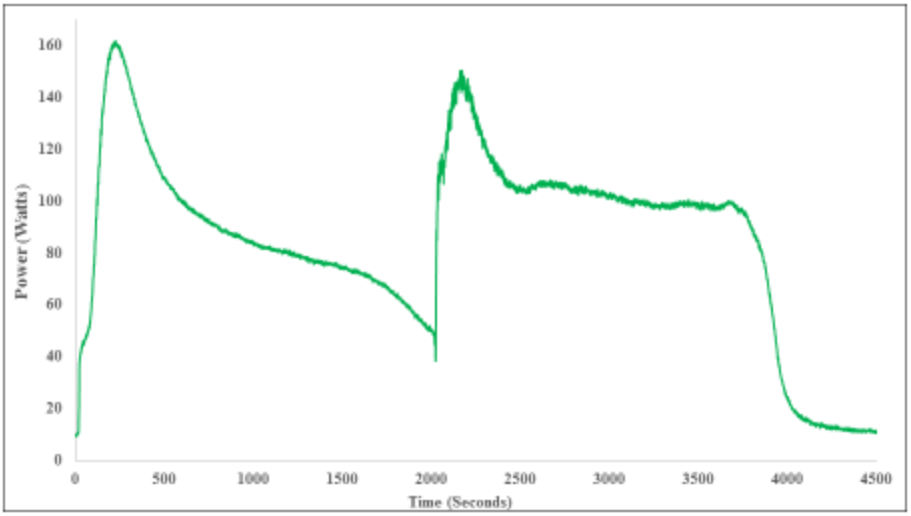

Figure 141: Counter-current, Instantaneous Power Rating for volumetric flow rate of 3 GPH with T_{hot} of 35 °C and T_{cold} of 20 °C (Case K).

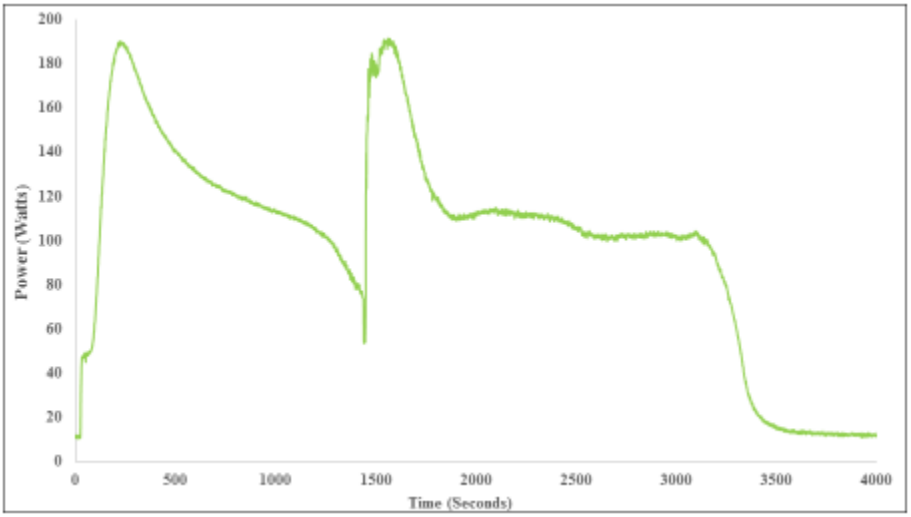

Figure 142: Counter-current, Instantaneous Power Rating for volumetric flow rate of 3 GPH with T_{hot} of 37.4 °C and T_{cold} of 20 °C (Case L).

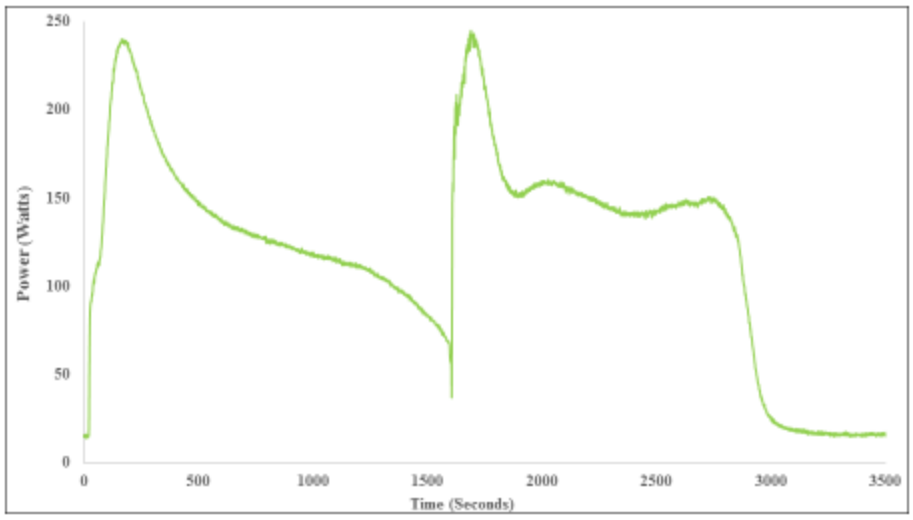

Figure 143: Counter-current, Instantaneous Power Rating for volumetric flow rate of 5 GPH with T_{hot} of 35 °C and T_{cold} of 20 °C (Case M).

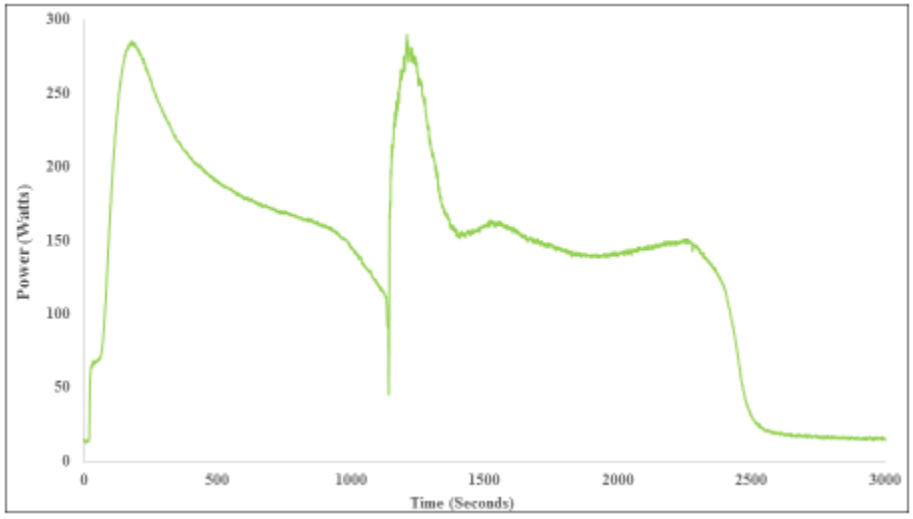

Figure 144: Counter-current, Instantaneous Power Rating for volumetric flow rate of 5 GPH with T_{hot} of 37.4 °C and T_{cold} of 20 °C (Case N).

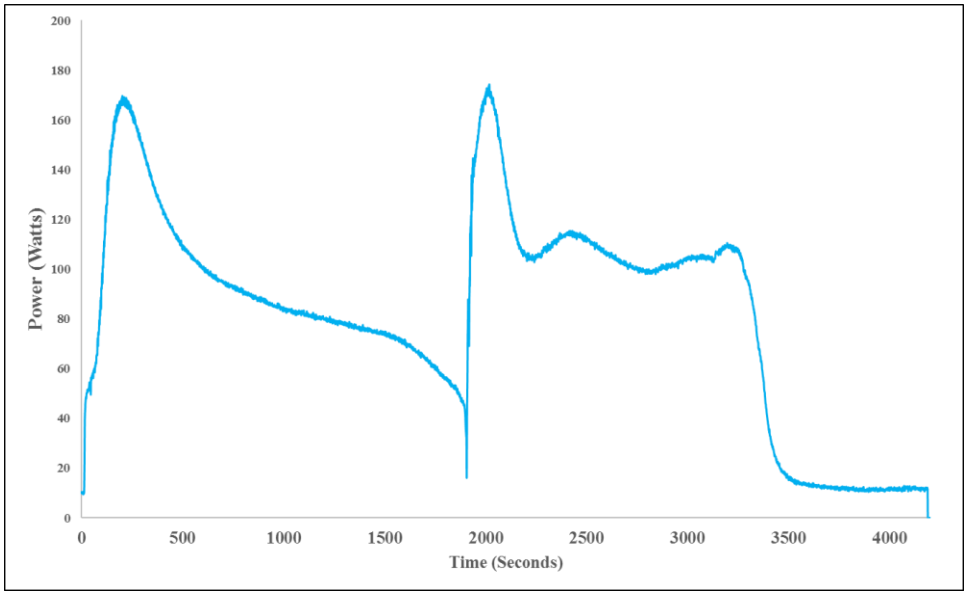

Figure 145: Counter-current, Instantaneous Power Rating for volumetric flow rate of 3 GPH with T_{hot} of 35 °C and T_{cold} of 20 °C (Case O).

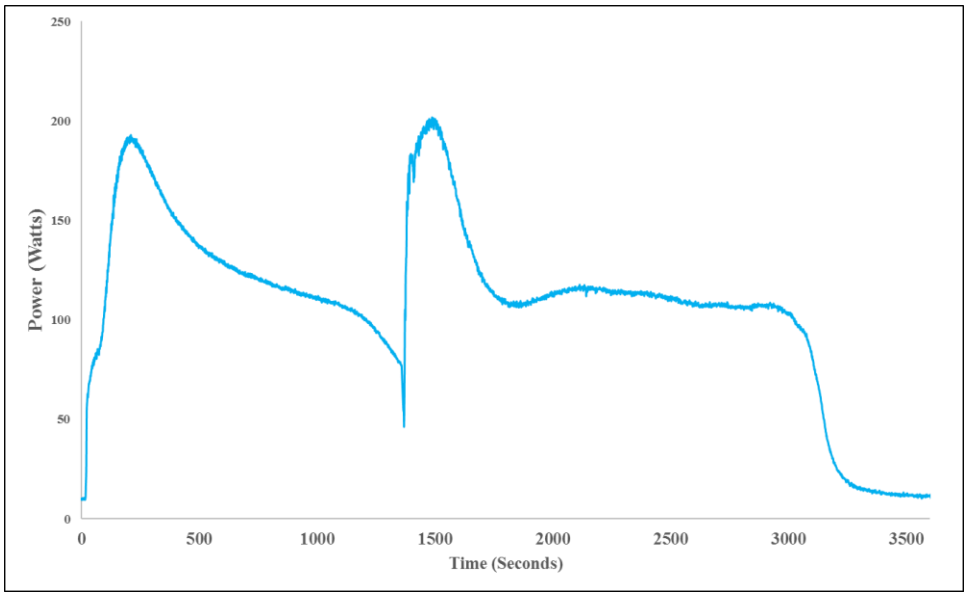

Figure 146: Counter-current, Instantaneous Power Rating for volumetric flow rate of 3 GPH with T_{hot} of 37.4 °C and T_{cold} of 20 °C (Case P).

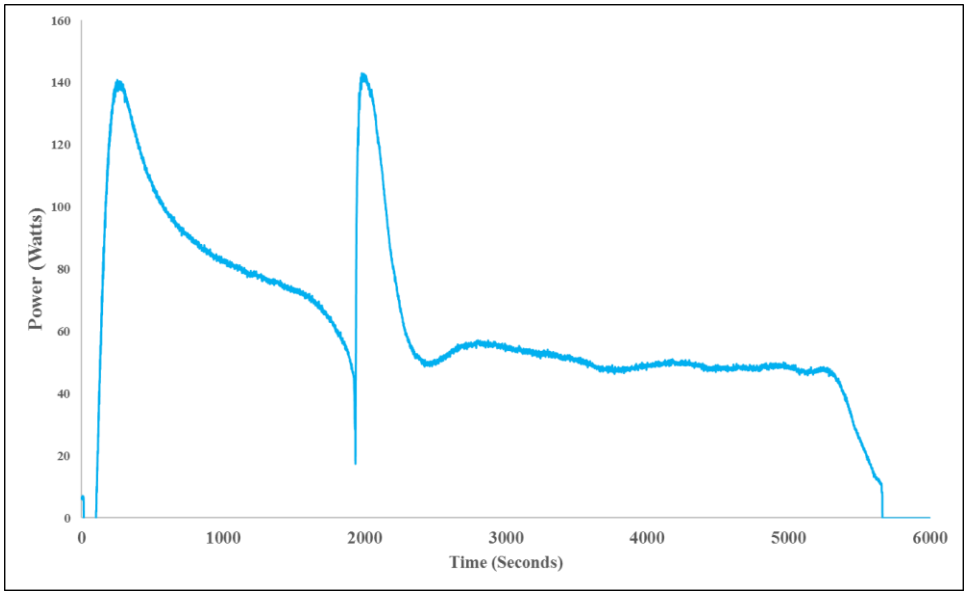

Figure 147: Counter-current, Instantaneous Power Rating for volumetric flow rate of 3 GPH with T_{hot} of 35 °C and T_{cold} of 25 °C (Case Q).

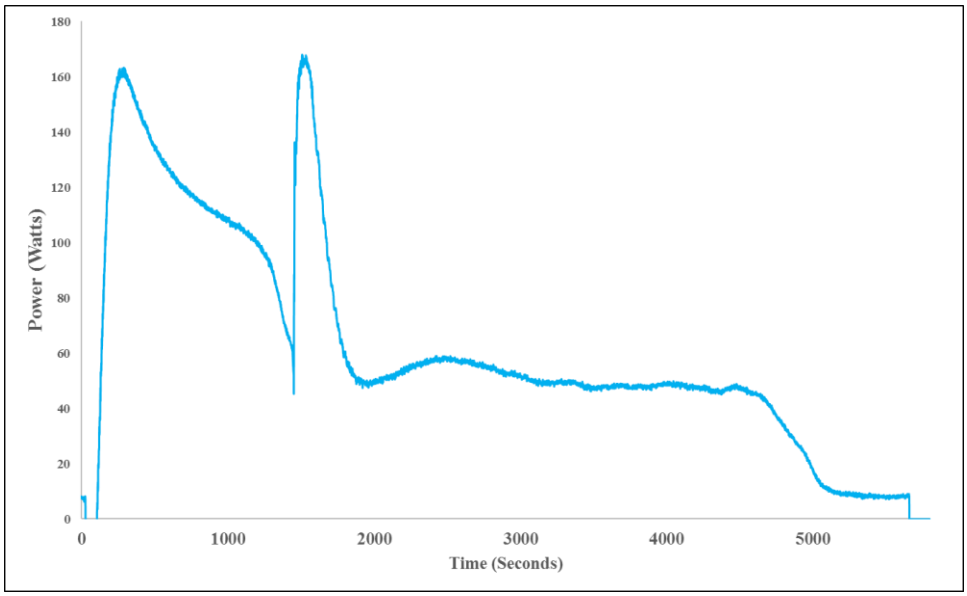

Figure 148: Counter-current, Instantaneous Power Rating for volumetric flow rate of 3 GPH with T_{hot} of 37.4 °C and T_{cold} of 25 °C (Case R).

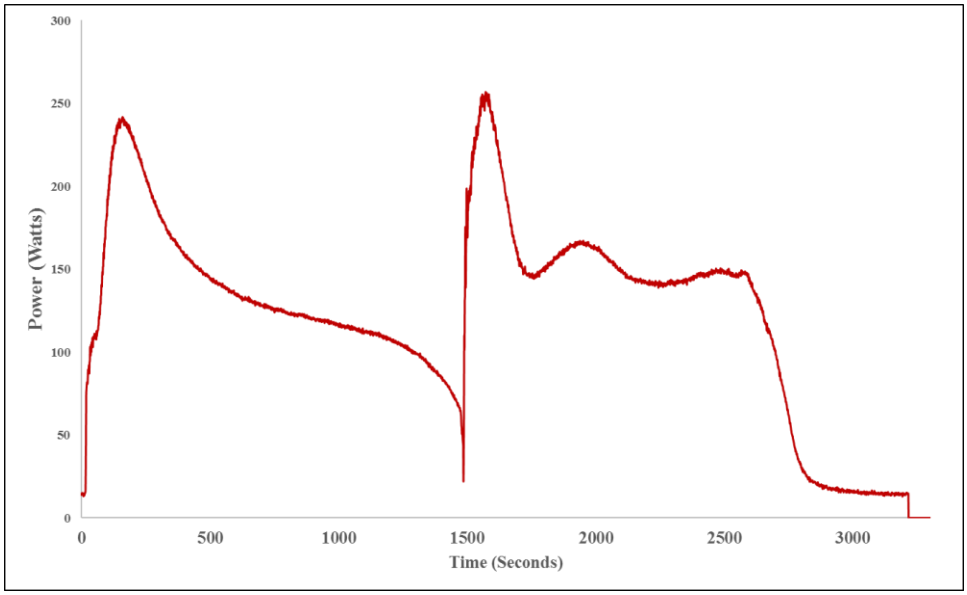

Figure 149: Counter-current, Instantaneous Power Rating for volumetric flow rate of 5 GPH with T_{hot} of 35 °C and T_{cold} of 20 °C (Case S).

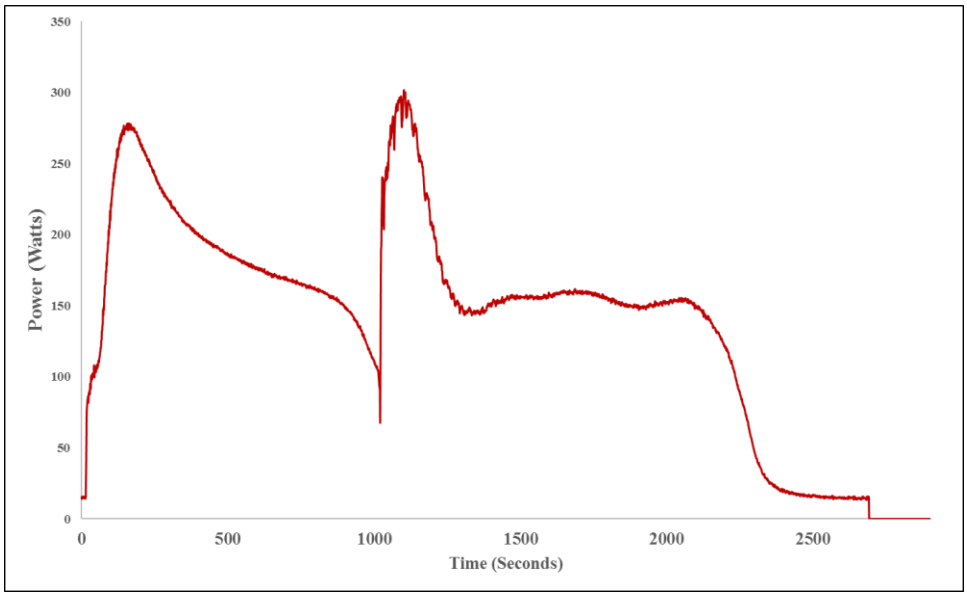

Figure 150: Counter-current, Instantaneous Power Rating for volumetric flow rate of 5 GPH with T_{hot} of 37.4 °C and T_{cold} of 20 °C (Case T).

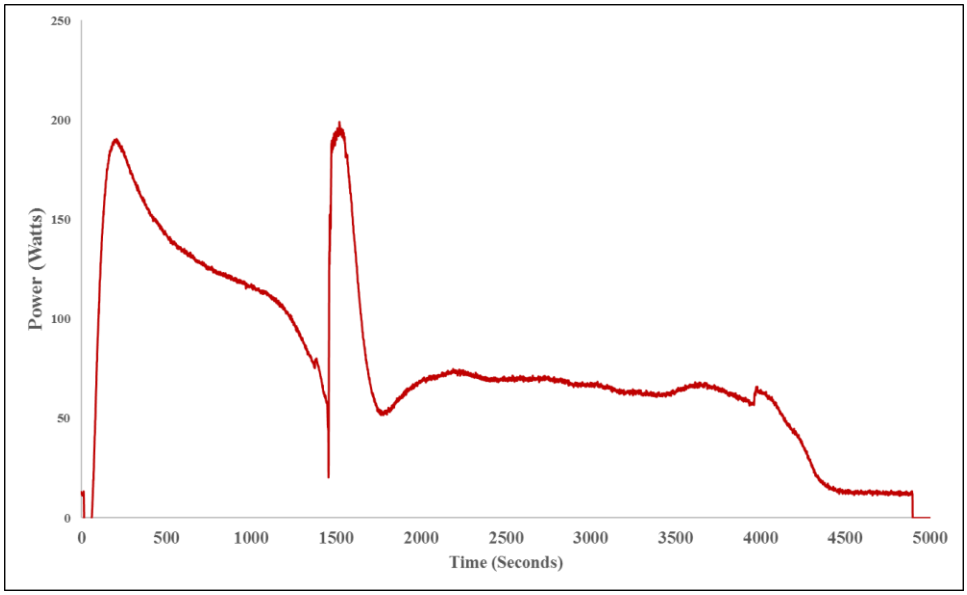

Figure 151: Counter-current, Instantaneous Power Rating for volumetric flow rate of 5 GPH with T_{hot} of 35 °C and T_{cold} of 25 °C (Case U).

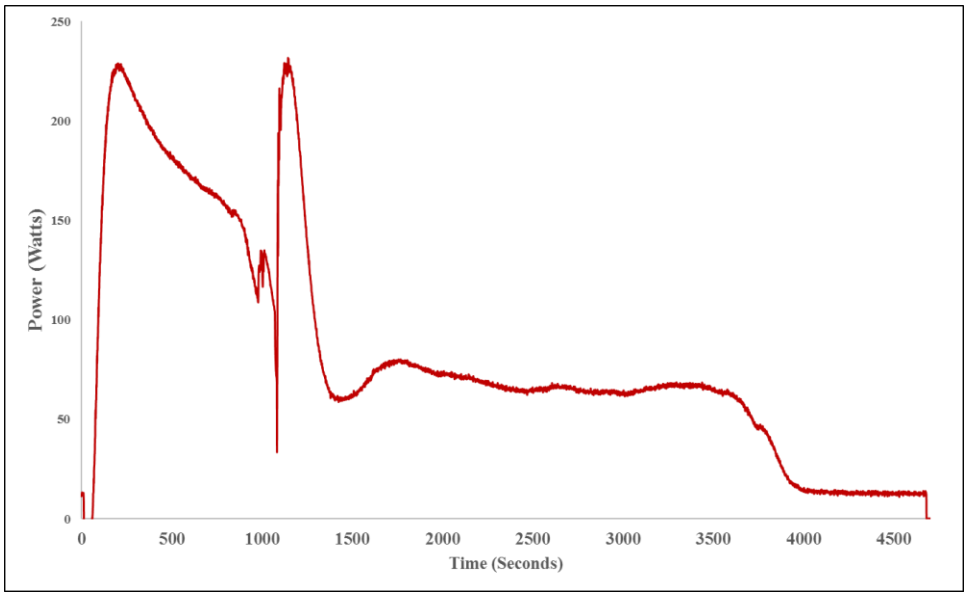

Figure 152: Counter-current, Instantaneous Power Rating for volumetric flow rate of 5 GPH with T_{hot} of 37.4 °C and T_{cold} of 25 °C (Case V).

APPENDIX G

This section provides a summary of the average power and ΔT_{HTF} for the non-insulated vs. insulated cases (pre-experiment calibration).

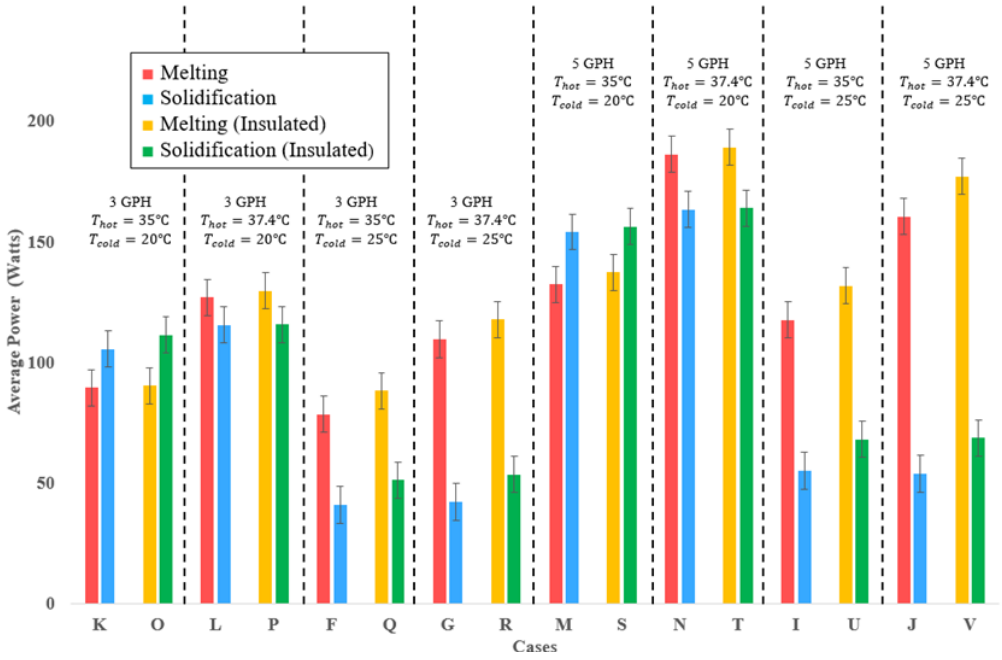

Figure 153: Average Power Rating for Non-insulated and Insulated Cases (at 90% Mass Fraction for melting).

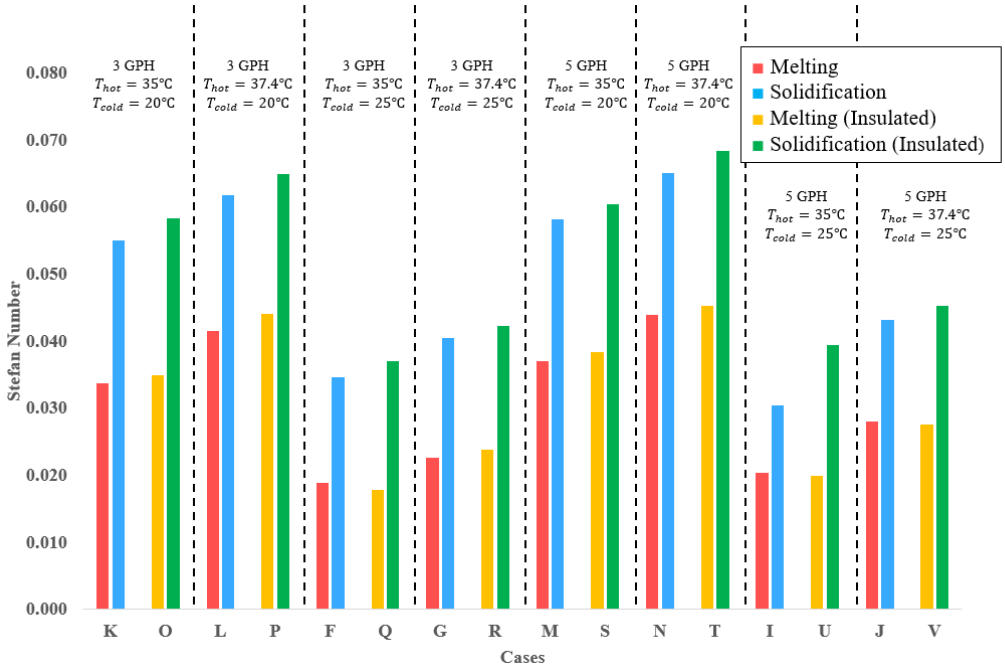

Figure 154: Duration of Phase Change for Non-insulated and Insulated Cases (at 90% Mass Fraction for melting).

APPENDIX H

This section provides a comparison of the experimental measurements and calculations using the pre-experiment and post-experiment calibration constants.

Table 31: Summary of experimental measurements and calculations for 90% melting case, with pre-experiment and post-experiment calibrations. At a flow rate of 3 GPH (co-current), inlet temperature of HTF during melting is 35 °C and during solidification is 25 °C (Case A).

90 % Melt	Pre-experiment Calibration		Post-experiment Calibration	
Case A	Melting (Dehydration)	Solidification (Hydration)	Melting (Dehydration)	Solidification (Hydration)
Inlet Temperature (°C)	35	25	35	25
Average Mass Flowrate (kg/sec)	0.0036	0.0037	0.0036	0.0037
ΔTHTF, Average (°C)	4.70	3.78	4.58	3.92
Total Energy Storage Capacity (KJ)	147.33	155.61	143.13	162.01
Duration of Phase Change (Seconds)	2107	2099	2107	2099
Duration of Phase Change (Minutes)	35.11	34.98	35.11	34.98
Average Power (Watts)	71.35	57.52	69.67	59.71
Effectiveness	0.8	1	0.8	1
Stefan Number	0.022	0.038	0.022	0.038

Table 32: Summary of experimental measurements and calculations for 90% melting case, with pre-experiment and post-experiment calibrations. At a flow rate of 3 GPH (co-current), inlet temperature of HTF during melting is 37.4 °C and during solidification is 25 °C (Case B).

90 % Melt	Pre-experiment Calibration		Post-experiment Calibration	
Case B	Melting (Dehydration)	Solidification (Hydration)	Melting (Dehydration)	Solidification (Hydration)
Inlet Temperature (°C)	37.4	25	37.4	25
Average Mass Flowrate (kg/sec)	0.0036	0.0037	0.0036	0.0037
ΔTHTF, Average (°C)	8.25	3.14	8.44	3.03
Total Energy Storage Capacity (KJ)	154.19	166.74	158.11	160.97
Duration of Phase Change (Seconds)	1216	2678	1216	2678
Duration of Phase Change (Minutes)	20.27	44.63	20.27	44.63
Average Power (Watts)	125.29	47.85	128.10	46.24
Effectiveness	0.8	1	0.8	1
Stefan Number	0.028	0.047	0.028	0.047

Table 33: Summary of experimental measurements and calculations for 90% melting case, with pre-experiment and post-experiment calibrations. At a flow rate of 5 GPH (co-current), inlet temperature of HTF during melting is 35 °C and during solidification is 25 °C (Case C).

90 % Melt	Pre-experiment Calibration		Post-experiment Calibration	
Case C	Melting (Dehydration)	Solidification (Hydration)	Melting (Dehydration)	Solidification (Hydration)
Inlet Temperature (°C)	35	25	35	25
Average Mass Flowrate (kg/sec)	0.0052	0.0052	0.0052	0.0052
ΔTHTF, Average (°C)	4.98	3.42	4.86	3.56
Total Energy Storage Capacity (KJ)	150.99	184.85	146.91	193.13
Duration of Phase Change (Seconds)	1449	1922	1449	1922
Duration of Phase Change (Minutes)	24.15	32.03	24.15	32.03
Average Power (Watts)	108.56	74.78	106.18	77.88
Effectiveness	0.8	1	0.8	1
Stefan Number	0.022	0.042	0.022	0.042

Table 34: Summary of experimental measurements and calculations for 90% melting case, with pre-experiment and post-experiment calibrations. At a flow rate of 5 GPH (co-current), inlet temperature of HTF during melting is 37.4 °C and during solidification is 25 °C (Case D).

90 % Melt	Pre-experiment Calibration		Post-experiment Calibration	
Case D	Melting (Dehydration)	Solidification (Hydration)	Melting (Dehydration)	Solidification (Hydration)
Inlet Temperature (°C)	37.4	25	37.4	25
Average Mass Flowrate (kg/sec)	0.0052	0.0052	0.0052	0.0052
ΔTHTF, Average (°C)	7.16	3.48	7.06	3.62
Total Energy Storage Capacity (KJ)	160.86	186.67	157.85	194.57
Duration of Phase Change (Seconds)	1074	1826	1074	1826
Duration of Phase Change (Minutes)	17.89	30.43	17.89	30.43
Average Power (Watts)	156.19	76.09	154.03	79.19
Effectiveness	0.8	1	0.8	1
Stefan Number	0.028	0.048	0.028	0.048

Table 35: Summary of experimental measurements and calculations for 90% melting case, with pre-experiment and post-experiment calibrations. At a flow rate of 3 GPH (counter-current), inlet temperature of HTF during melting is 33 °C and during solidification is 25 °C (Case E).

90 % Melt	Pre-experiment Calibration		Post-experiment Calibration	
Case E	Melting (Dehydration)	Solidification (Hydration)	Melting (Dehydration)	Solidification (Hydration)
Inlet Temperature (°C)	33	25	33	25
Average Mass Flowrate (kg/sec)	0.0036	0.0036	0.0037	0.0036
ΔTHTF, Average (°C)	3.98	3.38	3.87	3.28
Total Energy Storage Capacity (KJ)	173.57	189.52	168.54	183.14
Duration of Phase Change (Seconds)	2802	3412	2802	3412
Duration of Phase Change (Minutes)	46.69	56.86	46.69	56.86
Average Power (Watts)	60.52	50.96	58.82	49.41
Effectiveness	0.8	1	0.8	1
Stefan Number	0.016	0.031	0.016	0.031

Table 36: Summary of experimental measurements and calculations for 90% melting case, with pre-experiment and post-experiment calibrations. At a flow rate of 3 GPH (counter-current), inlet temperature of HTF during melting is 35 °C and during solidification is 25 °C (Case F).

90 % Melt	Pre-experiment Calibration		Post-experiment Calibration	
Case F	Melting (Dehydration)	Solidification (Hydration)	Melting (Dehydration)	Solidification (Hydration)
Inlet Temperature (°C)	35	25	35	25
Average Mass Flowrate (kg/sec)	0.0036	0.0037	0.0036	0.0037
ΔTHTF, Average (°C)	5.17	2.69	5.06	2.58
Total Energy Storage Capacity (KJ)	152.63	166.33	149.25	159.18
Duration of Phase Change (Seconds)	1861	3590	1861	3590
Duration of Phase Change (Minutes)	31.01	59.83	31.01	59.83
Average Power (Watts)	78.56	41.05	76.92	39.41
Effectiveness	0.8	1	0.8	1
Stefan Number	0.019	0.035	0.019	0.035

Table 37: Summary of experimental measurements and calculations for 90% melting case, with pre-experiment and post-experiment calibrations. At a flow rate of 3 GPH (counter-current), inlet temperature of HTF during melting is 37.4 °C and during solidification is 25 °C (Case G).

90 % Melt	Pre-experiment Calibration		Post-experiment Calibration	
Case G	Melting (Dehydration)	Solidification (Hydration)	Melting (Dehydration)	Solidification (Hydration)
Inlet Temperature (°C)	37.4	25	37.4	25
Average Mass Flowrate (kg/sec)	0.0036	0.0037	0.0036	0.0037
ΔTHTF, Average (°C)	7.22	2.75	7.12	2.64
Total Energy Storage Capacity (KJ)	156.56	162.13	154.19	155.46
Duration of Phase Change (Seconds)	1385	3278	1385	3278
Duration of Phase Change (Minutes)	23.09	54.63	23.09	54.63
Average Power (Watts)	109.62	42.30	108.12	40.66
Effectiveness	0.8	1	0.8	1
Stefan Number	0.023	0.040	0.023	0.040

Table 38: Summary of experimental measurements and calculations for 90% melting case, with pre-experiment and post-experiment calibrations. At a flow rate of 5 GPH (counter-current), inlet temperature of HTF during melting is 33 °C and during solidification is 25 °C (Case H).

90 % Melt	Pre-experiment Calibration		Post-experiment Calibration	
Case H	Melting (Dehydration)	Solidification (Hydration)	Melting (Dehydration)	Solidification (Hydration)
Inlet Temperature (°C)	33	25	33	25
Average Mass Flowrate (kg/sec)	0.0052	0.0053	0.0052	0.0053
ΔTHTF, Average (°C)	4.06	3.25	3.94	3.15
Total Energy Storage Capacity (KJ)	185.48	196.88	180.13	189.57
Duration of Phase Change (Seconds)	2077	2627	2077	2627
Duration of Phase Change (Minutes)	34.62	43.78	34.62	43.78
Average Power (Watts)	88.57	71.44	86.14	69.16
Effectiveness	0.8	1	0.8	1
Stefan Number	0.011	0.030	0.011	0.030

Table 39: Summary of experimental measurements and calculations for 90% melting case, with pre-experiment and post-experiment calibrations. At a flow rate of 5 GPH (counter-current), inlet temperature of HTF during melting is 35 °C and during solidification is 25 °C (Case I).

90 % Melt	Pre-experiment Calibration		Post-experiment Calibration	
Case I	Melting (Dehydration)	Solidification (Hydration)	Melting (Dehydration)	Solidification (Hydration)
Inlet Temperature (°C)	35	25	35	25
Average Mass Flowrate (kg/sec)	0.0052	0.0053	0.0052	0.0053
ΔTHTF, Average (°C)	5.40	2.50	5.29	2.39
Total Energy Storage Capacity (KJ)	168.56	160.63	165.03	153.18
Duration of Phase Change (Seconds)	1391	2550	1391	2550
Duration of Phase Change (Minutes)	23.18	42.51	23.18	42.51
Average Power (Watts)	117.74	54.99	115.42	52.62
Effectiveness	0.8	1	0.8	1
Stefan Number	0.020	0.035	0.020	0.035

Table 40: Summary of experimental measurements and calculations for 90% melting case, with pre-experiment and post-experiment calibrations. At a flow rate of 5 GPH (counter-current), inlet temperature of HTF during melting is 37.4 °C and during solidification is 25 °C (Case J).

90 % Melt	Pre-experiment Calibration		Post-experiment Calibration	
Case J	Melting (Dehydration)	Solidification (Hydration)	Melting (Dehydration)	Solidification (Hydration)
Inlet Temperature (°C)	37.4	25	37.4	25
Average Mass Flowrate (kg/sec)	0.0052	0.0053	0.0052	0.0053
ΔTHTF, Average (°C)	7.36	2.46	7.26	2.35
Total Energy Storage Capacity (KJ)	177.18	174.59	174.54	166.85
Duration of Phase Change (Seconds)	1058	2700	1058	2700
Duration of Phase Change (Minutes)	17.63	45.01	17.63	45.01
Average Power (Watts)	160.60	53.97	158.45	51.60
Effectiveness	0.8	1	0.8	1
Stefan Number	0.028	0.043	0.028	0.043

Table 41: Summary of experimental measurements and calculations for 90% melting case, with pre-experiment and post-experiment calibrations. At a flow rate of 3 GPH (counter-current), inlet temperature of HTF during melting is 35 °C and during solidification is 20 °C (Case K).

90 % Melt	Pre-experiment Calibration		Post-experiment Calibration	
Case K	Melting (Dehydration)	Solidification (Hydration)	Melting (Dehydration)	Solidification (Hydration)
Inlet Temperature (°C)	35	20	35	20
Average Mass Flowrate (kg/sec)	0.0036	0.0036	0.0036	0.0036
ΔTHTF, Average (°C)	5.89	7.09	5.79	7.01
Total Energy Storage Capacity (KJ)	179.46	208.21	176.34	205.31
Duration of Phase Change (Seconds)	1881	1736	1881	1736
Duration of Phase Change (Minutes)	31.34	28.93	31.34	28.93
Average Power (Watts)	89.57	105.55	88.01	104.40
Effectiveness	0.8	1	0.8	1
Stefan Number	0.034	0.055	0.034	0.055

Table 42: Summary of experimental measurements and calculations for 90% melting case, with pre-experiment and post-experiment calibrations. At a flow rate of 3 GPH (counter-current), inlet temperature of HTF during melting is 37.4 °C and during solidification is 20 °C (Case L).

90 % Melt	Pre-experiment Calibration		Post-experiment Calibration	
Case L	Melting (Dehydration)	Solidification (Hydration)	Melting (Dehydration)	Solidification (Hydration)
Inlet Temperature (°C)	37.4	20	37.4	20
Average Mass Flowrate (kg/sec)	0.0036	0.0036	0.0036	0.0036
ΔTHTF, Average (°C)	8.36	7.69	8.27	7.61
Total Energy Storage Capacity (KJ)	176.37	223.00	174.39	220.12
Duration of Phase Change (Seconds)	1301	1793	1301	1793
Duration of Phase Change (Minutes)	21.68	29.88	21.68	29.88
Average Power (Watts)	127.04	115.64	125.65	114.52
Effectiveness	0.8	1	0.8	1
Stefan Number	0.042	0.062	0.042	0.062

Table 43: Summary of experimental measurements and calculations for 90% melting case, with pre-experiment and post-experiment calibrations. At a flow rate of 5 GPH (counter-current), inlet temperature of HTF during melting is 35 °C and during solidification is 20 °C (Case M).

90 % Melt	Pre-experiment Calibration		Post-experiment Calibration	
Case M	Melting (Dehydration)	Solidification (Hydration)	Melting (Dehydration)	Solidification (Hydration)
Inlet Temperature (°C)	35	20	35	20
Average Mass Flowrate (kg/sec)	0.0052	0.0052	0.0052	0.0052
ΔTHTF, Average (°C)	6.07	7.07	5.96	6.99
Total Energy Storage Capacity (KJ)	213.40	212.85	209.87	209.81
Duration of Phase Change (Seconds)	1497	1218	1497	1218
Duration of Phase Change (Minutes)	24.95	20.29	24.95	20.29
Average Power Watts)	132.45	154.24	130.22	152.58
Effectiveness	0.8	1	0.8	1
Stefan Number	0.037	0.058	0.037	0.058

Table 44: Summary of experimental measurements and calculations for 90% melting case, with pre-experiment and post-experiment calibrations. At a flow rate of 5 GPH (counter-current), inlet temperature of HTF during melting is 37.4 °C and during solidification is 20 °C (Case N).

90 % Melt	Pre-experiment Calibration		Post-experiment Calibration	
Case N	Melting (Dehydration)	Solidification (Hydration)	Melting (Dehydration)	Solidification (Hydration)
Inlet Temperature (°C)	37.4	20	37.4	20
Average Mass Flowrate (kg/sec)	0.0052	0.0053	0.0052	0.0053
ΔTHTF, Average (°C)	8.55	7.44	8.45	7.37
Total Energy Storage Capacity (KJ)	203.51	220.81	201.31	217.86
Duration of Phase Change (Seconds)	1010	1268	1010	1268
Duration of Phase Change (Minutes)	16.83	21.13	16.83	21.13
Average Power (Watts)	186.46	163.55	184.47	161.90
Effectiveness	0.8	1	0.8	1
Stefan Number	0.044	0.065	0.044	0.065

Table 45: Summary of experimental measurements and calculations for 90% melting case, with pre-experiment and post-experiment calibrations. At a flow rate of 3 GPH (counter-current), inlet temperature of HTF during melting is 35 °C and during solidification is 20 °C (Case O).

90 % Melt	Pre-experiment Calibration		Post-experiment Calibration	
Case O	Melting (Dehydration)	Solidification (Hydration)	Melting (Dehydration)	Solidification (Hydration)
Inlet Temperature (°C)	35	20	35	20
Average Mass Flowrate (kg/sec)	0.0036	0.0037	0.00	0.00
ΔTHTF, Average (°C)	5.95	7.18	5.89	7.06
Total Energy Storage Capacity (KJ)	175.19	184.78	172.23	182.28
Duration of Phase Change (Seconds)	1817	1356	1817	1356
Duration of Phase Change (Minutes)	30.28	22.60	30.28	22.60
Average Power (Watts)	90.39	111.37	89.56	109.54
Effectiveness	0.8	1	0.8	1
Stefan Number	0.035	0.058	0.035	0.058

Table 46: Summary of experimental measurements and calculations for 90% melting case, with pre-experiment and post-experiment calibrations. At a flow rate of 3 GPH (counter-current), inlet temperature of HTF during melting is 37.4 °C and during solidification is 20 °C (Case P).

90 % Melt	Pre-experiment Calibration		Post-experiment Calibration	
Case P	Melting (Dehydration)	Solidification (Hydration)	Melting (Dehydration)	Solidification (Hydration)
Inlet Temperature (°C)	37.4	20	37.4	20
Average Mass Flowrate (kg/sec)	0.0036	0.0036	0.0036	0.0036
ΔTHTF, Average (°C)	8.55	7.62	8.45	7.54
Total Energy Storage Capacity (KJ)	169.80	221.20	167.91	218.41
Duration of Phase Change (Seconds)	1158	1722	1158	1722
Duration of Phase Change (Minutes)	19.29	28.70	19.29	28.70
Average Power (Watts)	129.82	115.72	128.45	114.58
Effectiveness	0.8	1	0.8	1
Stefan Number	0.044	0.065	0.044	0.065

Table 47: Summary of experimental measurements and calculations for 90% melting case, with pre-experiment and post-experiment calibrations. At a flow rate of 3 GPH (counter-current), inlet temperature of HTF during melting is 35 °C and during solidification is 25 °C (Case Q).

90 % Melt	Pre-experiment Calibration		Post-experiment Calibration	
Case Q	Melting (Dehydration)	Solidification (Hydration)	Melting (Dehydration)	Solidification (Hydration)
Inlet Temperature (°C)	35	25	35	25
Average Mass Flowrate (kg/sec)	0.0036	0.0037	0.0036	0.0037
ΔTHTF, Average (°C)	5.81	3.34	5.71	3.26
Total Energy Storage Capacity (KJ)	152.66	187.90	149.71	194.82
Duration of Phase Change (Seconds)	1681	3327	1681	3327
Duration of Phase Change (Minutes)	28.02	55.46	28.02	55.46
Average Power (Watts)	88.31	51.30	86.74	50.08
Effectiveness	0.8	1	0.8	1
Stefan Number	0.018	0.037	0.018	0.037

Table 48: Summary of experimental measurements and calculations for 90% melting case, with pre-experiment and post-experiment calibrations. At a flow rate of 3 GPH (counter-current), inlet temperature of HTF during melting is 37.4 °C and during solidification is 25 °C (Case R).

90 % Melt	Pre-experiment Calibration		Post-experiment Calibration	
Case R	Melting (Dehydration)	Solidification (Hydration)	Melting (Dehydration)	Solidification (Hydration)
Inlet Temperature (°C)	37.4	25	37.4	25
Average Mass Flowrate (kg/sec)	0.0036	0.0037	0.0036	0.0037
ΔTHTF, Average (°C)	7.76	3.44	7.66	3.39
Total Energy Storage Capacity (KJ)	152.79	195.23	150.69	199.78
Duration of Phase Change (Seconds)	1245	3372	1245	3372
Duration of Phase Change (Minutes)	20.74	56.21	20.74	56.21
Average Power (Watts)	117.83	53.52	116.39	52.85
Effectiveness	0.8	1	0.8	1
Stefan Number	0.024	0.042	0.024	0.042

Table 49: Summary of experimental measurements and calculations for 90% melting case, with pre-experiment and post-experiment calibrations. At a flow rate of 5 GPH (counter-current), inlet temperature of HTF during melting is 35 °C and during solidification is 20 °C (Case S).

90 % Melt	Pre-experiment Calibration		Post-experiment Calibration	
Case S	Melting (Dehydration)	Solidification (Hydration)	Melting (Dehydration)	Solidification (Hydration)
Inlet Temperature (°C)	35	20	35	20
Average Mass Flowrate (kg/sec)	0.0052	0.0053	0.0052	0.0053
ΔTHTF, Average (°C)	6.30	7.06	6.20	6.98
Total Energy Storage Capacity (KJ)	196.64	209.53	193.49	206.56
Duration of Phase Change (Seconds)	1316	1110	1316	1110
Duration of Phase Change (Minutes)	21.93	18.51	21.93	18.51
Average Power (Watts)	137.53	156.39	135.33	154.71
Effectiveness	0.8	1	0.8	1
Stefan Number	0.038	0.060	0.038	0.060

Table 50: Summary of experimental measurements and calculations for 90% melting case, with pre-experiment and post-experiment calibrations. At a flow rate of 5 GPH (counter-current), inlet temperature of HTF during melting is 37.4 °C and during solidification is 20 °C (Case T).

90 % Melt	Pre-experiment Calibration		Post-experiment Calibration	
Case T	Melting (Dehydration)	Solidification (Hydration)	Melting (Dehydration)	Solidification (Hydration)
Inlet Temperature (°C)	37.4	20	37.4	20
Average Mass Flowrate (kg/sec)	0.0052	0.0053	0.0052	0.0053
ΔTHTF, Average (°C)	8.68	7.46	8.58	7.38
Total Energy Storage Capacity (KJ)	189.42	217.73	187.44	214.85
Duration of Phase Change (Seconds)	910	1251	910	1251
Duration of Phase Change (Minutes)	15.17	20.86	15.17	20.86
Average Power (Watts)	189.26	164.17	187.30	162.52
Effectiveness	0.8	1	0.8	1
Stefan Number	0.045	0.068	0.045	0.068

Table 51: Summary of experimental measurements and calculations for 90% melting case, with pre-experiment and post-experiment calibrations. At a flow rate of 5 GPH (counter-current), inlet temperature of HTF during melting is 35 °C and during solidification is 25 °C (Case U).

90 % Melt	Pre-experiment Calibration		Post-experiment Calibration	
Case U	Melting (Dehydration)	Solidification (Hydration)	Melting (Dehydration)	Solidification (Hydration)
Inlet Temperature (°C)	35	25	35	25
Average Mass Flowrate (kg/sec)	0.0052	0.0053	0.0052	0.0053
ΔTHTF, Average (°C)	6.04	3.08	5.93	3.00
Total Energy Storage Capacity (KJ)	179.63	191.63	176.27	202.88
Duration of Phase Change (Seconds)	1275	2590	1275	2590
Duration of Phase Change (Minutes)	21.25	43.16	21.25	43.16
Average Power (Watts)	131.77	68.12	129.53	66.34
Effectiveness	0.8	1	0.8	1
Stefan Number	0.020	0.040	0.020	0.040

Table 52: Summary of experimental measurements and calculations for 90% melting case, with pre-experiment and post-experiment calibrations. At a flow rate of 5 GPH (counter-current), inlet temperature of HTF during melting is 37.4 °C and during solidification is 25 °C (Case V).

90 % Melt	Pre-experiment Calibration		Post-experiment Calibration	
Case V	Melting (Dehydration)	Solidification (Hydration)	Melting (Dehydration)	Solidification (Hydration)
Inlet Temperature (°C)	37.4	25	37.4	25
Average Mass Flowrate (kg/sec)	0.0052	0.0053	0.0052	0.0053
ΔTHTF, Average (°C)	8.13	3.10	8.03	3.00
Total Energy Storage Capacity (KJ)	177.18	205.73	174.89	208.97
Duration of Phase Change (Seconds)	951	2540	951	2540
Duration of Phase Change (Minutes)	15.85	42.34	15.85	42.34
Average Power (Watts)	177.22	68.71	175.17	66.40
Effectiveness	0.8	1	0.8	1
Stefan Number	0.028	0.045	0.028	0.045

Table 53: Summary of the difference for melting experimental measurement and calculation results for pre-experiment and post-experiment calibrations.

Cases for Melting	ΔTHTF, Average difference (%)	Total Energy Storage Capacity difference (%)	Average Power difference (%)
A	2.4	2.8	2.3
B	2.2	2.5	2.2
C	2.2	2.7	2.2
D	1.4	1.9	1.4
E	2.8	2.9	2.8
F	2.1	2.2	2.1
G	1.4	1.5	1.4
H	2.8	2.9	2.7
I	2.0	2.1	2.0
J	1.4	1.5	1.3
K	1.8	1.7	1.7
L	1.1	1.1	1.1
M	1.7	1.7	1.7
N	1.1	1.1	1.1
O	1.0	1.7	0.9
P	1.1	1.1	1.1
Q	1.8	1.9	1.8
R	1.3	1.4	1.2
S	1.6	1.6	1.6
T	1.1	1.0	1.0
U	1.7	1.9	1.7
V	1.2	1.3	1.2

Table 54: Summary of the difference for solidification experimental measurements and calculation of results for pre-experiment and post-experiment calibrations.

Cases for Solidification	$\Delta T_{HTF,\ Average}$ (%)	Total Energy Storage Capacity (%)	Average Power (%)
A	3.8	4.1	3.8
B	3.4	3.5	3.4
C	4.1	4.5	4.1
D	4.0	4.2	4.1
E	3.1	3.4	3.1
F	4.0	4.3	4.0
G	3.9	4.1	3.9
H	3.2	3.7	3.2
I	4.4	4.6	4.3
J	4.4	4.4	4.4
K	1.1	1.4	1.1
L	1.0	1.3	1.0
M	1.1	1.4	1.1
N	1.0	1.3	1.0
O	1.7	1.4	1.6
P	1.0	1.3	1.0
Q	2.4	3.7	2.4
R	1.3	2.3	1.2
S	1.1	1.4	1.1
T	1.0	1.3	1.0
U	2.6	5.9	2.6
V	3.4	3.4	3.4